CBM

Compressed Baryonic Matter experiment at FAIR

PROGRESS REPORT

2012

CBM Progress Report 2012

Dear Colleagues,

2012 was a very important and finally successful year for FAIR and CBM. FAIR received the building permit together with 526 Million Euros for civil construction from the German Ministry for Education and Research. The construction site has been cleared, giving an impression on the size and the shape of the future facility (see picture below). GSI has been restructured in order to focus all activities onto the realization of the SIS-100 accelerator and the FAIR experiments.

In December 2012, the CBM collaboration submitted Technical Design Reports for two major components of the experiment: the Superconducting Dipole Magnet, and the Silicon Tracking System. The TDRs for the Projectile Spectator Detector and for the Ring Imaging Cherenkov detectors will be submitted in spring 2013. Many thanks to all of you who participated in this effort.

Peter Senger

Contents

Status of the CBM Experiment at FAIR

P. Senger and the CBM Collaboration
GSI, Darmstadt, Germany

The Compressed Baryonic Matter (CBM) experiment is designed to explore the QCD phase diagram in the region of high net-baryon densities using novel diagnostic probes. The layout of the CBM detectors is driven by the experimental requirements concerning reaction rates, radiation tolerance, particle densities, and selectivity. The experimental setup comprises the following components.

The superconducting dipole magnet

In 2012 the design of the CBM SC dipole magnet was optimized. The magnet is of H-type with circular superconducting coils and with two cryostats (see Fig. 1). It has a large aperture (gap height 140 cm, gap width 260 cm) in order to host the Silicon Tracking System. The field integral is 1 Tm. The Technical Design Report was submitted to FAIR in December 2012.
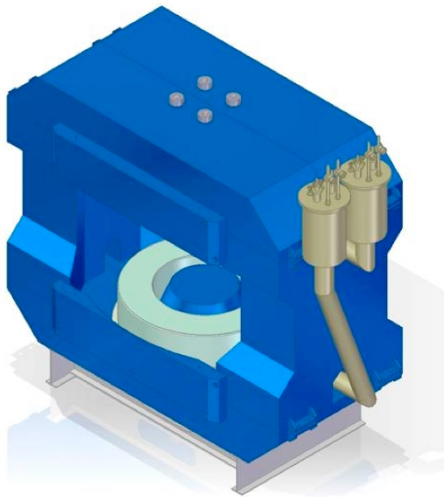
Figure 1: The CBM Superconducting Dipole Magnet

The Micro-Vertex Detector

The precise determination of the secondary decay vertices of charmed particles requires a highly-granulated, fast, radiation-hard, and low-mass detector system. We will use silicon pixel stations which are based on ultra-thin Monolithic Active Pixel Sensors (MAPS). Sensors have been developed which exhibit a high signal-to-noise ratio even after an integrated neutron dose of 10^{13} n_{eq}/cm^2. Prototype detectors comprising sensors, a read-out-system, a cooling and support structure have been successfully tested with a 120 GeV pion beam at CERN.

The Silicon Tracking System

The CBM Silicon Tracking System (STS) is based on double-sided micro-strip sensors with outer dimensions of 6.2×2.2 cm^2, 6.2×4.2 cm^2, and 6.2×6.2 cm^2. The front side strips are inclined by a stereo angle of $7.5°$. Short strips in the sensor corners will be interconnected to a strip in the opposite corner either via a second metallization layer or via an additional micro-cable. Both options are under investigation. Each sensor (2048 strips) is read out via 16 low-mass micro cables (128 wires each) by 8 free-streaming ASICs (2 channels each). The cables will be tab-bonded at both ends. Several of these modules consisting of a sensor, the cables and the front-end board carrying 8 ASICs will be mounted on a light-weight carbon ladder. Up to 16 of these ladders will be integrated into a detector station. The STS consists of 8 stations of increasing size and increasing granularity with increasing distance from the target (see Fig. 2). The STS will be operated in a thermal enclosure at about -10°C. The Technical Design Report was submitted to FAIR in December 2012.
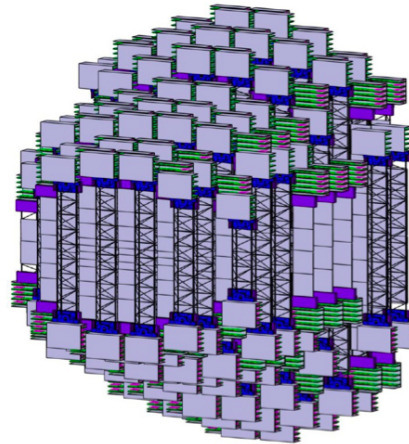
Figure 2: The CBM Silicon Tracking System

The Ring Imaging Cherenkov detector

The RICH photo-detector exhibits an active area of 2.4 m^2 and ∼55000 individual readout channels. In 2012, two additional options for photo sensors were investigated as possible alternative to the Hamamatsu H8500 baseline solution: The Hamamatsu R11265, a smaller 1" square

tube with enhanced quantum efficiency due to Super-Bialkali cathode; and a Micro Channel Plate (MCP) sensor from Photonis, XP85012, which is immune against magnetic stray fields. All three sensors were tested in parallel during a RICH test beam at CERN PS. In the beginning of 2012, the development of a new FPGA-TDC based readout concept for the RICH was started at the GSI electronic department. First prototype modules were successfully tested at CERN together with the previously used n-XYTER read-out, allowing for a direct comparison of the two different concepts.

The Muon Detection System

In order to identify soft muons from vector meson decays in a large combinatorial background, CBM will use an instrumented hadron absorber. The detection system comprises 6 iron slabs of varying thickness from 20 cm to 100 cm, with detector triplets behind each iron absorber. The technology of the gaseous muon tracking detectors is matched to the hit density and rate: behind the first and second hadron absorber (particle density up to $500\,\mathrm{kHz/cm^2}$) we will install Gas Electron Multiplier (GEM) detectors. Prototype GEM detectors with single-mask foils have been successfully tested with particle beams at CERN. Further downstream, where the hit density is reduced, straw-tube detectors will be used. Full size prototype straw-tube detector modules have been built and tested.

The Transition Radiation Detector

The CBM Transition Radiation detector (TRD) has to provide an electron/pion suppression factor of the order of 100 for momenta above $1\,\mathrm{GeV}/c$ at hit rates of $100\,\mathrm{kHz/cm^2}$. A pion suppression factor of 100 (corresponding to a pion efficiency of 1 %), together with an electron efficiency of better than 90 %, can be achieved with 9–10 layers of TRD chambers, resulting in an overall detector area of almost $600\,\mathrm{m^2}$. Several prototype detectors have been developed to fulfil the requirements, such as prototype fast multi-wire chambers with and without drift sec-

tion read-out by the self-triggered SPADIC chip. Moreover, a two-dimension position sensitive prototype TRD with diagonally split rectangular (i.e., triangular) read-out pads has been built. All prototype TRDs were successfully tested at CERN using a mixed beam of electrons and pions.

Timing Multi-gap RPCs

An array of Multi-gap Resistive Plate Chambers (MRPCs) will be used for hadron identification via TOF measurements. The TOF wall covers an active area of about $120\,\mathrm{m^2}$ and is located about 6 m downstream of the target for measurements at SIS-100, and at 10 m at SIS-300. The required time resolution is of the order of 80 ps. For 10 MHz minimum bias Au+Au collisions, the innermost part of the detector has to work at rates up to $20\,\mathrm{kHz/cm^2}$. Prototype MRPCs built with low-resistivity glass have been tested with a time resolution of $\sigma = 40 - 60\,\mathrm{ps}$ at $20\,\mathrm{kHz/cm^2}$. At small deflection angles the pad size is about $5\,\mathrm{cm^2}$, corresponding to an occupancy of below 5 % for central Au+Au collisions at $25A$ GeV. In order to optimize the number of gaps, the pad layout, and the read-out electronics, several prototype MRPCs have been tested with particle beams at CERN. At large polar emission angles, i.e. in most of the active area of the CBM TOF detector, the hit rate is of the order of $1\,\mathrm{kHz/cm^2}$. At these low rates, a conventional MRPC in multi-strip configuration with thin standard float glass can be used. For this application, a fully differential prototype MRPC has been built and tested successfully at COSY with a proton beam.

Online event selection

Measurements with high event rates require online event selection algorithms (and hardware) which reject the background events (which contain no signal) by a factor of 100 or more. The event selection system will be based on a fast online event reconstruction running on a high-performance computer farm equipped with many-core CPUs and graphics cards (GSI GreenIT cube).

Table 1: CBM subsystems, their status, and time of TDR submission

System	Status	TDR submission
Magnet	design ready	December 2012
Micro-Vertex Detector	successful prototype tests with beams	2014
Silicon Tracking System	design ready, successful prototype tests with beams	December 2012
Ring Imaging Cherenkov detector	design ready, successful prototype tests with beams	spring 2013
Muon Tracking Chambers (MUCH)	prototype MUCH successfully tested with beams	end of 2013
Transition Radiation Detector (TRD)	prototype TRDs successfully tested with beams	2014
Time-of-Flight wall (Multi-gap RPCs)	prototype MRPCs successfully tested with beams	2013
Electromagnetic Calorimeter (ECAL)	design ready, established technology	2013/2014
Projectile Spectator Detector (PSD)	design ready, established technology	spring 2013
DAQ/FLES	prototype tests with beams	2013 – 2016

Prototyping the CBM Micro-Vertex Detector

M. Koziel for the CBM-MVD collaboration

Institut für Kernphysik, Goethe-Universität, Frankfurt, Germany

The need for prototyping and characterizing the CBM Micro-Vertex Detector (MVD) motivated the construction of an ultra-low mass, high-precision detector setup incorporating several prototype stations. Each station consists of a "core module", that is two 50 μm thick MIMOSA-26 CMOS pixel sensors [1] adhesive-bonded to a mechanical support ensuring heat evacuation and wire-bonded to the dedicated Flex Print Cable. Three mechanical supports were used: 1 mm thick aluminium with openings and a 200 μm thick CVD diamond with and without (double-sided module) openings (Fig. 1). The openings are 16.5×8.2 mm^2 in size and are located in the middle of the active area of the MIMOSA-26 sensor. Modules with openings ensure stable mechanical support with minimum material budget of 0.05 %X$_0$ (Si only) at the region of openings. The double-sided unit features a material budget of 0.3 %X$_0$ (Si + adhesive + CVD).

Figure 1: CVD diamond support with openings to reduce the material budget

The detector setup discussed here incorporates four single-sided reference stations and one double-sided station in the middle, which is called Device Under Test (DUT) and serves for both a high-precision standalone tracking device and a test site for advanced integration concepts, with the focus on high-performance materials (e.g., CVD diamond). In addition, the full setup allows for validating the customized and scalable readout system design together with dedicated data analysis tools.
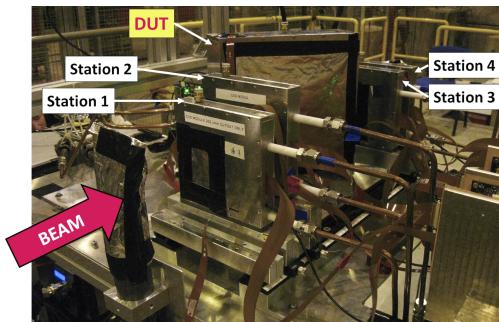
Figure 2: The IKF detector setup installed at the CERN-SPS (EHN1-North Area)

The beam test took place over five days in November 2012 at the CERN-SPS H6 extraction line. The setup is shown in Fig. 2. It highlighted several aspects as discussed in the following.

To validate our concepts regarding sensor integration and read-out, the main focus was put on reproducing the beam test results achieved with MIMOSA-26 sensors by IPHC Strasbourg: a detection efficiency above 99.5 % and a spatial resolution of about 3.5 μm (σ) were observed for an average fake hit rate (the average number of fake hits per pixel per frame) of about 10^{-5}, very well in accordance with the previously known sensor characteristics.

The precise knowledge of the sensor response to charged particles, needed to address proper simulations of the CBM detector, motivated the beam-test runs taken for different inclination angles (0°, 30°, 45°, 60°), beam energies (10, 80 and 120 GeV) as well as various DUT heat-sink temperatures (-6°C, +6°C, +17°C) and threshold voltages of the pixel discriminators housed by the chip. This analysis is ongoing, based on a precise alignment of the single-sided stations.

Since the double-sided CVD-diamond based prototype was designed to serve as a precise micro-tracking device, some test runs with a metal target in front of the DUT were taken.

The MIMOSA sensors have never been tested at running conditions imposing a high sensor occupancy. Since such conditions are expected for the CBM experiment, tests at high beam intensities were undertaken. The average flux was expected to be about 10 hits/frame, but because of non-uniformity of the beam, about 300 hits/frame are expected for some frames.

Simultaneously to data taking, it was possible to monitor the data quality and stability of the readout system. A typical frame rate was 8.68 kHz, corresponding to a data rate of 6 – 25 MB/s for the whole telescope (12 sensors running in parallel). The readout system was observed to be very stable for different data loads generated by ten MIMOSA-26 sensors working in parallel. No data loss or corrupted frames were observed. Moreover, sensors were synchronized with precision of one signal clock.

In summary, the prototype setup allowed to study various aspects of the sensor behavior and proved the mechanical stability and the flexibility of the DAQ system. The results of the beam test for different detector setups and for various sensor parameters and running conditions are considered very promising. The data analysis is in progress and announces further insights in sensor operation and integration concepts.

References

[1] C. Hu-Guo *et al.*, Nucl. Instrum. Methods **A 623** (2010) 480

Mechanical Integration of the CBM MVD Prototype

T. Tischler, S. Amar-Youcef, M. Deveaux, M. Koziel, C. Müntz, C. Schrader, and J.Stroth
for the CBM-MVD Collaboration
Institut für Kernphysik, Goethe-Universität, Frankfurt

The need for prototyping and characterizing the CBM-Micro Vertex Detector (MVD) motivated the construction of an ultra-low mass, high-precision detector setup comprising several stations. This setup aims at validating the detector concept (Fig. 1) and the selected technologies. The setup - one double-sided and four single-sided stations - was successfully tested at CERN SPS in November 2012.
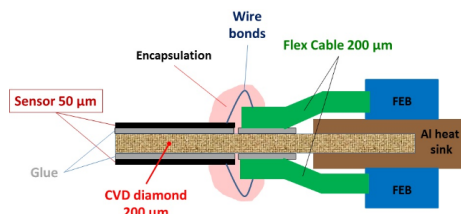
Figure 1: Schematic cross section

Each station contains two (single-sided station) or four (double-sided station) $50\,\mu m$ thick thinned CMOS sensors (MIMOSA-26 AHR [1], see Fig. 2 left), read-out by a customized data acquisition. The sensors are glued to $200\,\mu m$ thin CVD diamond carriers [2], which provide both mechanical support and efficient heat evacuation. The setup allows for different relative distances between the five detector stations, for different incident angles of the beam to the double-sided station, and for temperature cycling in a range between $-20°C$ and $+20°C$. The double-sided station - the ultra-thin, standalone tracking device with a material budget of $0.3\,\%X_0$ - represents the prototype being closest to the MVD geometry. Its active sensor area covers $1/4$ of that of the final detector. However, the relative position of the front- and backside sensors focus on standalone tracking (rather than on maximum acceptance). The four single-sided stations serve as reference system, also demonstrating the scalability of the read-out system. In contrast to the double-sided station, the CVD diamond carriers of the single-sided stations provide cut-outs in the major part of the active area of the sensors to achieve a minimum material budget for the reference system of $0.053\,\%X_0$ per station.

The integration of the $50\,\mu m$ thick thinned sensors calls for dedicated customized pick-up and positioning tools. The mechanical and thermal connection between the sensors and their carriers is realized with the low-viscosity glue E501 from Epotency. The thickness of the deposited glue has been evaluated to be less than $50\,\mu m$. The electrical connectivity between a dedicated FlexPrint-Cable (based on copper traces [3]) and the sensors is established

via wire bonding. The wire bonds were encapsulated with Sylgard 186 - a soft, silicon-based elastomer - to be protected against mechanical damage while handling.
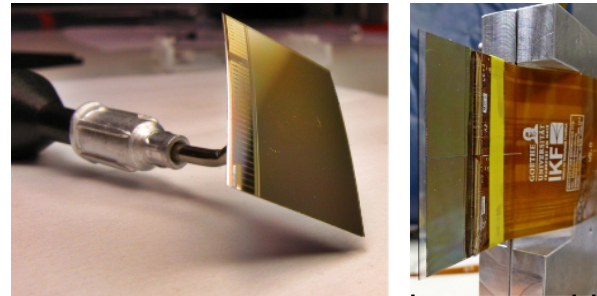
Figure 2: Curved MIMOSA-26 AHR, $50\,\mu m$ thick (left); assembled prototype (right)

For the first time, a detector station employing double-sided mounting of pixel sensors (MAPS) was realized with $50\,\mu m$ thick thinned sensors glued on both sides of a $200\,\mu m$ thin CVD diamond carrier as shown in Fig. 2 right. In contrast to the final CBM-MVD, the active area of the sensors is chosen to be overlapping to allow for micro-tracking with a fixed distance. The station thus forms a double-sided, ultra-thin tracking device with a thickness of only $0.3\,\%X_0$ (Fig. 3).

The reference stations provide precision tracking with a minimum material budget of $0.053\,\%X_0$ per station. A preliminary analysis of the recorded data shows a spatial resolution of the double-sided station of $< 4\,\mu m$ with a detection efficiency above $99.8\,\%$.
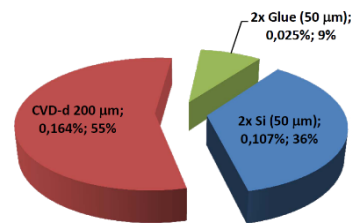
Figure 3: Material budget of the prototype

References

[1] C. Hu-Guo *et al.*, Nucl. Instrum. Methods **A 623** (2010) 480

[2] T. Tischler *et al.*, GSI Scientific Report 2010, p. 5

[3] C. Schrader *et al.*, GSI Scientific Report 2011, p. 8

Beamtime results of the MVD prototype DAQ network

B. Milanović, B. Neumann, M. Wiebusch, S. Amar-Youcef, M. Koziel, T. Tischler, Q. Li, I. Fröhlich, M. Deveaux, C. Müntz, and J. Stroth

IKF, Goethe University, Frankfurt, Germany

The CBM Micro Vertex Detector (MVD) is based on Monolithic Active Pixel Sensors (MAPS). In order to prove its suitability for upcoming experiments, a MVD prototype, representing one quarter of the first MVD station, was developed and tested during a beamtime at the CERN SPS accelerator in 2012 with high-energetic pion beams of varying intensity. The prototype (Device Under Test, DUT) employs four MIMOSA-26 AHR sensors thinned down to $50\,\mu m$ and glued back-to-back on the $200\,\mu m$ thick CVD diamond support. It therefore features double-sided MAPS sensors with excellent heat conductivity, material budget and non-ionizing radiation hardness. The test setup intended to demonstrate tracking capabilities of the MVD. Therefore the DUT was placed between four reference detector planes (see Fig. 1, left) also containing MIMOSA-26 AHR sensors.
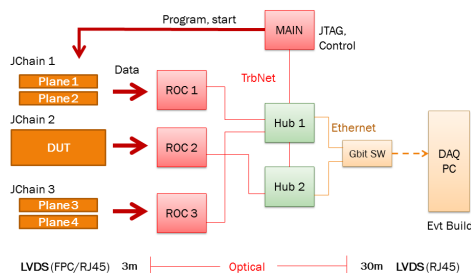
Figure 1: The prototype readout network

The sensors were operated via JTAG implemented on a central controller board called **M**VD **A**cquisition and **I**nteraction **N**ode (MAIN). The MAIN board is capable of controlling three independent JTAG chains with up to 6 MIMOSA sensors (tested). In total, 12 sensors were used in the setup (4 per chain). Specialized front-end electronics (FEEs), designed to sustain large radiation doses, were used to operate the sensors. The sensors were connected via short Flexprint Cables (FPCs) to the FEEs, and the FEEs were all connected with RJ45 cables over patch panels either to the MAIN board or to the Readout Controllers (ROCs) (see Fig. 1). The ROCs are responsible for the actual acquisition of data. Each ROC can process 4 sensors in parallel. The sensor data were checked online for errors, and a status report containing all the error bits was written with the data. For the implementation of the MAIN board and the ROCs, a TRBv2 board [1] with a general-purpose addon was used. The data were encoded using TrbNet [1] as network protocol and transmitted via optical links.

One single MIMOSA-26 AHR chip can produce up to 20 MB/s data at full occupancy. It can theoretically detect

up to 342 particles per event at an event rate of 8,68 kHz and under the asumption that each hit activates an area of 3×3 pixels. However, the data rate throughout the beamtime was very low. Even after achieving maximum beam intensity of 33 kHz, the entire setup featuring 10 active sensors produced 25,1 MB/s on average, half of which was noise. The peak sensor occupancy was 75 particles per event. After manually putting four sensors into saturation mode, a peak readout rate of 98 – 99 MB/s could be achieved. Under overload, the network synchronizes all frames by stopping the data buffers. New data are discarded until all buffers can take another event. Then, the data acquisition continues in a synchronous manner without errors. All sensors are synchronized within 10 ns because of a common clock and a simultaneous start signal provided by the MAIN board.

All power supplies, FPGAs and sensors were controlled and monitored actively (Fig. 2). An automated PERL script acquired data from 244 TrbNet registers and stored them in a local ASCII file for error analysis. Throughout the beamtime, no errors were observed. Merely two FEE boards had to be replaced because of mechanical damage. The presented network is highly scalable, meaning that more ROCs and Hubs can read out more sensors. In future, a new ROC based on TRBv3 will be implemented in order to support CBMNET and higher readout rates for the final MVD.

Figure 2: Beamtime DAQ monitoring tools

References

[1] J. Michel, *Development and Implementation of a New Trigger and Data Acquisition System for the HADES Detector*, PhD Thesis, Goethe University Frankfurt, 2012

Online data processing with the CBM-MVD prototype

Q. Li, S. Amar-Youcef, M. Deveaux, C. Müntz, and J. Stroth for the CBM-MVD Collaboration

Institut für Kernphysik, Goethe-Universität, Frankfurt, Germany

The CBM Micro Vertex Detector (MVD) will have to handle high data rates and occupancies, which calls for efficient data processing. We study the option to complement the on-chip zero suppression of the CMOS sensors by an online cluster finding and classification. The aim is to exploit the computing resources of the FPGAs controlling the sensors without increasing the network bandwidth needed for the consecutive data transport.
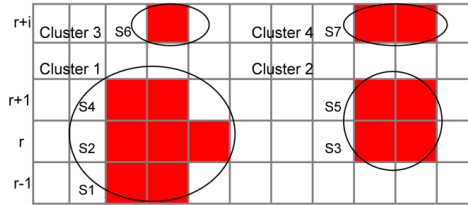
Figure 1: Clusters encoded in states

Our study relies on the MIMOSA-26AHR (M26) CMOS sensors [1] known from the MVD prototype. These sensors host digital circuits for data sparsification, which group up to four consecutive fired pixels in a line into a so-called state. This shape information is encoded together with the column number of the first pixel into a 16-bit word. Separate data words are needed to indicate the line number of the group. Figure 1 shows an example of four hit clusters comprising seven states (S1-S7) and four states for line information (not shown). In this example, 11 words of 16 bit are required to encode four clusters. In general, the precise number of states depends on the detector occupancy and the cluster shape.

Our strategy for data pre-processing is to perform a FPGA-based cluster finding and to fit each of the resulting clusters into a single 32-bit word. As 22 bits are needed for position information, 10 bits remain for encoding the cluster shape. This space is insufficient to encode the pixels bitwise. Therefore, it was considered to attribute a unique shape code to a given cluster shape. Provided the total number of different cluster shapes found in the MVD data remains below 1024, this concept allows for a lossless encoding of the experimental data.

To test this approach, the cluster finder was implemented in C++ and tested with data from CBMRoot simulations and with experimental data obtained from the beam test of the MVD prototype in November 2012 at the CERN-SPS. The six stations of the prototype allowed for a precise tracking of the traversing high energy pions and hence, for selecting high-purity tracks and clusters. Data on the shape of the clusters were recorded for various sensor temperatures, inclination angles, and discriminator thresholds. Figure 2 presents preliminary results on the dependence of the mean number of fired pixels per cluster on the inclination angle for three different applied discriminator thresholds. In general, the number of pixels in a cluster is smaller than known from earlier studies (see for example [2]). This is due to the more efficient charge collection mechanism found in the partially depleted active volume of the novel sensor [3]. Figure 3 shows the cluster shape distributions and the eight most frequent cluster shapes. Only substantially less than 0.01 % of all measured clusters (the ones with ShapeCode=0) could not be encoded with the shape code algorithm proposed.
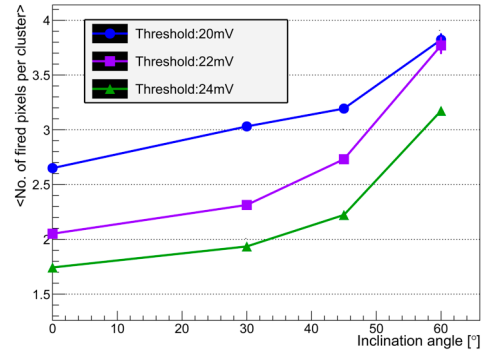
Figure 2: Mean cluster size
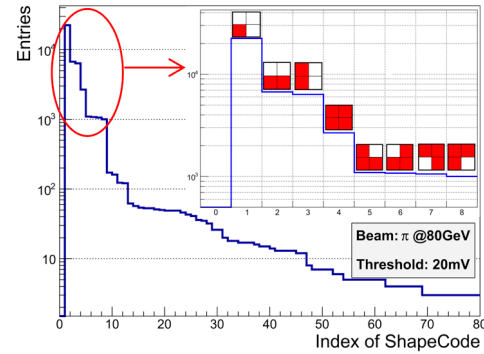
Figure 3: Cluster shape distribution

References

[1] C. Hu-Guo *et al.*, Nucl. Instrum. Methods **A 623** (2010) 480

[2] C. Dritsa *et al.*, PoS(BORMIO2010)015

[3] A. Dorokhov *et al.*, Nucl. Instrum. Methods **A 624** (2010) 432

Radiation tolerance of a CMOS Monolithic Active Pixel Sensor produced in a 0.18 μm CMOS process

D. Doering[1], J. Baudot[2], M. Deveaux[1], M. Goffe[2], S. Senyukov[2], J. Stroth[1], and M. Winter[2]

[1]Institut für Kernphysik, Goethe University, Frankfurt, Germany; [2]IPHC Strasbourg, France

So far, CMOS active pixel sensors (MAPS) matched the requirements of CBM in terms of spatial resolution and material budget. During several years, their radiation tolerance has been adapted to the needs of this experiment. In 2012, the radiation tolerance of a sensor, produced in an 0.18 μm CMOS process was tested. It could be demonstrated that this sensor provides the radiation tolerance required for CBM at SIS-100.

In a first step, the tolerance of MAPS to non-ionizing radiation was improved by more than one order of magnitude. This was reached by partially depleting the active volume of the sensors [1, 2]. Still, the tolerance of the sensors to ionizing radiation remained to be improved. This was done by migrating a simple imager sensor from the established 0.35 μm process to an 0.18 μm process. It was hoped that this would allow for exploiting the known higher intrinsic radiation tolerance of deep sub-micron CMOS processes. Besides providing benefits in terms of radiation tolerance, the 0.18 μm process comes with additional features which are expected to allow for a better time resolution of the device.

To explore the new technology, three different prototypes named MIMOSA-32 (V1-3) were designed by the PICSEL group of the IPHC and tested in the laboratory and at the CERN-SPS. Each flavor of MIMOSA-32 is composed of arrays of 32 different pixels with various parameters, which were put to study selected pixel parameters in a systematic way. To perform radiation tolerance studies, some of the sensors were irradiated with combined non-ionizing and ionizing doses of 10^{13} n_{eq}/cm^2 and 1 Mrad. Those radiation doses match the design requirements of CBM running at SIS-100.

After being irradiated, the sensors were tested by the PICSEL group at the CERN-SPS. Some results for the particularly unfavorable running conditions of $T > +15$ °C and for relatively high pixel pitches of 20×40 μm^2 are shown in Fig. 1. The non-irradiated sensor shows an excellent detection efficiency of $\gtrsim (99.78 \pm 0.08)\%$ independent of the operation temperature. The irradiated sensor keeps a very good detection efficiency of $(98 \pm 0.3)\%$ at even $T = +30$ °C. When operating the sensors with a slight cooling at $T = +15$ °C, this detection efficiency raises to $\gtrsim (99.5 \pm 0.3)\%$.

This work was complemented at IKF with studies exploring the properties of the sensor at higher ionizing doses of up to 10 Mrad. The gain shrinks slightly about 5% after 3 Mrad, while the noise of the sensor remains mostly con-
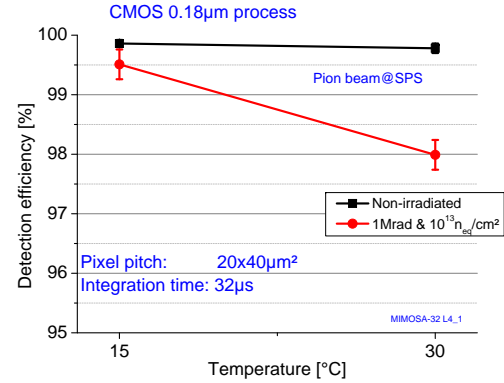
Figure 1: Detection efficiency of elongated pixels at a coolant temperature of $T = +15$ °C and $T = +30$ °C before and after irradiation (1 Mrad $+$ 10^{13} n_{eq}/cm^2).

stant. After a dose of 10 Mrad, the gain of the sensor is reduced by a factor of two and the noise raises by about 40%, which is not yet fully understood. The signal-to-noise ratio of this sensor was measured with a Sr-90 source and found to remain above 30 (Most Probable Value). This appears sufficient for obtaining a satisfactory detection efficiency for minimum ionizing particles.

We conclude that MAPS manufactured in a 0.18 μm CMOS process combined with a high-resistivity epitaxial layer provide the radiation tolerance required by the micro-vertex-detector of CBM at SIS-100. Moreover, there are first evidences that the technology might also match the higher needs of CBM at SIS-300. While this conclusion appears robust for simple imagers, it remains to be confirmed for the more complex sensors with integrated data processing circuits.

References

[1] A. Dorokhov *et al.*, Nucl. Instrum. Methods **A 642** (2010) 432

[2] M. Deveaux *et al.*, Nucl. Instrum. Methods **A 583** (2010) 134

Full-size silicon microstrip sensors for the CBM Silicon Tracking System

J. M. Heuser[1], C. J. Schmidt[1], J. Eschke[1], S. Chatterji[1], W. Niebur[1], W. F. J. Müller[1], P. Senger[1], C. Sturm[1], C. Simons[1], D. Soyk[1], T. Balog[1,2], A. Lymanets[3,4], I. Sorokin[5,4], M. Singla[5], P. Ghosh[5], Y. Murin[6], M. Merkin[7], V. M. Borshchov[8], M. Protsenko[8], and I. Tymchuk[8]

[1]GSI, Darmstadt, Germany; [2]Comenius University, Bratislava, Slovakia; [3]Eberhard Karls University, Tübingen, Germany; [4]Kiev Institute for Nuclear Research, Kiev, Ukraine; [5]Goethe University, Frankfurt, Germany; [6]JINR, Dubna, Russia; [7]Moscow State University, Moscow, Russia; [8]SE SRTIIE, Kharkov, Ukraine

The layout of the CBM Silicon Tracking System foresees the application of double-sided microstrip sensors in three sizes. All sensors have the same width of 6.2 cm, matching the width of the detector ladders that build up the tracking stations, and are segmented into 1024 strips of 58 μm pitch. The sensor heights, essentially corresponding to the strip lengths, are 6.2, 4.2 and 2.2 cm, depending on the position of the sensors within the tracking stations. Sensors close to the beam line, which are exposed to the highest track densities, have the shortest strip length. Towards the periphery of the STS, sensors with longer strips, even daisy-chained sensors can be used still yielding small enough particle hit occupancies for efficient pattern recognition. A first series of silicon microstrip sensors in all three sizes was designed in 2012. Their profiles are shown in Fig. 1. The projects, conducted in close cooperation of GSI (*CBM05, CBM05H4*) and JINR (*CBM05H2s*) complement the previous prototyping activities [1] in terms of design optimization towards the emerging silicon detector module structure, and high production yield. They will yield tested pre-series prototypes in 2013.

from one edge. The complex sensor structure was optimized based on the good results with a similar single-sided technology sensor *CBM03'* built in 2012.

The mid-size sensor (*CBM05H4*) is being realized in parallel with Hamamatsu Photonics. Since 2011, Hamamatsu offers again the fabrication of double-sided sensors. With *CBM05H4* we realize a double-sided sensor with double-metal interconnecting lines in the complementing dimensions 6.2 cm by 4.2 cm. The layout of the sensor is essentially identical to the *CBM05* layout, including a double metal layer on the p-side.

The small prototype sensor (*CBM05H2s*) is also developed in cooperation with Hamamatsu. The objective is to realize a sensor with minimum complexity to study an alternative for the double-metal interconnection layer. Its layout has no second metal layer but pads for the attachment of a separate microcable fulfilling the same function as the lines otherwise integrated into the sensor. The microcable is designed and produced at SE SRTIIE. A mock-up of the sensor fitted with its on-chip cable is shown in Fig. 2. The final sensor will be also produced as a double-sided structure.
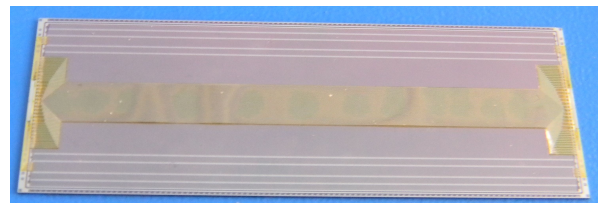
Figure 2: Microcable replacing the second metal layer mounted on a mockup of sensor *CBM05H2s*

CBM05H4, Hamamatsu
6.2 cm by 4.2 cm
double-sided

CBM05, CiS
6.2 cm by 6.2 cm
double-sided

CBM05H2s, Hamamatsu
6.2 cm by 2.2 cm
single-sided

Figure 1: Prototype microstrip sensors, *CBM05* family

The largest of the three sensors (*CBM05*) is currently in production at CiS [1]. It is a p-in-n type double-sided sensor of 300 μm thickness with a 7.5° stereo angle between front and back side strips. Strips of the corner regions of the stereo side are interconnected through lines on a second metal layer so that their full read-out can be achieved

References

[1] J. M. Heuser *et al.*, CBM Progress Report 2009, p. 10
    J. M. Heuser *et al.*, CBM Progress Report 2010, p. 10
    J. M. Heuser *et al.*, CBM Progress Report 2011, p. 17

[2] http://www.cismst.de

[3] http://www.hamamatsu.com

Development of on-sensor micro-cable technology for the CBM Silicon Tracking System

V. M. Borshchov[1], Yu. A. Murin[2], M. A. Protsenko[1], I. T. Tymchuk[1], R. A. Kushniruk[1], and V. A. Vassendina[2]

[1]1SE SRTIIE, Kharkov, Ukraine; [2]JINR, Dubna, Russia

The CBM STS comprises double-sided microstrip sensors with a strip orientation of 7.5° and 0° on the front and back sides of the sensors, respectively. On the side with inclined strips there are "short" strips in the corners of the sensor which have to be connected to the corresponding strips at the opposite edge. The number of "short" strip pairs to be shortcut depends on the sensor length: 41 pairs for the 22 mm long sensor, 87 pairs for 42 mm and 131 for 62 mm.

An approach for the interstrip interconnection via thin aluminium-polyimide microcables is being developed at SE SRTIIE in cooperation with JINR, introducing composite double-sided sensors as prototypes for the final CBM STS sensors. The composite sensors used so far are built from two single-sided sensors with STS-like strip topology, glued to each other back-to-back. For mounting the interstrip cable, additional contact pads connected to the short strips are provided on the sensor with inclined strips. The interstrip cables are made of the aluminium-polyimide FDI-A-24 foiled dielectric similar to [1, 2].

The composite double-sided sensor schematically shown in Fig. 1 comprises of five structural elements: (1) a single-sided sensor with vertical strips (300 μm silicon); (2) a single-sided sensor with 7.5° inclined strips (300 μm silicon); (3) back contact for sensor 1 (aluminium foil, 30 μm); (4) back contact for sensor 2 aluminium foil, 30 μm), and, finally, (5) the interstrip cable for sensor 2 (FDI-A-24).
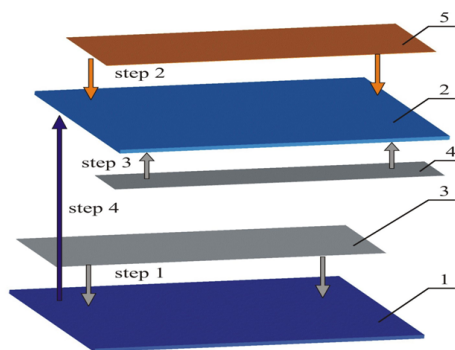
Figure 1: Configuration of a composite double-sided sensor and its assembly steps (see text)

The following sequence was developed for the assembly of the composite sensors. First, the back contact to sensor 1 was bonded, followed by ultrasonic bonding of the interstrip cable to sensor 2 with bond protection carried out afterwards. Next, bonding of the back contact to sensor 2 was done. The last step was gluing sensors 1 and 2 back-to-back by a conductive glue.
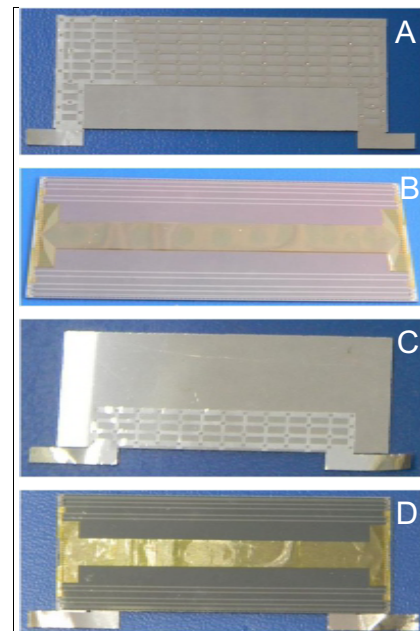
Figure 2: Evolution of the assembly of a composite sensor. A: sensor 1 with the bonded back contact; B: sensor 2 with the bonded interstrip cable; C: sensor 2 with the bonded back contact; D: a mock-up of the assembled double-sided sensor.

To check the practical realization of this approach, three mock-ups of the composite double-sided sensors of dimensions 22×62 mm^2, 42×62 mm^2 and 62×62 mm^2 were manufactured. Figure 2 shows the assembly steps for the 22 mm long mock-up. The obtained technological expertise will be used in the future manufacturing of double-sided sensors with interstrip cable connectivity for the CBM-MPD STS Consortium.

References

[1] V. M. Borshchov *et al.*, CBM Progress Report 2009, p. 15

[2] V. M. Borshchov *et al.*, CBM Progress Report 2010, p. 17

Design options for radiation tolerant microstrip sensors for the CBM Silicon Tracking System

S. Chatterji[1], *M. Singla*[2], *W. F. J. Müller*[1], *and J. M. Heuser*[1]

[1]GSI, Darmstadt, Germany; [2]Goethe University, Frankfurt, Germany

The maximal neutron fluence for the CBM STS is 10^{14} $n_{eq}cm^{-2}$, after which a replacement of sensors is foreseen. The main impact of radiation damage is the loss in the charge collection efficiency (CCE) limited by the breakdown voltage V_{bd}. In addition, we aim to minimize the capacitive noise, the dominant contributor to which comes from the interstrip capacitance C_{int}. To summarize, we aim to develop microstrip detectors having low C_{int}, high V_{bd} and maximum CCE.

Table 1 shows the expected neutron fluence for the first five years of CBM operation. In this table, the initial resistivity of silicon was taken to be 5.33 KΩcm; the lifetimes of electrons τ_e and holes τ_h were calculated using Kramberger's model [1] assuming an operating temperature of -10^0C. One can observe a deterioration of carrier life time with fluence, which will have an impact on the CCE, especially on the p-side since this side collects less mobile holes.

Table 1: Fluence profile of neutrons for the CBM STS

Year	Fluence [n_{eq} cm^{-2}]	N_{eff} [cm^{-3}]	τ_e [ns]	τ_h [ns]	V_{fd} [V]
1	2×10^{13}	2.8×10^{11}	1140	1050	28
2	4×10^{13}	-1.54×10^{11}	570	527	20
3	6×10^{13}	-5.35×10^{11}	380	351	44
4	8×10^{13}	-8.84×10^{11}	285	263	75
5	1×10^{14}	-12.1×10^{11}	228	211	100

In order to investigate the life time of sensors, it is imperative to extract the CCE as a function of fluence, for which one has to understand the strip isolation in particular on the ohmic side. Hence various isolation techniques have been explored both through prototyping as also through simulations, for example P-stop, P-Spray, Modulated P-spray (conventional isolation techniques) and also a new isolation technique, the Schottky barrier. The latter can be defined either through metal work function value or through barrier height, which in turn depends on the substrate type and the metal used for the Schottky contact. For Aluminum, the barrier height is 0.72 eV for n-type silicon while for p-type silicon, the barrier height is 0.58 eV [2]. A comparison of the conventional isolation techniques with Schottky barrier in terms of V_{bd}, C_{int} and CCE is shown in Table 2. One can infer that the Schottky barrier is the best choice in terms of V_{bd} and C_{int}. However in terms of CCE, the Schottky barrier gives the worst performance especially after type inversion. Therefore, Schottky barrier has not been opted as a suitable isolation technique.

Besides P-stop and P-spray, another isolation technique, the modulated P-spray, has also been explored, and an optimization of modulated P-spray has been performed. It was found that using a moderate P-stop width of around 15 μm and very low P-spray concentration of around 1×10^{15} $n_{eq}cm^{-3}$ gives the best performance in terms of V_{bd} and C_{int}; this is referred to as Optimized Modulated P-spray in Table 3. Finally, a comparison of P-stop, P-spray and Optimized Modulated P-spray after one year of operation and for the maximum fluence expected at the end of five years of CBM operation is shown in Table 3. One can notice from this table that using Optimized Modulated P-spray, V_{bd} is increased by around 60% and C_{int} is reduced by 25% while maintaining the same CCE as with conventional isolation techniques. In Tables 2 and 3, V_{bd}, C_{int} and CCE are simulated values confirmed with measurements. We conclude that Optimized Modulated P-spray is the best choice for isolation technique in terms of V_{bd}, C_{int} and CCE.

Table 2: Comparison of conventional isolation techniques with Schottky barrier

Isolation Technique	Fluence [n_{eq} cm^{-2}]	V_{bd} [V]	C_{int} [pF cm^{-1}]	CCE [%]
P-stop	3.93×10^{12}	1010	2.1	91.25
	20.60×10^{12}	890	2.29	86.25
P-spray	3.93×10^{12}	524	2.6	93
	20.60×10^{12}	450	2.7	86.25
Schottky Barrier	3.93×10^{12}	1450	2.05	79
	20.60×10^{12}	1350	1.80	77.5

Table 3: Comparison between p-stop, p-spray and optimized modulated p-spray at low and high fluence

Isolation Technique	Fluence [n_{eq} cm^{-2}]	V_{bd} [V]	C_{int} [pF cm^{-1}]	CCE [%]
P-stop	2×10^{13}	980	2.02	93.15
	1×10^{14}	720	2.03	88.87
P-spray	2×10^{13}	513	2.56	93.17
	1×10^{14}	495	2.44	89
Opt. Mod. P-spray	2×10^{13}	1600	1.58	93.22
	1×10^{14}	1150	1.60	89

References

[1] V. Cindro *et al.*, IEEE Nucl. Sci. Symp. **N09-2** (2006) 139

[2] http://www.pfk.ff.vu.lt/lectures/funkc_dariniai/diod/schottky.htm

Quality assurance tests of silicon microstrip sensors for the Silicon Tracking System in the CBM experiment at FAIR

P. Larionov and P. Ghosh

Goethe-Universität, Frankfurt am Main, Germany

The Compressed Baryonic Matter (CBM) experiment aims to explore the QCD phase diagram in the region of high net-baryonic densities and moderate temperatures. The core of the CBM experimental setup – the Silicon Tracking System – will consist of 8 stations based on double-sided silicon strip sensors and self-triggered read-out. It will have to cope with large track densities and event rates up to 10^7 s^{-1}, will have to enable high momentum resolution and detection efficiency as well as stand radiation doses of up to 10^{14} n$_{eq}$/cm^2.

A large amount of sensors (about 1400) will be required to construct the STS. For the proper operation of the system, each sensor requires a number of procedures to ensure proper production and to verify the full accordance to the technical specifications. Local laboratory tests are as important as verification of the technical specifications provided by the manufacturer. These tests will ensure that the sensors will be suitable for the STS detector and will satisfy its requirements. Both these two procedures define Quality Assurance for the Silicon Tracking System, which includes visual inspection, bulk and interstrip parameters measurements, sensor efficiency and total signal-to-noise ratio tests, measurements of irradiated sensors, low temperature performance and current stability tests. In the following, we report on QA tests of STS prototype sensors with 256 strips per side, 300 μm thickness and 58 μm strip pitch [1].

Bulk measurements – current-voltage (I-V) and capacitance-voltage (C-V) characteristics (see Fig. 1) – can serve as basic acceptance criteria. These measurements are a good instrument to assess the quality of the sensor, to verify the manufacturer data and to make sure there has been no damage during sensor manufacturing or handling.
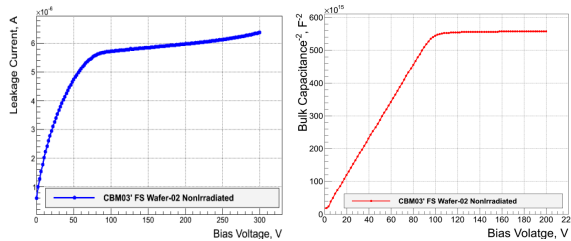
Figure 1: Bulk measurements. Left: current-voltage; right: capacitance-voltage.

In addition, some passive electrical characteristics were measured for different strips of the sensor. These measurements aim to investigate the charge collection and the equivalent noise charge of the sensor. The value of cou-

pling capacitance (Fig. 2) allows to judge about the transmission of the signal. The ratio of coupling and interstrip capacitances affects the value of the signal transmitted to the read-out electronics. For these measurements, the wafer prober Süss-PA300 was adapted in the clean room with temperature and humidity control.
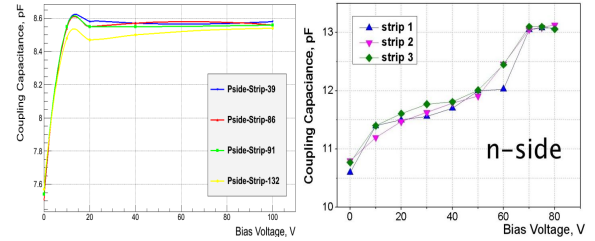
Figure 2: Coupling capacitance measurements. Left: p-side of the sensor; right: n-side of the sensor.

Figure 3 indicates the variation of current-voltage curves for sensors that were irradiated with different fluences. As a part of QA, these measurements were carried out to investigate the sensor's behavior and perfomance after irradiation.

Future QA activities for the STS include long-term stability tests, low temperature performance measurements and optimization of the measurement procedures via LabView software.
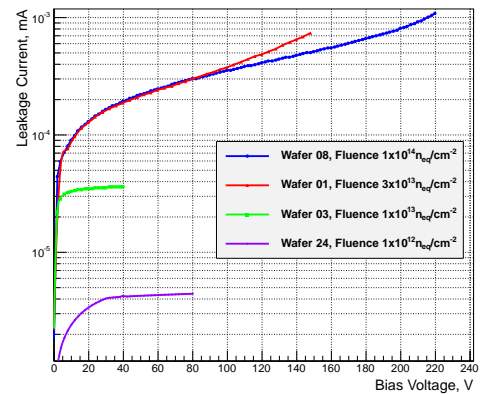
Figure 3: Current-voltage curves for irradiated sensors

References

[1] J. M. Heuser *et al.*, CBM Progress Report 2011, p. 17

Characterization of double sided silicon micro-strip sensors with a pulsed infra-red laser system for the CBM experiment

P. Ghosh[1,2] and J. Eschke[2,3]

[1]Goethe-Universität, Frankfurt am Main, Germany; [2]GSI Darmstadt, Germany; [3]FAIR GmbH, Darmstadt, Germany

The Silicon Tracking System (STS) of the Compressed Baryonic Matter (CBM) experiment at FAIR is composed of 1292 double-sided silicon micro-strip sensors. For the development and the quality assurance of produced sensors a laser test system has been built up. The main aim of the sensor scans with the pulsed infra-red laser system is to determine the charge sharing between strips and to measure the uniformity of the sensor response over the whole active area. The prototype sensors CBM02 tested so far with the laser system have 256 strips with a pitch of 50 μm on each side [1]. They are read out by the self-triggering n-XYTER prototype read-out electronics.

The wavelength of the laser was chosen to be 1060 nm because the absorption depth of infra-red light with this wavelength is of the order of the thickness of the silicon sensors [2]. Figure 1 shows the measurement setup in a schematic view. The laser light is transmitted through a 6 μm (inner diameter) thick optical fibre to a two-lens focusing system, which focuses the light to a spot size of about 15 μm diameter; the working distance is about 10 mm. Figure 2 shows the number of fired strips as a function of the distance of the laser to the sensor surface. The best focusing was obtained at position 7 w.r.t the reference level.

Figure 1: Schematic representation of the laser setup

The laser system is intended to measure the sensor response in an automatized procedure at several thousand positions across the sensor with focused infra-red laser light ($\sigma_{spotsize} \approx 15$ μm). The duration ($\sim$5 ns) and power (few mW) of the laser pulses are selected such that the absorption of the laser light in the 300 μm thick silicon sensors produces about 24k electrons, which is similar to the charge created by minimum ionizing particles (MIP) there.
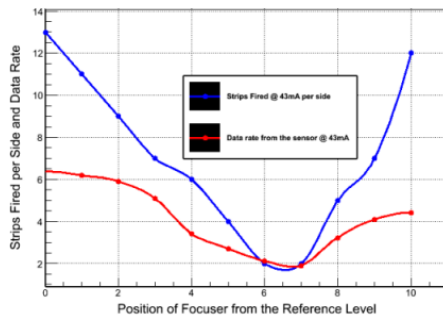
Figure 2: Dependence of number of fired strips on the distance to focuser from the sensor surface

Figure 3: Distribution of hits per strips on the n-side
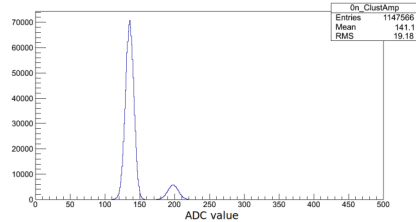
Figure 4: ADC amplitude distribution (n-side)

We have illuminated a prototype sensor with a focused pulsed laser and could achieve a spot size of a little more than one strip (fig. 3). The preliminary results demonstrate that we are successful in inducing charge similar to 1 MIP (24k electrons). Figure 4 shows that the number of single-strip clusters is about an order of magnitude higher than that of two-strip clusters. The next step of our work will be to investigate the charge sharing function between the strips.

References

[1] J. M. Heuser *et al.*, CBM Progress Report 2011, p.17

[2] P. O'Connor *et al.*, Proc. SPIE 6276 (2006) 62761W, p. 2

Signal transmission in low-mass readout cables for the CBM Silicon Tracking System

M. Singla[1,2], S. Chatterji[2], W. F. J. Müller[2], V. Kleipa[2], and J. M. Heuser[2]
[1]Goethe University, Frankfurt am Main, Germany; [2]GSI, Darmstadt, Germany

In the Silicon Tracking System of the CBM experiment, readout cables will bridge the distance between the microstrip sensors and the electronics placed at the periphery of the tracking stations. Since the length of the cables can reach up to 50 cm for the inner modules, it is very important to extract the expected transmission losses in the cables as these will be reflected in the signal-to-noise ratio. Mixed-mode simulations have been done to assess the transmission loss in the cables. The mixed-mode capability of the Sentaurus Device (a sub-package of SYNOPSYS [1]) allows the simulation of a circuit that combines any number of Sentaurus devices of arbitrary dimensionality (1D, 2D, or 3D) with other devices based on compact models (SPICE).
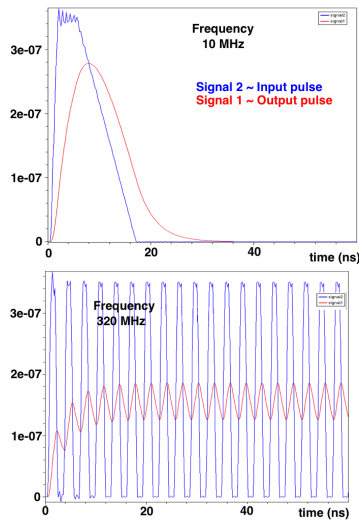
Figure 1: Dependence of transmission losses on input pulse period using mixed-mode simulations. Upper panel: input pulse period 100 ns; lower panel: input pulse period 3.13 ns.

To study the impact of input pulse frequency, square pulses are injected through the sensor, and the output pulse is seen at the end of the cable. Figure 1 shows the impact of input pulse frequency on the output pulse. For higher frequencies, the signal amplitude decreases and the pulse broadens at the input of the front end electronics, which may lead to charge loss depending on the RC time constant of the read-out chip shaper. The decrease in signal amplitude may enforce a lower threshold, which could result in more noise again depending on the RC time constant of the integrator. Secondly, the pulse broadening may lead to the charge loss if we use fast electronics, i.e. a short shaping time of the preamplifier.

For higher frequencies, a pile-up effect can be observed, when the second pulse arrives relatively early and rides on the falling tail of the first pulse. Also a baseline shift can be observed for higher frequency pulse output. For example, in the lower panel of Fig. 1 the baseline shift is around 18% of the input pulse amplitude (0.6×10^{-7}). In our calculations, baseline corrections have been taken into account.

For validation of the transmission (dB) loss determined using mixed-mode simulations, the dB loss in a CBM prototype cable with aluminum traces has been measured using a Vector Network Analyser [2]. Figure 2 (left) shows the comparison of measured values with simulations up to 240 MHz. The simulated data match with measurements withing 5% error thus validating the simulation approach. In the simulations, continuous attenuation with frequency can be seen since the readout cable acts as a low-pass filter. Figure 2 (right) shows the dependence of the transmission loss on the length of the cables. Again, simulations and measurements match well. A mathematical model for the dependence of transmission loss on the length of cables has been extracted.

The transmission losses increase with pulse frequency and with the length of the cable. For the frequency range of interest for the present prototype front-end chip in the fast shaper mode (25 MHz), the transmission is expected to be around 85% for a 30 cm long cable.
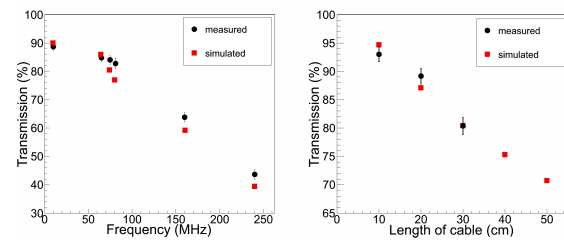
Figure 2: (left) Comparison of measured transmission coefficient with simulations for a CBM prototype readout cable of length 30 cm; (right) dependence of transmission loss on the length of cables.

References

[1] http://www.synopsys.com/home.aspx
[2] http://www2.rohde-schwarz.com/product/ZVA.html
    Vector Network Analyzer ZVRE, 10Hz/9KHz...4GHz

Transconductance calibration of n-XYTER 1.0

I. Sorokin[1,2], T. Balog[3,4], V. Krylov[5], and C. J. Schmidt[4]

[1]Goethe University, Frankfurt a. M., Germany; [2]KINR, Kiev, Ukraine; [3]Comenius University, Bratislava, Slovakia;
[4]GSI, Darmstadt, Germany; [5]Kyiv University, Ukraine

Since long, the n-XYTER 1.0 [1] has been used as a prototype readout chip for the Silicon Tracking System (STS), the muon and Cherenkov detectors of the CBM experiment. The transconductance calibration of the n-XYTER was already reported [2]. However, it was done with only one channel of one chip, only at one polarity and without thermal stabilization of the chip. An inconsistency between this calibration and results of measurements with various microstrip detectors done by the CBM-STS group [3] necessitated to repeat the calibration thoroughly.

The n-XYTERs were operated on the front-end boards rev. D, with thermal stabilization and in conjunction with a 12-bit ADC (AD9228, dynamic range –1...1 V). To generate reference charge pulses, voltage steps were applied to the n-XYTER input over a capacitor. The injected charge in this case is $C \cdot \Delta V$. The voltage steps were generated with an ordinary laboratory pulser and attenuated down to the millivolt level with passive attenuators. In order to minimize the systematic error, the actual attenuation factors were measured with high precision, and also their independence of the frequency was checked. The capacitance (including parasitics) was also measured precisely (1.051±0.001 pF). As a cross-check, the calibration of one channel was repeated with a capacitor of a different type and value, and a good agreement was observed. Finally, the independence of the n-XYTER response of the width of the injected pulse was checked (as expected, observed roughly up to 50 ns).

The calibration was done on 3 chips and 42 channels at negative polarity and 10 channels at positive. Within the same polarity the data from all channels were combined and fitted with a 4th order polynomial (Fig. 1). The results are[1]:

$$Q_- = 0.2025 + 2.053 \cdot 10^{-2} \cdot A - 6.733 \cdot 10^{-6} \cdot A^2 +$$
$$+ 1.324 \cdot 10^{-8} \cdot A^3 - 3.566 \cdot 10^{-12} \cdot A^4$$
$$Q_+ = 0.3966 + 1.921 \cdot 10^{-2} \cdot A + 2.603 \cdot 10^{-6} \cdot A^2 -$$
$$- 1.062 \cdot 10^{-8} \cdot A^3 + 1.227 \cdot 10^{-11} \cdot A^4$$

where $Q_\pm$ is the input charge in fC, and A is the n-XYTER output amplitude in ADC LSB (least significant bit).

A straight-line fit in the linear range (0–700 LSB) yields

$$Q_- = 0.07757 + 0.02051 \cdot A = 0.07757 + 1.002 \cdot 10^{-2} \cdot U$$
$$Q_+ = 0.3718 + 0.01960 \cdot A = 0.3718 + 9.573 \cdot 10^{-3} \cdot U$$

---

[1]Parameter values were not rounded because their uncertainties were not calculated. Instead the total uncertainty will be specified below.
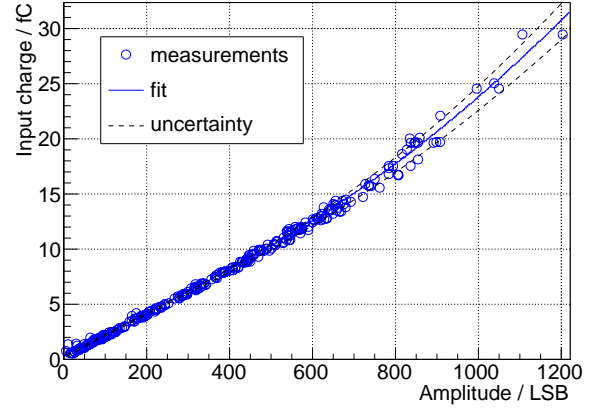
Figure 1: n-XYTER calibration at negative polarity

Here, U is the n-XYTER output amplitude in mV.

The dominant contribution to the calibration uncertainty comes from the fact that a single calibration curve is applied to all channels, even though they have slightly different gains. This uncertainty was parametrized with a 2nd order polynomial w.r.t. the amplitude and estimated by requiring that it compares to the dispersion of the data. Because of the small number of data points at positive polarity, the uncertainty was assumed to be the same for both polarities (ΔQ in fC, A in ADC LSB):

$$\Delta Q = 0.1 - 4 \cdot 10^{-4} \cdot A + 1.4 \cdot 10^{-6} \cdot A^2$$

As a cross-check against possible systematic errors, a planar silicon detector was connected to one n-XYTER channel, and the amplitude corresponding to the 59.6 keV line of ^{241}Am was measured (114 ADC LSB). According to the calibration of the same channel, the amplitude corresponds to a charge of 2.57 fC, which is in a very good agreement with the expected value of 2.64 fC (2.7 % difference).

References

[1] A. S. Brogna *et al.*, Nucl. Instrum. Methods **A 568** (2006) 301

[2] C. J. Schmidt *et al.*, CBM Progress Report 2009, p. 50

[3] J. M. Heuser *et al.*, CBM Progress Report 2010, p. 19

n-XYTER 2.0 operative and tested

D. Dementyev[3], *V. Krylof*[2], *S. Löchner*[1], *C. J. Schmidt*[1], *and I. Sorokin*[1,4]

[1]GSI, Darmstadt, Germany; [2]Kyiv University, Kiev, Ukraine; [3]JINR, Dubna, Russia; [4]KINR, Kiev, Ukraine

n-XYTER is a self-triggered multi-channel charge sensitive detector readout chip, originally developed for the signal readout of thermal neutron detectors [1] and similar to FSSR2 [2]. It is being employed in many detector prototyping activities for the FAIR experiments and others [3, 4], as it is the only front-end chip available which realizes a self-triggered architecture, is applicable for both polarity signals and finally has sufficiently high gain for the detection of MIP size signals in Silicon.

The first prototype version 1.0 has been extensively tested and turned out to show a severe temperature coefficient in the DC-signal levels of about 4%/K, which made its employment very tedious and difficult, as the slightest temperature variations resulted in enormous pedestal drifts.

With the aim to repair the temperature coefficient, the chip underwent a redesign, which primarily focussed upon the supply of several biasing potentials from outside the chip, the correction of various layout deficiencies and finally the introduction of a switch that would change the gain by about a factor of 4 and thus extend the dynamic range by the same factor.

The submission of n-XYTER 2.0 was realized as an engineering run, which served to supply a sufficient number of dies for the use in FAIR detector prototyping activities as well as thermal neutron detector developments targeted at the Physikalisches Institut Heidelberg. The design was submitted in the AMS 0.35 μm process; twelve wafers were produced in total. For risk mitigation purposes, one out of four locations on the reticle was filled with the original design of n-XYTER 1.0, the other three locations realized n-XYTER 2.0.

The chip was taken into operation on a PCB previously employed for n-XYTER 1.0 through the use of a little fudge board, which carried the four adjustable external bias sources that need to be supplied with this version of the chip. The strategy for setting these biases turned out comparatively simple: the bias for the pre-amp is to be set such that the DC output of the pre-amp is identical to the input potential. Further, the three DC-bias voltages for the fast shaper circuit as well as the two successive slow shaper circuits can easily be set with the target of setting the output DC levels to adequate values.

The temperature coefficient was measured for every channel on a chip and found at a level of 0.12 mV/K or $\sim 2 \cdot 10^{-4}$/K, an improvement by a factor of 200 as compared to n-XYTER 1.0.

Then the internal charge injection circuit was tested and calibrated for two individual chips by comparison to the response of a very well calibrated external charge injection circuit. Variations were found on the level of $\pm 5\%$, which may be attributed to variations of the effective input coupling capacitance of the internal test circuits.

Likewise the gain of every channel was individually determined. Fig. 2 shows the histograms of the channel gain of one chip for positive and negative signal polarities.
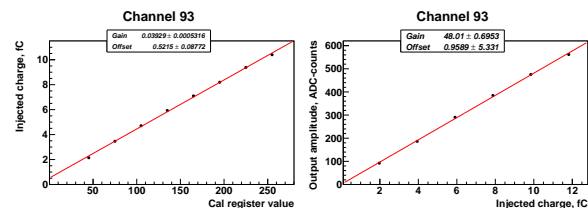
Figure 1: Calibration of the test pulse circuit, using a highly accurate external injection circuit (right) and comparing the signal response to the signals generated by the internal circuit (left)
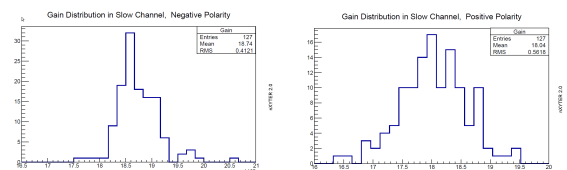
Figure 2: Histograms of measured gain for positive (right) and negative (left) input signals

The newly introduced feature, the switchable dynamic range through switchable gain, did result disappointing. Gain may indeed be changed by about a factor of 2.5. The dynamic range however resulted to remain the same, as the analogue output operating window is in effect reduced by the same factor. In conclusion, this feature may only be realized with much more sophisticated changes in the circuitry, which for this submission was omitted to minimize risk of failure.

In conclusion, n-XYTER 2.0 is functional. The temperature coefficient has been abolished. By now, the full set of tools for an automated serial test has been set up and may now be employed for a wafer-scale test campaign to characterize this batch of chips.

References

[1] A. Brogna *et al.*, Nucl. Instrum. Methods **A 568** (2006) 301

[2] V. Re *et al.*, IEEE Nucl. Sci. Symp. **N16-1** (2005) 896

[3] J. Heuser *et al.*, CBM Progress Report 2008, p. 11

[4] J. Heuser *et al.*, CBM Progress Report 2009, p. 8

Optimization of the technology of mounting n-XYTER ASICs on FEBs with the use of flexible micro-cables to improve heat dissipation

V. M. Borshchov[1], *M. A. Protsenko*[1], *D. V. Dementyev*[2], *Yu. A. Murin*[2], *I. T. Tymchuk*[1],
Y. Y. Kostyshyn[1], *S. N. Bazylev*[2], *L. V. Klimova*[1], *C. S. Schmidt*[3], *and V. Kleipa*[3]

[1]1SE SRTIIE, Kharkov, Ukraine; [2]JINR, Dubna, Russia; [2]GSI, Darmstadt, Germany

To simplify the assembling of the front-end board (FEB) while maintaining a high level of reliability and good heat dissipation from the n-XYTER ASIC, a new double-layer micro-cable for the connection of the ASIC to the FEB was designed with the number of output contacts on the board reduced nearly by half relative to the previous design [1].

Five FEBs with the n-XYTER v1 ASIC and micro-cables (Fig. 1) were developed and assembled jointly by JINR and SE SRTIIE with the cables realized for the two existing versions of the ASIC. This approach opens the practically important opportunity for testing of the ASIC after bonding to the cable in a standard auxiliary frame as shown in Fig. 2.
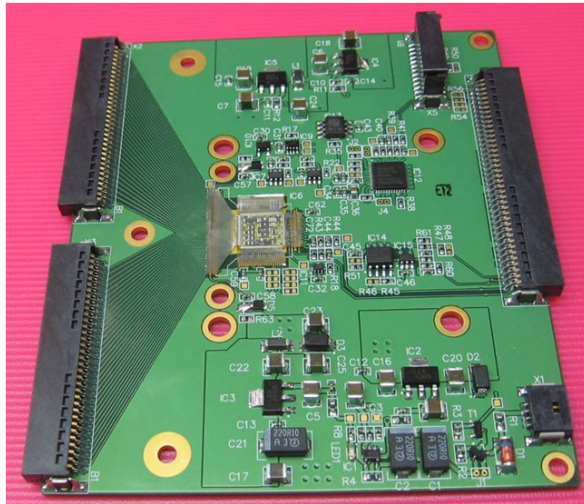
Figure 1: FEB with a chip connected by micro-cable
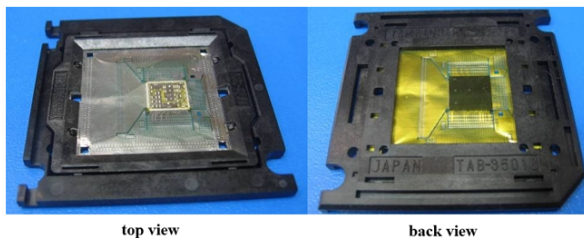
Figure 2: A micro-cable with the n-XYTER chip in an auxiliary frame

Comparative estimations of thermal regimes of the n-XYTER mounted on multi-layer PCBs were carried out for three options of FEB: without and with a hole through the PCB in the place of the chip, and with direct mounting of the ASIC on a primary copper heat sink as depicted in Fig. 3. The estimations were performed for normal environment conditions ($T = 25°$C) and for a silicon ASIC of size $8.8 \times 8 \times 0.8$ mm^3 dissipating a thermal power of 1.5 W.
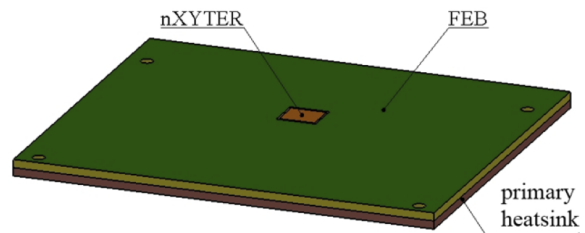
Figure 3: n-XYTER chip with the FEB on a primary copper heat sink

For a PCB comprising three 0.25 mm thick basic FR4 layers, two 0.2 mm and two 0.12 mm prepreg layers and eight metallization layers, overheating of the ASIC measured relative to the environment depends on the way the ASIC is attached to the heat sink. If the chip is glued to the metallized area of the upper layer of the PCB, the maximal overheating is $59°$C. In case it is glued to the metallized area with 30 through-plate holes with a diameter of 0.8 mm each, filled with a heat-conductive glue (EpoTek E4110 with $\lambda =1.5$ W/(m·K)), the maximal overheating is $13.4°$C. The best results are obtained when the chip is attached to a pedestal of the primary heat sink located in a big hole of the PCB which is in turn glued to the heat sink. In this case, the maximal overheating of the ASIC is expected to be $11.1°$C.

The obtained results will be validated during the assembly of the n-XYTER v2 chip with a PCB and a primary heat sink. The experience gained in creation of a new FEB with improved heat dissipation will be useful for manufacturing future FEBs for the CBM-MPD STS Consortium.

References

[1] V. M. Borshchov *et al.*, CBM Progress Report 2010, p 17

STS-XYTER - a prototype silicon strip detector readout chip for the STS

P. Grybos, K. Kasinski, R. Kleczek, P. Otfinowski, and R. Szczygiel

AGH-UST, Krakow, Poland

The STS-XYTER prototype readout ASIC for the CBM STS detector was designed in 2012. It is a full-size prototype dedicated for signal detection from the double-sided microstrip sensors in the CBM environment. The self-triggering ASIC provides both timing and energy information for each incoming signal in its channels.

The chip includes 128 channels. The input current pulse from the detector is processed by the charge-sensitive amplifier (CSA). The signal path is then split into a fast and a slow one (Fig. 1). The fast path includes a fast shaper with a typical shaping time of 30 ns, a discriminator and a timestamp latch. It is optimized to provide good timing resolution ($<$10 ns). The slow path consists of a slow shaper with a typical shaping time of 80 ns, a 5-bit flash ADC and a digital peak-detecting logic. It is optimized for energy measurement and noise performance.
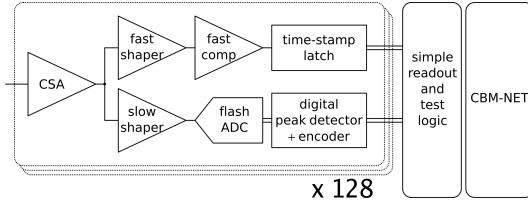
Figure 1: Block scheme of the STS-XYTER chip

For a particle hit, each channel provides the timestamp and the ADC value corresponding to the deposited charge. Data from the channels are read out using a token-ring structure, controlled by a readout controller. The gathered data are sent out via up to four 500 Mbit/s LVDS serial data links. The data transfer to and from the chip is implemented according to the CBMnet protocol description. The HDL code of the CBMnet-related digital part was provided by ZITI, Univ. Heidelberg [1]. A simplified I2C interface allows to configure the chip without protocol overhead for test purposes. A summary of the most important parameters is given in Table 1.

The essential new feature compared to the n-XYTER architecture is an effective two-level discriminator scheme. The discriminator in the fast signal lane triggers the latch of the timestamp at high timing resolution. Because of the higher bandwidth of the fast lane, the noise level and thus the noise-related trigger rate is comparatively high in such a self-triggered system if the discriminator level is kept low. The noise-related trigger rate is determined by the Rice formula. If the discrimination level is kept below 3σ, noise-related hits will swamp data channels and create dead time, while if kept too high, the essential low-level hits will re-

Table 1: Design parameters of the ASIC

Number of channels	128 + 2 test
Pad / channel pitch	58 μm
Input signal polarity	positive and negative
Accepted input leakage current	10 nA
ENC @ 30 pF det. capacitance	900 e-
Voltage gain in slow path	25 mV/fC
Voltage gain in fast path	71 mV/fC
ADC range	16 fC
Input clock frequency	250 MHz
Timestamp resolution	$<$10ns
Power consumption	$<$10 mV/channel
Operating temperature range	0°C $<$ T $<$ 40°C
Digital interface standard	4x 500 Mbit/s LVDS

main undetected. The two-level trigger scheme employed in the STS-XYTER adds a veto to the transmission of data in case the flash ADC has generated "zero". The discrimination level of the LSB is controlled by an internal register and effectively serves as a secondary discriminator that is exposed to the low-bandwidth, low-noise energy signal. This strategy makes the Rice formula applicable to the signal of the energy channel while keeping the high time resolution achieved from triggering on the fast timing channel.
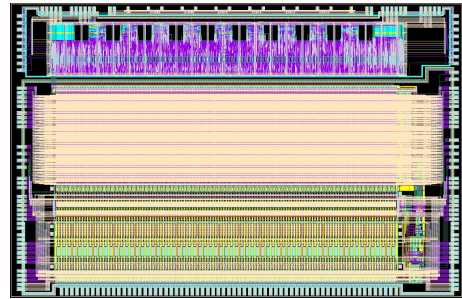
Figure 2: STS-XYTER ASIC layout

The ASIC was designed using the UMC 180 nm process and was sent for manufacturing in October 2012. The die size is 6.5 mm x 10 mm (Fig. 2). A detector is to be connected via a Kapton cable attached to the ASIC using tab bonding. The power supply, biasing and digital interface pads are designed for wire bonding. Particularly sensitive elements of the chip were made radiation hard.

References

[1] F. Lemke *et al.*, IEEE Trans. Nucl. Sci. **57** (2010) No. 2, 412

An assembly concept for modules of the CBM Silicon Tracking System

C. J. Schmidt[1], J. M. Heuser[1], W. F. J. Müller[1], V. Kleipa[1], C. Simons[1], D. Soyk[1], U. Frankenfeld[1],
V. M. Borshchov[2], M. Protsenko[2], I. Tymchuk[2], and H. R. Schmidt[3]

[1]GSI, Darmstadt, Germany; [2]SE SRTIIE, Kharkov, Ukraine; [3]Eberhard Karls University, Tübingen, Germany

The functional building block in the layout of the CBM experiment's Silicon Tracking System (STS) is a detector module, definded as the assembly of a single double-sided silicon microstrip sensor or several daisy-chained sensors, micro cables and two front-end electronics boards, one for each sensor side. Various module types will be applied, differing in the sensor arrangement and the length of the read-out cables to the front-end electronics at the top and bottom periphery of the STS. A module is a non-reworkable unit, which in case of failure will need to be replaced as a whole. Due to the thin micro cables it is a very delicate device that can be mounted onto and dismounted from the ladder structure only by means of specialized assembly tools and procedures.

Components

The components of a module as shown in Fig. 1 are:

- Sensor: Double-sided silicon strip sensor with 7.5° stereo angle and 1024 strips of 58 μm pitch per side. One or several daisy-chained sensors of 6.2 cm width and either 6.2, 4.2 or 2.2 cm length are used.

- Microcables: Single-layer Aluminum cables on polyimide carrier, 64 leads at a pitch of 116 μm. Two staggered layers at twice the pitch will be used to connect all sensor channels. Eight doubly-layered cables read out the 1024 channels per sensor side. The total number of cable stacks per module is 16.

- Readout ASIC: The dedicated STS-XYTER chip comprises 128 readout channels.

- Front-end board: A FEB receives eight read-out ASICs and serves 1024 input channels. The digital data from the chips are channeled by the data aggregator HUB chip into four high-speed serial links. Two FEBs are applied per module.

Assembly

The following sequence of assembly steps has been worked out from an analysis of ladder manufacturing options taking into account risk and yield evaluation [1, 2]. The scheme aims to minimize the overall risk, to maximize complete assembly yield and to minimize production costs while avoiding the shift of crucial challenges to later assembly steps. Current work is focused on a detailed refinement of the technological steps and the demonstration of their feasibility.

1. FEB is fully populated with parts including the HUB chip. STS-XYTER chips not yet installed.

2. Tab bonding of first 64-channel micro cable onto the STS-XYTER chip in a dedicated tool followed by a connectivity test.

3. Tab bonding of second 64-channel micro cable onto the STS-XYTER chip; connectivity test.

4. Tab bonding of micro cables with attached read-out chips to the p-side of a sensor; connectivity test.

5. Tab bonding of micro cables with read-out chips to the n-side of a sensor; connectivity test.

6. Installation of first row of four chips to FEB.

7. Wedge-wedge wire bonding of chips to FEB; successive application of glob top.

8. Installation of second row of four chips to FEB.

9. Wedge-wedge wire bonding of chips to FEB; application of glob top.

10. Flipping upside down of module. Repetition of the installation of read-out chips into the second FEB.

11. Functional test of FEBs with connectivity test of the sensor through the micro cables.
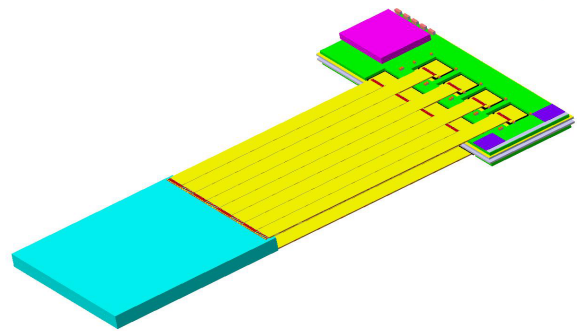
Figure 1: Schematical view of an assembled STS module

References

[1] Workshop on quality assurance for the CBM Silicon Tracking System, Univ. Tübingen, 14-15 June 2012, `https://indico.gsi.de/conferenceDisplay.py?confId=1621`

[2] Workshop on Module Assembly for the CBM Silicon Tracking System, GSI Darmstadt, 3-7 December 2012, `https://indico.gsi.de/conferenceDisplay.py?confId=2021`

Performance of a first prototype module for the CBM Silicon Tracking System

T. Balog[1,2], I. Sorokin[3,4], and J. M. Heuser[1]

[1]GSI, Darmstadt, Germany; [2]Comenius University, Bratislava, Slovakia; [3]Goethe University, Frankfurt a.M., Germany; [4]KINR, Kiev, Ukraine

The building block of the CBM Silicon Tracking System is a detector module, a functional unit of one or several daisy-chained double-sided silicon microstrip sensors, read-out cables and front-end electronics. Ten modules will be located on a detector ladder. Several ladders build up a STS tracking station [1].

A first prototype module comprises the CBM01 double-sided sensor with 1024 channels on both sides. On every side, 1/8 of the channels are read out via low-mass cables connected to two front-end boards each hosting one n-XYTER chip (Fig. 1). Three of such prototypes with different cable lengths were tested in the laboratory.
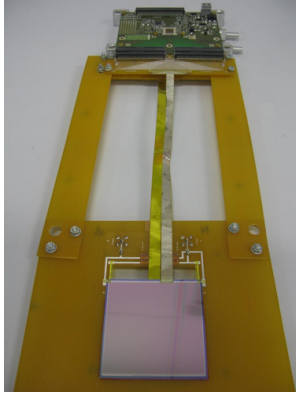
Figure 1: Photo of the prototype module

The noise performance of the systems was determined using external triggers on the baselines of the read-out electronics. The main noise source in the silicon strip detectors with cables is the interstrip capacitance, which was determined for all three prototypes (Table 1). In the analysis, Gaussian fits of the baseline distributions were calculated and their standard deviations (σ) taken as a measure of the noise in the channels. According to the n-XYTER ADC calibration [2], the noise is then expressed in equivalent noise charge (ENC) - the amount of charge seen by the read-out electronics (Fig. 2)

Afterwards the charge collection efficiency for all three demonstrators was measured using a ^{241}Am source with the silicon detector. Its 59.5 keV gamma line corresponds to 114 ADC units. As shown in Fig. 3, the signal amplitude depends on the length of the cable connected to the sensor. Within the measured prototypes, the charge collection efficiency was above 85%.
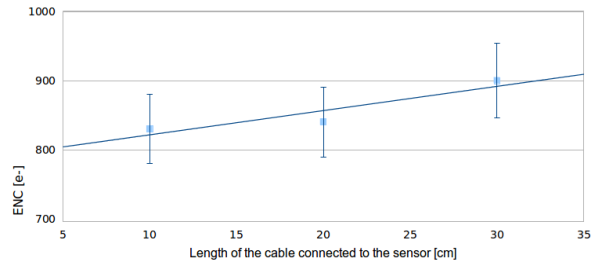
Figure 2: Noise performance of the prototype modules as a function of read-out cable length
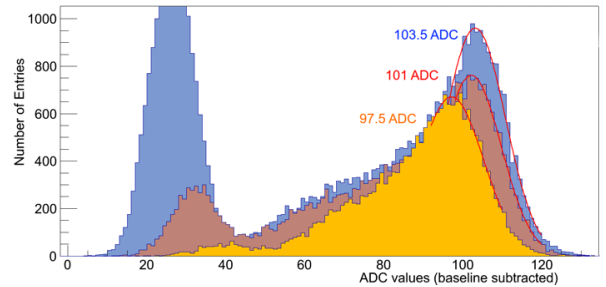
Figure 3: ^{241}Am spectra from the prototype modules

For efficient track recontruction with the STS, the noise of the read-out module is required to be below 4k e$^-$. The measurements with the prototype modules achieved a noise level well below 3k e$^-$ (measure of 3σ). According to the measured noise and the charge collection efficiency, the expected signal-to-noise ratio for minimum-ionizing particles in the prototype modules is above 20.

Table 1: Measured interstrip capacitances of prototypes

Length of read-out cable [cm]	Interstrip capacitance [pF]
10 cm	16.5 pF
20 cm	22.1 pF
30 cm	26.8 pF

References

[1] A. Kotynia and J. M. Heuser, CBM Progress Report 2010, p. 8

[2] I Sorokin *et al.*, *Transconductance calibration of n-XYTER 1.0*, this report

CO_2 cooling for the CBM Silicon Tracking System

E. Lavrik[1], A. Lymanets[1,2], and H. R. Schmidt[1]

[1]University of Tübingen, Tübingen, Germany; [2]Institute for Nuclear Research, NASU, Kiev, Ukraine

The CBM Silicon Tracking System (STS) is a compact array of silicon strip sensors [1]. The operation of the detector requires the silicon sensors to be permanently kept at a temperature of -7°C or below to avoid thermal runaway and reverse annealing of radiation effects. Thus, the detector array is housed in a thermal enclosure of about $2\,m^3$ of volume, which is located inside the CBM dipole magnet. The 2133k channels of the frontend readout dissipate about 40 kW of heat, which is produced in a relatively small volume defined by the location of the frontend readout boards (FEBs) attached to both ends of the STS ladders. The density of heat dissipation is thus extremely high and requires a cooling system with high volumetric cooling efficiency.

For this, evaporative bi-phase cooling [2] has been considered. Fig. 1 shows the volumetric heat transfer coefficient for different cooling agents as a function of the tube diameter. The best (volumetric) cooling performance is achieved for liquid CO_2 passed through 2 mm tubes.
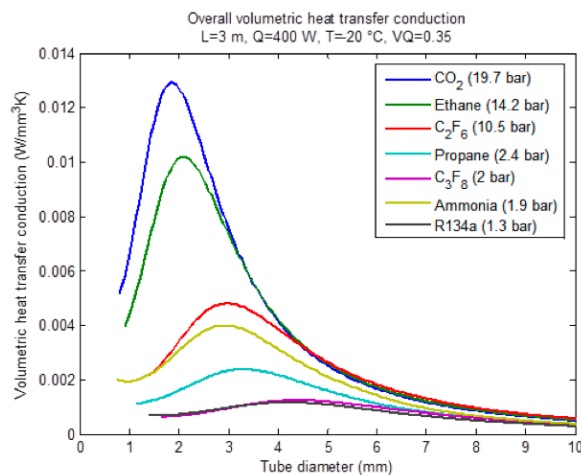
Figure 1: Volumetric heat transfer coefficient versus tube diameter for different cooling agents (courtesy B. Verlaat)

A first task is the verification of the cooling efficiency, i.e., it has to be demonstrated that 200 W dissipated in a FEB box can be removed under the given geometrical constraints. For these tests, a simple open-loop CO_2 cooling system has been constructed at the University of Tübingen. In parallel, a closed-loop prototype system (TRACI-XL) with 1 kW cooling power is being designed at GSI [3].

The operation principle of the open-loop system is sketched in Fig. 2. The liquid CO_2 flows from a pressure bottle at 63 bar and at room temperature through a heat ex-

changer, where it is cooled down to -25°C. Expansion behind a needle valve brings the liquid to 10 bar and -40°C, i.e., to the the bi-phase boundary, from whereon the latent heat can be used for cooling: when flowing through the heater simulating the thermal load, the liquid starts to evaporate, and the bi-phase mixture is formed.
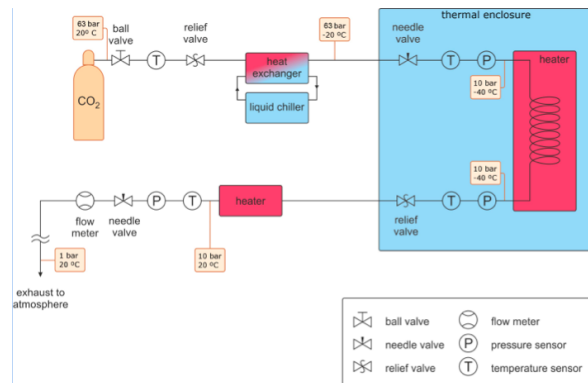
Figure 2: Scheme of the open-loop CO_2 cooling system

The heater simulates in detail the FEB box with its 10 frontend boards dissipating 20 W each. About 2 m of 2 mm stainless steel tube is compactly casted into an aluminum block of dimension $105 \times 70 \times 30\,mm^3$, which then serves as a heat exchanger for the FEB box. The assembly is mounted into a thermal enclosure to exclude heat flow from the outside. After leaving the thermal enclosure, the bi-phase mixture with about 50 % of gas is evaporated in a second heater and exhausted to the air. Those parts of the transport line which can be isolated by the valves and thus trap the liquid (dead volumes) are equipped with relief valves that prevent accidents due to overpressure (which can be as high as 720 bar). The overall pressure and the flow are controlled by a needle valve and a flow meter, respectively, which are installed after the second heater. Pressure and temperature are controlled at several points along the line to ensure proper operating conditions.

References

[1] J. M. Heuser *et al.*, Nucl. Instrum. Methods **A 568** (2006) 258

[2] B. Verlaat, M. van Beuzekom and A. van Lysebetten, *CO_2 cooling for HEP experiments*, Proc. TWEPP 2008, http://indico.cern.ch/contributionDisplay.py? contribId=152&sessionId=21&confId=21985

[3] J. Sánchez *et al.*, *TRACI-XL, the test cooling system for the CBM Silicon Tracking System*, this report

TRACI-XL, the test cooling system for the CBM Silicon Tracking System

J. Sánchez[1], *J. M. Heuser*[1], *C. J. Schmidt*[1], *P. Petagna*[2], *B. Verlaat*[2], *L. Zwalinski*[2], *H. R. Schmidt*[3], *and A. Lymanets*[3]

[1]GSI, Darmstadt, Germany; [2]CERN, Geneva, Switzerland; [3]Eberhard Karls University, Tübingen, Germany

An evaporative bi-phase cooling system based on CO_2 has been chosen as the best option to extract the heat produced by the read-out electronics in the CBM Silicon Tracking System. In the framework of the EU-FP7 project CRISP, the system TRACI (Transportable Refrigeration Apparatus for CO_2 Investigation), developed at NIKHEF/CERN to provide support to the ATLAS and LHCb experiments, is being upgraded at GSI from 100 W to 1 kW cooling power. This system TRACI-XL will be used as a testing device for the CBM application.

The I-2PACL principle (Integrated 2 Phase Accumulator Controlled Loop) was created as simplification of the 2PACL systems by using the CO_2 line to condensate the gas inside the accumulator instead of using a branched line derived from the condensing unit. Therefore the control is reduced to one cartridge heater controlled by PLC Siemens Simatic S7-1200. The size of the control unit is decreased, and it allows a wider range of possible operating temperatures from -30° C up to room temperature.
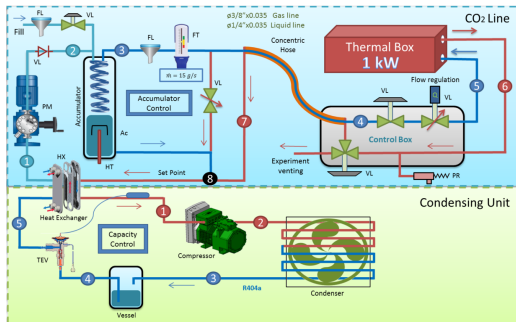
Figure 1: Process diagram of TRACI-XL

This range is obtained because of the implementation of a condensing unit equipped with a Bitzer 2DC-3.F1Y Varispeed compressor and Swep heat exchanger with the following system performance:

- at 30 Hz; Q_0 = 0,55 kW, T_0 =-45° C, $T_{suction}$ = -30° C, T_c = +35° C, T_{sub} = 3 K, R404a.

- at 87 Hz; Q_0 = 1.59 kW, T_0 = -45° C, $T_{suction}$ = -30° C, T_c = +35° C, T_{sub} = 3 K, R404a.

A LEWA membrane pump with remote head design, as innovation to avoid the addition of residual heat in the coolant, transports sub-cooled CO_2 to the evaporator in the thermal box (1-2-3-4-5 in Fig. 1). The CO_2 is heated up to the right evaporation temperature by a heat ex-change produced inside an inner hose with the returning CO_2

line (6-7). Due to the pulses generated by the metering pump the installation of a pulsation dampener is needed.
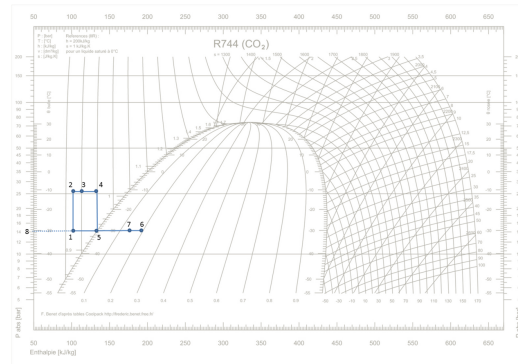
Figure 2: Cycle in the enthalpy-pressure diagram for R744

The heat generated in the read-out electronics is absorbed and extracted by the evaporator capillaries inside the thermal box (5-6). The return line (8-1) contains a bi-phase mixture which is liquefied by the condensing unit named previously below the operating temperature. By controlling the pressure inside an accumulator, the evaporation temperature can be fixed. This vessel contains two-phase CO_2 in contact (see Fig. 3).

(a) Full model   (b) CO_2 Line
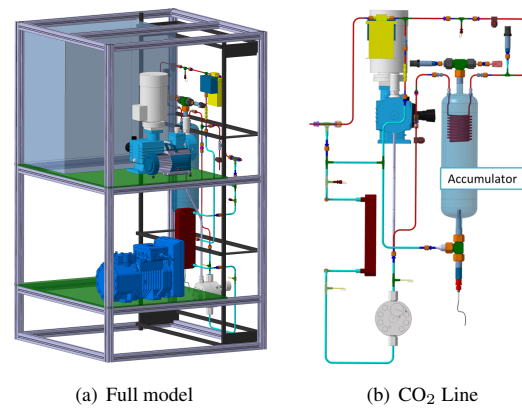
Figure 3: CAD model with CO_2 line detail

References

[1] B. Verlaat, *Controlling a Two-Phase CO2 Loop Using a Two-Phase Accumulator*, International Conference of Refrigeration 2007, Beijing, China, ICR07-B2-1565

System integration of the CBM Silicon Tracking System

U. Frankenfeld[1], S. Belogurov[2], J. Eschke[3,1], J. M. Heuser[1], V. Kleipa[1], P. Koczon[1], A. Kolosova[2], J. Kunkel[1], W. F. J. Müller[3,1], J. Sanchez Rosado[1], C. J. Schmidt[1], H. R. Schmidt[1,4], P. Senger[1,5], C. Sturm[1], and D. Soyk[1]

[1]GSI, Darmstadt, Germany; [2]ITEP, Moscow, Russia; [3]FAIR, Darmstadt, Germany; [4]Eberhard Karls University, Tübingen, Germany; [5]IKF, Frankfurt, Germany

For the system integration task of the Silicon Tracking System (STS) of the CBM experiment, a top-down approach has been chosen, starting from the physics requirements of the CBM experiment: interaction rates, radiation environment, tracking aperture and detector segmentation. A functional plan of the STS and its surrounding structural components is being worked out, from which the STS system shape is derived and the power need, cooling, the connector and cable space requirements, live span of components, and installation / repair aspects etc. are determined.
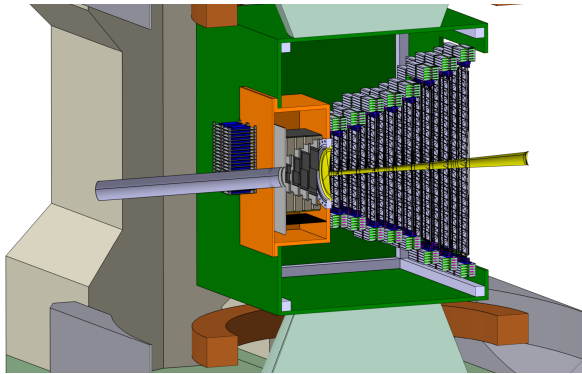
Figure 1: Detailed view of the STS in its envelope, MVD, beam pipe and target

The Silicon Tracking System will be installed into the superconducting dipole magnet, sharing the confined space with the target, the micro-vertex detector (MVD) and the beam pipe. The STS stations will be surrounded by a thermal enclosure to minimize radiation damage to the silicon sensors. This envelope is the supporting structure for the STS detector as well as for the MVD detector, which is located in its own vacuum vessel, the target and the beam pipe. The MVD vacuum chamber is mounted to the front side of the STS. The MVD detector itself is mounted on a flange and can therefore be removed without opening the STS volume. The MVD flange also supports the target. Figure 1 shows a sectional view of the STS isolation envelop (green) with the eight half stations of the STS. The beam pipe (yellow) and the MVD vacuum vessel (orange) are integrated into the isolation volume.

The STS envelope will be installed into the magnet from the upstream beam side. It is mounted on rails with prolongations which allow the insertion into the magnet. The position of the rails and the maximum dimensions of the STS envelope are predetermined by the dimensions of the dipole magnet, which is being designed by a separate workgroup. The so called H-type magnet allows the STS envelope dimensions to be $1400 \times 2000 \times 1100$ mm^3.

All Services like HV, LV, data and monitoring signals and cooling lines will be routed through the front panel into the STS envelope. This allows the dismounting of a half station through the open side panel of the STS box. The exact position will be optimized in order to minimize the interference between the MVD and the STS while dismantling one of the detectors for service work. The services have to be fed through the front panel such that its thermal isolation properties are preserved.
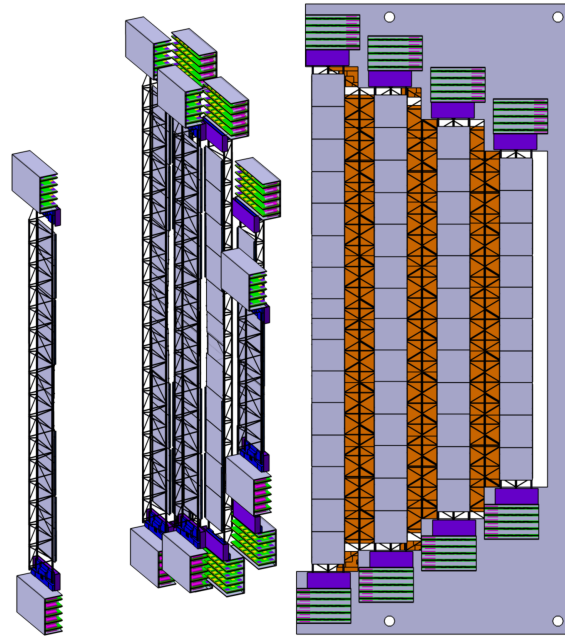
Figure 2: STS ladders assembled to a half station

The installation procedure of the STS will consist of the assembly of ladders equipped with modules (sensors and front end electronic) to a half station (see Fig. 2). The half station will be installed into the STS box. After installation of the services, the STS will be inserted into the magnet.

In the case of maintenance it is required to remove the STS, to get access to an arbitrary half station without dismantling the others and then to remove an arbitrary ladder leaving the other ladders in place.

In-beam test of a prototype CBM Silicon Tracking System at COSY

J. M. Heuser[1], W. Niebur[1], J. Eschke[1], S. Chatterji[1], C. J. Schmidt[1], W. F. J. Müller[1], I. Vassiliev[1], V. Kleipa[1], C. Simons[1], T. Balog[1,2], S. Linev[1], J. Adamczewski-Musch[1], B. Kolb[1], P. Zumbruch[1], A. Lymanets[3,4], I. Sorokin[5,4], A. Kotynia[5], and H. Malygina[5]

[1]GSI, Darmstadt, Germany; [2]Comenius University, Bratislava, Slovakia; [3]Eberhard Karls University, Tübingen, Germany; [4]Kiev Institute for Nuclear Research, Kiev, Ukraine; [5]Goethe University, Frankfurt, Germany

In January 2012, a prototype setup of the Silicon Tracking System (STS) for the CBM Experiment was tested in a 2.4 GeV/c proton beam at the COSY synchrotron of Research Center Jülich, Germany. The experiment aimed at a full-sytem test of prototype detector stations, data acquisition system, detector controls and online monitoring. Hit and cluster finding algorithms were applied to evaluate the performance of neutron-irradiated prototype sensors. A simple track reconstruction algorithm was applied to the acquired data to determine the position resolution of the system.
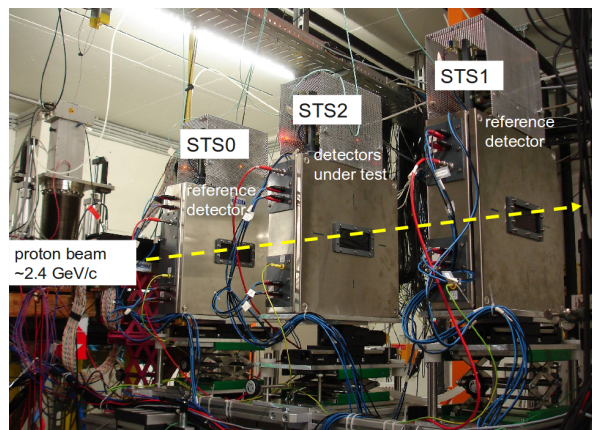
Figure 1: Beam test set-up of the prototype STS

The experiment in the JESSICA cave is shown in Fig. 1. It comprised three silicon detector stations and two scintillating fiber hodoscopes for beam monitoring. A further CBM prototype detector for the muon detection system was installed downstream of the silicon stations. All detectors were read out with self-triggering front-end electronics based on the n-XYTER1.0 ASIC that delivered time-stamped digitized analog data to the acquisition system. The two outer silicon stations, operated already in the 2010 beam test [1], included *CBM02* prototype sensors and were used as reference detectors. In the middle station, which could be rotated around the vertical axis to allow for different beam incidence angles, *CBM04* prototype sensors were under test irradiated with neutrons up to the maximum fluence 10^{14} n_{eq}/cm^2 expected in the CBM experiment. The sensors are described in [2].

The amplitude distributions of particle hits in the sensors

demonstrated clear separation of the signal from the noise. An example of a strip hit pattern is shown in Fig. 2 (left). With increasing beam incidence angle, the charge spread over clusters of adjacent strips grows as expected, which is shown in Fig. 2 (right). After geometrical alignment of the system, a simple track algorithm was applied to selected events with single particle hits, as depicted in Fig. 3. The spatial resolution obtained in both transverse coordinates was of the order of 35 μm for the reference stations, about a factor two worse than expected from the 58 μm strip pitch alone. The resolution of the irradiated sensors was slightly worse. It has to be further investigated how the increased currents with irradiated sensors and thus imposed higher thresholds, and other factors, impact on those results.
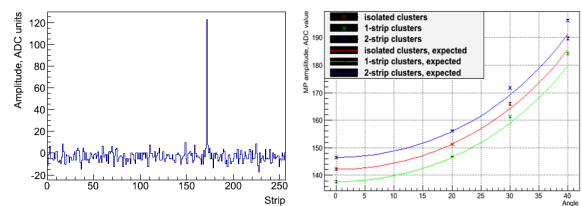
Figure 2: (left) Example of a single strip fired by a passing proton in a test sensor with 256 strips; (right) Cluster charge as a function of the beam incidence angle
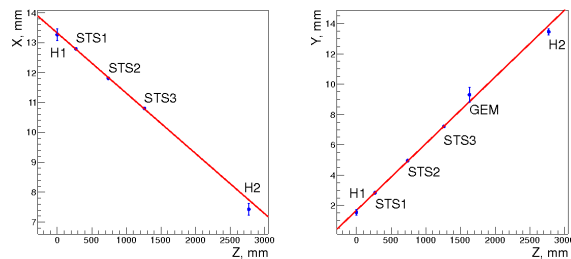
Figure 3: A reconstructed track shown in two projections

References

[1] J. Heuser *et al.*, CBM Progress Report 2010, p. 19

[2] J. Heuser *et al.*, CBM Progress Report 2009, p. 10
   J. Heuser *et al.*, CBM Progress Report 2011, p. 15

Charge sharing in micro-strip sensors determined from beam test data

I. Panasenko[1], J. Heuser[2], V. Kyva[1], V. Pugatch[1], and I. Sorokin[1,3]

[1]KINR, Kyiv, Ukraine; [2]GSI, Darmstadt, Germany; [3]FIAS, Frankfurt, Germany

In January 2012, prototype modules of the CBM Silicon Tracking System were tested in a 2.4 GeV/c proton beam at COSY, Forschungszentrum Jülich, Germany. The double-sided sensor CBM02-B2 (256 orthogonal strips per side with 50 μm pitch) was assembled into a demonstrator board; the readout was performed by 4 nXYTER chips. The sensor was operated at a bias voltage of 100 V, the full depletion voltage being 80 V.

1-strip and 2-strip clusters were reconstructed. It was found that in the case of proton penetration in the middle between two strips, the full charge of the cluster is approximately 10 % lower than in the case of proton penetration into one strip. Therefore there is a charge loss of less than 10 % in the interstrip gap, which is too small to significantly affect the performance of the sensor.

The correlation of the charges registered in two adjacent strips are shown in Fig. 1 for both the p-side and the n-side of the investigated sensor. The charge on the p-side peaks at about 130 ADC units, corresponding to the most probable signal from minimum ionizing particles (82 keV). The signal on the n-side is approximately 10 ADC units less than that on the p-side. The calculated signal-to-noise ratio is around 19 for the p-side and 18 for the n-side. This is sufficient for a reliable registration of useful events on top of the background for the not irradiated sensor of 285 μm thickness.
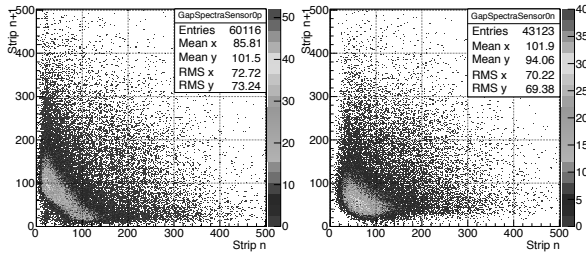
Figure 1: Charge correlation for two adjacent strips. Left: p-side, right: n-side of the sensor.

For tracks generating enough charge on two adjacent strips to exceed the threshold value in both of them, the position can be determined more precisely if the charge sharing function (η-function) is known. η is defined as the ratio of the charge collected by the right strip to the total charge of the cluster. Fig. 2 shows the distribution of η obtained from the experimental data. Only 2-strip clusters were taken into account for this analysis.

The presence of two peaks in the η distribution signals that the charge division between the two strips is far from
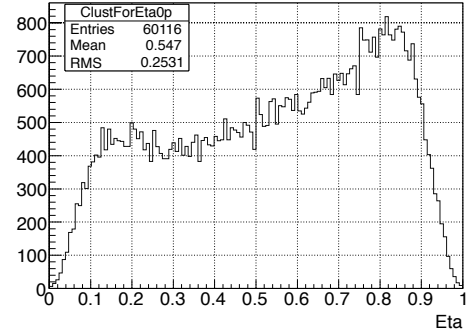
Figure 2: Experimental distribution of η for the sensor CBM02-B2 with a pitch of 50 μm

being linear. The capacitive coupling between the strips moves the peaks towards the center of the distribution, because a certain fraction of charge is always collected in the neighbouring strips.

Since the beam is much broader than the strip pitch, the distribution dN/dx is constant. Then, the hit position between two adjacent strips, in units of the strip pitch, is given by:

$$x_0 = \frac{1}{N_t} \int\limits_0^{\eta_0} \frac{dN}{d\eta} d\eta \qquad (1)$$

where N_t is the total number of entries is the dN/dη distribution and η_0 the fraction of the signal collected by the right strip in the considered event. Thus, from Fig. 2 the dependence of η on the hit position between the to strips can be derived. The result is shown in Fig. 3.
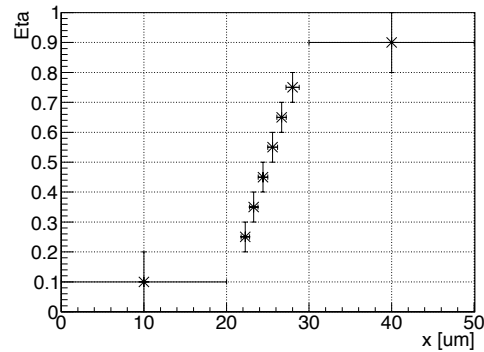
Figure 3: Variable η versus hit position between two adjacent strips.

Performance simulations of the CBM-STS with realistic material budget

V. Friese[1] *and A. Kotynia*[2]

[1]GSI, Darmstadt, Germany; [2]Goethe-Universität, Frankfurt, Germany

The task of the Silicon Tracking System (STS) of the CBM experiment is to reconstruct the trajectories of up to 600 charged particles created in nucleus-nucleus collisions. For the performance of the system, its material budget is a crucial issue since multiple scattering in the detector material will lead to a decrease in both track finding efficiency and momentum resolution. In order to assess these performance figures, a realistic implementation of active and passive materials in the simulations is required.

The system is composed of double-sided micro-strip sensors of 300 μm thickness, which was found to be the best balance between signal-to-noise ratio and material budget. In addition to these active sensors, cables transporting the analog signals from the inner sensors to the read-out at the top or bottom of the system add to the material in the acceptance. Lately, a detailed design of the analog cables was developed [1], which now allows to have a realistic description of the material budget as input to the simulations.

The signals will be transported by two staggered layers of Aluminum cables on polyimide carriers. In the simulation geometry, these two layers are represented by a single volume of 100 μm silicon (0.1 % X_0) as equivalent material budget. At the vertical periphery of a STS station, up to four of such cable volumes overlap. Consequently, the material budget within one station varies with the vertical distance from the beam; its maximal value is about 0.8 %. As an example, the material budget distribution of station 4 at z = 60 cm is shown in Figure 1.
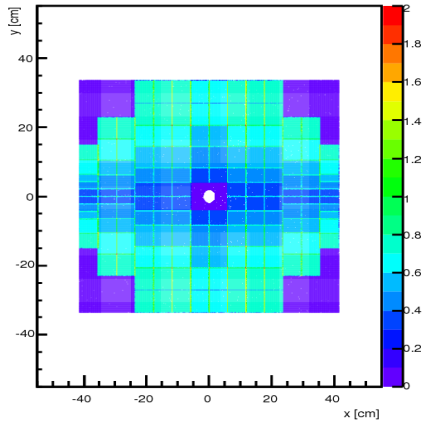
Figure 1: Distribution of material budget in tracking station 4

This model of the STS was implemented in the CBM software framework and subjected to simulations of Au+Au collisions in the CBM detector setup. A realistic detector response was applied as described previously [2].

The tracks were reconstructed by the Cellullar Automaton track finder algorithm; their parameters were determined by the Kalman Filter. The results of these simulations are shown in Fig. 2. The average efficiency for primary tracks above 1 GeV is 96 %, only 1 % less than obtained in previous simulations without the cable materials. Similarly, the efficiency for secondary tracks is hardly affected by the additional material. A more noticeable, but still moderate effect of the cable material is seen in the momentum resolution. Its average value is found to be 0.98 % (Gaussian σ), compared to 0.87 % without cables.
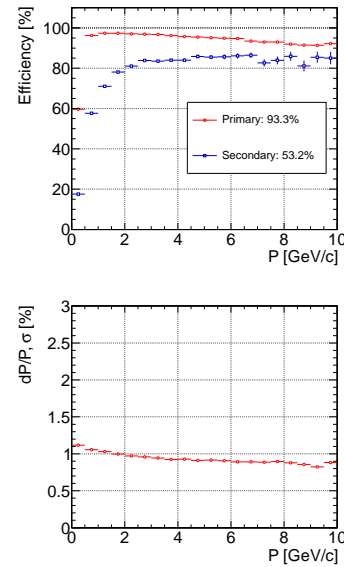
Figure 2: Track reconstruction efficiency (upper panel) and momentum resolution (lower panel) in the STS as a function of the momentum for all tracks in central Au+Au collisions at 25 AGeV projectile energy

In summary, the current simulations of the STS comprise a realistic material budget, including the analog read-out cables. The support structures made of carbon fibre are not yet included, but their contribution to the total material is minor. Within our simulations, we find the track reconstruction efficiency and the momentum resolution to match the CBM requirements. The module concept for the STS can thus be considered as validated.

References

[1] C. J. Schmidt *et al.*, *An assembly concept for modules of the CBM Silicon Tracking System*, this report

[2] A. Kotynia and J. M. Heuser, CBM Progress Report 2010, p 8

Neutron shielding for the CBM silicon tracker

A. Senger

GSI, Darmstadt, Germany

The CBM experiment is designed as a multi-purpose device which will be able to measure hadrons, electrons and muons in heavy-ion collisions. The core detector of the CBM setup is a Silicon Tracking System (STS) located in the gap of a superconducting dipole magnet. Electrons will be identified with a Ring-Imaging Cherenkov Detector (RICH), a Transition Radiation Detector (TRD), and a Time-of-Flight Detector (ToF). In order to measure muons, the RICH will be replaced by Muon Tracking Chambers (MuCh). The MuCh consists of 6 hadron absorbers and tracking stations in between. The first 20 cm iron absorber is located 5 cm behind the last silicon tracking station. FLUKA [1, 2] calculations predict an increased non-ionizing energy loss (NIEL) level in the STS with the muon setup.

The main reason for the increase of the NIEL level is back-scattered neutrons from the hadron absorber. This was studied with a simple model presented in Fig. 1. It consists of the CBM target (250 μm Au foil), the magnet, and the beam pipe. The neutron flux at the position of the last STS station (see scoring plane in Fig. 1) was calculated with and without 20 cm iron absorber. The neutron distributions are shown in Fig. 2 (blue and red lines). The number of neutrons increases up to 10 times if the hadron absorber is put in. In order to shield the neutrons from the absorber, a borated polyethylene layer was placed between the scoring plane and the iron. The neutron distributions with 5 cm neutron shielding for different fractions of boron are presented in Fig. 2 (light blue and green lines). The number of neutrons decreases up to 4 times if a 5 cm 5% borated polyethylene layer is put between the scoring plane and the iron. Figure 3 shows the NIEL distribution in the last STS layer for the electron setup (right), for the muon setup (left), and for the muon setup with the neutron shielding (middle). The NIEL level decreases substantially if the

neutron shielding is used.

In summary, the FLUKA study demonstrated the possibility to shield neutrons from the iron absorber. The 5 cm 5% borated polyethylene layer allows to reduce the NIEL level in the last STS station by a factor of up to five.
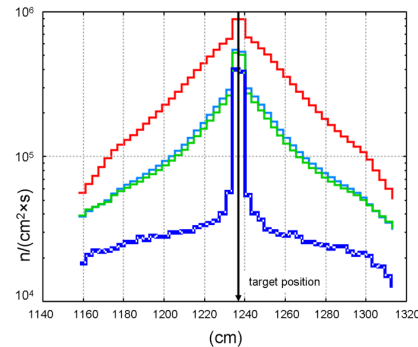
Figure 2: Neutron distributions in the position of the last STS station calculated with FLUKA. Blue: without 20 cm iron absorber, red: in front of the absorber without neutron shielding, light blue: with 5 cm 5% borated polyethylene layer, green: with 5 cm 30% borated polyethylene.
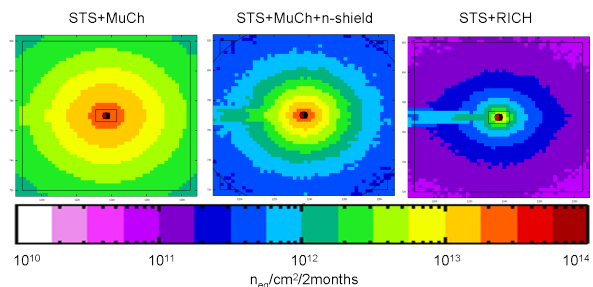
Figure 3: NIEL distributions in the last STS station for 35 GeV/u Au beam after 2 months of run with an intensity of 10^9 ions per second for the electron setup (right), for the muon setup with 5 cm neutron shielding (middle), and for the muon setup without shielding (left)

Figure 1: The FLUKA geometry for optimization of the neutron shielding

References

[1] G. Battistoni, S. Muraro, P. R. Sala, F. Cerutti, A. Ferrari, S. Roesler, A. Fasso' and J. Ranft: *The FLUKA code: Description and benchmarking*, in: Proceedings of the Hadronic Shower Simulation Workshop 2006, Fermilab 6-8 September 2006, M. Albrow, R. Raja (eds.), AIP Conference Proceeding **896** (2007) 31

[2] A. Fasso', A. Ferrari, J. Ranft and P. R. Sala: *FLUKA: a multi-particle transport code*, CERN-2005-10 (2005), INFN/TC_05/11, SLAC-R-773

Results from the CBM-RICH in-beam test 2011 at the CERN-PS

J. Kopfer[1], V. Dobyrn[5], C. Dritsa[4], M. Dürr[3], J. Eschke[2], I. Galm[3], C. Höhne[4], K.-H. Kampert[1],
L. Kochenda[5], P. Kravtsov[5], D. Kresan[4], S. Lebedev[4], E. Lebedeva[4], T. Mahmoud[4], C. Pauly[1],
J. Pouryamout[1], J. Rautenberg[1], S. Reinecke[1], E. Roshchin[5], V. Samsonov[5], J. Song[6], E. Vznuzdaev[5],
M. Vznuzdaev[5], J. Yi[6], and I.-K. Yoo[6]

[1]Bergische Universität, Wuppertal, Germany; [2]GSI Darmstadt, Germany; [3]Hochschule Esslingen, Esslingen, Germany; [4]Justus-Liebig-Universität, Gießen, Germany; [5]Petersburg Nuclear Physics Institute, Russia; [6]Pusan National University, Korea

The real-size CBM-RICH prototype was operated for the first time in 2011 in a common beam test together with other CBM groups at the CERN PS/T9 beamline [1]. The aim was to verify the concept of the CBM-RICH detector, to validate the CBM-RICH simulations with the `cbmroot` framework by testing the ring finding and fitting algorithms, and to get experience in building and running the RICH detector including gas-system, mirror alignment, data read-out, and ring reconstruction.

The experimental setup is described in [1]. Here, we will present results on the single photon detection capabilities of the photon detector, the influence of the radiator gas on ring parameters, fitted Cherenkov ring radii, the number of detected photoelectrons per ring (hit multiplicity) for different types of MAPMT photocathodes and number of dynode stages, for MAPMTs with wavelength shifting (WLS) films on the front window, and the electron pion separation capability which are important parameters in order to evaluate the overall prototype performance. A second beam test was carried out in 2012 [2].

The CBM-RICH prototype geometry has been implemented in the `cbmroot` framework including the measured properties of its components as the wavelength dependent quantum efficiency of different MAPMT types, the additional hit fraction due to crosstalk, and the mirror reflectivity.

The time difference between the hits and the trigger as well as a typical single photon ADC spectrum from one channel are shown in Fig. 1. The extremely low rate of un-correlated noise [1], together with a time cut with a width of 100 ns, permit an almost noiseless detection of Cherenkov rings. A cut on the signal amplitude turns out not to be necessary to further suppress noise.
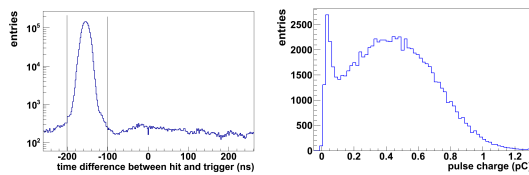
The relative detection efficiency of each MAPMT pixel is extracted from a measurement with homogeneous single photon LED illumination at 350 nm, a wavelength at which the WLS films are transparent. It is observed that the detection efficiency of pixels within one MAPMT varies by a factor of 1.72 at most. The detection efficiency between different MAPMTs varies by a factor of 1.16 when additional hits due to crosstalk between neighbouring pixel are subtracted. In the analysis, the data were normalized with the relative detection efficiency of each channel (correction factor, Fig. 2 left) leading to the same hit multiplicity for the same MAPMT type. That way of correcting for tube-to-tube and channel-to-channel variations is an essential prerequisite to estimate the effect of the usage of a WLS coating on the MAPMT window.
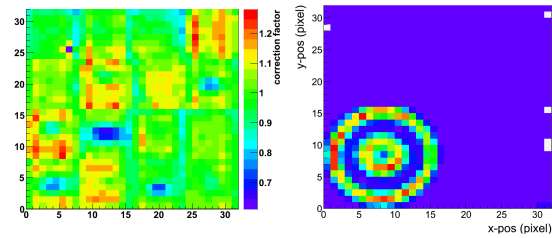
Figure 2: Left: number of detected photoelectrons for a homogeneous single photon illumination normalized to an average of 1 (correction factor) for the 1024 channels of the CBM-RICH prototype. Right: event display of accumulated electron, muon, and pion rings at 5 GeV/c.

During the beam test, temperature and pressure of the radiator gas varied with weather conditions. Figure 3 shows, for the same detector settings, fitted ring radius r and hit multiplicity N as function of the refractive index of the radiator which is calculated from temperature and pressure. Comparing the measurement to the expected curves (red), it can be seen that the experimental data are understood. Temperature and pressure correction have been performed by normalizing values to the conditions at $T = 20\ °C$ and $p = 958$ mbar.

The number of Cherenkov photons arriving at the photon detector is sensitive to the gas purity since e.g. O_2 and H_2O molecules absorb UV photons. Increasing the O_2 content from the nominal value of 50 ppm to 350 ppm does not

Figure 1: Time and amplitude distribution for individual hits before cuts. In order to reduce noise, only hits between 200 ns and 100 ns before the (delayed) trigger are selected.

deteriorate the Cherenkov ring hit multiplicity noticeably. Thus no correction has been made for the O_2 and H_2O content.
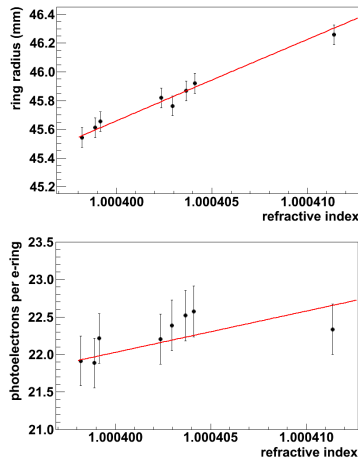
Figure 3: Fitted radius (top) and hit multiplicity (bottom) of electron rings as function of refractive index of the radiator gas. The red lines indicate the expectation from theory.

As electrons are ultra-relativistic in the momentum range of PS/T9, the parameters of electron rings are constant and therefore a good quantity for systematic studies. Depending on the position of the Cherenkov ring on the photon detector, the electron ring radius extracted from the beam test data is 4.58 to 4.67 cm which is in agreement with simulation (4.67 cm). With such a radius one Cherenkov electron ring fits on 2×2 MAPMTs (Fig. 2 right).

An important quantity for the efficiency of ring finding and the quality of ring fitting is the hit multiplicity. Counting the hits per ring leads to hit multiplicities between 21.4 and 23.4 per electron ring for the standard MAPMTs (BA photocathode, 12 dynode stages) depending on the efficiency of the MAPMTs, temperature and pressure. Note that these numbers include additional hits due to crosstalk. Simulations with realistic quantum efficiency, crosstalk, and mirror reflectivity reveal a value of 23.7. It is found that the hit multiplicity per ring covered by two 8-stage/SBA and two standard MAPMTs is (7.7 ± 1.4) % lower. This means that the higher quantum efficiency of the SBA photocathode does not compensate the disadvantage of the lower gain of the 8 dynode stages. Because of the relatively low gain, the performance of the 8-stage MAPMTs, however, depends on the signal attenuation necessary when using the n-XYTER chip [3]. This result has to be considered as preliminary. Therefore, the 8-stage MAPMTs were tested again with optimized signal attenuation during the 2012 beam test.

Four standard MAPMTs were coated with WLS films by means of dip-coating in order to enhance the detection of UV photons. The data show that the use of WLS films does not increase the number of additional crosstalk hits.

The hit multiplicity is increased by (12.2 ± 1.7) % when using WLS coated instead of bare MAPMTs. This result is in agreement with a simulation considering the measured quantum efficiency curves of WLS coated MAPMTs, which predicts an increase of 12.4 %.

During the beam test, the momentum of electrons and pions was varied between 2 and 10 GeV/c in steps of 1 GeV/c. Figure 4 shows the simulated and measured ring radius for electrons and pions as function of particle momentum. A good agreement between simulation and data is seen. To quantify the electron-pion separation capability of the detector, a Gaussian is fitted to the radius distribution. For particles with momenta of 8 GeV/c the separation of electrons and pions (in terms of ring radius) is larger than 7 σ_π, where σ_π is the width of the Gaussian fit to the pion radius distribution (Fig. 5).
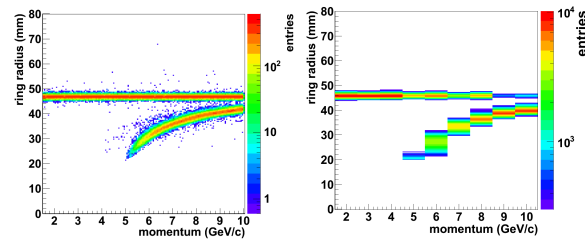
Figure 4: Ring radius vs. incident particle momentum in simulation (left) and data (right)
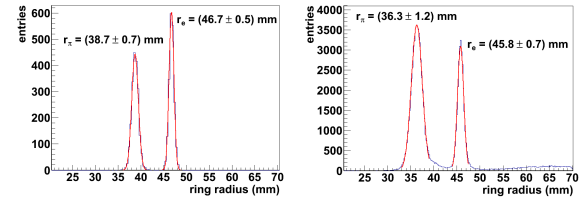
Figure 5: Fitted ring radius for electrons and pions at 8 GeV/c in simulation (left) and data (right). Note that the ratio between electrons and pions in simulation is 1:1 whereas in data it is approximately 1:2. The tail of the pion peak to large radii in the data is due to imperfectly subtracted muons.

In summary, the successful operation of the CBM-RICH prototype at the CERN PS can be seen as a proof of principle for the proposed RICH layout. The ring finding and fitting algorithms were tested with real data for the first time. Results show good agreement with simulation.

References

[1] J. Kopfer *et al.*, CBM Progress Report 2011, p. 32

[2] S. Reinecke *et al.*, *Overview of the RICH-prototype beam test 2012 at the CERN-PS*, this report

[3] C. Pauly *et al.*, CBM Progress Report 2011, p. 35

Crosstalk between neighbouring channels in multianode PMTs

J. Kopfer, K.-H. Becker, K.-H. Kampert, C. Pauly, J. Pouryamout, S. Querchfeld, J. Rautenberg, and S. Reinecke

Bergische Universität, Wuppertal, Germany

The photon detector of the CBM-RICH is foreseen to be built from multianode photomultiplier tubes (MAPMTs). The usage of MAPMTs has the advantage of good time and spatial resolution and a very low dark rate. Up to now, R&D was focussed on the Hamamatsu metal channel dynode type PMTs H8500 and R11265. The H8500 has 64 pixels of 5.8 x 5.8 mm^2 each. The R11265 has 16 pixels with the same pixel size. The suitability of the H8500 for single Cherenkov photon detection has been demonstrated in laboratory tests [1] and in beam tests [2, 3].

In a RICH detector the number of registered photons per Cherenkov ring is important for the efficiency of ring finding and the quality of the ring fitting. In order to evaluate the number of registered photons, crosstalk has to be taken into account, of which there are two different sources: firstly, optical crosstalk from the incident light spread in the front window and from photo electrons travelling on a curved trajectory from photo cathode to first dynode, and secondly, electrical crosstalk from the splitting of the electron avalanche between the dynodes during secondary electron multiplication and on the segmented anodes. Optical crosstalk will mainly cause a smearing of position information and does not influence the number of registered photons whereas electrical crosstalk generates additional hits in the neighbouring pixels.

Crosstalk measurements for the H8500 have already been done by illuminating one pixel with a pulsed 350 nm LED/tungsten lamp with the help of an aperture mask or optical fibre [4, 5]. Here, we present measurements of additional hits caused by crosstalk on the single photon level at a wavelength of 275 nm.

The measurement is based on a homogeneous single photon illumination of the MAPMT without usage of an aperture mask or light fibre, which has the advantage that the photons hit the pixel not only at the central part but homogeneously distributed over the whole surface as it will be the case in the RICH detector. Single photons hitting the outer parts of a pixel will create more crosstalk than those hitting the centre. The data readout is described in [3]. In order to estimate the number of additional hits in neighbouring pixels due to crosstalk, the distribution of the geometrical distance of hits in events with exactly two hits per MAPMT (2-hit-events) is compared to a simulation without crosstalk (Fig. 1). The normalized excess of entries in the bin corresponding to direct and diagonal neighbours in the data compared to the simulation quantifies the crosstalk.

The crosstalk extracted by this method depends on the threshold applied to the ADC signal. Figure 2 shows the
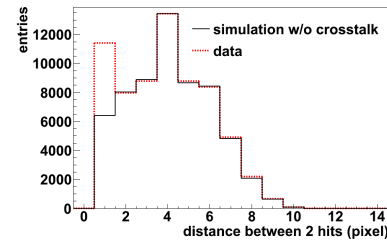
Figure 1: Geometrical distance of hits in 2-hit-events within one MAPMT in simulation (solid line) and data (dashed line). Because of crosstalk, simulation and data differ in the second bin ("neighbour bin").

additional hit fraction (crosstalk) as function of MAPMT gain for 12 H8500 and 7 R11265. For a common threshold for all MAPMTs, the crosstalk rises with gain. This is expected as for high-gain MAPMTs the relatively small ADC values of the crosstalk hits are more likely to pass the threshold. If, however, individual thresholds for every MAPMT at 10 % of the single photo-electron peak are applied, the crosstalk is fairly constant. When averaging the values we see that for H8500 (6.8 ± 1.2) % additional crosstalk hits are found; the corresponding amount for R11265 is (3.2 ± 0.7) %.
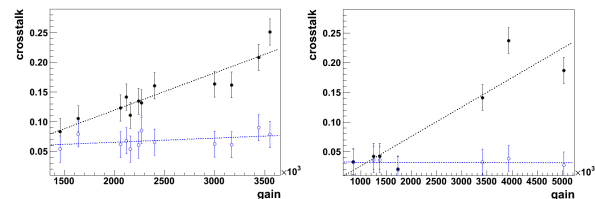
Figure 2: Crosstalk as function of gain for common threshold (solid circles) and for threshold at 10 % of the single photon peak (open circles) for H8500 (left) and R11265 (right). Linear fits to the data are shown as dashed lines. Every data point corresponds to one MAPMT. The HV of all MAPMTs was set to the same nominal value of 1 kV.

References

[1] C. Pauly *et al.*, CBM Progress Report 2010, p. 26

[2] J. Eschke *et al.*, CBM Progress Report 2010, p. 24

[3] J. Kopfer *et al.*, CBM Progress Report 2011, p. 32

[4] J. Eschke *et al.*, CBM Progress Report 2010, p. 28

[5] Hamamatsu Photonics K.K., *Photomultiplier Tubes: Basics and Applications*, Word Technical Writing Inc., 2007

Overview of the RICH-prototype beam test 2012 at the CERN-PS

S. Reinecke[1], K.-H. Becker[1], V. Dobyrn[5], C. Dritsa[4], M. Dürr[3], C. Höhne[4], K.-H. Kampert[1],
L. Kochenda[5], J. Kopfer[1], G. Krauss[3], P. Kravtsov[5], S. Lebedev[4], E. Lebedeva[4], T. Mahmoud[4],
E. Ovcharenko[7], C. Pauly[1], J. Pouryamout[1], J. Rautenberg[1], Y. Riabov[5], E. Roshchin[5], V. Samsonov[5],
J. Song[6], E. Vznuzdaev[5], M. Vznuzdaev[5], J. Yi[6], and I.-K. Yoo[6]

[1]Bergische Universität, Wuppertal, Germany; [2]GSI, Darmstadt, Germany; [3]Hochschule Esslingen, Esslingen,
Germany; [4]Justus-Liebig-Universität, Gießen, Germany; [5]Petersburg Nuclear Physics Institute, St. Petersburg, Russia;
[6]Pusan National University, Pusan, Korea; [7]ITEP Moscow, Russia

In October/November 2012 the RICH prototype was tested again at the CERN-PS/T9 beam line together with prototypes of the TRD and TOF sub-systems of CBM.

The real-size RICH prototype that was build and successfully tested in a beam test at CERN in 2011 [1] has been improved and extended for this years test at CERN. The changes with respect to the 2011 beamtime can be summarized as follows:

- new photon camera design including 3 different types of MAPMTs/MCPs for comparison,
- alternative read-out electronics for direct comparison with standard n-XYter solution [2],
- improved WLS (optimized thickness) coating on several different MAPMTs [3],
- laser based monitoring system of MAPMTs/MCPs,
- fully functional EPICS based mirror-control system offering high flexibility and convenient positioning of the mirror positions [4],
- new EPICS based temperature and pressure monitoring system [5],
- second beam hodoscope for full single track reconstruction [6].

As an alternative to the H8500 MAPMTs, several R11265 MAPMTs were included in the new photon camera design (see Fig. 1). Unlike the H8500 the R11265 is explicitly recommended by Hamamatsu for single-photon measurements. Micro-channel plates (MCPs) from Photonis of type XP85012 were tested as well because they can still work in magnetic fields up to 1 T. Using these MCPs would therefore release all constraints on the RICH performance with respect to the magnetic stray field [7].

Some of the MAPMTs were covered with a wavelength shifting film (WLS) of optimised thickness. These were removed during the beam time to get a better quantitative understanding of the influence of the WLS on the photon detection efficiency. In addition, some H8500 MAPMTs which have particularly been selected as "bad" from Hamamatsu were tested under realistic conditions. With these additional testing units the layout of the camera was slightly modified as shown in Fig. 1.

A new feature of this year's beam time was a pulsed-laser-driven system to simultaneously take data of Cherenkov rings, covering only a small part of all channels, and of homogeneously distributed single photons over the whole camera surface. The light pulses were coupled via an optical fibre and a diffuser, positioned on top of the mirror frame and pointing towards the camera.

The slow-control system based on EPICS allowed for control and recording of all high voltage values and the mirror position. Parameters from the stand-alone gas-system control [8] such as temperature and pressure, being essential for the calculation of the refractive index and thus for later calibration of the data, were handed over to EPICS and saved within this control system. In addition a new set of temperature sensors allowed for a detailed measurement of temperatures in the gas and electronics unit.

With these modifications the goals for the beam time can be summarized as:

- evaluation and comparison of MAPMT/MCP solutions alternatively to the H8500,
- final evaluation of WLS coating, adding the R11265 MAPMT with SBA cathode,
- test newly developed FPGA-TDC read-out electronics under beam conditions,
- improved understanding of the RICH prototype performance (e.g. mirror misalignment [9]).
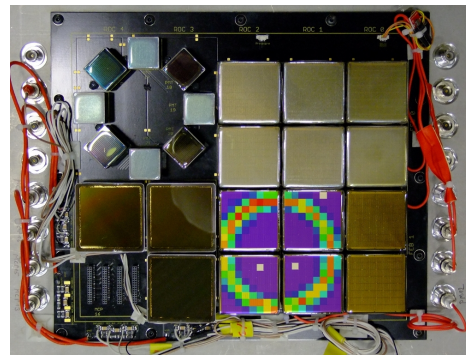
Figure 1: Photograph of photon detector tested in 2012, overlayed with one integrated ring image of scaled size. The 3×4 MAPMTs on the right half are of type H8500, the 8 ring-shape arranged MAPMTs in the upper left corner of type R11265 and the 3 ones in the lower left corner are the Photonis XP85012 MCPs. MAPMTs covered with WLS can be recognized by their milky-looking surface ($6\times$ H8500 + $4\times$ R11265).

The analysis of the beam time data has only been started yet. Details on hit multiplicities per Cherenkov ring, single photon spectra for the different photon detectors and read-out electronics together with noise rates and crosstalk and more will be investigated. Here, only a few preliminary impressions shall be given.

Already from the Go4 online analysis during the beam time it became clear that the MCPs register many more hits than the MAPMTs. The ongoing analysis shows that this is partially caused by the increased crosstalk of the MCPs and also by the increased efficiency in the UV-region due to the quartz window of the MCPs (the MAPMTs in contrast have only UV-extended borosilicate glass).
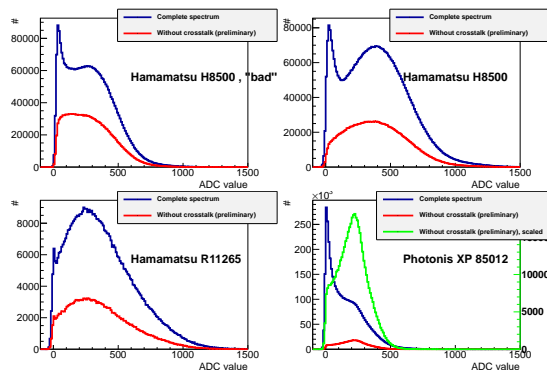
Figure 2: Typical single-photon spectra for LED events (blue: all data taken, red: without crosstalk, green: red line scaled up). Top left: H8500 selected as "bad" by Hamamatsu, top right: H8500, bottom left: R11265, bottom right: XP85012 MCP.

One parameter to judge the different MAPMTs/MCPs are the single-photon spectra. In Fig. 2 the single-photon spectra for LED events (blue: all events, red: remaining hits after subtracting hits probably caused by crosstalk by applying a condition on hits in neighbouring pixel) for four different MAPMTs/MCPs are shown (for the MCP with additionally scaled peak in green). The "bad" MAPMT shows a clear difference compared to a normal one, as there is no well defined single-photon peak visible. In contrast the MCP shows a pronounced peak with a good peak-to-valley ratio. In this preliminary check the performances of a standard H8500 and a R11265 MAPMT are very comparable.

Detailed mirror misalignment studies have been performed in order to establish limits on the later precision for mirror alignment [9].

Within less than one year a new type of read-out electronics was developed, which could serve as a first prototype for the final RICH read-out. This read-out is based on the existing TRB3 board [10] and is described in more detail in [2]. 4 Modules were implemented serving for the read-out of 4 MAPMTs, i.e. allowing to measure a complete Cherenkov ring. This concept proved to work well, although the noise performance and efficiency still need to be improved. Figure 3 shows a comparison of an event in-

tegrated Cherenkov ring image read out with the n-XYTER and TRB3 electronics in the left and right half, respectively. Systematic tests of the different photon detectors as well as read-out electronics were performed by varying the HV and thresholds.
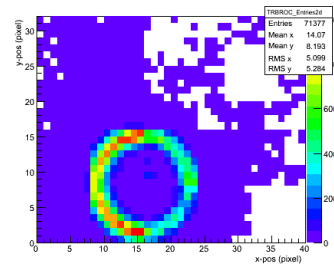
Figure 3: Integrated ring image of a combined read-out of n-XYTER (left half of the ring) and the newly developed RICH-TRB3 electronics (right half of the ring) with H8500 MAPMTs.

The gas system worked very reliably, and it could be shown that even a high contamination of the RICH radiator gas ($O_2 > 1000$ ppm, $H_2O > 230$ ppm) does not influence the detector performance in a significant range [11].

With the wealth of data taken through this successful beam time, enough information should be available to make final design decisions on certain layout parts of the RICH detector.

We would like to thank J. Adamczewski-Musch and S. Linev for their valuable support in all DAQ and analysis related issues as well as J. Michel, M. Traxler and C. Ugur for making this first test of a TRB3 based MAPMT/MCP read-out possible within less than a year.

References

[1] J. Kopfer *et al.*, CBM Progress Report 2011, p. 32

[2] C. Pauly *et al.*, *First lab tests of a new RICH readout electronic prototype module*, this report

[3] T. Schweizer *et al.*, *MAPMTs with wavelength-shifting films on UV-extended windows - dependence of quantum efficiency on layer thickness*, this report

[4] J. Song and I.-K. Yoo, *Slow control system for the RICH prototype*, this report

[5] K.-H. Becker, C. Pauly and K.-H. Kampert, *Development of an ARDUINO-based slow-control monitoring system with EPICS integration*, this report

[6] C. Pauly *et al.*, CBM Progress Report 2011, p. 31

[7] C. Pauly *et al.*, CBM Progress Report 2010, p. 26

[8] P. Kravtsov *et al.*, CBM Progress Report 2010, p. 32

[9] T. Mahmoud and C. Höhne, *Mirror displacement tests - simulation and preliminary results*, this report

[10] M. Traxler *et al.*, JINST **6 C** (2011) 12004

[11] L. Kochenda *et al.*, *Results of the RICH prototype gas system during the 2012 beam test*, this report

Slow control system for the CBM-RICH prototype

J. Song and I.-K. Yoo

Pusan National University, Busan, Korea

In order to control and monitor the RICH prototype during beam operation, a slow control system has been developed which is based on the open source software package EPICS (Experimental Physics and Industrial Control System) [1]. We developed control systems for mirror positioning and high voltage and a monitoring system for environmental sensors (pressure and temperature for gas and electronic modules) with EPICS and integrated all control systems to one IOC (Input Output Controller) system. The scheme of the slow control system is shown in Fig. 1.
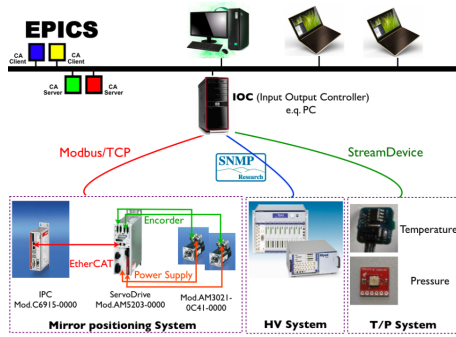
Figure 1: EPICS architecture for slow control systems

A GUI (Graphical User Interface) based on the EPICS client software CSS (Control System Studio) has been developed for easy online control of all parameters. Most of these parameters such as mirror tilt angles, HV values etc. were stored in the DAQ data stream during the beamtest at the CERN-PS.

For the mirror positioning control, we used two servo motors (AM3021-0C41-0000), servo drives (AX5203-0000) and an Industrial PC (IPC, C6915-0000) from Beckhoff [2]. The IPC is connected to the servo drive and communicates via EtherCAT. The TwinCAT (The Window Control Automation Technology) program is installed in this IPC based on the Windows CE operating system. Finally the TwinCAT program in the IPC is linked with IOC via the Modbus/TCP protocol. As an EPICS server the IOC provides information and services to the EPICS clients via the CA (Channel Access) protocol.

For a more flexible use of mirror positioning, a GUI has been newly developed based on CSS (Fig. 2). This GUI enables us to save any mirror positions for complex measurement sequences. This new version was fully operational for the beamtest in October 2012 at the CERN-PS.

For the HV control, a Mpod crate and HV modules are connected to an EPICS server (IOC) via SNMP (Simple Network Management Protocol) as explained in [3].
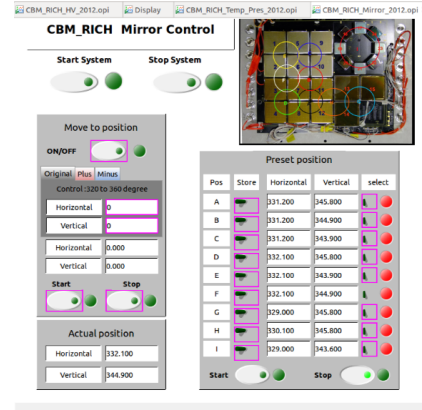
Figure 2: GUI for the mirror positioning control system. Left: Previous version; right: new version.

A new ARDUINO-based development for the slow control of temperature and pressure (TP) as described in [4] has been implemented in EPICS by reading data from these sensors via StreamDevice. A GUI for the TP monitoring system has also been developed based on CSS as shown in Fig. 3. An alarm function is added for warning of high temperatures with indicating which modules are over-heated.
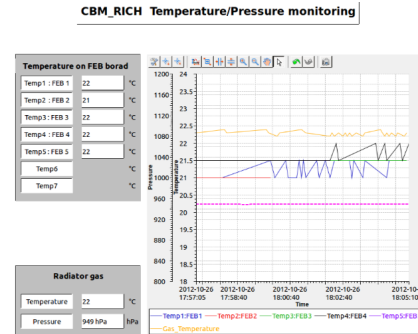
Figure 3: GUI for the TP monitoring system

References

[1] http://www.aps.anl.gov/epics/about.php

[2] http://infosys.beckhoff.com/index_en.htm

[3] J. Song, C. Son and I.-K. Yoo, CBM Progress Report 2011, p. 41

[4] K. H. Becker *et al.*, *Development of an ARDUINO-based slow control monitoring system with EPICS integration*, this report

Development of an ARDUINO-based slow-control monitoring system with EPICS integration

K.-H. Becker, C. Pauly, and K.-H. Kampert

Bergische Universität, Wuppertal, Germany

The monitoring (and control) of parameters like temperature, pressure, currents and voltages is a common task to ensure stable detector operation during beam tests. The CBM detector slow control will be based on EPICS ("Experimental Physics and Industrial Control System"), which is a set of Open Source software tools to provide software infrastructure for building distributed control and monitoring systems [1]. A central component in EPICS are Input-Output Controllers (IOC), of which many can be distributed over the network and each control or monitor a certain subset of Process Variables (PV).

We developed a new slow control hardware interface for easy integration and readout of many different input/output channels, in particular inexpensive, commercially available I2C sensor devices. The interface connects via Ethernet to a standard EPICS IOC client running on a Linux PC.

The interface is based on the commercially available ARDUINO board, utilizing the ATMEL ATmega2560 embedded processor. A photograph of the interface box is shown in Figure 1. The ARDUINO board provides various input/output interface connections for sensor readout: 54x simple digital I/O pins, 16x 10bit analog ADC inputs, 1x I2C interface, 4 UARTs etc. Additional functionality can be achieved by standardized add-on boards, called shields. We attach an Ethernet shield for communication to the EPICS-IOC. During the recent CBM-RICH prototype beamtest at CERN/PS [2] we used the system in connection with integrated temperature and pressure sensors as shown in Fig. 2 to monitor the radiator gas temperature and pressure, as well as the temperature of each individual readout module. Resolution of these sensors is very good, 0.01 mbar / 0.1 K. The sensors were read out via a common I2C bus implemented on the RICH photon camera read out board. The I2C-bus on the camera was extended via long (3m) cable to the ARDUINO interface box, which acted as I2C bus master. A maximum of 7 temperatur sensors of type TMP75 (plus one embedded into the pressure sensor) and a pressure sensor (type BMP085) could be read out like this.

The IOC requests data every 5 seconds from the Arduino via standard stream device, and provides the data as Process Variables (PV) with following names via the network: CBM:RICH:press_0 and CBM:RICH:temp_0 for the pressure sensor and its build-in temperature sensor, and CBM:RICH:temp_1 to CBM:RICH:temp_7 for the dedicated temperature sensors. The DAQ system polls these variables regularly and stores them as EPICS subevent in the data stream for offline analysis. In parallel, the data can be displayed by any EPICS CA client, e.g. StripTool. A
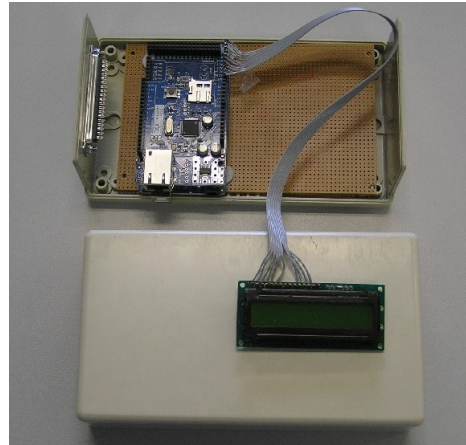
Figure 1: Photograph of the ARDUINO based slow control box. The display is used to show the IP address obtained via DHCP.

graphical user interface based on CSS was developed for online data visualization and alarm monitoring [3].

During the beam test the system was running very smoothly, and it is a cheap and reliable alternative to commercial solutions. For the future we plan to move to the Raspberry Pi platform [4], which will allow to integrate the IOC functionality into the interface box rendering the need for an external Linux IOC client.

Figure 2: Pressure sensor (left) and temperature sensor (right) with integrated I2C interface

References

[1] www.aps.anl.gov/epics

[2] S. Reinecke *et al.*, *Overview of the RICH-prototype beam test 2012 at the CERN-PS*, this report

[3] J. Song and I.-K. Yoo, *Slow control system of the CBM RICH prototype*, this report

[4] www.raspberrypi.org

First lab tests of a new RICH readout electronic prototype module

C. Pauly[1], *K.-H. Kampert*[1], *J. Kopfer*[1], *S. Reinecke*[1], *M. Traxler*[2], *and C. Ugur*[2]

[1]Bergische Universität, Wuppertal, Germany; [2]GSI, Darmstadt, Germany

A new electronic readout module (first prototype see Fig. 1) is currently being developed at GSI by M. Traxler et al. for readout of the CBM RICH detector. The board design is based on the HADES TRB3 readout board [1] and comprises 64+1 channels of FPGA-TDC, individual analog input amplifiers, 8 channel DAC for threshold control (common threshold for each group of 8 input channels), a digital TRBnet backend and SFP-connection for data transport. Analog signal discrimination is implemented using LVDS differential line receivers on the FPGA. The goal is to develop a compact, inexpensive readout board providing excellent time resolution ($\sigma < 500$ps) for MAPMT signals and moderate amplitude information via Time-over-Threshold (ToT).
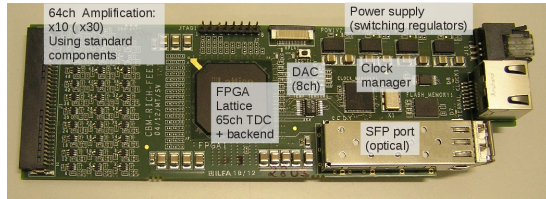
Figure 1: First prototype of the newly developed TRB3 based FPGA-TDC readout module for the RICH

Characterization of first prototype boards in the lab has been started using signals from a fast analog pulser of variable amplitude to mimic the PMT signals. Of particular interest here is the threshold spread among all channels in view of the novel discrimination approach. Figure 2 (left side) shows the threshold variation (pulse detection efficiency as function of signal amplitude) for all 64 channels (gray) if a single common threshold value is used. A group of 8 inputs belonging to the same DAC channel is highlighted (magenta). The main contribution to the observed threshold dispersion is the gain variation of the amplifier stages and tolerances of the LVDS receivers. A next board iteration will comprise individual DACs for each input channel to compensate for threshold dispersion (and MAPMT gain non-uniformity).

A second important characteristic tested here is the achieved time resolution. It was determined by simultaneously splitting the same pulser signal to several input channels. Figure 3 shows the measured time difference between such pairs of inputs; a Gaussian fit to the correlation peak gives an estimate on the time resolution. A time resolution in the order of 100 ps is achieved in most channel pairs (Fig. 3, right side); however, some channels perform significantly worse, which is probably a matter of further FPGA firmware tuning. The present prototype per-
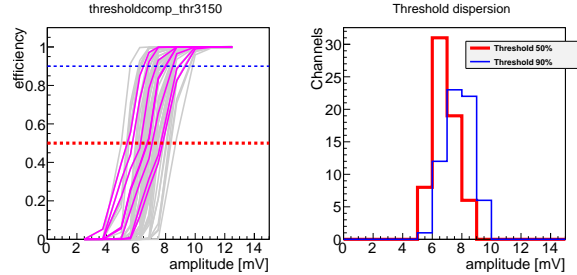
Figure 2: Threshold behaviour for all 64 channels (left, gray) and 8 channels belonging to same DAC (left, magenta). Threshold dispersion (50% and 90%) is shown in the histogram to the right.

formance is partly limited by problems due to oscillations of the densely packed input amplifiers, which will be addressed in a next prototype iteration. On a similar development project ("PADIWA") this problem could be solved already.
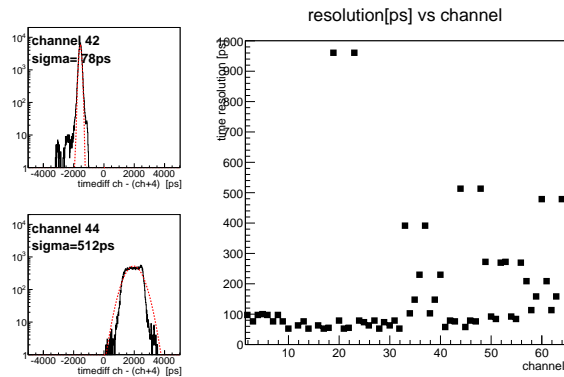
Figure 3: Individual time difference between pairs of input channels connected to the same pulser signal (left) and overview for all channels (right)

The new prototype readout board could also be tested during the recent RICH prototype beam test at CERN-PS [2], where it was partially used for readout of the photon detector in parallel to the presently used n-XYTER solution. Analysis of the data is in progress; first results look promising.

References

[1] M. Traxler *et al.*, JINST **6 C** (2011) 12004

[2] S. Reinecke *et al.*, *Overview of the RICH-prototype beam test 2012 at the CERN-PS*, this report

MAPMTs with wavelength-shifting films on UV-extended windows – dependence of quantum efficiency on layer thickness

T. Schweizer[1], *D. Spies*[1], *J. Kopfer*[2], *C. Pauly*[2], *K.-H. Kampert*[2], *and M. Dürr*[1]

[1]Hochschule Esslingen, Esslingen, Germany;　[2]Bergische Universität, Wuppertal, Germany

Wavelength shifting (WLS) films which consist of p-terphenyl (PT) as active material and paraloid as binder were applied on MAPMTs with UV-extended windows by means of dip coating from a dichloromethane-solution. In contrast to PMTs with standard windows [1], the quantum efficiency of PMTs with UV-extended windows shows a more pronounced dependence on layer thickness, which necessitates a systematic study.

Using different pulling speeds for the dip coating process, a layer thickness between 50 and 180 nm was realized; good film quality was achieved for the covered range of thicknesses (Fig. 1). QE-curves of the employed MAPMTs (H8500-3) without and with WLS film are compared in Fig. 2 (top). For all measurements, an increase of QE for $\lambda \leq 300$ nm is observed. In contrast to the evaporated films of larger thickness [2], the QE does not decrease for wavelengths $\lambda \geq 300$ nm.

Unfortunately, the QE-curves of the bare PMTs differ significantly, and a direct comparison of the influence of the WLS films with different layer thickness is difficult. In order to minimize the influence of the bare PMTs, a normalized increase of the QE was calculated according to

$$\Delta QE(\lambda) = [QE_{\text{film}}(\lambda) - QE_{\text{bare}}(\lambda)] \times QE_{\text{bare}}^{\text{max},*} / QE_{\text{bare}}^{\text{max}}$$

with $QE_{\text{bare}}^{\text{max},*}$ being the maximum QE of the best of the PMTs used. The respective curves are shown in Fig. 2 (bottom) for the PMTs with the three dip-coated layers as well as for the PMT which was coated with PT by means of evaporation [2]. For wavelengths $\lambda \leq 300$ nm, the increase caused by the dip coated layers is higher than for the evaporated film. Within the series of dip-coated layers, the increase in QE increases with increasing layer thickness. From absorption and fluorescence measurements (not
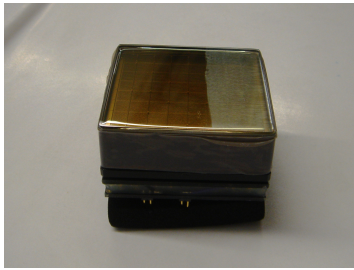
Figure 1: H8500D-03 MAPMT with part of the original WLS coating removed on the left hand side. The homogeneous film on the right hand side is clearly discernible.
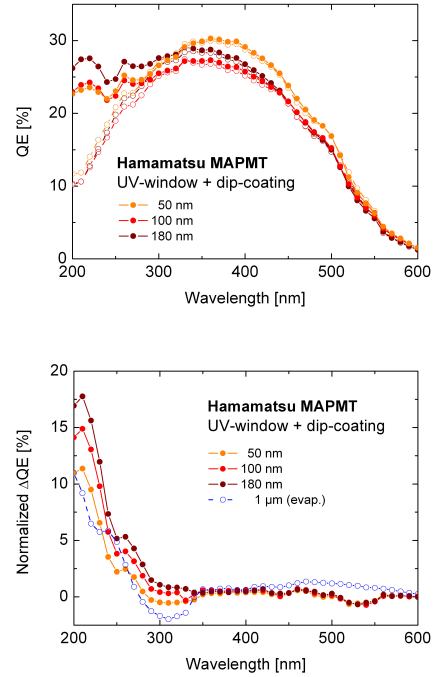
Figure 2: Top: QE as a function of wavelength as measured for H8500-03 MAPMTs without (open symbols) and with dip-coated WLS films (filled symbols, 3 different layer thicknesses). Bottom: Normalized difference $\Delta QE(\lambda)$ as deduced for the three MAPMTs with different layer thickness from the top panel as well as deduced for the MAPMT with an evaporated PT film.

shown), no further increase towards thicker layers is expected. Whereas the evaporated film shows a decrease in QE around $\lambda \approx 300$ nm, no such decrease is observed for the much thinner dip-coated layers.

MAPMTs with WLS films of about 180 nm were used in the RICH beam tests in 2011 and 2012 [3, 4].

References

[1] C. Höhne *et al.*, Nucl. Instrum. Methods **A 639** (2011) 294

[2] I. Galm *et al.*, CBM Progress Report 2011, p. 36.

[3] J. Kopfer *et al.*, *Results from the CBM-RICH in-beam test 2011 at the CERN-PS*, this report

[4] S. Reinecke *et al.*, *Overview of the RICH-prototype beam test 2012 at the CERN-PS*, this report

Results of the RICH prototype gas system during the 2012 beam test

L. Kochenda[1], *P. Kravtsov*[1], *Y. Ryabov*[1], *C. Höhne*[3], *C. Dritsa*[3], *T. Mahmoud*[3], *and J. Eschke*[2]

[1]PNPI, Gatchina, Russia; [2]GSI, Darmstadt, Germany; [3]Justus Liebig University, Giessen, Germany

The CBM RICH prototype gas system [1] was built to provide pure CO_2 gas to the RICH prototype at a constant differential pressure of about 2 mbar. During the October/November 2012 beam test at CERN, the gas system worked successfully with the RICH prototype. The differential pressure was stabilized in the detector at the level of 2.0 ± 0.15 mbar although the barometric pressure changed in the range of 37 mbar (Fig. 1). Since the gas system provides pure CO_2 gas without admixtures, the slow control system operating the mass controller to stabilize the internal detector pressure acted on adding more or less fresh pure gas (Carbon Dioxide).
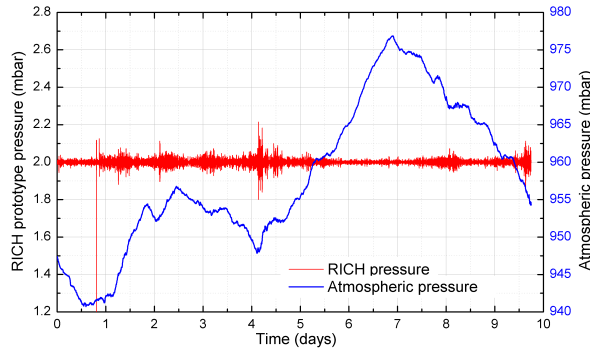
Figure 1: RICH pressure stability

Both the purifier and dryer were regenerated prior to the beam time. These units remove moisture and oxygen from the recirculation flow. The dryer was filled with Zeolite NaX and the purifier with pure copper. The final impurity levels downstream of the purifier and the dryer were 9 ppm of oxygen and 15 ppm of moisture.

The control system [2] performed well except for a single accident after a power failure: the temperature-indicating controller for the purifier then accidentally overheated the purifier. This accident decreased the purifier efficiency, which however was still good enough to keep an oxygen level of 200–230 ppm.

For technical reasons we had a very good opportunity to investigate the influence of the oxygen to the RICH detector performance. In the middle of the run, the prototype vessel was opened to remove the wavelength shifting film (WLS) from some of the MAPMTs. This opening of the box resulted in an extremely high content of oxygen (up to 1 %) and moisture (up to 1000 ppm) in the chamber (Fig. 2). The efficiency of the RICH detector was measured during cleaning of the detector volume from oxygen. The results of the measurents are shown in Fig. 3. The

behaviour of the ring radius and the number of hits per ring showed a surprisingly small dependence on the oxygen content. The ring reconstruction in the RICH prototype was reliable even at 9000 ppm of oxygen.
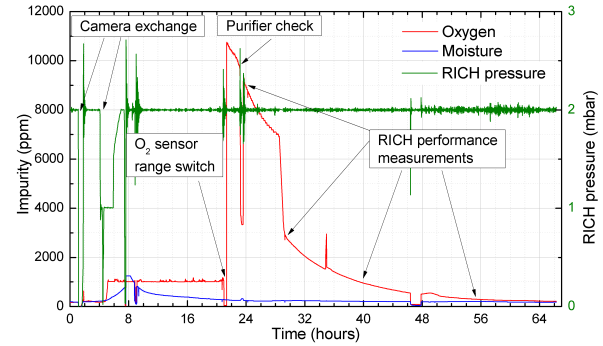
Figure 2: Oxygen and moisture content after camera exchange
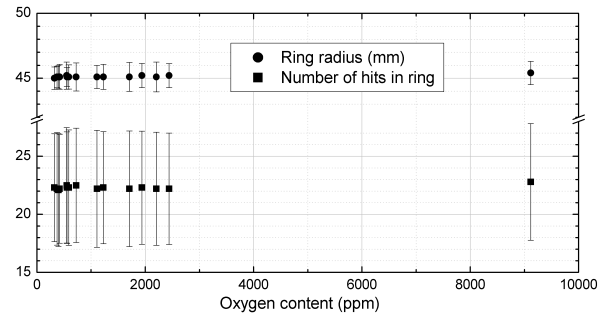
Figure 3: Influence of the oxygen content to ring radius and number of hits

In general, the gas system provided stable operation with stabilization of all required gas parameters in the RICH prototype. It was reliably controlled by the control system, providing all system parameters to the central slow control system based on EPICS. The RICH prototype vessel ($3.5\,\mathrm{m}^3$) was checked for leaks prior to the beamtime. The leak rate was estimated by the pressure decrease in the vessel. It turned out to be quite reasonable for the gas system operation (170 sccm).

References

[1] L. Kochenda *et al.*, CBM Progress Report 2010, p. 31

[2] P. Kravtsov *et al.*, CBM Progress Report 2010, p. 32

Ring reconstruction for the RICH prototype beam test data 2012

S. Lebedev[1,2] and C. Höhne[1]

[1]Justus-Liebig-Universität, Gießen, Germany; [2]LIT JINR, Dubna, Russia

The real-size prototype of the Ring Imaging Cherenkov detector (RICH) was tested for the second time together with other CBM groups at the CERN PS/T9 beam line in October 2012 [1]. One of the goals was a test of the ring reconstruction and fitting algorithms which were implemented in CBMROOT with a real data. In this report the analysis of the ring reconstruction is presented.

The event reconstruction includes several steps. First, all hits which belong to one event are collected. Then the rings are reconstructed using an algorithm base on the Hough Transform method [2]. The parameters of the rings are precisely estimated by circle and ellipse fitting procedures [2]. These are all standard algorithms for the ring finding and fitting in the CBMROOT framework.

For a better understanding of the RICH prototype performance and also for the validation and debugging of the reconstruction procedure it is quite useful to have a visual representation of events. For this purpose a RICH prototype event display was implemented. It displays information about the event like all hits and hits which were assigned to the ring by the ring finder. It also draws fitted circles and ellipses and their parameters. Two example events are shown in Fig. 1.

less than 6 hits cannot be found by the ring finder. The quality of rings with a small number of hits is very low, and many of them are rejected by the ring finder.

Approximately 3% of events contain two rings. An example of such an event is presented in the right panel of Figure 1.

One of the criteria of the ring finder performance is correct fitting of the found rings. For the evaluation of the fitting efficiency it was assumed that a ring is correctly fitted by the circle fitter if its radius is in the range 3 – 6 cm, which corresponds to the mean radius of electron rings (4.5 cm ± 1.5 cm). For the ellipse fitter the major and minor half axis should lie in the same range. The fitting efficiency is defined as the number of correctly fitted rings divided by the number of events with at least one hit. The efficiency of circle (blue line) and ellipse (red line) fits is shown in Fig. 2. The circle fitting efficiency is almost 100%, which means that if a ring is found it can be correctly fitted as circle. For the ellipse fitting the efficiency for the events with low number of hits is worse, because more hits are required for correct estimation of 5 ellipse parameters instead of 3 circle parameters.

Figure 1: Examples of the events for the RICH prototype

Since the analysis was performed for real data there was no possibility to use Monte-Carlo information. For the efficiency calculation of the ring finder the following definition was established: the number of events in which at least one ring was reconstructed divided by the number of events with at least one hit. Only electron events were selected by cuts on both Cherenkov detectors [1]. The quality of reconstructed rings was also checked using the event display; however, this could be only done for a limited sample.

Figure 2 shows the ring reconstruction efficiency (black line) in dependence on the number of hits in the event. The integrated efficiency over all events is 99.1%. The efficiency drops down for events with less than 10 hits: the mean efficiency for events with 9 – 11 hits is 81%, it decreases to 36% for events containing 6 – 8 hits. Rings with

Figure 2: Efficiency of the ring reconstruction, circle fitting and ellipse fitting in dependence on the number of hits in an event

In summary, the ring finding and fitting algorithms were tested with real data and showed very good efficiency.

References

[1] S. Reinecke *et al.*, *Overview of the RICH-prototype beam test 2012 at the CERN-PS*, this report

[2] S. Lebedev *et al.*, J. Phys. Conf. Ser. **396** (2012) 022029

Mirror displacement tests - simulation and preliminary results

T. Mahmoud and C. Höhne

Justus-Liebig-Universität, Gießen, Germany

When constructing the mirror plane of the CBM RICH detector, misalignment between the mirror tiles relative to each other and to the nominal common spherical surface cannot be completely avoided. Such misalignment leads to displacements of a mirror tile along the z-axis at one or more of its sides, which results in displacing the hit position of a reflected photon on the detector plane. This can corrupt the shape and properties of Cherenkov rings that are reflected at displaced borders. To determine displacement tolerances this aspect was simulated within the `cbmroot` simulation framework and addressed during the beam time at CERN in fall 2012 [1] with the real-size RICH prototype [2]. In the simulations the prototype has been implemented according to its technical design and the measured optical properties of the mirror, photon detector and gas absorption. The mirror system of the prototype consists of 4 real size mirror tiles (see Figs. 1 and 2).
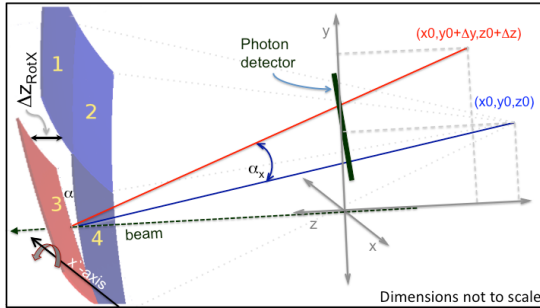
Figure 1: Displacement at the top side of mirror number 3, Δz_{RotX}. The blue (red) line connects the beam position on the mirror surface with the middle point of the sphere before (after) the rotation.
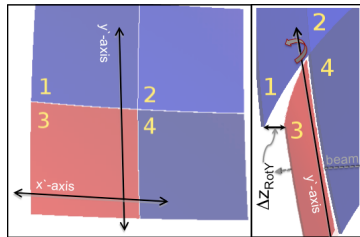
Figure 2: Left: Visualisation of the $x' - y'$-plane on the mirror surface. Right: same as Fig. 1 for the y'-axis.

Study environment: The upper side of mirror 3 was displaced backwards and the left side forwards. These displacements are called Δz_{RotX} and Δz_{RotY}, respectively. As illustrated in Figs. 1 and 2, Δz_{RotX} corresponds to a rotation around the x'-axis by an angle α_X and Δz_{RotY} to a rotation around the y'-axis by an angle α_Y. Figure 3 shows the relation between $\alpha_{X(Y)}$ and Δz_{RotX} (Δz_{RotY}).

In the prototype the x'- and y'-axis are defined by the mounting points of the mirrors to the holding frame via remotely operated actuators. The beam centre runs exactly between mirrors number 3 and 4.

The effect of the displacements was simulated and measured using an electron beam with 3 GeV/c momentum. The main focus was on the half major axis, A-axis, of an elliptic fit on the reconstructed Cherenkov rings.
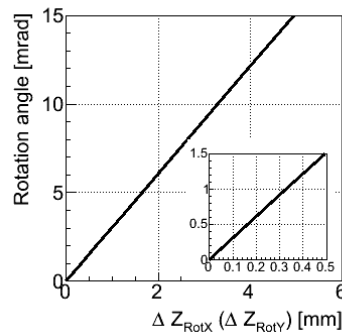
Figure 3: Rotation angle α_X as a function of Δz_{RotX}

Rotation around x'-axis: Figure 4 shows the A-axis distributions as a function of Δz_{RotX}. Not all entries in the distributions are affected by border displacements. Since the beam cross-section is about 1.3×1.2 cm^2 [3], the Cherenkov cones of some electrons are reflected entirely on one of the two mirrors. In other cases the cones are shared between both. Hence, in each distribution distorted and undistorted rings are mixed.
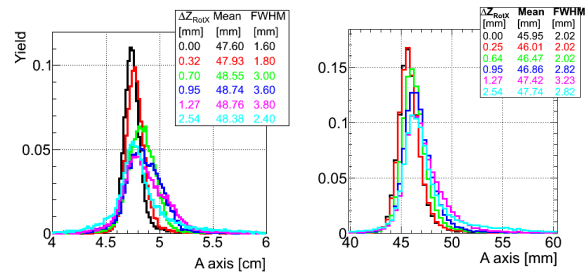
Figure 4: A-axis distributions for several Δz_{RotX} displacements. Left: simulations. Right: data from the 2012 beam test with the RICH prototype.

Qualitatively, simulations show that starting from the ideal case with Δz_{RotX}=0, the maximum and the FWHM of the A-axis distribution grow with Δz_{RotX} until a displacement of 1 mm, where they start falling again. To un-

derstand this behaviour consider only those events where the electrons run exactly between the two mirrors (completely distorted rings). One half of the ring is reflected on mirror number 3 and the other on number 4.
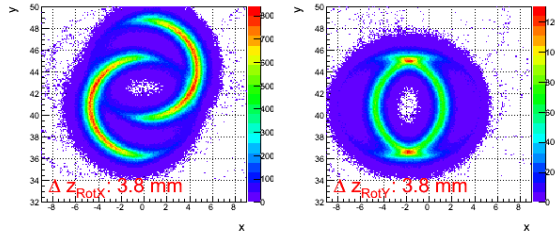
Figure 5: Integrated rings for a displacement of 3.8 mm

The half which is reflected on the rotated mirror moves along the photon detector plane upwards. For small displacements the ring finder still finds one ring and the ring fitter fits it but with a larger A-axis. The larger the displacement the more pronounced is the splitting of both halves, and consequently the A-axis grows more and more leading to wider distributions. At $\Delta z_{RotX} \approx 1$ mm the splitting is pronounced enough for the ring finder to recognise two rings (left panel of Fig. 5). They can be fitted with more realistic values of the A-axis leading to narrower distributions. This partially *regenerating* of the distribution shape is deceptive because we have two rings coming from one electron. In summary, and from the point of view of Δz_{RotX}, a displacement of 0.32 mm, corresponding to an α_X of about 1 mrad, is still tolerable.

The right panel of Fig. 4 shows preliminary results from beam data, which confirm the trend observed in the simulated data, although not so pronounced (see later).

Rotation by $y^{'}$-axis: Rotations of the mirror around the $y^{'}$-axis have even more pronounced effects as can be seen in Fig. 6. With increasing Δz_{RotY} the maximum and the mean value of the distribution decrease and its FWHM increases up to $\Delta z_{RotY} \approx 1.27$ mm, where the distribution splits into two peaks. To understand this behaviour see the
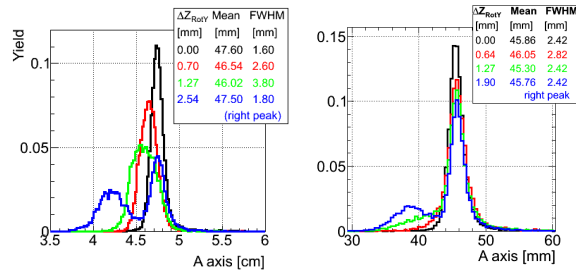
right panel of Fig. 5 and, again, consider only events where electrons run exactly between the two mirrors. The rotation moves one half of the ring towards the other; the ring is *squeezed* leading to lower values of the A-axis. The shrinking of the latter reduces the mean value and finally forms the left peak of the distribution. The right peak contains all events with Cherenkov cones being reflected entirely (or mostly) on one of the mirrors. Also from the point of view of Δz_{RotY}, simulations show that a rotation by $\alpha_Y \approx 1$ mrad is tolerable.

The right panel of Fig. 6 shows preliminary results from beam data. The double peak effect and the reduction of the maximum abscissa are observed but not the clear reduction of the mean value and increase of the FWHM.

Simultaneous rotations around $x^{'}$- and $y^{'}$-axes: Preliminary investigations of the measured data show that mirror misalignment was already present in the starting position of the measurements. This is why the maximum of the A-axis distribution does not rise (fall) as expected by rotations around the $x^{'}$-axis ($y^{'}$-axis); the effects partially cancel each other. However in real experiments the ring position is not fixed as in our case. For a given position, if one rotation cancels the corruption caused by another, it enhances it at a different *corner*, i.e. the opposite side.

Other displacements: The discussed results in this section take only Δz_{RotX} backwards and Δz_{RotY} forwards into account. Δz_{RotX} forwards has same effects as backwards because of symmetry reasons. Δz_{RotY} backwards has an opposite effect as Δz_{RotY} forwards. Instead of being *squeezed*, the ring is *stretched* causing a wider distribution of the A-axis. The two ring halves separate quickly at Δz_{RotY} of about 0.4 mm, and the ring finder recognises two rings. This keeps our conclusions regarding tolerances unchanged.

Conclusion: We have studied effects of mirror displacements on the A-axis of an elliptic fit to the Cherenkov rings in detailed simulations. Together with preliminary beam data they show that displacements caused by rotations of 1 mrad can be tolerated.
In addition, results not discussed in this report show that a displacement of the entire mirror along the z-axis up to 10 mm does not affect the A-axis distribution noticeably.

Figure 6: A-axis distributions for several Δz_{RotY} displacements. Left: simulations. Right: data from the 2012 beam test with the RICH prototype. In the ledge, the values of the split peak are of the right part only.

References

[1] S. Reinecke, *Overview of the RICH-prototype beam test 2012 at the CERN-PS*, this report

[2] T. Mahmoud, CBM progress report 2011, p. 34

[3] http://ps-div.web.cern.ch/ps-div/Reports/ PA9321/Tables/Table9.html

RICH mechanical development

Yu. Ryabov[1], V. Dobyrn[1], C. Höhne[2], E. Leonova[1], C. Pauly[3], V. Samsonov[1], O. Tarasenkova[1], E. Vznuzdaev[1], and M. Vznuzdaev[1]

[1]PNPI, Gatchina, Russia; [3]Bergische Universität Wuppertal, Germany; [2]Justus Liebig University, Giessen, Germany

The conceptual layout of the CBM experiment assumes that the RICH detector is located right behind the magnet. The total length of the detector along the z-axis is 2 m. It occupies the same location as the CBM MUCH detector. The two detectors will be used alternately with a typical exchange period of one year. The acceptance of the RICH detector has to cover an angular range up to 609 mrad ($\sim$35°) in the horizontal (x-z) plane and up to 435 mrad ($\sim$25°) in the vertical (y-z) plane. The detector will be operated at ambient temperature and pressure. CO_2 gas is used as a radiator. The average radiator length is 170 cm. The remaining space is reserved for two horizontally divided mirror halves, their mounts and support frames. The photo detector planes are located above and below the beam axis. Each mirror half is a part of a sphere with a radius of 300 cm. The area of the reflecting surface of each half of the mirror is 6.48 m^2. The slope angle of each mirror half currently is one degree. All these parameters were used in the overall RICH mechanical design prepared in 2012. This design includes a mirror splitting scheme, mirror supporting frame, photo detector support and gas box.

In the current design each of the halves of the mirror is split into 36 parts (tiles): four rows with nine mirrors in each row (see Fig.1).
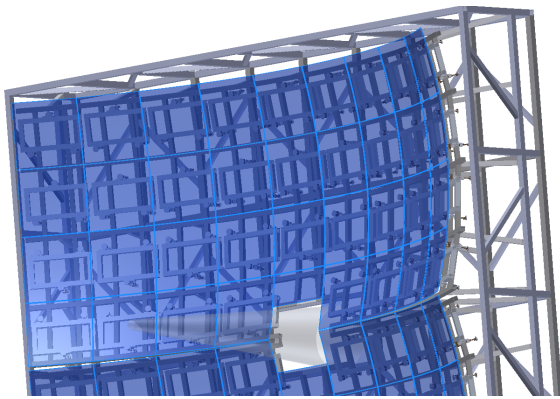
Figure 1: Splitting of one from two mirrors halves and mirror tiles support frame

Two types of tiles with different sizes are used. The two middle rows consist of nine trapezoidal tiles of 430 (425.6) mm × 425 mm in an arc. The reflecting surface area of the tile is 0.182 m^2. The remaining two rows consist of nine trapezoidal tiles of 425.5 (412.5) mm × 425 mm in an arc. The reflecting sur-

face area of the tile is 0.178 m^2. This splitting scheme allows for reasonable size of the tiles close to that used in the prototype and provides acceptable gaps between the mirrors (about 4 mm).

A three-point (tripod) mount concept is chosen as the basic idea for the tiles mount geometry, with the three mount points on the tile forming an equal-sided triangle [1]. The proposed mount leg structure is shown in Fig. 2 (right). These mounts allow to rotate tiles along three axes, as well as to move them along the z-axis. It consists of the Cardan joint connected to the mirror tile through the ring plate at the mount point. A rotating rod is inserted into the opposite side of the hinge, which is the base axis of the mount leg. It passes through the support and ends up in a manual screw. A linear actuator of Firgelli L12 type [2] is fixed on one side of this support in parallel to the screw. The Cardan joint itself consists of a couple of hinges where one hinge can only rotate around its rotation axis but the second hinge, in addition, has freedom of translation along its rotational axis. The layout of the 3-point mount geometry shown in Fig. 2 (left).
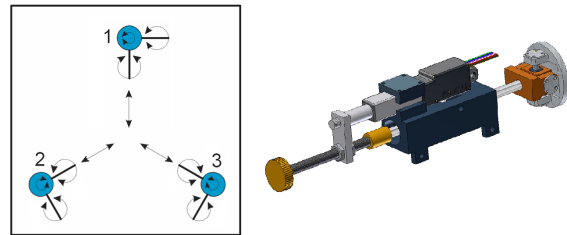
Figure 2: The layout of the 3-point mount geometry. The arrows indicate the rotational and translational degrees of freedom (left). Mount leg structure (right).

In the current project we use a mirror mount design which can be controlled remotely and manually. Any of these options can be removed from the final version of the design. Each of the three mounting legs of the mirror tiles is attached to a special aluminum rectangle (see Fig. 3, right). The rectangle in turn is attached to the frame, as shown in Fig. 3 (left). In the region close to the beam pipe, the tiles will be partly cut off. Therefore, a special mounting scheme is required in this zone.

The design of the supporting frame utilizes aluminum profiles of 40 mm × 40 mm and 30 mm × 30 mm. The frame consists of four "belts" (zones) corresponding to the four rows of tiles (see Fig. 3, left). Vertical and horizon-
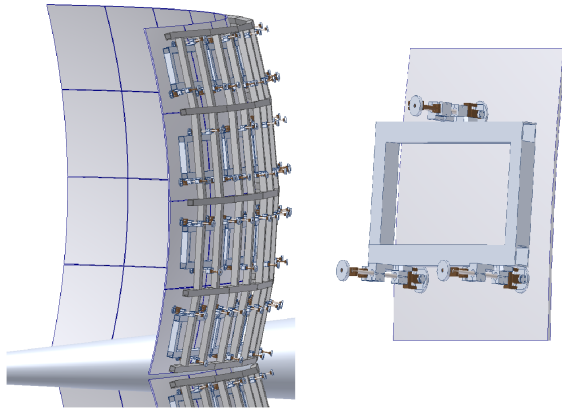
Figure 3: Mirror tiles support frame (left). One tile with three mounting legs attached to a special aluminum rectangle (right).

tal cross beams form cells that match the size of the tiles. Each cell is parallel to the plane of the tiles included in the corresponding row.

All four "belts" are attached to a rectangular base frame, as shown in Fig. 1. This base is common for both mirrors. This design contains a number of connections with non-standard angles. Precise cuts of aluminum profiles and home-made joining details are to be used for the project. For joining aluminum parts of the frame which are at 90° and 45° with respect to each other, the design uses industrially produced details.

Each of the two photon detection systems (above/below the beam pipe) is horizontally split into two sub planes with dimensions of ~ 1000 mm $\times$ 600 mm. These two parts are arranged at an angle of 5° with respect to each other in order to optimize the focusing. Thus the full photon camera system of the RICH consists of four such detector subplanes, two above and two below the beam pipe. Each of these planes is divided into four sub-parts, corresponding to four printed circuit boards (PCB) carrying the photon sensor devices. Figure 4 shows the photon detector supporting frame as well as a possible installation and sealing scheme for the individual PCBs. For fine tuning of the position of the photon detector supporting frame, special spacers can be used.
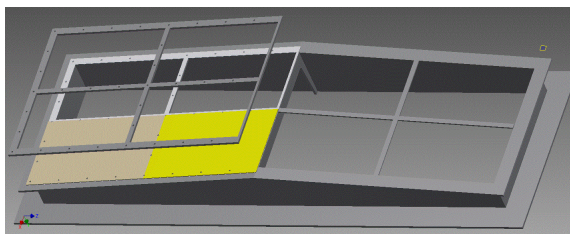
Figure 4: One of the photon detector support frames as seen from inside the gas box. Two single sensor PCBs are sketched in yellow.

The design of the gas box is based on solutions tested with the prototype [3] and contains a reinforced frame welded from 100 mm $\times$ 100 mm $\times$ 5 mm channel bars (Fig. 5), covered with rigid panels on all sides. A reinforced design of the gas box is necessary for the possibility to move the detector using a crane. The design enables disassembly of the gas box for transportation in a standard container. Part of one of the side panels can be dismounted for installation of the mirror supporting frame. The front and rear panels can also be removed for access to the supporting frame and photon detectors. The front and rear panels are made of Kapton foil with a thickness of 200 μm. Alternatively, a 2 mm plastic sheet may be used for the rear panel. The corresponding parts of the frame will have structures for support of the beam pipe.

A general view of the supporting frame with mirrors, gas box and the photon detector planes is shown in Fig. 5.
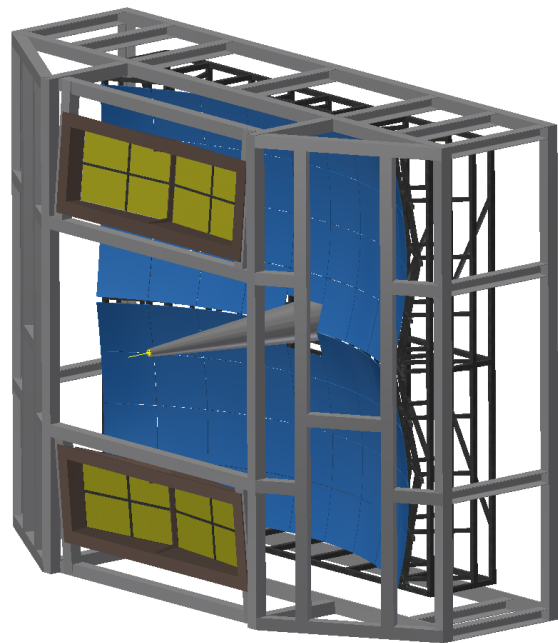
Figure 5: A general view of the supporting frame with mirrors, gas box and the photon detector planes

References

[1] V. Dobyrn *et al.*, CBM Progress report 2011, p. 39

[2] http://www.firgelli.com

[3] T. Mahmoud *et al.*, CBM Progress report 2011, p. 34

RICH design with tilted mirrors

C. Welzbacher[1], *T. Mahmoud*[1], *C. Pauly*[2], *and C. Höhne*[1]

[1]Justus-Liebig-Universität, Gießen, Germany; [2]Bergische Universität, Wuppertal, Germany

In the current RICH layout, the photon detector plane is located directly behind the magnet yoke. The expected stray fields are too large for the anticipated photon sensors. An obvious way to reduce the magnetic stray field in the photon detector plane is to move the planes outward by tilting the RICH mirrors. A disadvantage of this ansatz is that with large angles the rings get distorted in their projection onto the photon sensors and it also becomes more difficult to get a good focussing of all rings. Some more generic studies of this ansatz have been made in the `cbmroot` simulation framework and shall be reported in the following.
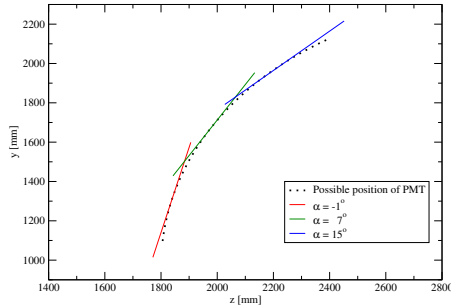
Figure 1: Position for the center of the photodetector plane for different tilt angles of the mirror with three examples for possible configurations
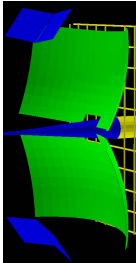
Figure 2: Visualization of the implemented geometry with a 10° tilt of the mirror

Positions of the photon detector plane have been calculated analytically to first order in dependence on the tilting of the RICH mirror. Fig. 1 shows the positions of the center of the photon detector plane for different tilt angles of the mirror with three examples for possible configurations. As can be clearly seen, tilting the mirror moves out the photon detector plane in z and y from the magnetic stray field. The larger the tilt is, the more the photon detector plane approaches a horizontal position. For an illustration Fig. 2 shows the visualization of one of those geometries in `cbmroot`. Connected to the larger reflection angles for photons is a decreased quality of the ring projection: The ring distortions measured through the ellipticity B/A (ratio of

Table 1: Comparison of the ellipticity B/A (distortion) of the rings and focus (thickness ΔR) of the rings

Tilt angle α	B/A	ΔR[cm]
-1°	0.9040	0.2791
5°	0.8938	0.3090
10°	0.8740	0.3540
15°	0.8415	0.4022

minor and major half axis when fitting an ellipse) increase as well as the width of the focussed ring ΔR (mean of distances of single Cherenkov photon impacts to the fitted ring). Fitting the focussed rings, the ellipticity B/A and the ring focus (thickness) ΔR were extracted and summarized in Tab. 1 for different tilting angles. The increased thickness is still below the granularity of the anticipated photomultipliers (pixel size of 5.8×5.8 mm^2) and thus should have little effect. The increased ellipticity however poses a challenge for the ring finding: currently there is a 6 % efficiency drop from the standard geometry to the one with mirrors tilted by 10°.

The resulting reduction of the magnetic field has been studied using the most up-to-date field map available in `cbmroot` (field_v12b) not yet including any shielding. Fig. 3 shows the effect of magnetic field reduction due to different positions of the photon detector plane. For tilt angles larger than 10°, values below 5-6 mT are reached even in the innermost region of the photon detector plane.

We expect that including a proper shielding and a tilt of the mirror of $\geq 10°$, magnetic field values of less than 1 mT can be achieved in the photon detector plane. The ring reconstruction routines have to be improved in order to cope with the (predictable) elliptic shapes of the rings.
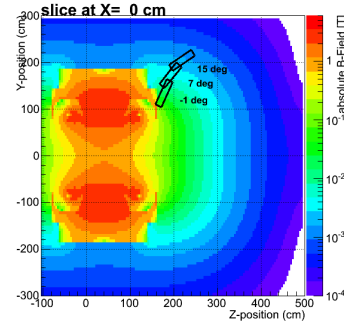
Figure 3: Visualization of different photon detector positions with respect to the magnetic field (field_v12b). The field is shown in the $y - z$ plane at $x = 0$ cm.

A modified RICH detector design with an additional second mirror

S. Reinecke, K.-H. Kampert, J. Kopfer, C. Pauly, J. Pouryamout, S. Querchfeld, and J. Rautenberg

Bergische Universität, Wuppertal, Germany

Because of the large magnetic stray field in the region of the RICH camera and thus the significantly decreasing detection efficiency of the multianode photomultipliers [1], an alternative design of the RICH detector with an additional second mirror was simulated. The second mirror can either be plane or spherical, both solutions having different advantages and disadvantages. The second mirror is placed at the original position of the photon camera with the camera being moved to a new position above/below the first mirror where the magnetic stray field is significantly reduced.

As a result of the increased path length of the Cherenkov light, the radius of curvature of the first mirror has to be increased from 3 m to a value around 4.5 m - 5.5 m, and its tilting angle must be increased from -1° to 5° - 8°.

An unavoidable drawback of any two-mirror geometry is the reduced number of detected photons per ring, as the mirrors have reflectivities less than 100% (see e.g. [2]). Calculations show a loss of around 10% corresponding to 3 - 4 photons when adding a second mirror.

Several parameters were investigated in simulations, namely the number of photons per ring, ring radius r, ring width dR, ring ellipticity B/A and momentum-dependend efficiency of ring finding.
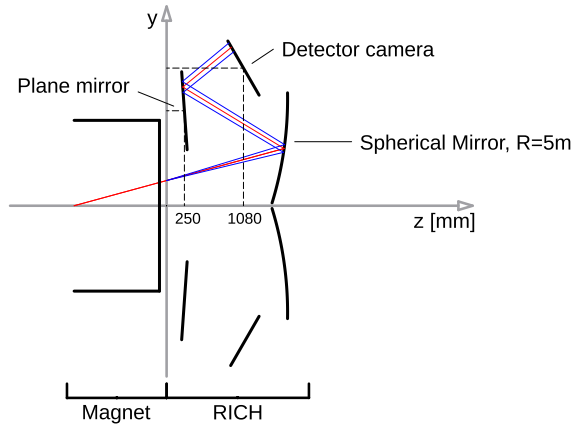
Figure 1: Exemplary RICH detector design with two mirrors (side view); the red line shows a particle track with the envelope of all Cherenkov photons shown in blue.

A sketch of the design using a plane second mirror can be seen in Fig. 1. A plane second mirror has no direct influence on the optical shape of the produced Cherenkov rings, as it only folds the light path. This leads to an increased ring radius from 5 cm to around 7 cm - 8 cm, because the ring radius r is correlated with the mirror radius R and Cherenkov opening angle ϑ according to $r = R/2 \cdot \tan\vartheta$.

According to present simulations the quality of the rings and the efficiency of ring finding and fitting nearly stay the same compared to the original geometry. The only important disadvantage, and this is a decisive factor regarding the costs, is the need for a bigger camera size (factor of nearly 2.5, proportional to R^2) to keep the same acceptance.
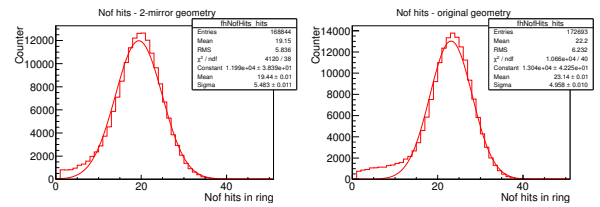
Figure 2: Comparison of the number of hits per Cherenkov ring in the original geometry (left) and in the 2-mirror geometry (right)

With an additional spherical mirror it is possible to keep the camera at nearly the same size as in the original geometry, as a smaller effective focal length f_{eff} can be achieved, with the effective focal length of the combined mirror system being $f_{\mathrm{eff}}^{-1} = f_1^{-1} + f_2^{-1} - d \cdot f_1^{-1} \cdot f_2^{-1}$, with f_1 and f_2 the focal lengths of the two spherical mirrors ($f_i = R_i/2$) and d the distance between them. Using this design the ring radius can be kept at around 5 cm. However this layout would produce more ellipsoidal rings, and the degree of ellipticity seems not to be homogeneously distributed over the surface, becoming worse to the upper and lower sides of the camera.

Another disadvantage is the highly increased complexity of aligning all single mirror tiles of two spherical mirrors.

Both design considerations show that it is possible to include a second (plane or spherical) mirror in the RICH detector. Using an additional plane mirror seems no alternative to the original layout because of the highly increased size and costs for the detector camera, even if the optical qualities would approximately stay the same. The usage of an additional spherical mirror would not result in significantly increased costs but has worse optical qualities of the produced Cherenkov rings and needs much more effort when aligning all single mirror tiles.

References

[1] C. Pauly *et al.*, CBM Progress Report 2010, p. 26

[2] S. Reinecke *et al.*, CBM Progress Report 2011, p. 38

Segmentation optimization for the MUCH detector

H. Ansari, N. Ahmad, and M. Irfan

Department of Physics, Aligarh Muslim University, Aligarh, India

The main aim of the present study is to search for an optimized MUCH segmentation layout for SIS-300 collision energies. We simulated central Au+Au collisions at beam energy of $E_{\text{lab}} = 35A$ GeV. As signal particle we considered the ω meson generated by the PLUTO event generator [1]. The background was simulated using the UrQMD event generator. The full event reconstruction was performed in the `cbmroot` framework (trunk version 18224) [2]. The geometry used is the standard geometry. It includes 6 iron absorbers and 18 detector layers, 3 detector layers behind each absorber. The total absorber length in the current design is 225 cm. The segmentation is implemented at the digitization level of the simulation.

The study of the segmentation is important for a) the determination of occupancy and multi-hit probability, which eventually determines the feasibility of tracking and the efficiency of muon measurements; b) the total number of pads, which influences the cost, and c) the small pad size, important from the point of view of fabrication and signal strength.
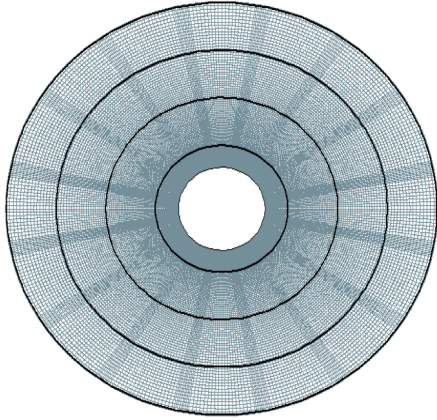
Figure 1: Segmentation scheme for a MUCH station

Figure 1 shows the segmentation scheme for the detector layers of the MUCH system. Different annular regions are segmented into pads by dividing the azimuthal angle. The annular regions are filled with square pads ($dr = r\Delta\phi$) with the pad size increasing with radius. This segmentation scheme helps to keep the occupancy close to a constant, which in turn enables to avoid a radial dependence of the detector response. Figure 2 shows the variation of occupancy with the angular segmentation $\Delta\phi$ for the entire layer.

Figure 3 shows the variation of the number of unmatched
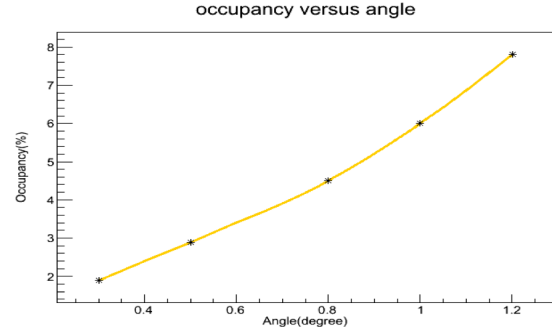
Figure 2: Variation of occupancy with segmentation angle

background tracks per event for primary and secondary tracks passing through 12 and 15 layers of MUCH. The mismatch between tracks increases with segmentation angle for secondary tracks, but remains nearly constant for primary tracks. We conclude that a segmentation angle of $1°$ seems to be the optimum choice.
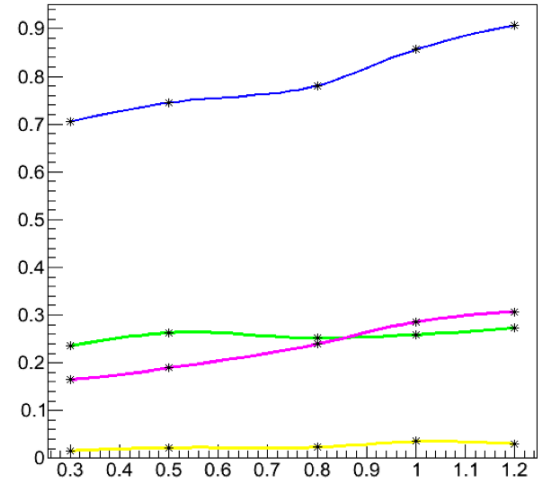
Figure 3: Number of unmatched tracks per event as function of segmentation angle. Magenta: primary tracks, 12 layers; yellow: primary tracks, 15 layers; blue: secondary tracks, 12 layers; green: secondary tracks, 15 layers

References

[1] http://www-hades.gsi.de/computing/pluto

[2] http://cbmroot.gsi.de

Study of secondaries produced in the MUCH detector of the CBM experiment

S. Ahmad and M. Farooq

University of Kashmir, Srinagar, India

The secondaries produced by the muon absorber system of CBM need careful study as they affect the design criteria of both STS and MUCH. The absorber layout of MUCH has been analysed in simulations for central Au+Au collisions at $25A$ GeV for 1000 events. The primary particles are produced with the UrQMD event generator, and the GEANT3 transport code is used to propagate the particles through the detector material and to create secondary particles. We used a full version of the muon detection system, consisting of 6 absorber layers and 18 tracking chamber planes, grouped in triplets behind each absorber slab. The total absorber thickness is kept constant at 225 cm, whereas the thickness of the first layer is varied between 7 and 50 cm. The multiplicity of secondaries behind the first absorber can be reduced by increasing the thickness of the iron plate. In this case, however, small-angle scattering in the absorber material is increased, and the matching efficiency between the ingoing and outgoing tracks decreases.

multiplicity decreases also strongly with increasing radial distance from the beam. This effect is important for the segmentation of the tracking chambers, which may vary in size by more than one order of magnitude from the inner to the outer area of the detector.

In a second step, we investigated the influence of the magnetic field, the beam pipe and the beam pipe shielding (tungsten) on the secondary electron-positron pairs as well as on the small number of neutrons observed on the last STS station. The results of this study are shown in Fig. 2. We find that with the removal of the beam pipe shielding, while keeping the magnetic field and the beam pipe in the setup, the number of secondaries is greatly reduced, indication that the W shielding is the main source of secondaries.

Figure 1: Much/STS multiplicity ratio for different particles as a function of Fe absorber thickness

In a first step, we studied the particle multiplicity before and after the first iron absorber, i.e. on the last STS layer and on the first MUCH layer, respectively, as a function of the absorber thickness. Figure 1 shows the ratio of (primary and secondary) particle multiplicities detected before and after an iron absorber of variable thickness. The multiplicity at zero thickness corresponds to the number of particles in front of the absorber. The particle multiplicity is dominated by the yield of secondary electrons, which rises steeply up to an absorber thickness of about 5 cm and then drops with increasing material thickness. The particle

Figure 2: Positron multiplicity in the last STS station as a function of absorber thickness and with removal of magnetic field, beam pipe and beam pipe shielding

Finally, an additional Graphite absorber of different thickness was introduced between STS and MUCH to reduce the back-scattered neutrons in the STS while keeping the first MUCH absorber thickness fixed. Our results showed that there is a slight decrease in the number of neutrons, which can be reduced to zero if the beam pipe shielding is removed completely.

We conclude that the number of secondary electron-positron pairs as well as of neutrons can be reduced if the beam-pipe shielding material is re-optimized in this respect by trying different materials at different regions of the beam pipe.

Response of a triple GEM chamber with high-intensity X-ray source

A. K. Dubey, J. Saini, S. Chattopadhyay, and G. S. N. Murthy

Variable Energy Cyclotron Centre, Kolkata, India

The first few stations of the CBM muon chambers have to cope with a high rate of about $1\,\mathrm{MHz/cm^2}$. A high-rate gas detector based on Gas Electron Multipliers (GEM) has been envisaged. In this regard, we have tested several prototype detectors having an active area of $10\,\mathrm{cm} \times 10\,\mathrm{cm}$ using self-triggered readout electronics. One of the key issues has been to study the efficiency of charged particle detection by varying the incident particle flux. In the beam tests performed so far, rates up to several hundred kHz/cm^2 could be reached. In order to study the response of the detector at higher rates, we have tested the chambers with a high-intensity X-ray source facility at the RD51 laboratory at CERN. This Cu-target X-ray source with a characteristic energy of 8 keV was incident from a narrow tube having an aperture of about 2 mm diameter. A triple GEM chamber of $10\,\mathrm{cm} \times 10\,\mathrm{cm}$ active area and consisting of 512 readout pads was used for the tests. Since it is not possible to generate a trigger while using the X-ray source, the test was done with standard Ortec electronics instead of the n-XYTER. For this, each of the 8 zones of the readout plane was individually shorted using 8 different connectors, and the signal was readout from one such zone where the detector was illuminated. The drift gap, transfer gap and induction gap of the triple GEM chamber were 3 mm, 1 mm and 1.5 mm, respectively. The biasing chain consisted of a protection resistor of $12\,\mathrm{M\Omega}$ across the top surface of each GEM foil. The chamber was tested at a HV of 3200 V (ΔV_{gem} across each GEM was about 358 V). The intensity of the Copper X-rays was varied by changing the filament current. Figure 1 depicts the prototype chamber under test. The X-ray tube is placed about 2 cm away from the chamber.

The pulse height spectra corresponding to seven different intensities are shown in Fig. 2. The spectrum with highest intensity (about 1.37 MHz/cm2) is represented by the outermost curve, while the one with lowest intensity corresponds to 93 kHz/cm^2. The position of the major peak is found quite stable in spite of the change in the rate of incident particles by a factor of about 12. The intensity of the incident X-rays was calculated from the frequency of the signal collected from the bottom last GEM.
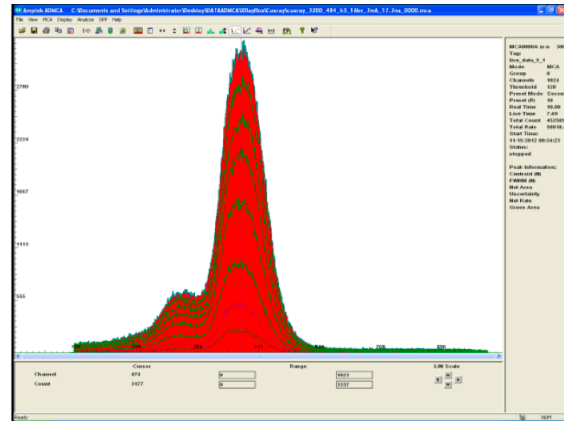
Figure 2: Cu X-ray pulse height spectra for varying incident intensities

The anode pads from the zone being readout were coupled to a picoammeter to have an independent and quantitative estimate of the change in gain. The detector was operated at a gain of $\sim 7 \cdot 10^3$, and the observed change based on the anode current measurement was found to be around 10 % for the range of intensities studied (see Fig. 3). This value is close to what can be gathered from the mean positions of the major peak in the pulse height spectra shown in Fig. 2. Further investigations of this data are underway.
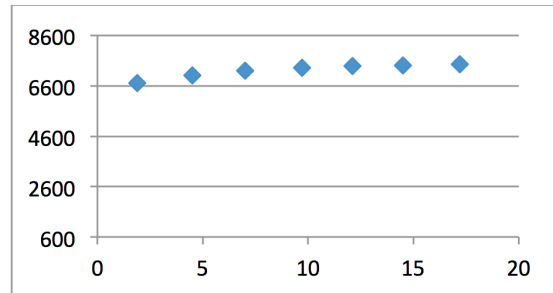
Figure 3: Variation of detector gain with anode current

Figure 1: Photo of the triple GEM chamber under test with the X-ray source

High-rate study of GEM detectors with n-XYTER readout

J. Saini, S. Chattopadhyay, A. K. Dubey, and S. R. Naryana

Variable Energy Cyclotron Centre, Kolkata, India

The n-XYTER is a self-triggered ASIC with various biasing parameters designed to operate at high frequencies of up to 1.6 MHz. We have been using this ASIC since 2010 for the prototype testing of GEM detectors. In these tests, we have observed the following issues at high rates above 5 kHz per channel: (i) low overall efficiency, (ii) reduction of ADCs, (iii) missing hits in the center of the beam spot at high rate and (iv) significant rate and amplitude dependent crosstalk. GEM detectors have been demonstrated to work at very high rates ($> 1\,\text{MHz}/\text{mm}^2$), and therefore the issues mentioned above appear to be related to the readout electronics. To resolve this, a systematic study was performed, and the results reported here demonstrate that the problems can be traced to the electronics bias settings of the n-XYTER.
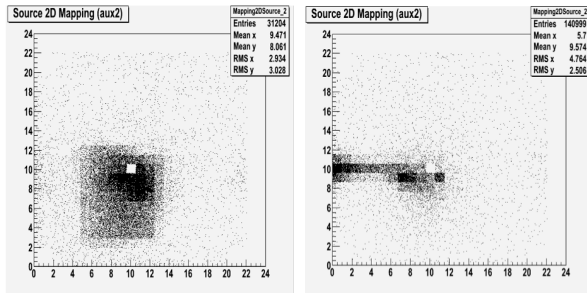
Figure 1: Left: beam spot with low intensity. The spot is clearly visible in the central region. Right: Beam spot with high intensity. Hits are missing in the central region, and crosstalk is generated in uncorrelated pads.

The test data showed 99 % detection efficiency of muons at low rates ($\sim 1.7\,\text{kHz}/\text{cm}^2$), but with high rate of incident pions ($> 5\,\text{kHz}/\text{cm}^2$), the overall efficiency reduces drastically and the central cell shows less hits then the nearby cells as shown in Fig. 1 for low and high intensity runs, respectively.

Test with pulse input to the the n-XYTER FEE

In the laboratory, a ladder-type waveform is specially designed to inject 9 consecutive charge pulses to the test channel of the n-XYTER without a discharge unlike normal square pulses. This type of waveform was generated to simulate the detector input charge faithfully. With this input, we have studied the n-XYTER output waveforms by varying Vbfb, which controls the feedback impedance of the charge-sensitive preamplifier (CSA). Increasing Vbfb

decreases the feedback impedance, resulting in lowering the discharge time of the CSA. Figure 2 shows scope screenshots, where the pink waveform is a ladder pulse as an input to a 1 pF capacitor which injects the charge in the test channel of the n-XYTER. The yellow and green waveforms are the fast and slow shaper output responses of the n-XYTER, respectively. The pulse injection frequency is 500 kHz with a pulse height of 15 mV, injecting a charge of 15 fC per pulse step. The left side shows the situation for Vbfb = 25 as was used in test beams. It can be clearly seen that with consecutive pulses, the CSA of the n-XYTER gets saturated and the shaper pulse amplitude gets reduced. With Vbfb set to 70 (right side), we see the restoration of all pulse amplitudes.
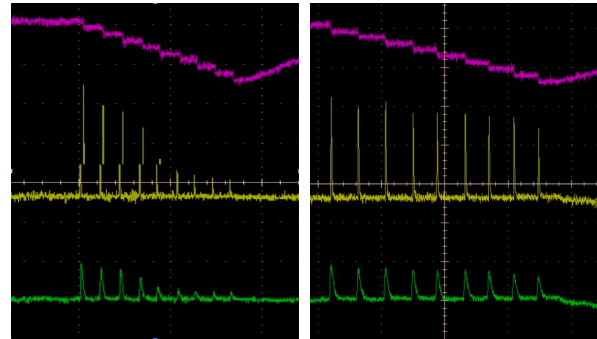
Figure 2: Scope screenshots with Vbfb = 25 (left) and Vbfb = 70 (right). The frequency is 500 kHz, the input charge is 15 fC.
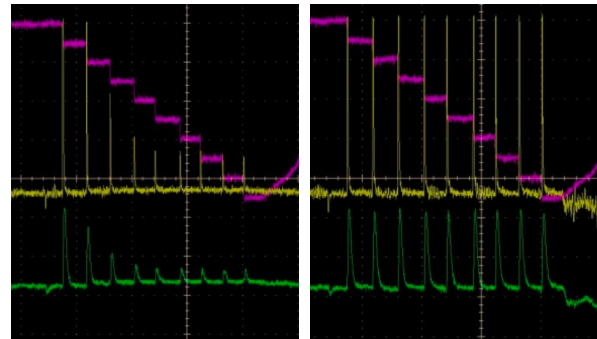
Figure 3: Scope screenshots with input charge 50 fC at a frequency of 500 kHz. Left: Vbfb = 70, right: Vbfb = 100.

We have also studied the effect of high input charge. Figure 3 (left) shows that with a charge input of 50 fC, the distortion of amplitudes persists even with Vbfb = 70. So we

increased Vbfb further to 100 to nullify this effect as shown in the right side of Fig 3.

Test with source on the detector and n-XYTER electronics

Tests were also carried out with a GEM detector using the n-XYTER FEE board and with Fe-55 and Co-60 sources emitting X-rays and γ rays, respectively. With the Co-60 source, Fig. 4 (left) demonstrates that with Vbfb = 25, hits are missing for the central region of the beam spot and crosstalk starts appearing. With increasing of Vbfb to 55, we see that the peak of the beam spot is well centered with no crosstalk (right side of Fig. 4).
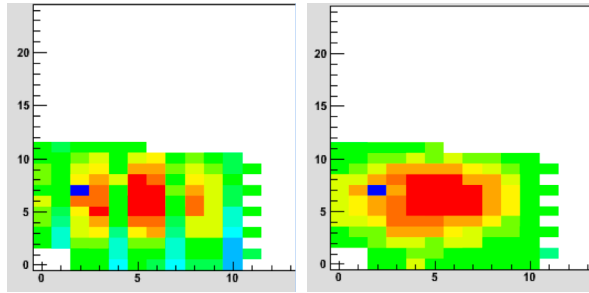
Figure 4: 2-d hit distribution from a Co-60 source. Left: Vbfb = 25; hits are missing in the central region. Right: Vbfb = 55; well defined beam spot.

For the data with Fe-55 source, we have, in addition to the 2-d plots, identified a central channel and studied the evolution of ADC with Vbfb. Figures 5, 6 and 7 show the results for Vbfb = 6, 25 and 55, respectively. A well-defined beam spot is visible for high Vbfb settings. The signal in the central channel is not visible above the noise for Vbfb = 6. With increasing Vbfb, the characteristic X-ray peaks of Fe-55 appear, which are clearly visible for Vbfb = 55, including the escape peak. It should be noted that the ADC spectrum of the n-XYTER is inverted, showing lower pulse height in higher channels.
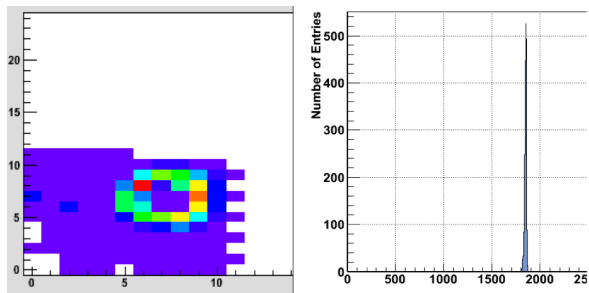
Figure 5: Results of the tests with a Fe-55 source for Vbfb = 6. Left: 2-d hit distribution; right: ADC spectrum of a central channel.

In conclusion, it has been shown by both injecting an input pulse to the n-XYTER FEE and source tests using
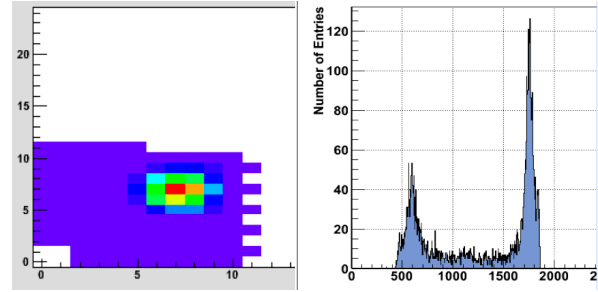
Figure 6: Same as Fig. 5, but for Vbfb = 25
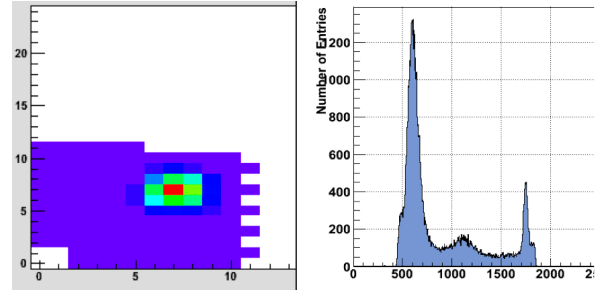
Figure 7: Same as Fig. 5, but for Vbfb = 55

a GEM detector coupled to n-XYTER electronics that the setting of Vbfb can cause the efficiency loss, the incorrect ADC and the cross talk effect which were seen in previous test beams. Crosstalk seems to be the effect of pile-up of multiple hits which results in surpassing the threshold in uncorrelated cells whose tracks in the detector PCB are lying nearby the track of the central cell with the actual hit.

Ageing studies of GEM foils for the CBM-MUCH detector

S. Biswas[1,2], D. J. Schmidt[1], A. Abuhoza[1], U. Frankenfeld[1], C. Garabatos[3], J. Hehner[1], V. Kleipa[1], T. Morhardt[1], C. J. Schmidt[1], H. R. Schmidt[4], and J.Wiechula[4]

[1]GSI, Darmstadt, Germany; [2]Variable Energy Cyclotron Centre, Kolkata, India; [3]CERN, Geneva, Switzerland; [4]Eberhard-Karls-Universität, Tübingen, Germany

The ageing and long-term stability of GEM-based detectors for the CBM Muon Chamber (MUCH) was studied in the GSI Detector Laboratory employing both X-ray and Fe^{55} sources. One GEM detector was tested for 15 days continuously at the voltages 400 V, 395 V and 390 V with a gas mixture of Ar/CO_2 (70:30). The drift, induction and transfer field were set to be 2.5 kV/cm, 2 kV/cm and 3 kV/cm, respectively. The Fe^{55} X-ray spectra were taken for a 10-minutes interval. The mean position of the 5.9 keV Fe^{55} X-ray peak was recorded continuously, as well as the ambient temperature T and pressure p. A definite correlation between peak position and T/p was observed, which is well known for any gas detector. Therefore, a corrected and normalized gain g was computed from the effective gain G according to

$$g = \frac{G}{Ae^{BT/p}} \; .$$ (1)

A and B are fit parameters, determined by fitting the exponential function

$$G(T/p) = Ae^{BT/p}$$ (2)

to the correlation plot. The exponential dependence in Eq. 2 is deduced by assuming inverse proportionality of the Townsend coefficient α to the mass density ρ; and thus $\alpha \propto 1/\rho \propto T/p$.
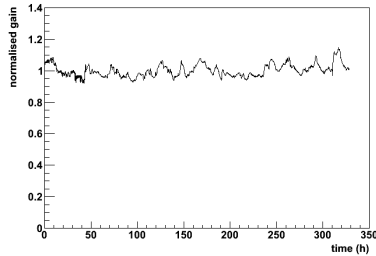
Figure 1: Normalized gain vs. time for a GEM detector irradiated by a Fe^{55} source

The variation of the normalized gain as obtained by Eq. 1 is shown in Fig. 1. There is a peak-to-peak variation of about 10 %, originating from the variation of the O_2 concentration in the gas as well as from the variation of the gas ratio due to changes of the characteristics of the mass flow controller with temperature.

The ageing study of one GEM module was performed by using a 8 keV Cu X-ray generator to verify the stability and integrity of the GEM detectors over a period of time.

The GEM was operated at 395-390-385 V with drift, induction and transfer field at 2.5 kV/cm, 2 kV/cm and 3 kV/cm, respectively. The centre of the upper part of the GEM (region A) was exposed to high-rate Cu X-rays for 10 minutes. Subsequently, the Fe^{55} spectra were observed for 1 minute each from the upper and lower part (region B) of the GEM. The Fe^{55} source was placed in such a way that the Fe^{55} X-rays direct toward the upper part of the GEM in the same spot which was exposed to Cu X-ray. The ratio of the mean position of 5.9 keV Fe^{55} X-ray peak from the upper side and the lower side of the GEM is the normalized gain and corrects the effect of pressure and temperature variations. The whole measurement was performed for about 70 hours. The rate of the Cu X-ray was about 240 kHz.
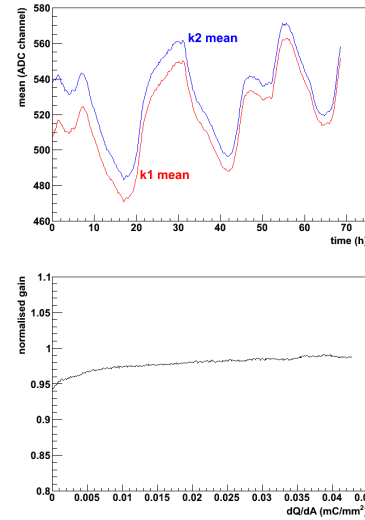
Figure 2: Top: Mean peak positions vs. time. Bottom: Normalized gain as a function of accumulated charge per unit area.

The mean Fe^{55} peak positions of region A and B as a function of time are shown in Fig. 2 (top). They vary with time because of the change of pressure and temperature. The gain from the two regions are slightly different because of the difference in gain of the pre-amplifiers.

The accumulated charge on the detector is calculated from the rate of the X-ray and the average gain of the detector. The normalized gain as a function of accumulated charge per unit area is shown in Fig. 2 (bottom). No sign of ageing is observed after accumulation of more that $0.04 \, mC/mm^2$.

Straw-based coordinate muon chamber

V. Peshekhonov, G. Kekelidze, V. Myalkovskiy, I. Zhukov, and A. Zinchenko

JINR, Dubna, Russia

A prototype MUCH module based on straw tubes was designed by considering the feasibility of constructing standard modules convenient for assembly into large-area detecting systems that can operate at high gas pressure of up to 4 bar and are not affected by variations of environmental parameters such as humidity and temperature[1]. The one-layer prototype contains 48 straws with an inner diameter of 9.56 mm and of 2 m length with a carbon-coated cathode. The thickness of the straw wall is ~60 μm and the sensitive area is 2×0.5 m^2. The developed prototype has a rigid planar structure containing N (multiple of 8) straws covered with epoxy resin. The structure thickness is only 0.2 mm larger than the straw diameter because of the increase of 0.1 mm on each surface. The production technique allows to preserve both the straightness and the straw diameter as well as a constant gap between the adjacent straws.

Two tubular gas manifolds (GMs) are mounted on one side of the structure near the ends of the straws. The manifolds are used for the supply and return of the gas mixture, and they are joined together with side profiles in a common frame and are covered with epoxy resin later on. Fig. 1 displays the installation of the GMs. Each manifold is connected with the inner volume of each straw by using metallic capillary tubes passing through holes made beforehand in the end plugs and the straw walls and are placed orthogonally to the straw plane.
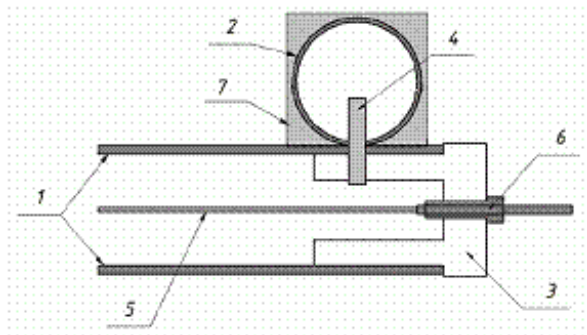
Figure 1: Schematic layout of the gas manifold mounted on straw planar structure. 1 - straw walls, 2 - Al tube of 8 mm diameter and 0.4 mm wall thickness, 3 - plastic end-plug, 4 - metal capillary tube, 5 - anode, 6 - crimping pin, 7 - epoxy resin.

The motherboards (MBs) and termination boards (TBs) are mounted near the crimping pins, and the anodes are galvanically connected with the corresponding buses on the boards. Therefore, the prototype module has two tubular GMs on one side which serve as the parts of its frame. In the adopted design scheme, the GMs do not contain any material which would contaminate the gas mixture, and the MBs and TBs are connected to the anodes without passing through hermetic gaseous volumes. A gas-tightness check for the prototype has demonstrated that the gas leak at 4 bar was about 2.4 mbar/h, which was caused by a leaky joint between the Cu tube and the plastic covering of the crimping pins. Epoxy sealing of these seams removes the leak. Long tests of the prototype during one year on the bench with a fixed composition of the gas mixture and the anode voltage for different gas pressures of up to 4 bar demonstrated the high stability of the prototype parameters for different environmental conditions.

The radiation thickness of the straw is less than 0.05 % X_0. It is instructive to compare this parameter for the straw-based detector and the detector based on aluminum tubes. Assuming the same radiation thickness for the two types of detectors, the relation between the wall thickness (h) for the aluminum tubes and the straw diameter (d) is displayed in Fig. 2. It is safe to say that the increase of radiation thickness of the constructed module with straws of small diameter (4-6 mm) is negligible.
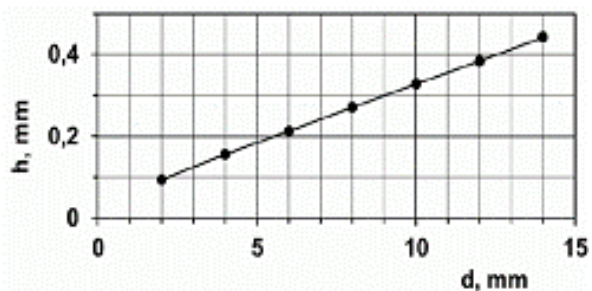
Figure 2: The relationship between the thickness h of the Al tube wall and the straw diameter d, for the same radiation thickness of a high-pressure gaseous detector

We conclude that the double-layer coordinate detectors based on straw tubes of small diameter, created by this technology, can not only be used for the muon detector.

References

[1] V. D. Peshekhonov *et al.*, *Straw based Coordinate Muon Chamber*, submitted to Instrum. and Exp. Tech., arXiv:1210.5849

Study of the longitudinal spatial resolution of long straw tubes using the direct timing method

V. Peshekhonov, A. Makankin, V. Myalkovskiy, S. Vasilyev, and A. Zinchenko

JINR, Dubna, Russia

In gaseous drift chambers, the radial coordinate is determined with high precision by measuring the drift time of the ionization electrons produced by charged particles passing through the chamber. The coordinate along the anode wire can be measured by, e.g., the charge-division method, when the signals are read out from two ends of the resistive anode wire. A spatial resolution of $\sigma = 6.0$ cm near the ends of a 1.52 m long straw for MIPs was shown [1, 2]. We considered the possibility of using the direct timing method (DTM) [3, 4] for processing signals from a prototype constructed of 2 m long straws with an inner diameter of 9.53 mm. The anodes were made of 30 μm gold-plated tungsten wire with a resistivity of 70 Ω/m. The gas mixture Ar/CO_2 (80:20) under a pressure of 1 or 3 bar was used.

The layout of the experimental setup is shown in Fig. 1. A straw under study was irradiated with either 5.9 keV gammas from a Fe-55 source or with beta rays from a Ru-106 source through slit collimators. In the latter case, the electrons passing through the straw were detected by a scintillation counter with two photo-multipliers. Low-energy electrons were stopped in the absorber located between the straw and the counter. Amplifiers based on a MSD-2 microcircuit with a gain of 35 mV/μA, a rise time of about 4 ns and an input impedance of 120 Ω are installed close to the anode ends and connected with minimum parasitic capacitance and inductance. Such amplifiers are commonly used for straw detectors. The pulses from the outputs of the amplifiers are fed into two channels (1 and 3) of the DRS4 Evaluation Board. This board is based on the DRS4 chip, which can sample an input signal with a sampling speed of up to 5 GB/s and store an analog waveform in a time window the size of which is determined by the capacitor array [5].
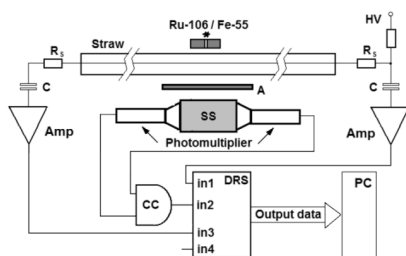
Figure 1: Schematic view of the setup with absorber (A), scintillation counter (SC), amplifier (Amp), coincidence circuit (CC) and Domino Ring Sampler (DRS)

If the avalanche origin is displaced along the anode wire by δy from its center, two signals arriving at the amplifiers pass the distance $L/2 \pm \delta y$, where L is the anode length, and have a time difference of $\delta\tau = 2\delta y/v$, where v is the propagation velocity of the electromagnetic wave along the anode wire. The difference between the leading edges of the pulses determines the coordinate along the anode.

A Fe-55 source was used for measurements of the pulse attenuation and its propagation velocity along the anode. The pulse attenuation over a length of 2 m is 1.17, and the propagation velocity was found to be 3.49 ns/m. A distance of 1 cm corresponds to a difference in the time delay of 69.8 ps if two signals are registered at the ends of the straw. The large dynamic range of MIP signals as well as the clustering of the ionizing losses lead to larger distortions of the pulse waveform compared to those from the Fe-55 source. This can result in a nonlinearity in the determination of the pulse arrival time, which, however, can be corrected for during the data analysis procedure.

The longitudinal resolution obtained in the case of electron registration from Ru-106 is shown in Fig. 2. The resolution varies from $\sim$1 cm in the center of the straw to $\sim$2 cm near the straw end.
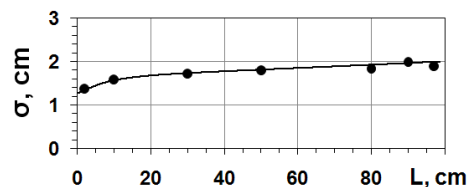
Figure 2: Longitudinal resolution as a function of the distance of the Ru-106 source from the straw center. The gas mixture pressure is 1 bar and the gas gain is about 8×10^4.

The measurements conducted with the detector prototype have demonstrated the feasibility of using the DTM for determination of the longitudinal coordinate in 2 m long thin-walled drift tubes to an accuracy below 2 cm (σ). The longitudinal resolution for a 1.5 m straw is 2 cm instead of 6 cm provided by the charge-division method. Fast current amplifiers can be used for measurements of both the radial coordinate from the electron drift time and the longitudinal one by the DTM technique.

References

[1] C. Bino *et al.*, Nucl. Instrum. Methods **A 271** (1988) 417

[2] A. Sokolov *et al.*, Nucl. Instrum. Methods **A 574** (2007) 50

[3] R A. Boie *et al.*, IEEE Trans. Nucl. Sci. **28** (1988) 471

[4] A. M. Makankin *et al.*, arXiv:1301.6018v1 [physics.ins-det]

[5] Paul Scherrer Inst., DRS4 Evaluation Board User's Manual, http://drs.web.psi.ch/datasheets

Prototype ASIC of analog frond-end for MUCH

E. Atkin, E. Malankin, and V. Shumikhin

National Research Nuclear University "MEPhI", Moscow, Russia

During 2012 a prototype FEE ASIC for the MUCH detector system was under development at MEPhI. The basic task was to design, prototype and study a building block of preamp-shaper fitting the expected specifications of the MUCH. The ASIC was designed according to the rules of the CMOS UMC 180 nm MMRF process. This paper presents the structure of the chip and first lab test results.

During the design, the following specifications were used as guidelines:

- input signal range 1.5 – 100 fC;

- negative charge polarity;

- noise less than 0.3 fC;

- detector capacitance up to 100 pF;

- maximum hit rate per channel 1.6 MHz.

Since several options of MUCH implementation currently exist, the accent in designing the ASIC was made on the elaboration of two preamp versions – a current and a charge-sensitive one. Each of them was designed as a four-channel structure, supplemented by a fifth (test) channel allowing to monitor intermediate points of that. The basis of both versions is the traditional folded cascade, supplemented by an additional boost amplifier and output source follower. The geometry of the preamp input transistor was chosen to be 4 mm × 360 nm. In both versions a feedback capacitance of 200 fF was used. In case of the current preamp, the feedback resistor was set such that it provides the required bell-shape response, corresponding to a maximum hit rate per channel not less than 2 MHz. In the alternative FEE version, shown in Fig. 1, the charge-sensitive amplifier (CSA) is followed by a shaper of the $CR - RC^2$ type. The latter is based on the non-inverting Sallen-Key filter scheme, and its parameters define the above mentioned channel hit rate. The shaper has two additional adjustments: *TAIL* for tail cancellation and *SHBL* for baseline tuning. The ASIC is manufactured using the UMC 180 nm CMOS MMRF process via Europractice. Its layout is shown in Fig. 2 (left) and has a size of $1525 \times 1525 \,\mu\mathrm{m}^2$.
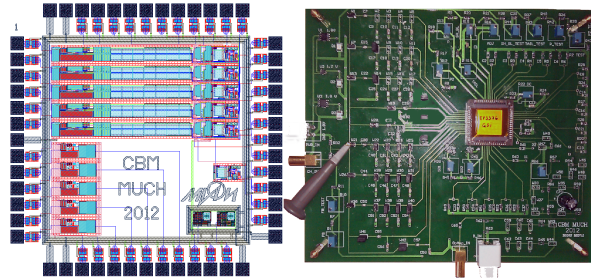
Figure 2: The ASIC layout (left) and the test board (right)

All prototyped chips were packed into CLCC 68 cases and a test board, based on the corresponding socket, was developed (Fig. 2 (right)). The CSA has a gain of 5 mV/fC and a power consumption of less than 2 mW. A typical response of the shaper for an input charge of 80 fC is shown in Fig. 3 (left). The right panel of Fig. 3 shows the transfer function of the chain, measured in the input range of 10 to 100 fC.
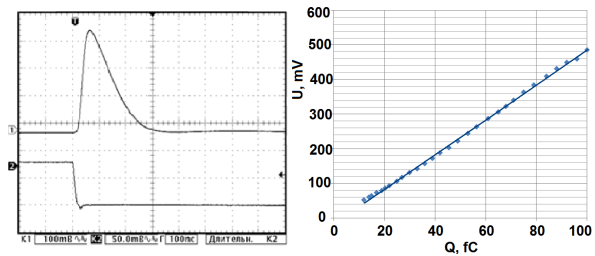
Figure 3: Shaper response (left) and transfer function (right)

Further plans on studying the prototype chips comprise refining the test board, detailed noise measurements and chip tests with MUCH prototypes.

Figure 1: Preamp-shaper structure

Development of the Münster CBM TRD prototypes and update of the TRD geometry to version v13a

D. Emschermann

Institut für Kernphysik, Münster, Germany
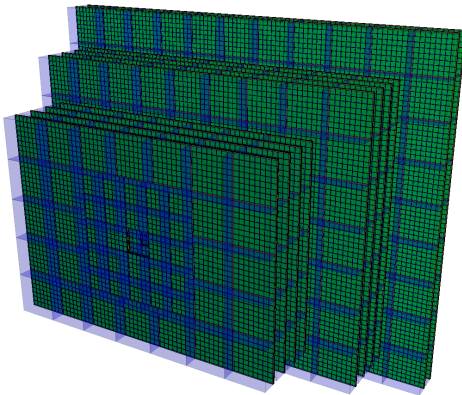
Figure 1: TRD geometry v13b, with 10 layers, for SIS-300

Figure 3: Excessive mis-alignment of the TRD modules

One of the challenges in the design of a TRD module is to minimise the loss of transition radiation between the radiator and the detection volume. A thin kapton foil acting as gas barrier can fulfill this criterion. The deformation of this foil depends on its mechanical tension, the size of the detector module and the differential pressure. In return, gain variations across the detector module must stay at an acceptable level; therefore the deformation of the entrance window should be kept at a minimum. Real-size CBM TRD modules will be built with an edge length in the range of 60 cm to 100 cm (Fig. 2). For such dimensions, a simple foil window can develop a considerable bulgy deformation, due to atmospheric pressure variations.

Figure 2: A small (60×60 cm^2 size) TRD module, with highest pad granularity. The readout electronics is densely packed on the backside (left). The yellow lattice grid, helps to stabilise the green gas window (center, right).

The distortion of the entrance window due to external underpressure can lead to an increase of the gas thickness. This in turn impacts on the electrical fields in the gas, which can alter the gas gain. In the worst case, at external overpressure, the foil (acting as drift cathode) can be pressed

into the cathode wire grid (with ground potential) and cause an electrical short.

A lattice grid reinforcement, stabilising the drift electrode, was incorporated to the 2012 TRD prototypes from Münster [1]. This grid limits the maximum deformation of the foil window to less than 1 mm at 1 mbar overpressure on a 60 cm detector. A large volume TRD gas system, as for example in the ALICE TRD, can be operated at a nominal differential overpressure of around 0.1 mbar. In addition one needs to take into account the hydrostatic pressure difference for Xenon of 0.4 mbar/m within the vertically positioned detector modules. In summary, we conclude that the total deformation of a lattice grid reinforced foil window is on the safe side, when the latter is used as drift cathode for a MWPC containing a small drift section.

The layout of the 2012 modules was then implemented as a Root geometry in the `cbmroot` simulation package. Compared to the former TRD version [2], this allowed to introduce an optional mis-alignment for each individual TRD module (Fig. 3). One can specify a range of maximum displacement along or rotation around the x, y and z axes, which is then randomly applied to each detector module. A check for overlaps in the mis-alignment geometry is not performed. The offline alignment procedure can now be studied with these mis-aligned TRD geometries.

References

[1] C. Bergmann *et al.*, *Test of Münster CBM TRD prototypes at the CERN-PS/T9 beam line*, this report

[2] D. Emschermann *et al.*, CBM Progress Report 2011, p. 45

Construction and simulations of full-size CBM-TRD prototypes without drift region

E. Hellbär, H. Appelshäuser, A. Arend, C. Baumann, T. Bel, C. Blume, P. Dillenseger, K. Reuß, F. Roether, and M. Seidl

Institut für Kernphysik, Goethe-Universität, Frankfurt am Main, Germany

To provide a fast and efficient e/π separation and charged particle tracking for the Compressed Baryonic Matter (CBM) experiment, a Transition Radiation Detector (TRD) based on a thin Multiwire Proportional Chamber (MWPC) without an additional drift region is considered [1]. Corresponding to this design, two full-size prototypes have been developed and built with an anode-cathode spacing of 4 mm and 5 mm, respectively, resulting in amplification regions of 8 mm and 10 mm depth. The gold-plated tungsten wires with a diameter of 20 μm have a pitch of 2.5 mm. They are glued on distance ledges which are attached to the frame of the detector made out of aluminium with the dimensions 60×60 cm^2. The back side consists of a honeycomb structure supporting the pad plane. The common pad plane design features different pad sizes, where the read-out pads used during tests have a size of 7.125×75 mm^2. A second frame to seal the MWPC includes a thin aluminized mylar foil serving as the entrance window as well as an optional support structure. Figure 1 shows a technical drawing of the prototypes with the aforementioned components.
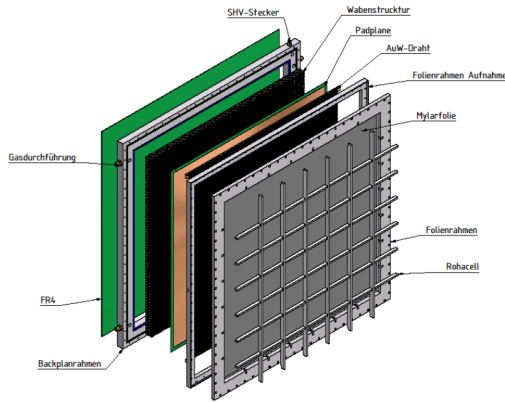
Figure 1: Technical drawing of a full-size TRD-prototype without drift region

To avoid large changes of the gas gain due to its deformation, the thin mylar foil has to be stretched uniformly and with appropriate tension. To achieve this requirement, a method based on thermal expansion is being used [2]. The foil is fixed to a plexiglass frame which is heated up by heating coils resulting in an expansion of the frame and thus a mechanical stretching of the foil. To quantitatively analyse the bulge of the stretched foil caused by overpres-

sure inside the chamber, the deformation of the entrance window and the mechanical stress of the MWPC body are simulated with the Abaqus software package [3]. According to these simulations, the entrance window stretched at a plexiglass temperature of 55°C gets deformed by 160 μm at an overpressure of 0.01 mbar, which is verified by measurements. The resulting gain variation as a function of the modified distance between the entrance window and the anode wires is simulated with Garfield [4] and shown for three detector geometries without drift region in Fig. 2. Keeping the deformation of the entrance window below 120 μm leads to a gain variation of less than 10% and can be achieved by limiting the differential gas pressure variations to less than 0.01 mbar.
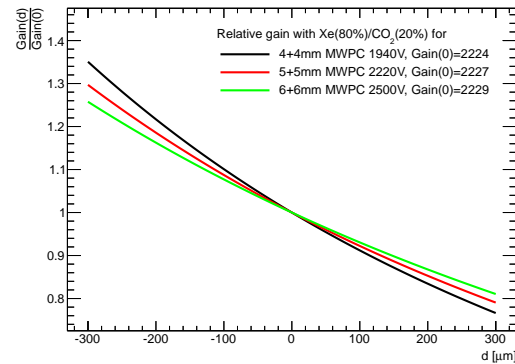
Figure 2: Relative gain depending on the displacement of the entrance window for three detector types without drift region

The full-size prototypes described in this article were tested along with several other considered prototype geometries with dedicated drift regions at the common test beam campaign at CERN-PS in October 2012 [5].

References

[1] P. Reichelt, H. Appelshäuser and M. Hartig, CBM Progress Report 2010, Darmstadt 2011, p. 39

[2] M. Staib *et al.*, RD51-Note-2011-004

[3] `http://www.3ds.com/de/products/simulia/` `portfolio/abaqus/overview/`

[4] `http://garfield.web.cern.ch/garfield/`

[5] P. Dillenseger *et al.*, *In-beam performance studies of the first full-size CBM-TRD prototypes developed in Frankfurt*, this report

SPADIC 1.0 – a self-triggered amplifier/digitizer ASIC for the CBM-TRD

T. Armbruster, P. Fischer, M. Krieger, and I. Peric

ZITI, Heidelberg University, Germany

For the charge readout of the future CBM-TRD sub-detector, the mixed-signal readout chip SPADIC (Self-triggered Pulse Amplification and Digitization asIC) is being developed in a 180 nm technology. After the well-established version 0.3, in 2012 the first full-blown SPADIC version 1.0 became available, and first measurements were performed [1]. SPADIC 1.0 provides 32 autonomous read-out channels, each of which produces complex digital messages for every charge pulse that is injected (free-running system). A central feature of SPADIC is the recording of complete pulses, which makes the ASIC behave similarly to an oscilloscope and allows for flexible data processing and feature extraction.

Briefly summarized, each SPADIC 1.0 channel consists of an analog preamplifier (80 ns shaping time, simulated ENC about $800\,e^-$ @ 30 pF load), a continuously running pipeline ADC (25 MS/s, 8 bit effective resolution), an IIR filter (16 bit internal resolution, 4 first order stages) for ion-tail cancellation and baseline stabilization, and a hit detection and message building logic (including features like for instance neighbor readout or data value selection). In order to transport the recorded information out of the ASIC, the messages of 16 channels (plus those of a dedicated epoch marker channel) are arbitrated to one message stream (conserving the message order in terms of their time-stamp), which is further fed into a CBMnet protocol block [2]. The generated CBMnet data packages are physically transported over two serial 500 Mbps (DDR) LVDS links to the next DAQ stage (either an FPGA or another ASIC).

Being a part of the CBM DAQ system, SPADIC 1.0 makes use of the synchronization techniques provided by CBMnet. The main chip clock (250 MHz) enters the ASIC via the CBMnet interface and all derived internal SPADIC clocks (125 and 25 MHz) therefore run synchronously to all other CBMnet nodes in the DAQ system. Via short control telegrams called DLMs (Deterministic Latency Messages), which are guaranteed to have a fixed (and measurable) path delay from one DAQ node to any other DAQ node, all operations required for synchronization can be performed. Examples are the reset of the internal time-stamp counter or the start/stop of data taking.

All building blocks of SPADIC 1.0 have already been successfully operated, and also first full-system measurements have been performed. Moreover, during the TRD beam-time at CERN/PS in November 2012, some first TRD chamber pulses could be recorded with SPADIC 1.0 [3]. The provisional setup that thereby has been used is shown in Fig. 1. So far, the overall functionality of SPADIC 1.0 seems to be satisfactory, even though some more comprehensive measurements will have to be performed. Updated status information can be found on the SPADIC website [4].

In 2013 the main focus will lie on the improvement of the SPADIC 1.0 setup (e. g. more reliable firmware, minimized pickup noise), on the complete characterization of the analog parts (mainly CSA and ADC), and on measuring the actual radiation tolerance. Depending on the results, a submission of another prototype or even the final SPADIC iteration in the end of 2013 is conceivable.
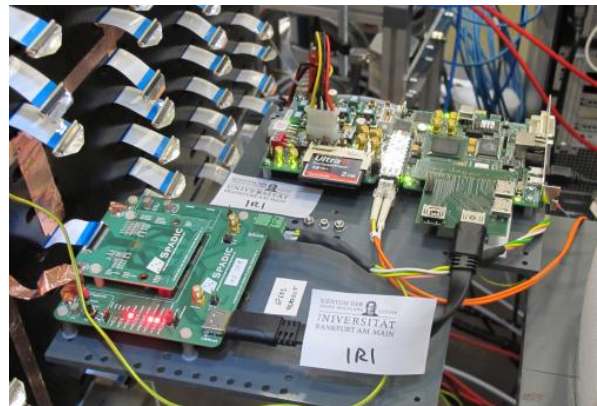
Figure 1: SPADIC 1.0 front-end PCB connected to a TRD prototype during the CERN/PS beam-time in 2012. The front-end PCB is further connected via CBMnet (transported over an HDMI cable) to a Xilinx SP605 FPGA board.

References

[1] T. Armbruster *et al.*, *Multi-Channel Charge Pulse Amplification, Digitization and Processing ASIC for Detector Applications*, to appear in IEEE-NSS (2012)

[2] F. Lemke *et al.*, *Status of CBMnet integration and HUB design*, this report

[3] C. Garcia *et al.*, *Beam test results of the CBM-TRD feature extraction using SPADIC v1.0*, this report

[4] `http://spadic.uni-hd.de`

FPGA-based free running mode acquisition for a high counting rate TRD

F. Constantin

Horia Hulubei National Institute of Physics and Nuclear Engineering, Bucharest, Romania

A new acquisition system, Free Running Mode for in-beam tests of the TRD prototypes, was developed; it is based on the Virtex-6 FPGA ML605 Evaluation Kit (see Fig. 1). This activity is a continuation of the one presented in [1], aiming for a secure synchronization with MBS DAQ system.

Figure 1: General view of the acquisition system

The signals from the TRD, amplified by a FEE based on FASP ASIC, are transported via a twisted pair cable to a fast ADC (MAX1434), a 10-bit analog-to-digital converter which features fully differential inputs, a pipelined architecture, and digital error correction incorporating a fully differential signal path. The MAX1434 offers a maximum sample rate of 50 Msps [2].

The main tasks of ML605 [3] are:

- clock generation,

- de-serialization of data delivered by MAX 1434 ,

- reading the synchronization signal generated by MBS,

- Ethernet communication.

The VHDL language was used in order to perform the required tasks; 16 analog channels, corresponding to 16 TRD pads, were processed.

The sync signal from MBS was used in order to correlate the information delivered by the MAX data with the other Read Out Controllers (mainly with the QDC operated in the VME crate which was used for lead glass and Cherenkov detectors). The information from ML605 was directed also to the general acquisition system, and the data were made available in the Go4 environment, thus being used to monitor the whole system during data taking.

Figure 2 shows the electron-pion separation using a fibre radiator and one of the TRD prototypes of the Bucharest group based on MWPC architecture with 2x4 mm amplification zone and 4 mm drift region [4]. Electrons and pions were selected using the information from the Cherenkov detector and the lead glass calorimeter [5]. Although still preliminary, the results show that the information delivered by the high counting rate prototypes developed for CBM and amplified by FASP could be processed by the free running mode architecture, conserving their performance. The activities towards a higher integration of the present solution are in progress.
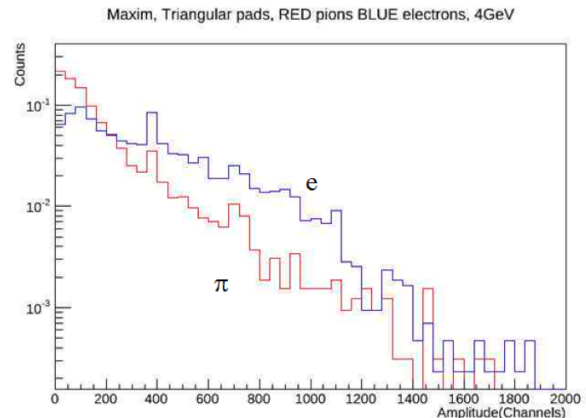
Figure 2: Pulse height spectrum for pions and electrons

References

[1] F. Constantin and M. Petcu, CBM Progress Report 2011, p. 53

[2] http://www.maximintegrated.com/datasheet/index.mvp/id/4906

[3] http://www.xilinx.com/products/boards-and-kits/EK-V6-ML605-G.htm

[4] M. Petriş *et al.*, *e/π identification and position resolution of a high-granularity TRD prototype based on a MWPC*, this report

[5] C. Bergmann *et al.*, *Test of Münster CBM TRD prototypes at the CERN-PS/T9 beam line*, this report

Test of Münster CBM TRD prototypes at the CERN-PS/T9 beam line

C. Bergmann[1], R. Berendes[1], D. Bonaventura[1], D. Emschermann[1], N. Heine[1], J. Hehner[2], B. Kolipost[1], W. Verhoeven[1], and J. P. Wessels[1]

[1]Institut für Kernphysik, Münster, Germany; [2]GSI, Darmstadt, Germany

The Münster real-size CBM TRD prototypes [1] of 59×59 cm^2 shown in Fig. 1 are derived from the design of the ALICE TRD modules. An amplification region of $3.5 + 3.5$ mm is combined with a 5 mm drift section leading an active gas volume thickness of 12 mm. Signals are induced on rectangular pads of 7.125 mm width, allowing charge collection on three adjacent pads. This design corresponds to the smallest module size next to the beam-pipe, required for 12% of the total CBM TRD area, and is scalable to detector modules of 1 m^2-size.

Figure 1: Münster TRD protoypes in the CBM beam test

Various radiator types were investigated on these three TRD prototypes during the common CBM beam test in 2012. The read-out was performed with the SPADIC v0.3 / Susibo [2], SPADICv1.0 [3] and FASP [4] front-ends. The setup was entirely EPICS controlled, allowing online monitoring of the HV settings and the gas flow and inclusion of these values in the DAQ stream. First results of the ongoing analysis are shown in Fig. 2.

One important aspect of radiator choice is to match of the TR-emission spectrum to the absorption spectrum of the detector. For a detailed investigation, we have built different radiator types: regular foil and irregular foam, fiber and sandwiches. Ideally, a radiator should yield an optimal TR performance while keeping the material budget as low as possible. While this consideration favors regular foil radiators, they usually require a significant external support frame to keep the foils stretched and in position. This additional frame material is avoided in our first micro-structured self-supporting radiators (Kshort, K, K++). First results using self-supporting radiators of type K (Fig. 3) are promising and comparable to the classical radiator type B with the same parameters, as e.g. the number of foils, and made from the identical material.
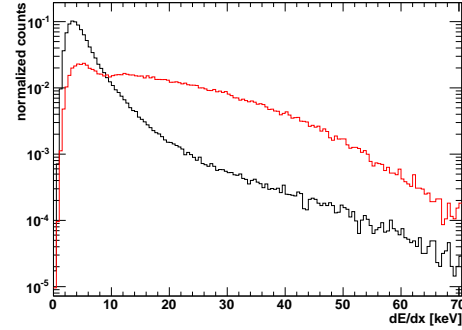
Figure 2: ADC spectra for π (black) and e (red), integrated and calibrated, for the second TRD prototype operated with Xe/CO$_2$ (80:20) gas in combination with a 350 foil layer micro-structured self-supporting radiator (K++) at 3 GeV/c
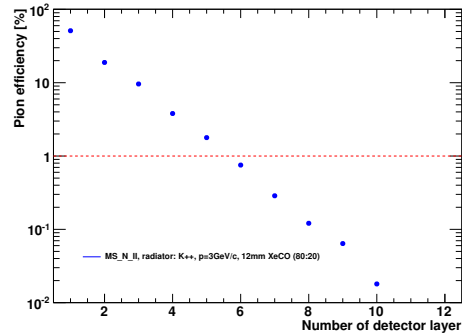
Figure 3: Extrapolated pion efficiency for a TRD consisting of up to 10 layers with a micro-structured self-supporting radiator (K++). The dashed line indicates the design goal of 1% π efficiency at 90% e efficiency, which in this configuration is reached with 6 layers.

References

[1] D. Emschermann, *Development of the Münster CBM TRD prototypes and update of the TRD geometry to version v13a*, this report

[2] T. Armbruster, P. Fischer and V. Perić, CBM Progress Report 2010, p. 45

[3] T. Armbruster *et al.*, *SPADIC 1.0 - a self-triggered amplifier/digitizer ASIC for the CBM TRD*, this report

[4] V. Catanescu, D. Bartos and Gh. Caragheorgheopol, CBM Progress Report 2009, p. 47

In-beam performance studies of the first full-size CBM-TRD prototypes developed in Frankfurt

P. Dillenseger, H. Appelshäuser, A. Arend, C. Baumann, T. Bel, C. Blume, E. Hellbär, K. Reuß, F. Roether, and M. Seidl

Institut für Kernphysik, Goethe-Universität, Frankfurt am Main, Germany

For the Compressed Baryonic Matter (CBM) experiment at the Facility for Antiproton and Ion Research (FAIR), a Transition-Radiation Detector (TRD) is being developed. Its goal is to provide good particle identification and tracking performance in the high particle-density environment of the experiment. The aim is to achieve 90 % electron efficiency with a pion mis-identification below 1 %. For the test beam at the CERN-PS in October 2012 [1], full-size prototypes were built and used. Detailed information about these prototypes and their manufacturing can be found in [2].

To match the challenge of the high-flux environment in the CBM experiment, we employ thin symmetric Multi-Wire Proportional Chambers (MWPC), with a single wire plane, 8 or 10 mm thick gas volume regions, and a $20 \, \mu$m thick aluminized mylar-foil as cathode plane and at the same time as entrance window. In order to maximize the electron-identification power the optimization of the radiator performance is essential. During the test runs in October 2012, several different types of radiators were tested, including regular and irregular foil radiators, several foam radiators and fibre radiators. In addition to the radiator scan, the dependence of the gas gain on the differential gas pressure inside the chambers was measured in order to investigate the deformation of the mylar foil and its influence on the gas gain.

Two prototypes with the dimensions $60 \times 60 \ \mathrm{cm}^2$, one with a 4+4 mm and the other one with a 5+5 mm gas gap [2], were used with the SPADIC rev 0.3 readout chain [3] for the measurements at the CERN-PS. The radiator scan included 15 different radiators and was performed with a 3 GeV/c mixed electron-pion beam.

Figure 1 displays the signal of electrons and pions averaged over one run. The dashed curve corresponds to electrons measured with FFM R002 (shown in Fig. 2) as radiator, the signal below the dashed curve are electrons measured without a radiator and the filled area is the average pion signal. The radiator used here is made out of polyethylene foam with a bubble diameter of about 1 mm, which corresponds to approximately 260 surface boundaries for a total radiator thickness of 26 cm. The measurement shows a difference of more than a factor two between the electron signal with and without the FFM R002 radiator. At the same time the FFM R002 is cost efficient and mechanically stable, which makes it an attractive choice for the radiator material.

Figure 2: The radiator FFM R002. It consists of polyethylene foam with a bubble-diameter of about 1 mm.

The next steps of the CBM-TRD development will be to investigate combinations of the thin entrance window and the stiff radiator in order to minimize the deformation of the entrance window.
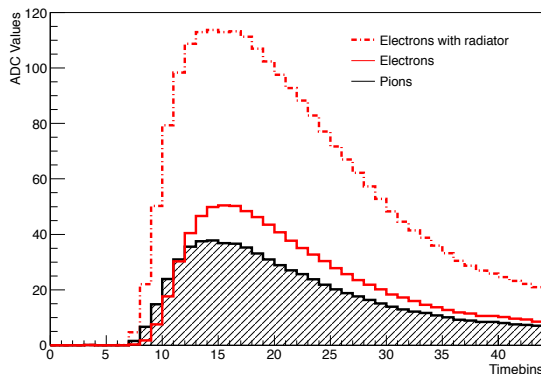
Figure 1: Average electron and pion signal of the 5+5 mm prototype without radiator and with the FFM R002 radiator

References

[1] D. Emschermann *et al.*, *Common CBM beam test of the RICH, TRD and TOF subsystems at the CERN-PS/T9 beam line in 2012*, this report

[2] E. Hellbär *et al.*, *Construction and simulations of full-size CBM-TRD prototypes without drift region*, this report

[3] T. Armbruster *et al.*, CBM Progress Report 2010, Darmstadt 2011, p. 45

Beam test results of the CBM-TRD feature extraction using SPADIC v1.0

C. Garcia[1], C. Bergmann[2], D. Emschermann[2], M. Krieger[3], and U. Kebschull[1]

[1]IRI, Goethe University, Frankfurt/Main, Germany; [2]Institut für Kernphysik, Münster, Germany; [3]ZITI, Heidelberg University, Germany

The feature extraction is a data processing stage of the proposed data acquisition chain (DAQ) for the CBM-TRD detector aiming to deliver event-filtered and bandwidth-reduced data to the First Level Event Selection (FLES). The feature extraction processing stage will be implemented at the Data Processing Board (DPB) located in the TRD-DAQ. A data rate of about 1 TB/s and a high event rate of approximately 10 MHz is expected for the final experiment [1].

In October and November 2012 a common beam test of the CBM subsystems RICH, TRD and TOF was performed at the CERN Proton Synchrotron (PS) T9 accelerator beam line. A full size ($59{\times}59$ cm^2) TRD detector prototype from Münster [2], with an amplification/drift region of 7.0/5.0 mm thickness was used for this study. The readout and signal processing of the TRD module was performed by the Self-triggered Pulse Amplification and Digitization asIC (SPADIC) version 1.0 [3]. The SPADIC chip reads out 32 channels in self-triggered mode and, compared to the previous SPADIC v0.3 chip, implements new features which are of importance for the feature extraction (e.g. neighbor channel-trigger readout).
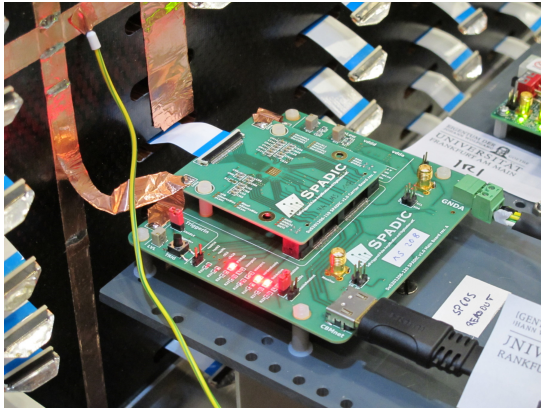
Figure 1: Full-size TRD prototype and SPADIC v1.0 PCB as tested at the CERN-PS/T9 in 2012

In order to perform further developments for the feature extraction stage, obtaining real data samples from full-size TRD prototypes employing the new SPADIC v1.0 chip was one of the purposes of the beam test at the CERN-PS/T9. The experimental data acquisition setup was composed of the SPADIC v1.0 connected by a HDMI cable to a Readout Controller (ROC). The latter was interfaced with an optical connection to an Active Buffer Board (ABB) in a data ac-

quisition computer. The communication protocol used was CBMnet 2.0 [4]. An effective area of 16 channels was read out in self-triggered mode, while a total area of 8 channels was read out using the neighbor channel-trigger feature. A set of recorded data was acquired during the beam test; however, this data set lacks synchronization to any other detector subsystem.

An online cluster reconstruction is currently being designed using beam test data. Even if it is not possible to reconstruct the whole physical event, it helps to simulate specific scenarios of high particle rates in order to develop a DPB feature extraction module. As shown in Fig. 2, a three-pad cluster and its approximated position reconstruction were obtained using a clusterizer algorithm that is easily parallelizable. Furthermore, the firmware migration of the actual feature extraction processing board (Xilinx SP605 FPGA) into the new SysCore v3 [5] will be one of the main tasks in 2013.
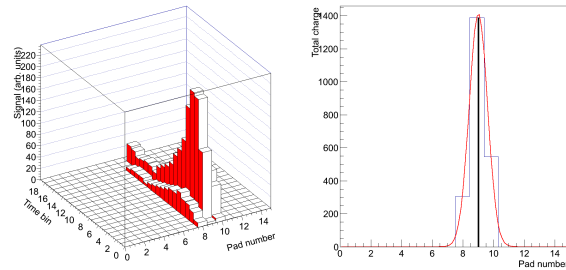
Figure 2: Left: reconstructed TRD cluster for a single particle; right: hit position approximation by a fit to the total charge deposition. The vertical line indicates the reconstructed hit position.

References

[1] J. de Cuveland and V. Lindenstruth, J. Phys. Conf. Ser. **331** (2011) 022006

[2] C. Bergmann *et al.*, *Test of Münster CBM TRD prototypes at the CERN-PS/T9 beam line*, this report

[3] T. Armbruster *et al.*, *SPADIC 1.0 – a self-triggered amplifier/digitizer ASIC for the CBM-TRD*, this report

[4] F. Lemke *et al.*, *Status of CBMnet integration and HUB design*, this report

[5] J. Gebelein *et al.*, *SysCore3 – a universal Read-Out Controller and Data Processing Board*, this report

Two dimensionally position sensitive real size CBM-TRD prototype

M. Târzilă[1], *M. Petriş*[1], *M. Petrovici*[1], *V. Simion*[1], *V. Aprodu*[1], *D. Bartoş*[1], *G. Caragheorgheopol*[1], *V. Cătănescu*[1], *F. Constantin*[1], *L. Prodan*[1], *A. Radu*[1], *J. Adamczewsky-Musch*[2], *and S. Linev*[2]

[1]NIPNE, Bucharest, Romania; [2]GSI, Darmstadt, Germany

For the planned Compressed Baryonic Matter (CBM) experiment we have constructed and tested a real size CBM-TRD prototype (539.8 x 557.8 mm^2) with an architecture based on a MWPC coupled with a drift zone. The chamber design concept was retained from a previous small prototype [1]: a 2x4 mm thick amplification region and a drift zone of 4 mm thickness, an anode pitch of 3 mm and a cathode pitch of 1.5 mm.
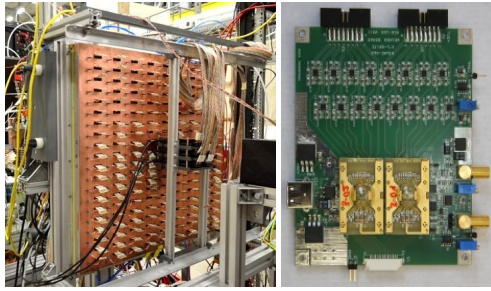
Figure 1: The back side of the detector with signal flat cables (left side); associated 16 channel FEE based on two FASP chips (right side).

The drift electrode, made from a 9 mm thick honeycomb plate placed between two Rohacell plates of 3 mm thickness, each one coated on the outer side with an aluminized Kapton foil of 25 μm thickness, closes one side of the gaseous chamber. The other side is closed by the read out electrode made from a 300 μm thick PCB reinforced by a 2 cm honeycomb plate sandwiched between two layers of 100 μm carbon fiber. The pad plane has a structure of 9 columns and 20 rows with 144 triangular pads per row, each of ~ 1 cm^2 area, which are read out individually. Signals delivered by the pads are routed in groups of 16 to the flat cables as can be seen in Fig. 1 (left), and processed by FASP [2] FEE (see Fig. 1, right).

The TRD prototype was tested with a mixed electron-pion beam of 2-8 GeV/c momenta, made available at T9 beam line of CERN Proton Synchrotron. The chamber was flushed with a 80%Xe+20%CO_2 gas mixture and operated at an anode voltage of 2000 V and a drift voltage of 800 V.

The electron and pion events are identified and selected using the correlation between signals provided by a Cherenkov detector and a lead-glass calorimeter positioned in front and at the end of the beam line, respectively.

The obtained pulse height distributions for electrons and pions at 3 GeV/c beam momentum are presented in Fig. 2. The results are from measurements when the prototype was operated with a regular foil radiator of the type 20/250/220

(20 μm foil thickness, 250 μm gap, 220 foils).
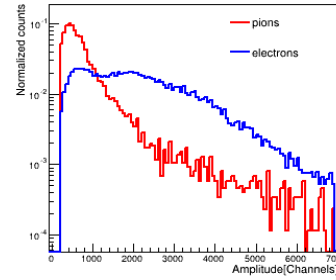
Figure 2: Pulse height distributions for pions (red line) and electrons (blue line).

The distributions obtained with one layer (Fig. 2) allow to estimate the electron identification capability of the full TRD as a function of the number of layers. The results are shown in Fig. 3 (left) for particle momenta of 3 GeV/c and for three types of radiators.
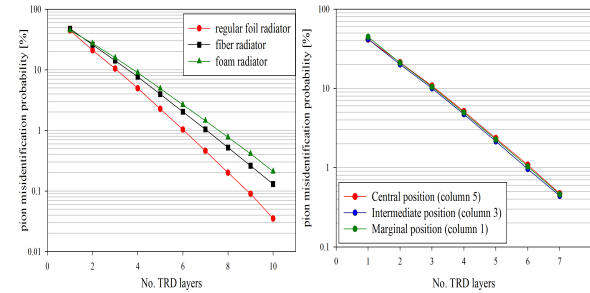
Figure 3: Extrapolated electron-pion identification performance as a function of: number of layers (left side); position of the illuminated area across the detector's surface (right side).

For a regular foil radiator a performance of $\sim$1% was estimated for a configuration of six layers.

Fig. 3 (right) shows that the electron-pion separation performance is not dependent on the position across the detector's surface, proving that the deformation of the drift electrode due to the slight overpressure of the circulated gas mixture is negligible.

References

[1] M. Petriş *et al.*, CBM Progress Report 2011, p. 47

[2] V. Cătănescu *et al.*, CBM Progress Report 2009, p. 47

e/π identification and position resolution of a high-granularity TRD prototype based on a MWPC

M. Petriş[1], M. Târzilă[1], M. Petrovici[1], V. Simion[1], V. Aprodu[1], D. Bartoş[1], A. Bercuci[1],
G. Caragheorgheopol[1], V. Cătănescu[1], F. Constantin[1], L. Prodan[1], A. Radu[1],
J. Adamczewski-Musch[2], and S. Linev[2]

[1]NIPNE, Bucharest, Romania; [2]GSI, Darmstadt, Germany

A high-granularity TRD prototype was designed and built as a single multi-wire proportional chamber (MWPC) with 2x4 mm amplification region coupled with a 4 mm drift zone. The readout electrode has triangular shaped pads of 2.7 cm height and 0.7 cm width corresponding to the granularity requirements of the innermost zone of the first CBM-TRD station of 1 cm^2 readout cell area. Details on the architecture of this type of TRD prototype were already reported in Ref. [1]. The present contribution is focused on the e/π discrimination and position resolution.
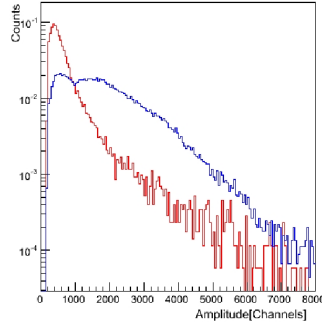
Figure 1: Pulse height distributions for pions (red line) and electrons (blue line) at 3 GeV/c

The in-beam tests were performed at the T9 beam line of the PS accelerator at CERN using a mixture of electrons and pions of 2–8 GeV/c momentum. The electrons and pions were selected using the information from a Cherenkov and a Pb glass calorimeter positioned in front and at the end of the beam line, respectively. The detector was flushed with a 80%Xe+20%CO$_2$ gas mixture. The triangular pads were read out by FASP front-end electronics [2, 3] using a shaping time of 40 ns. The measured pulse height distributions for electrons and pions at 3 GeV/c are shown in Fig. 1 for 2000 V anode voltage and 800 V drift voltage. The pion misidentification probability as a function of number of TRD layers was obtained by a Monte Carlo simulation based on the measured pulse height spectra. A pion misidentification probability of 1.25 % for a six-layer configuration (Fig. 2) was obtained using a regular foil radiator (220 foils of 20 μm thickness and 250 μm air spacing). A 1 % pion misidentification probability was estimated for a configuration with seven TRD layers with a fibre radiator.

The position across the pads was reconstructed by the charge shared among consecutive rectangular pads: the pad with maximum signal (pad i) and its left (pad $i-1$)/ right
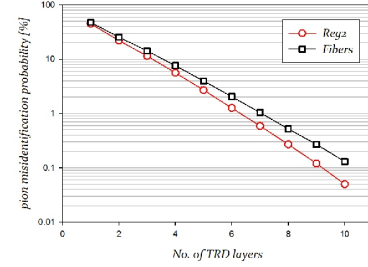
Figure 2: Pion misidentification as a function of number of TRD layers for 90% electron efficiency

(pad $i+1$) neighbours. The finite digitization of the signal, (i.e. three pads) obviously introduces systematic errors. For this reason corrections based on Monte Carlo simulations for the finite digitization and amplitude fluctuations are applied to the reconstructed position. The position resolution was determined from the standard deviation of a Gauss function fitted to the difference between the reconstructed position with two identical detectors. A position resolution of 493 μm across the pads was achieved considering equal contributions of both chambers (Fig. 3, left). The beam profile obtained from the position information shows no discontinuities due to the reconstruction procedure (Fig. 3, right). For the position reconstruction along the pads the algorithm described in [4] will be considered.
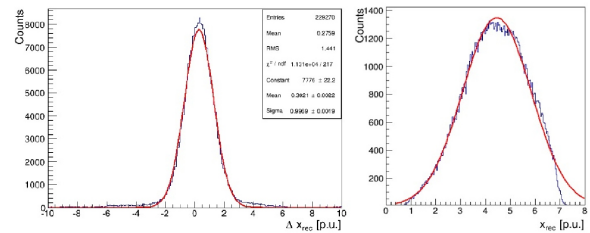
Figure 3: (left) Difference between the reconstructed position across the pads with two identical detectors, fitted with a Gauss function; (right) reconstructed beam profile

References

[1] M. Petriş et al., CBM Progress Report 2011, p. 47

[2] V. Cătănescu et al., CBM Progress Report 2009, p. 47

[3] A. Caragheorgheopol et al., CBM Prog. Report 2010, p. 46

[4] M. Petriş et al., CBM Progress Report 2011, p. 48

Results of the CBM-TRD beam test in 2011

S. Chernenko[1], O. Fateev[1], S. Lebedev[2], G. Ososkov[1], S. Razin[1], Yu. Zanevsky[1], and V. Zryuev[1]

[1]JINR, Dubna, Russia; [2]Justus-Liebig-Universität, Gießen, Germany

The test results of Dubna TRD prototype detectors obtained during the CBM beam test run 2011 are presented [1]. The measurements were carried out using a mixed electron-pion beam with momentum of up to 8 GeV/c. The experimental setup is shown in Fig. 1.
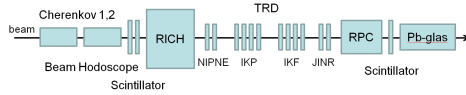
Figure 1: The layout of the CBM TRD beam test installation.

Two detectors are based on MWPCs with pad readout and a 2 mm anode wire pitch. The active area of the detector is 96 mm × 90 mm. The gap between the anode wire plane and the cathode wire plane is 3 mm. The drift gap is 6 mm. We used irregular radiators of the same type as employed in the ALICE-TRD with 48 mm thickness [2]. The detectors were filled with gas mixtures $Ar(80)/CO_2(20)$ or $Xe(80)/CO_2(20)$. The pad size is 6 x 45 mm^2, and the total number of channels is 32. The MWPC was equipped with FEE based on the 16-channel PASA-CBM preamplifier and shaper (designed by H. Solveit, Univ. Heidelberg) with the following parameters: ENC 460e, Kq 12 mV/fC and shaping time ~70 ns. A VME-based peak sensing ADC was used. The signal from the anode plane was used as reference signal.

The prototypes were tested at different gas gains, beam intensities and momentum. For beam particle identification the data from the Cherenkov and the lead glass detectors were used. The electron and pion events are selected by an off-line analysis using the correlation between the signals delivered by the Cherenkov and lead glass detector. The
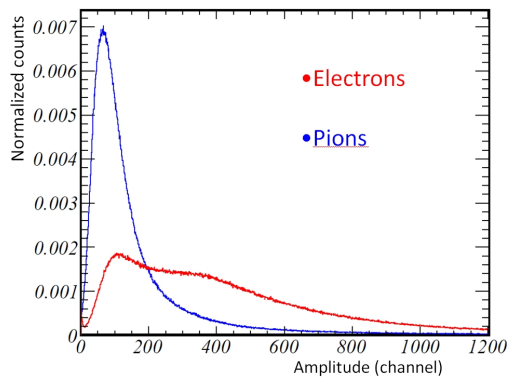
Figure 2: Total charge distributions for electron (red line) and pion beams (blue line) with a momentum of 3 GeV/c
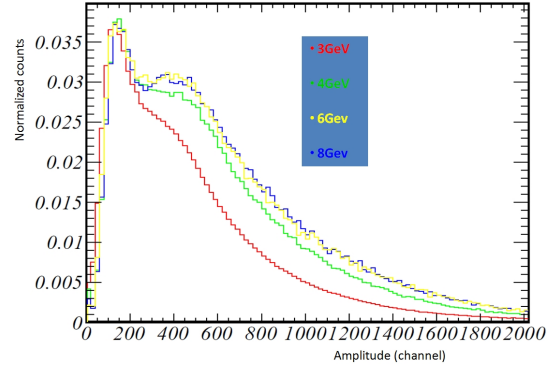
Figure 3: Total charge distributions for electron beams with momenta of 3 GeV/c, 4 GeV/c, 6 GeV/c and 8 GeV/c

result of data analysis for electron beam (red line) and pion beam (blue line) with a momentum of 3 GeV/c is presented in Fig. 2.

In Fig. 3 the distributions of the total charge are shown for electrons with momenta of 3 GeV/c, 4 GeV/c, 6 GeV/c and 8 GeV/c and a gas mixture of Xe/CO_2. The data obtained for 3 GeV/c and 8 GeV/c were used in the simulation framework (`cbmroot`) of the CBM experiment.
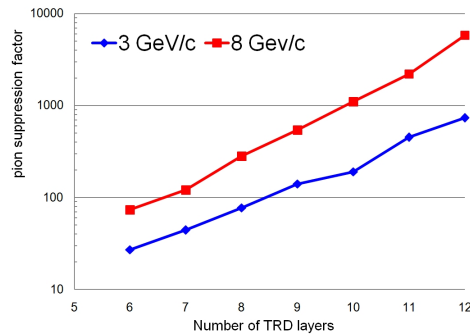
Figure 4: The pion suppression factor in dependence on the number of TRD layers

The pion suppression factor for different number of TRD layers is presented in Fig. 4. Thus, in order to achieve a pion suppression factor about 100 at 8 GeV/c beam momentum, we have to use nine layers of the TRD.

References

[1] C. Bergmann *et al.*, CBM Progress Report 2011, p. 4

[2] The ALICE Collaboration, *Technical Design Report of the Transition Radiation Detector*, CERN/LHCC 2001-21

Analysis of TRD beam test data of 2011 in CBMROOT

A. Lebedev[1,3], S. Lebedev[2,3], and G. Ososkov[3]

[1]IKF, Goethe University, Frankfurt, Germany; [2]Justus Liebig University, Giessen, Germany; [3]LIT JINR, Dubna, Russia

Transition Radiation Detector (TRD) prototypes from the Frankfurt [1] and Münster [2] groups were tested at the CERN PS/T9 beam line in October 2011. In this report we present some results from the data analysis employing electron identification algorithms developed within the `cbmroot` framework.

An example of energy loss spectra for electrons and pions with a momentum of $3\,\mathrm{GeV}/c$ for the foam radiator is shown in Fig. 1. The energy loss data for our study were generated from measured energy loss distribution histograms assuming that all TRD layers are identical with respect to energy loss measurements.
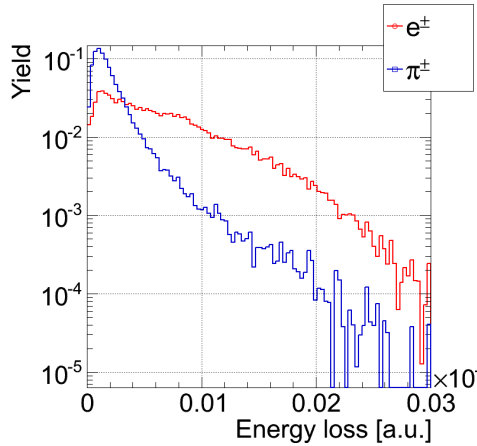
Figure 1: Energy loss spectra for electrons and pions with $p = 3\,\mathrm{GeV}/c$

Several electron identification algorithms were developed in `cbmroot`, including algorithms based on the Artificial Neural Network (ANN) [3], Boosted Decision Tree (BDT) [4], Likelihood method, threshold on the mean value, and on threshold on the median value.

The number of TRD layers required to achieve the necessary pion suppression level is a crucial parameter for the TRD; it was evaluated with the different algorithms. Figure 2 shows the pion suppression requiring 90% of electron identification efficiency. According to our results, the required pion suppression level of better than 100 can be achieved with $9-10$ TRD layers both with regular foiled radiators as well with irregular foam radiators.

Different radiator types were investigated with the TRD prototypes. Here we present results for selected radiators tested by the Münster group (B, F: regular foil radiator, H++: irregular foam, G30: fiber) and by the Frankfurt group (5mm_fibre: a fiber radiator as used in the ALICE TRD, 4mm_foam: a polypropylene foam radia-
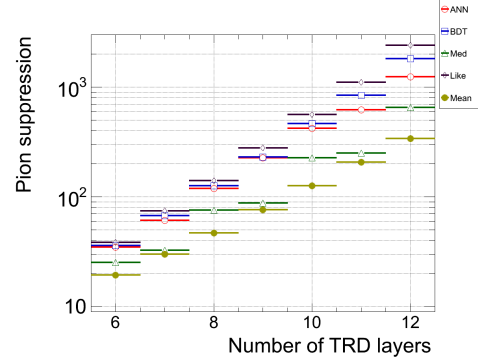
Figure 2: Pion suppression level as function of the number of TRD layers for $4\,\mathrm{mm}$ foam radiator from the Frankfurt group

tor, 4mm_f350: regular foil radiator). The best results were achieved for the regular foil type radiator (see Fig. 3). Such radiators usually require a significant external support frame to keep the foils. However, a reasonable pion suppression can also be achieved with irregular foam radiators, which are self supporting and much cheaper than regular ones.

Comparing the different algorithms for electron identification, the best performance is obtained by the Likelihood, ANN and BDT methods.
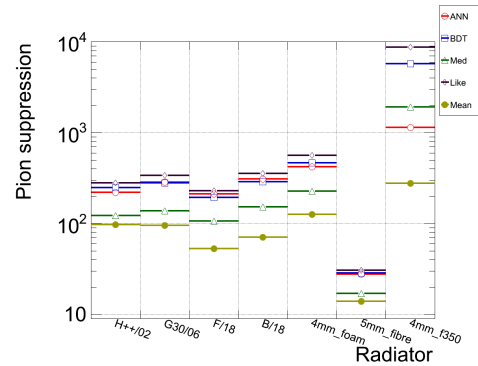
Figure 3: Pion suppression level for different radiator types

References

[1] A. Arend *et al.*, CBM Progress Report 2011, p. 51

[2] C. Bergmann *et al.*, CBM Progress Report 2011, p. 50

[3] E. P. Akishina *et al.*, CBM Progress Report 2009, p. 82

[4] S. Lebedev *et al.*, J. Phys.: Conf. Ser. **396** (2012) 022029

A CBM Time-of-Flight outer wall layout

I. Deppner[1], *N. Herrmann*[1], *P.-A. Loizeau*[1], *C. Simon*[1], *C. Xiang*[1,2], *M. Ciobanu*[3], *J. Frühauf*[3], *M. Kis*[3], *and the CBM-TOF working group*

[1]Physikalisches Institut, Universität Heidelberg, Heidelberg, Germany; [2]Institute of Particle Physics, Central China Normal University, Wuhan, China; [3]GSI, Darmstadt, Germany

The key element providing hadron identification at incident energies between $2A$ and $10A$ GeV is a Time-of-Flight (ToF) wall covering the polar angular range from $2.5°$–$25°$ and full azimuth [1]. The ToF wall is subdivided into different regions covered by different counters arranged in super modules (SM). In this report, a possible layout of the outer wall is presented.
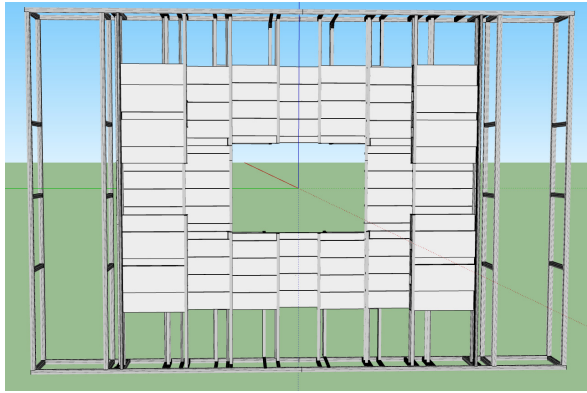
Figure 1: 3-D drawing of the outer CBM ToF wall as designed for the start version of CBM. For details see text.

Figure 1 shows a 3-D drawing of the outer part of the ToF-wall, designed for the starting phase of CBM. In the start version of CBM it is planned to locate the wall 6 m downstream of the target. Upon completion of SIS-300, the wall will be extended and relocated to 10 m downstream from the interaction point, which demands flexible positioning of the counter elements. The main frame (15 m $\times$ 10 m) is designed in such a way that it is usable for both positions, which minimizes the cost for the upgrade substantially. The SMs are mounted on commercial bars made of aluminum profiles running in vertical direction, which allows for shifting of the SM in this direction (see Fig. 1). The bars placed in front of the active detector material have a typical radiation length of about 6 %. The bars carrying most of the load are placed behind the active detector material. The outer wall is built from two types of SMs only: s small SM of size 1800 mm $\times$ 490 mm $\times$ 100 mm and a big SM (1800 mm $\times$ 740 mm $\times$ 130 mm). Hence the cost for development and production is reduced. In addition, the same size of the SM allows a better and more compact staggering in order to avoid holes in the acceptance.

Both types of SM are constructed in the same way. The SM boxes are made of aluminum. The counters mounted in the small chamber are staggered in two ways. For the central column of the wall, the staggering of the RPCs is done symmetrically in an alternative fashion. In the other columns, the counters are tilted with respect to the beam by a certain angle and overlap like roof tiles. The preamplifier cards [2, 3] carrying 2 PADI chips each are mounted inside the super modules directly to the readout electrode of the counter in order to improve shielding and thus stability. The discriminated signals are transmitted via twisted pair cables to a multilayer PCB acting as a feed-through. The outer side of the PCB contains connectors in which the TDC (GET4 or FPGA-TDC) can be plugged. A data collector board combining all TDCs sends the data via glass fiber cable to a FPGA-based pre-processing board. This solution decreases the amount of cables leaving the wall tremendously.

The super modules are based on two types of counters only: a small RPC (27 cm $\times$ 32 cm) using low-resistivity glass and a large RPC (53 cm $\times$ 52 cm) using window glass. The dimensions of the active area of the counter modules are compatible with the production limitations of the respective glasses. In order to implement impedance matching with the FEE strip widths of about 7 - 8 mm, a gap number between 8 and 9 and a gap width of 220 μm have to be used, fixing the strip number of the counters to 56 (32) for the large (small) modules, respectively. Some of the technical characteristics are summarized in Table 1. Further detailed information about the performance of the differential strip RPCs can be found in [4, 5].

Table 1: Technical characteristics of the super modules

	small SM	big SM
# of RPCs	5 small RPC	3 large RPC
# of strips	160	168
# of channels	320	336
# of FEE-cards	40	42
total active area	152×27 cm^2	152×53 cm^2
overlap to next SM	h.: 2 cm, v.: 2 cm	h.: 3 cm, v.: 2 cm

References

[1] I. Deppner *et al.*, Nucl. Instrum. Methods **A 661** (2012) S121

[2] M. Ciobanu *et al.*, *PAD-6 and PADI-7, new prototypes for CBM ToF*, this report

[3] J. Frühauf *et al.*, *Hardware development for CBM ToF*, this report

[4] I. Deppner *et al.*, JINST 7 (2012) P10008

[5] C. Simon *et al.*, *RPC test with heavy-ion beams*, this report

RPC test with heavy-ion beams

C. Simon[1], *N. Herrmann*[1], *I. Deppner*[1], *P.-A. Loizeau*[1], *J. Frühauf*[2], *C. Xiang*[1,3], *M. Kiš*[2], *M. Petriş*[4], *M. Petrovici*[4], *and the CBM-TOF working group*

[1]Ruprecht-Karls-Universität, Heidelberg, Germany; [2]GSI, Darmstadt, Germany; [3]Central China Normal University, Wuhan, China; [4]NIPNE, Bucharest, Romania

The Time-of-Flight (ToF) wall of CBM, conceptualized on the basis of high-resolution timing Multi-gap Resistive Plate Chambers (MRPC), is intended to account for concise hadron identification at an unprecedented event rate of 10 MHz. For the layout of the outer wall, strip-MRPCs are foreseen [1]. To explore the performance and limitations of the current design, high-rate tests with GSI/SIS-18 heavy-ion beams irradiating the full surface of a $30 \times 30 \, \mathrm{cm}^2$, fully differential multi-strip MRPC demonstrator [2] were performed in the fall of 2012. In order to test the equipment under realistic conditions, data were taken from several heavy-ion reactions Kr+Pb, Ni+Pb and d+Pb at beam energies of $1A - 2A$ GeV with particle fluxes on the detector surface between $50 \, \mathrm{Hz/cm}^2$ and $20 \, \mathrm{kHz/cm}^2$. In this report, we present preliminary results from the Ni+Pb beamtime in early November 2012, where the incident particle flux amounted to $\sim 50 \, \mathrm{Hz/cm}^2$.

The test beam setup (Fig. 1) consisted - looking downstream - of a diamond start counter, the target, two plastic counters of size $2 \times 2 \, \mathrm{cm}^2$ for cross checks, the MRPC demonstrator and a reference MRPC constructed by the Bucharest group [3], enabling us to determine the efficiency and timing resolution of the demonstrator against a substantial area ($85 \, \mathrm{cm}^2$) of the reference counter.
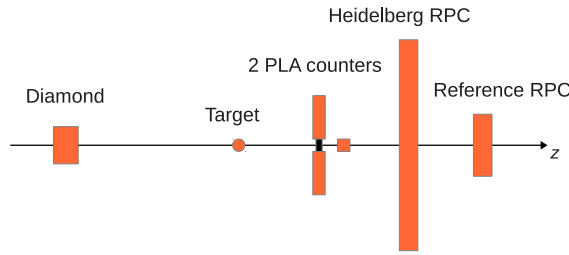
Figure 1: Testbeam setup in November 2012

A calibration scheme, based on ROOT and Go4 and adjusted to the layout of the prototype, is currently under development [4]. First, hits are built and clustered in both the demonstrator and the reference counter. A matching algorithm then assigns the geometrically most suitable pendant in the demonstrator to clusters originating from one-cluster events in the reference counter. We find that our demonstrator is capable of dealing well with multi-hit exposure (Fig. 2 left), thus facilitating the study of inter-hit dependencies.

Furthermore, we studied the counter response in terms of the cluster size (Fig. 2 right), which averages at about
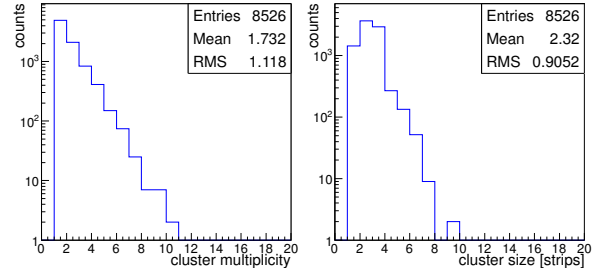
Figure 2: Cluster multiplicity (left) and cluster size (right) of the demonstrator

2.3 strips. On the strip level, we found the resolution of the cluster mean time difference to be $80 \, \mathrm{ps}$ (Fig. 3), which approximately translates into a single-counter timing resolution of $57 \, \mathrm{ps}$ for our demonstrator. This promising result was achieved so far only for the small area ($4 \, \mathrm{cm}^2$) covered by the plastic counters which were requested to have clean conditions. The analysis of the efficiency as function of the hit rate on the counter surface, a task of utmost importance, is in progress.
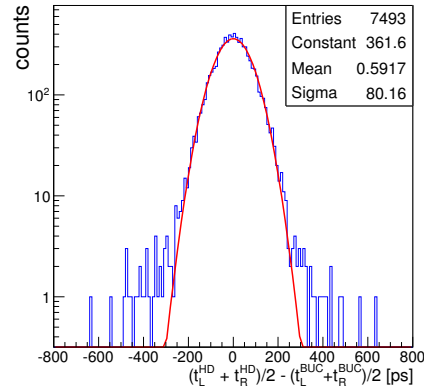
Figure 3: Timing resolution on the strip level

References

[1] I. Deppner *et al.*, *A CBM Time-of-Flight outer wall layout*, this report

[2] I. Deppner *et al.*, CBM Progress Report 2011, p. 57

[3] M. Petriş *et al.*, CBM Progress Report 2011, p. 56

[4] P.-A. Loizeau *et al.*, *Status of the CBM TOF free streaming electronics chain*, this report

Status of the CBM TOF free streaming electronics chain

P.-A. Loizeau[1], N. Herrmann[1], I. Deppner[1], C. Simon[1], C. Xiang[1,2], M. Ciobanu[3], H. Deppe[3], H. Flemming[3], J. Frühauf[3], M. Kiš[3], K. Koch[3], S. Linev[3], S. Manz[4], and the CBM ToF working group

[1]Physikalisches Institut, Universität Heidelberg, Germany; [2]Institute of Particle Physics, Central China Normal University, China; [3]GSI, Darmstadt, Germany; [4]IRI, Goethe-Universität, Frankfurt, Germany

The CBM experiment will have a data acquisition system operating in free-streaming mode for most of its detectors. In the case of the CBM Time-of-Flight (ToF) wall electronics chain, this new readout mode applies first to the Time to Digital Converter (TDC) and then to one or more FPGA based boards acting as Readout Controller (ROC) and Pre-Processor [1], until the input of the computer farm.

A first prototype of this readout chain consisting of the PADI3 and GET4 prototype ASICs and of the Syscore v2 ROC was assembled and tested in beam with Resistive Plate Chamber (RPC) prototypes[2]. Results of these test helped for the development of the GET4 v1.0 chip [3] and new versions of the PCB boards [4].
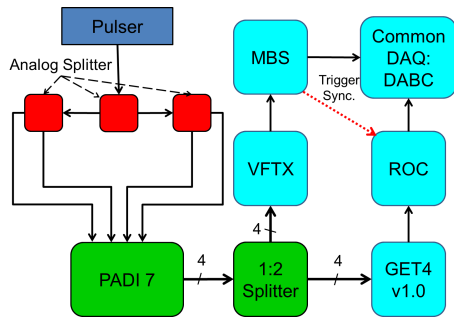
Figure 1: Sketch of the setup used to take pulser data with GET4 and VFTX in parallel.

These new developments were tested in beam with heavy ions at GSI in November 2012 and later in the laboratory with pulser signals. During the beam test, an RPC detector was equipped with PADI6 discriminators and two Plastic scintillators readout by Photo-multipliers (PMT) were equipped with PADI7 discriminators. The signals from the PADI boards were then splitted. On one side they were readout in a MBS/VME based triggered system using VFTX boards [5] as digitizer. On the other side the GET4 v1.0 based free-streaming system was used. Additionally, a signal from the trigger board of the VME system is inserted in the data stream of the free-streaming system. This provides synchronization points between both systems. This also allows a comparison in the free streaming part between an event reconstruction based on using data themselves to detect events and a "triggered-like" event reconstruction. The pulser test is performed by replacing the 4 PMT signals with a single analog splitted pulser signal. A sketch of this setup is shown in figure 1.

The analysis software composed of an unpacker based on the GO4 framework and ROOT macros is now the same for the triggered and free streaming systems. A class for the VFTX unpacking and calibration and a class for the GET4 v1.0 unpacking and event building are feeding the same classes describing the detectors hits and clusters. The data taken in parallel can also be merged in a single output event using the event index sent from the triggered system to the free-streaming system. This allows direct comparison of the results, in particular time difference distributions, obtained with the two systems.
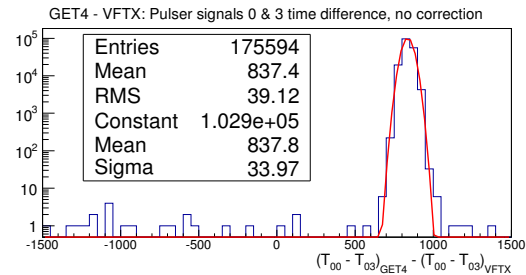
Figure 2: Example of a VFTX to GET4 comparison with pulser signals.

In the pulser test, the time differences between each pair of signals in each system are fitted with gaussian distributions. The difference between the time differences obtained in each system is also computed and fitted with a gaussian. Figure 2 shows an example of timing performances comparison between VFTX and GET4 based systems for the pulser test in the laboratory. Table 1 presents the mean sigma of the 6 possible signal combinations for each TDC and for their comparison.

	σ[ps]
PADI7 + VFTX	17.5
PADI7 + GET4	27.5
GET4 - VFTX	34.5

Table 1: Mean sigma of the Gaus fit for each distributions in the pulser test for a 20mV pulse and a 150mV threshold.

References

[1] C. Xiang *et al.*, *The online data pre-processing for CBM-TOF*, this report

[2] P.-A. Loizeau *et al.*, CBM Progress report 2011, p. 59

[3] H. Flemming *et al.*, *GET4 1.0*, this report

[4] J. Frühauf *et al.*, *Hardware Development for CBM ToF*, this report

[5] J. Frühauf *et al.*, *VFTX (VME-FPGA-TDC 10ps)*, this report

Hardware Development for CBM ToF

J Frühauf[1], N Herrmann[2], M Ciobanu[3], H Flemming[1], H Deppe[1], P. A Loizeau[2], and I. Deppner[2]

[1]GSI, Darmstadt, Germany; [2]Universität Heidelberg, Germany; [3]ISS, Bucharest, Romania

The CBM-ToF-Readout-Chain is based on preamplifier and discriminator ASICs (PADI)[1] and event-driven TDC ASICs (GET4)[2] as front-end electronic. These ASICs are specially developed for the CBM-ToF detector.

For the preamplifier it is necessary to go nearby to the RPC to reach the best performance. Therefore it is decided to go even inside of the RPC-GAS-Box with the preamplifiers for the outer part of the ToF-Wall. Here we have a direct connection from the RPC to the FEE. The PCB layout was done in a way that there is one baseboard for power distribution, SPI-DAC-interface and connector for the output signals and OR signals from PADI. Each add-on PCB is equipped with two PADI-ASICs and the connector for the RPC.
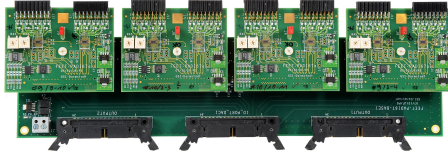
Figure 1: PADI-FEE (32 Channel)

Two single ended pulses are injected into two input channels of PADI. The measurement was done for different signal amplitude as well as the threshold level of PADI was modified. The LVDS output signal was measured with an oscilloscope (Tektronix TDS6154C). The results of this measurement are shown in figure 2. The resolution be-
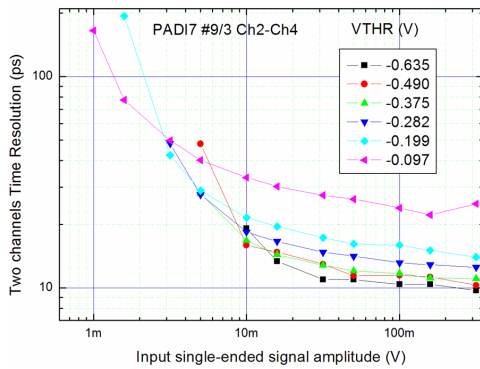
Figure 2: Resolution between two channels

tween two channels for input signal amplitudes between 10mV and 100mV at different thresh-old values is below 20ps, which fulfils the CBM-ToF requirements.

The test PCB for the GET4 1.0 ASIC is shown in the following picture. The main goal of this design is to test on board clock and power distribution, different supply voltages (5V; 12V and 48V) as well to test the new ASIC. One baseboard (Figure 3) can be equipped with four add-on PCBs, where each of them is equipped with four GET4 ASICs. On the left side of the picture the four add-on PCBs
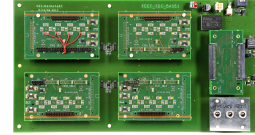
Figure 3: GET4-FEE (64 Channel)

are seen. In the upper right corner the different power injections and in the lower right corner the two clock inputs as well as the sync signal input send out by CLOSY[3] are placed. In between, although as add-on PCB, the connector for the readout controller is placed.

The result of a pulser test in the laboratory is depicted in figure 4. The same LVDS signal is injected into two chan-
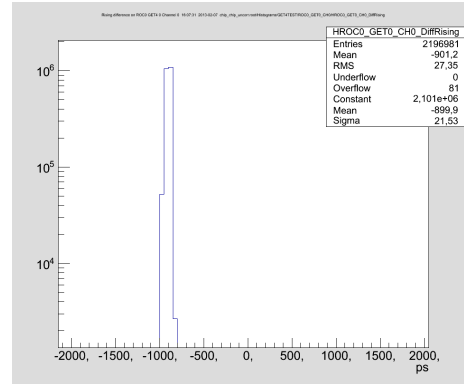
Figure 4: Resolution between two channels

nels of two GET4 ASICs to mark each rising and falling edge with a time-stamp. The resolution between two channels is 27ps.

New frontend cards with specific layouts for each detector as well as test pcbs for the upcoming version of PADI and GET4 will be developed.

References

[1] M. Ciobanu *et al.*, *PADI-6 and PADI-7, new prototypes for CBM ToF*, this report

[2] H. Flemming *et al.*, *GET4 1.0*, this report

[3] K. Koch, GSI Scientific Report 2009, p. 82

Toward a RPC basic structure for the inner zone of CBM RPC-TOF wall

M. Petriş[1], M. Petrovici[1], V. Simion[1], V. Aprodu[1], D. Bartoş[1], A. Bălaceanu[1], G. Caragheorgheopol[1],
F. Constantin[1], V. Duţă[1], L. Prodan[1], A. Radu[1], L. Rădulescu[1], I. Deppner[2], N. Herrmann[2],
P. Loizeau[2], and M.C.S. Williams[3]

[1]NIPNE, Bucharest, Romania; [2]Physikalisches Institut, Universität Heidelberg, Germany; [3]INFN, Bologna, Italy

For the inner zone of the CBM-TOF wall (polar angles between 50 mrad and 220 mrad) we proposed as basic unit a completely differential Multi-strip Multi-gap Resistive Plate Chamber (MSMGRPC) with a new geometry for the readout electrode of 7.1 mm strip pitch (5.6 mm strip width) and 96 mm strip length [1, 2]. With this value of the pitch size, the number of readout channels is reduced to one third of the estimated values of readout channels for the case of considering as basic unit the MGMSRPC with 2.5 mm strip pitch. High counting rate tests performed at COSY-Jülich with a proton beam of 2.5 GeV/c showed that even at 100,000 particles/cm^2·sec, the time resolution is better than 70 ps and the efficiency higher than 90% [2]. Constrained by the available dimensions of low resistivity glass ($\sim$10^{10} Ωcm) [3], the solutions foreseen for the present design is based on glass electrodes of 300 mm x 96 mm size.
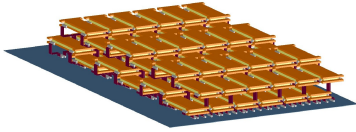
Figure 1: 3D image of RPC cells inside a supermodule

A modular structure divided in eight supermodules (SM) is proposed for the inner region of the CBM-TOF. A continuous coverage of the active area requires a staggered arrangement of RPC cells inside a supermodules and of supermodules, one relative to the other, as can be followed in Fig.1 and Fig.2, respectively.
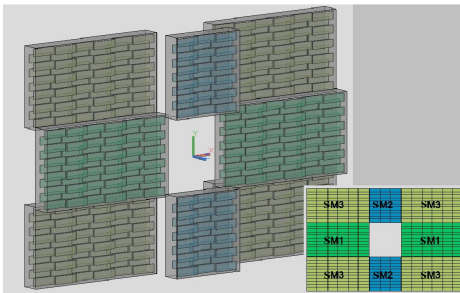
Figure 2: The 8 SM covering the inner wall active area

A demonstrator for the basic architecture of a supermodule contains four identical chambers staggered along (16.5 mm overlap) and across (17.5 mm overlap) the readout strips inside a gas tight box as it is illustrated in Fig3. The RPC cell structure is identical with the one reported in [1, 2].
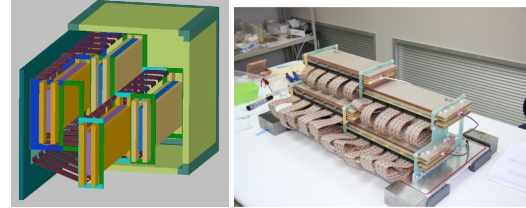
Figure 3: Sketch (left side) and photo (right side) of a basic architecture proposed for the inner zone of the CBM-TOF

The lateral and front walls of the tight gas box are constructed from honeycomb sheets of 10 mm, sandwiched between two stesalit layers of 0.4 mm plated on the inner side by a pcb of 0.13 mm. The back plate, made from aluminum of 12 mm thickness supports the RPC cells. On rectangular openings machined on the plate are glued pcb plates with the connectors, for signal transmission from RPC cells to the front-end electronics.

The in beam test was performed at T9 beam line of CERN PS accelerator with a mixed electron and pion beam of 2 - 8 GeV/c momenta.
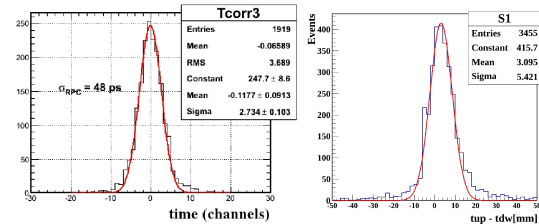
Figure 4: The TOF spectrum (left side); calibrated difference of the times measured at both strip ends (right side)

Figure 4 left side shows the obtained time resolution of 48 ps measured for the overlapping zone along the strips of two MGMSRPC cells, after walk correction, including the electronics contributions. The 5.4 mm position resolution along the strip shown in Fig.4 right side was obtained from the calibrated time difference measured at both strip ends using position information from narrow strip reference RPC [2].

References

[1] M.Petriş *et al.*, CBM Progress Report 2011, p. 56

[2] M. Petrovici *et al.*, JINST **7** (2012) P11003

[3] Yi Wang *et al.*, CBM Progress Report 2010, p. 50

[4] M. Petriş *et al.*, CBM Progress Report 2011, p. 55

ToF-ROC FPGA irradiation tests 2012

S. Manz, J. Gebelein, A. Oancea, H. Engel, and U. Kebschull

Infrastruktur und Rechnersysteme in der Informationsverarbeitung (IRI), Goethe University, Frankfurt, Germany

Ionizing radiation can severely disturb the operation of electronic devices, especially SRAM-based electronics like *Field Programmable Gate Arrays* (FPGAs). The theory of radiation-induced failures is well known, and radiation mitigation techniques have been developed [1, 2]. However, when using commercial off-the-shelf electronics the internal details of electronic circuits are generally not known and the efficiency of the mitigation techniques needs to be tested in experiments before the usage of those electronics can be approved. Here we show the result of a test carried out at the accelerator facility at the FZ Jülich, Germany, in August 2012. Contrary to previous tests, our intention was not to characterize the chip's internal logic cells using an academic test design. We evaluate the efficiency of the radiation mitigation technique *scrubbing* on logic of an actual firmware that is currently used for readout of the GET4 TDC [3]. For characterizing the efficiency we do not use the particle flux as reference but directly count the induced upset rate in the configuration memory of a second identical device in the beam. The firmware itself was running on a Xilinx Virtex-4 FPGA operating directly in a $2\,\mathrm{GeV}$ proton beam at a particle rate in the order of $10^7\,\mathrm{s}^{-1}\mathrm{cm}^{-2}$.
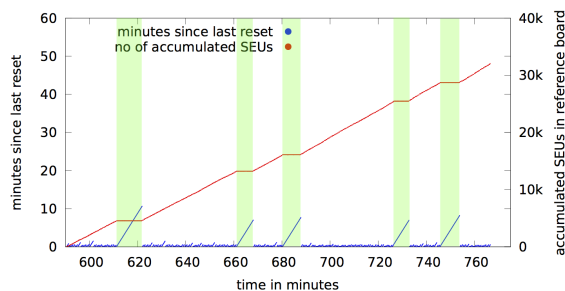
Figure 1: Number of SEUs collected in the reference board (red) and time since the last full reset of the setup (blue) with scrubbing disabled. Every return-to-zero of the blue curve refers to an unrecoverable failure of the setup caused by radiation. A full reset of the setup is required in less than a minute. The setup is only stable when the beam is turned off for technical reasons (highlighted time periods).

Figures 1 and 2 show a direct impression of the values recorded during the beam time. Both diagrams show the results of a three hours run, where scrubbing is disabled (Fig. 1) and enabled (Fig. 2). The in-beam tests showed very promising results when using the *scrubbing* technique on an operational detector read-out firmware. The dead time of the device could be reduced by almost a factor of

50, and corrupted data could be reduced by a factor of 200 while the ressource utilization increased by less than a factor of two.
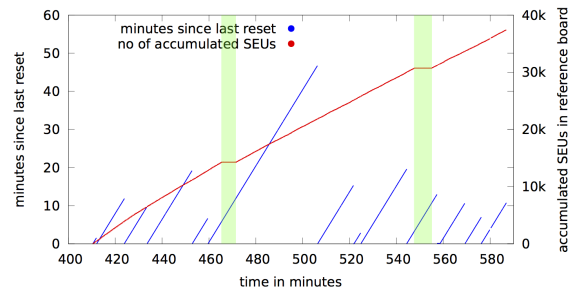
Figure 2: Same as Fig. 1, but with scrubbing enabled. The setup runs stable for several minutes.

From the high efficiency of the configuration scrubber, we conclude that an FPGA-based read-out controller for the CBM-ToF front-end electronics is absolutely feasible. For the real CBM experiment the occurrence of an SEU needs to be logged directly in the data stream for data analysis. A concept for doing so needs to be developed and experimentally approved, also considering new possibilities that emerge with the Xilinx series 7 FPGAs [4].

References

[1] H.Quinn *et al.*, *An Introduction to Radiation-Induced Failure Modes and Related Mitigation Methods For Xilinx SRAM FPGAs*, in: Proc. Engineering of Reconfigurable Systems and Algorithms (ERSA) 2008, CSREA Press 2008, p. 139

[2] M. J. Wirthlin, *FPGAs Operating in a Radiation Einvironment: Lessons Learned from FPGAs in Open Space*, JINST **8** (2013) C02007

[3] H. Flemming and H. Deppe, *The GSI event-driven TDC with 4 channels GET4*, IEEE Nucl. Sci. Symp. Conf. Rec. 2009, 295

[4] *7 Series FPGAs Configuration User Guide, UG470 (v1.5)*, Xilinx Inc, 2012

The GSI Event driven TDC GET4 V1

H. Flemming and H. Deppe

GSI, Darmstadt, Germany

In 2009 results of a first test design of the GET4 TDC ASIC have been obtained[1]. In the meantime additional analysis of the behavior of this ASIC in beamtimes as well as the submission of two test chips to improve the linearity of the TDC core have been done. Based on these activities in march 2012 the first fully equipped GET4 V1 was submitted to the IC foundry.
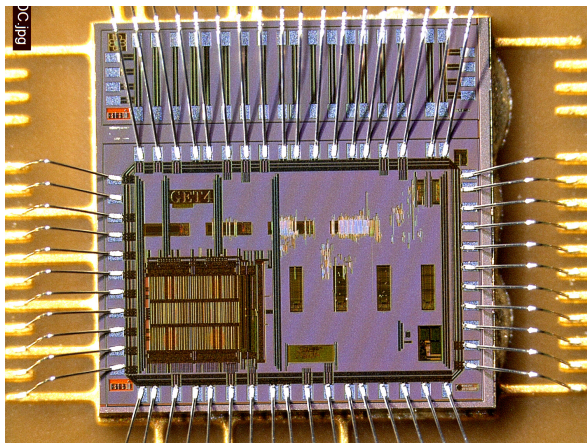
Figure 1: Die picture of the GET4 ASIC.

The full custom designed TDC core of the GET4 V1 is based on the same architecture as the one of the first GET4 ASIC but is improved in many details. The TDC core is visible on the lower left side of the die picture in figure 1. The readout logic of the GET4V1 is completely new developed and automatically synthesised from a vhdl code. It contains a 24 bit readout mode that is compatible to the old GET4 ASIC and a new 32 bit mode that can cope with higher event rates. The 32 bit mode provides an internal time over threshold calculation and more slow control information. More information about internal structure, programming and data format can be found in the ASIC documentation[2]. The tests and measurements of the GET4 V1 could confirm the good results of previous test chips. Figure 2 shows a pulse width spectrum and a time difference spectrum of a test signal generated with an internal test pattern generator. The width of the time difference peak is 27.9 ps rms. After division by $\sqrt{2}$ one gets an uncorrelated time resolution of 19.7 ps for time differences. As the pulse width measurement contains the jitter of the internal ring oscillator as additional error contribution the result is slightly worse than the resolution for the time difference.
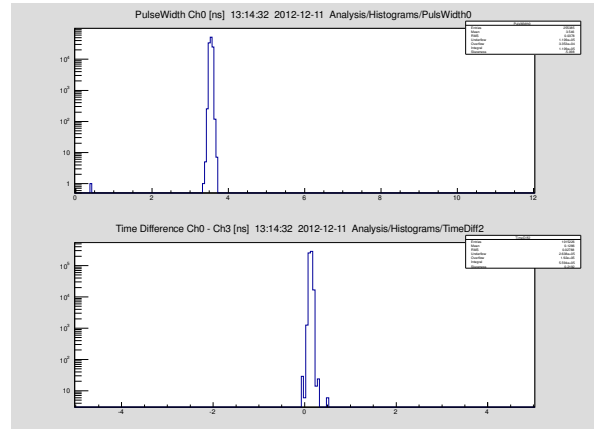
Figure 2: Pulse width and time resolution spectra.

Beside the very good TDC performance during tests also a few bugs have been found[3]. These bugs have been corrected in the design and on February 11th, 2013 a second iteration of this ASIC has been submitted to the foundry. This chip is expected to be produced in May. So for a new beam test campaign end of 2013 a bug fixed GET4 V1.2 will be available. In parallel the development of a programmable readout controller[4] will be continued with the second prototype that now fits to the 32 bit readout mode of the GET4 V1, delivered in February 2013. Tests will start in spring 2013.

References

[1] H. Deppe and H. Flemming, CBM Progress Report 2009, p. 48

[2] H. Deppe, and H. Flemming, *The GSI Event driven TDC with 4 Channels GET4 Version 1.20*, `http://wiki.gsi.de/pub/EE/GeT4/get4.pdf`

[3] H. Flemming, *Results of GET4 Tests, Known Bugs and Performance*, `http://wiki.gsi.de/pub/EE/EEMeetVortragArch/GET4V1.10Bugs.pdf`

[4] H. Flemming and J. Frühauf, *A CPU Controlled SEU Hardened Readout Controller for the GET4 TDC Readout*, GSI Scientific Report 2011, p. 254

VFTX - a VME module for high accuracy timing measurements

J. Frühauf, J. Hoffmann, E. Bayer, and N. Kurz

GSI, Darmstadt, Germany

For high accuracy timing measurements the VME-Module VFTX (Figure 1) has been developed at GSI Experiment Electronic Department. It has an FPGA based TDC design using the tapped delay line method [1].
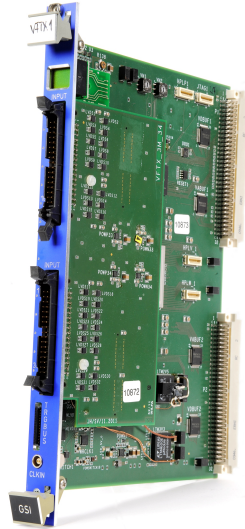
Figure 1: VFTX Module

The VFTX can handle up to 32 LVDS input signals or with a different add-on pcb 16 NIM signals. Available programs are:

- 16 Channel 7ps (leading edge)

- 32 Channel 10ps (leading edge)

- 28 Channel   10ps with time over threshold information (leading edge and trailing edge)

An external clock input allows having more than one module running on the same clock. An external reset Input and a reset command via VME command assures that the modules clock counter are reset at the same time. Due to that there is no need of a reference signal in each TDC and no loss of $\sqrt{2}$ in resolution. The readout of this module is trigger based and the used data acquisition is MBS (Multi Branch System).

Figure 2 shows a simplified block diagram of the test setup in the laboratory. In grey the clock generator CLOSY [2] with the clock distribution can be seen. In orange the signal generator with the signals splitter, to have 10 times the same input pulse available. The blue blocks are the VME modules VFTX and the necessary modules for MBS readout. The LEVCON (Level-Converter) is used for sending out the trigger in different levels.
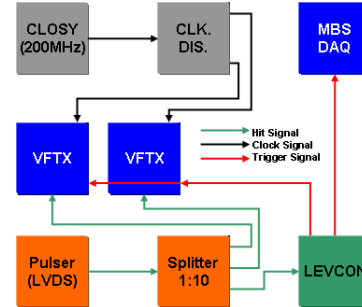
Figure 2: Block diagram Pulser Test.

The result of this measurment are despicted in Figure 3. On the left side of the picture the time resolution for a 28 channel (TOT) design with 9.5ps and on the right hand side the time resolution for a 16 channel design with 6.6ps time resolution are shown. These two results are measured both on the same VFTX module.
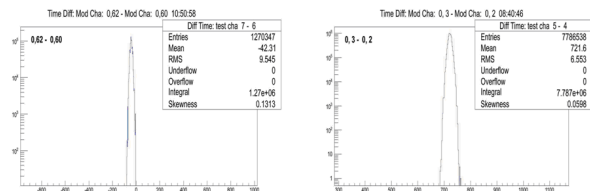
Figure 3: Time resolution between two channels.

Measurements between two VFTX modules have a resolution of 12ps for a 10ps design and 9ps for a 7ps design between two channels. This loss of 2ps is due to the clock splitter, which provides the master 200MHz clock for the different modules.

The VFTX Module shows nice result in the laboratory tests and was already used successfully in beam by the CBM-ToF Group for RPC readout. New hardware for direct connection to the RPC Box with a non-triggered readout is under developement.

References

[1] E. Bayer and M. Traxler, *Development of a High-Resolution (<10 ps RMS) 32-channel TDC in a Field-Programmable-Gate-Array*, GSI Scientific Report 2009, p. 325

[2] K. Koch, *CLOSY: A very Precise Clock Generation for Timing Measurements and Synchronization of the CBM ToF Wall*, GSI Scientific Report 2009, p. 82

PADI-6 and PADI-7, new ASIC prototypes for CBM ToF

M. Ciobanu[1], *N. Herrmann*[2], *K. D. Hildenbrand*[3], *M. Kiš*[3], *A. Schüttauf*[3], *H. Flemming*[3], *H. Deppe*[3], *J. Frühauf*[3], *P. A. Loizeau*[2], *I. Deppner*[2], *and M. Träger*[3]

[1]ISS, Bucharest, Romania; [2]Universität Heidelberg, Germany; [3]GSI, Darmstadt, Germany

We designed a general purpose PreAmplifier-DIscriminator (PADI) ASIC which can be used as a Front-End-Electronics for Resistive Plates Chambers in future CBM at FAIR. The low power PADI-chip can be used for different flavors of RPC's, with strip / pad like anode structures. These timing devices have signal rise times t_R<300ps and primary charges in the range of 10 to 500fC, which needs a preamplifier-discriminator stage with an intrinsic electronic resolution of σ_{t_E}<15ps. We developed and tested different 4 channels prototypes in CMOS 0.18m technology [1, 2] with the following key design parameters: fully differential using a 50Ω input impedance at a preamplifier gain of G_p >100 with a bandwidth of BW_p >300MHz having a peaking time for the signal of t_{p_k} <1ns and a noise related to input of V_{N-IN} <25V_{RMS}. We use a DC feedback loop for offset and threshold stabilization; the threshold range is between +/- 500mV. As auxiliary functions PADI offers an OR-out. For the last prototypes, the increase of the charge responsivity and the decrease of the DC offsets were the main tasks. The Monte Carlo simulation shows that the preamplifier schematics must be drastically changed (Fig.1)
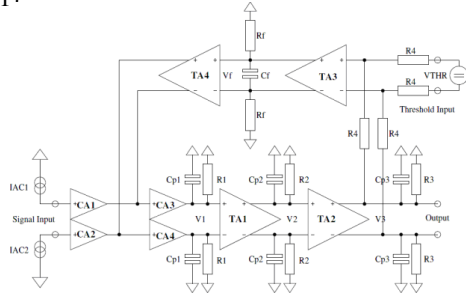
Figure 1: The simplified ac schematic of the preamplifier.

The feedback path is now unique for signals and threshold voltage. The whole schematic can be evaluated like a full differential operational transconductance amplifier (OTA), having two inputs (VTHR and Signal) and one output. The resistive feedback realized with 4 identical resistors (R4) assure a linear DC transfer function. Except Rf, all resistors in schematic are physical resistors like in PADI-1. This solution achieves a maximum preamplifier bandwidth with good Monte Carlo results in matching of components or taking into account the technological dispersions. The threshold voltage is obtained from a DC bridge realized by 6 resistors R. This bridge is supplied from VDD and can be controlled internally by two 10 bits DACs (PADI-6) or externally (PADI-6 and PADI-7), by a

potentiometer connected between VREF+ and VREF- pads and having the cursor at ground potential. These pads are common for all channels and one potentiometer can control all channels. The two DACs (PADI-6) are complementary commanded and the common mode voltage is not affected by the DAC code value. We have changed the type of the interface from I2C to the very often used SPI (Serial Protocol Interface) which is more simple and robust [3]. The SPI interface is currently used in many types of microcontrollers (e.g. the PIC family) and the implementation of PADI test equipment will be easier. In Fig.2 the simulated transient response of the new preamplifier to the input charge 1-2048 fC is shown, in Fig.3 the measured time resolution between two channels excited by the same signal (1- 300 mV), for different threshold voltages.
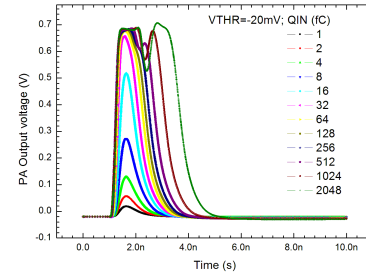
Figure 2: Simulation: PADI-6,-7 charge responsivity.
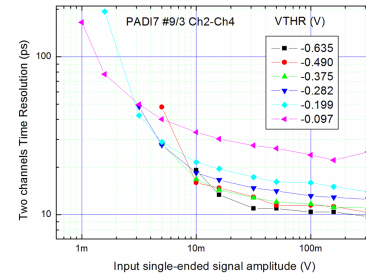
Figure 3: Measurement: Two channels time resolution versus input signal amplitude dependence to VTHR.

References

[1] M. Ciobanu *et al.*, IEEE Nucl. Sci. Symp. **N30-18** (2008) 2018

[2] M. Ciobanu *et al.*, IEEE Nucl. Sci. Symp. **N13-44** (2009) 401

[3] J. Frühauf *et al.*, *Hardware Development for CBM ToF*, this report

Development of extreme high-rate timing ceramics RPCs

A. Laso Garcia[1], J. Hutsch[1], B. Kämpfer[1], M. Kaspar[1], R. Kotte[1], L. Naumann[1], M. Sobiella[1],
D. Stach[1], C. Wendisch[1], and J. Wüstenfeld[1]

[1]Helmholtz-Zentrum Dresden-Rossendorf, Germany

Recent progress on development of ceramics RPCs has pushed the rate capabilities of this detectors to new frontiers. Different prototypes developed with semiconductor SiC/Si_3N_4 composites have been built and their performance under high irradiation was studied. These detectors are four gap RPCs with $250\mu m$ gap width. The active surface is $20\times20\,cm^2$. The tests have been performed with 30 MeV electrons at the ELBE facility at HZDR and 2.5 GeV/c protons at COSY at FZ-Jülich [1, 2, 3].

The beam at ELBE had a beamspot of approximately 20 cm^2 calculated as $FWHM_x \times FWHM_y$ where the parameters were extracted from the time difference spectrum in the RPC. The detector was aligned such that the center part was the most irradiated one. The efficiency and time resolution dependence on the flux and field strength is shown in Figures 1 and 2. It is shown that the efficiency remains higher than 80% for fluxes up to $40\times10^3\,cm^{-2}\,s^{-1}$ for the highest electric field in the gap. At the same time the time resolution remains below 70 ps. The time resolution shown here corresponds to the combination RPC+FEE. Although the efficiency appears to be low for the CBM ToF requirements, it is important to note that this result has been achieved with a four gap RPC. Increasing the number of gaps will increase the efficiency.

The cluster size, or average number of strips simultaneously fired by an avalanche has been calculated. In Fig. 3 the cluster size dependence on the electric field in the gas gap is presented. In this figure, the average value and the RMS of the distribution is plotted. The cluster size for this prototype ranges from 1 to 4, which translates in the large RMS shown. However, the average cluster size increases from 2 to 2.4 when the electric field in the gas gap is increased.

A new prototype, fully differential six gap ceramic RPC is in development. It is planned to be tested at ELBE in May 2013.

References

[1] L. Naumann et al., NIM **A 628** (2011) 138

[2] L. Naumann et al., NIM **A** 635 (2011) 113

[3] A. Laso Garcia et al., JINST **7** (2012) 10012
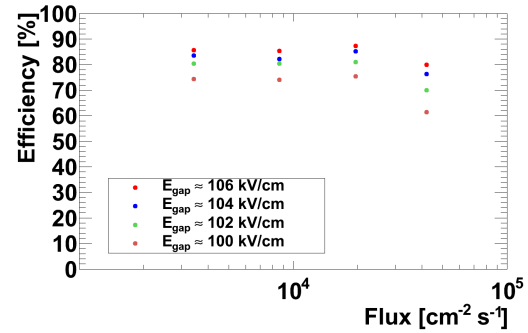
Figure 1: Efficiency dependence on the flux for different electric fields.
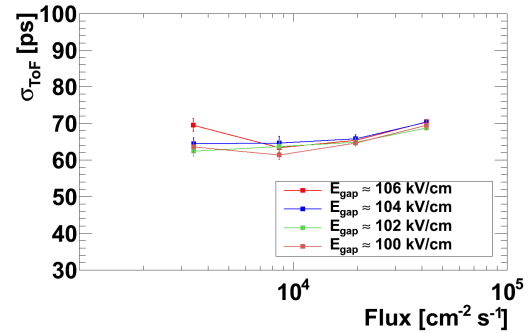
Figure 2: Time resolution dependence on the flux for different electric fields.
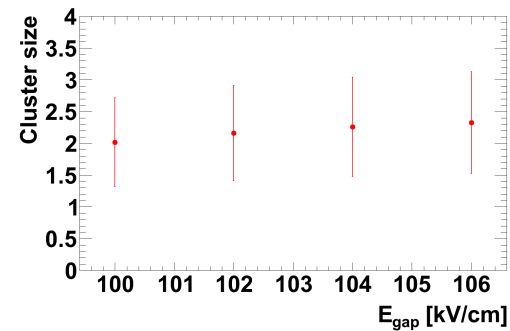
Figure 3: Cluster size dependence on the electric field in the gas gap.

Aging effects on low-resistive high-rate ceramics RPCs

A. Laso Garcia[1], A. Akindinov[2], J. Hutsch[1], B. Kämpfer[1], M. Kaspar[1], R. Kotte[1], D. Mal'kevich[2],
L. Naumann[1], A. Nedosekin[2], V. Plotnikov[2], M. Sobiella[1], D. Stach[1], K. Voloshin[2], F. Wagner[3],
C. Wendisch[1], and J. Wüstenfeld[1]

[1]Helmholtz-Zentrum Dresden-Rossendorf, Germany; [2]Institute for Theoretical and Experimental Physics, Moscow,
Russia; [3]Technische Universität München, FRMII, Germany

During the last years, RPCs built with Si_3N_4/SiC ceramics electrodes have been proven to be able to operate under high irradiation conditions [1, 2]. Further tests have been performed to determine radiation hardness of neutron exposure on the ceramics material. Two probes of $5{\times}5\,cm^2$ have been exposed to non-ionizing radiation doses in the order of $10^{13}\,n_{eq}$/cm^2 at the neutron beam of the MEDAPP facility of the FRM II. This dose is what has been calculated for one year of CBM operation for the STS exposure region and two orders of magnitude higher than the one expected for the ToF ($10^{11}\,n_{eq}$/cm^2/year) [3]. The bulk resistivity of both probes was measured before and after the irradiation. A factor 2 decrease of the bulk resistivity has been observed. This decrease is not a problem for efficiency and time resolution. Further studies are planned to improve our understanding of this effect. Previous studies of irradiation of Al_2O_3 ceramics with up to 10^{15} neutrons/cm^2 showed no changes in the material except for a color change from white to yellow on the substrate [4].

A new special kind of ceramics RPC has been developed in collaboration with the Institute of Theoretical and Experimental Physics (ITEP) in Moscow. This prototype is a two gap RPC with the floating electrode built of HZDR ceramics with a bulk resistivity in the order of $10^9\,\Omega$ cm. However the outer electrodes are Al_2O_3 ceramics with a Cr layer evaporated on one side, a groove separates the Cr evaporated surface from the edge of the Al_2O_3 ceramic (Figure 1). Thus the electric field at the edges is reduced by simply separating the edges of the HV applied surface and the floating electrode. This structure minimizes the leakage current formed by discharges at the edge of the detector. A drastic decrease of the current has been observed: from tenths of nA/cm^2 on a normal two gap structure to less than 5 nA/cm^2 on the grooved structure. In addition this RPC architecture is such, that the gas is forced to flow directly through the gas gaps in opposition to normal RPCs were the flow of gas through the gaps is due to diffusion. However, during operation the formation of whiskers or small polymer filaments was observed (Figure 2). This small whiskers grew as much as one third of the gas gap increasing the electric field in that region and creating sparks in the detector. This effect is due to iButane. After removal of iButane from the mixture no whiskers were observed. Also, the efficiency was measured during a beam test at ELBE in November 2012, shown in Fig. 3.
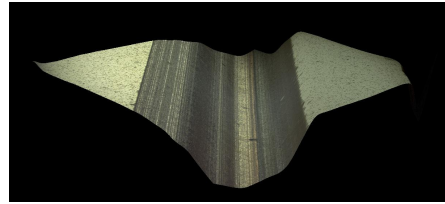
Figure 1: Groove separating the Cr evaporated surface from the edge of the Al_2O_3 ceramic.
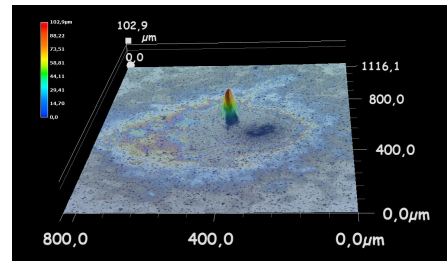
Figure 2: Polymer growing on the cathode. The height reaches up to $100\,\mu$m.
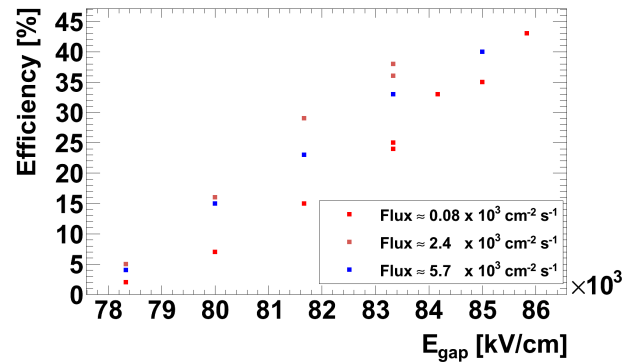
Figure 3: Efficiency dependence on electric field in the gas gap for different fluxes for a two gas gap RPC with gap size of $300\,\mu$m.

References

[1] L. Naumann et al., NIM A 635 (2011) 113

[2] A. Laso Garcia et al., JINST 7 (2012) 10012

[3] A. Senger, CBM Progress Report 2011

[4] A. Arefiev et al., NIM A 373 (1996) 43

Performance of real-size MRPC modules based on low-resistive glass

J. Wang and Y. Wang

Department of Engineering Physics, Tsinghua University, Beijing, China

In the current CBM conceptual design, the whole TOF wall is arranged in four 'rate regions' [1]. In the inner region of the wall (region 1), pad readout MRPCs based on low-resistive glass can be efficiently used to cope with the high particle flux (up to 25kHz/cm^2) at an optimal segmentation (4–6 cm^2 per pad), while strip-readout MRPCs represent a natural choice for the outer region (0.5-8 kHz/cm^2) where the system occupancy and flux are orders of magnitude lower.

Recently, at Tsinghua University, we have managed to develop a stable production line of a new type of low-resistive doped glass. Following the encouraging results obtained with small-area MRPC prototypes based on this material [2], two real-size MRPC modules were produced in order to suit the current design of the CBM-TOF wall. The basic structures of the two modules are depicted in Fig. 1.

The pad-readout MRPC has 10 gas gaps and consists of two (mirrored) stacks of plates made of 0.7 mm-thick low-resistive glass plate with a resistivity of about 2×10^{10} Ωcm. It has 6×2 pads of size 2 cm×2 cm each, with an interval between pads of 2 mm. The gas gap is 0.22 mm. The high voltage electrodes are covered with colloidal graphite spray, yielding a typical surface resistivity of about 2 MΩ/sq.
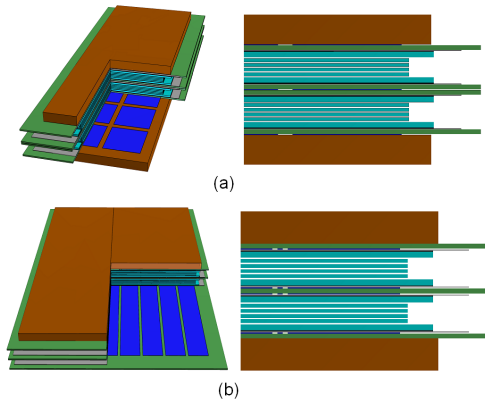
Figure 1: Real-size MRPC modules

As compared to the pad-design, the strip-counter has slightly larger gaps of 0.25 mm. The readout strips have 12.5 cm length and 2.2 cm width. The intervals between the strips are 3 mm.

The counters have been thoroughly characterized with a 30 MeV electron beam at the Electron Linac with high Brilliance and low Emittance facility (ELBE) at Helmholtz-Zentrum Dresden-Rossendorf (HZDR).The results of HV scans are summarized in Fig. 2.
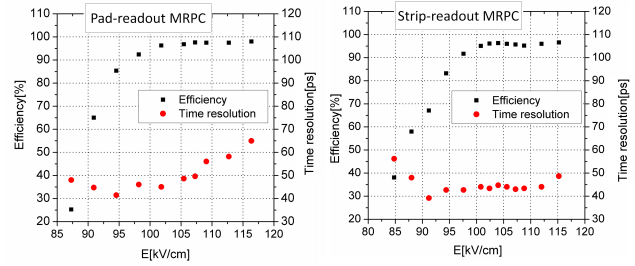
Figure 2: HV scan of the modules

The high-flux behavior of the efficiency and time resolution for the two modules is shown in Fig. 3. The beam shape was determined by the reference scintillators. The flux is defined as the average flux over the considering area [3].
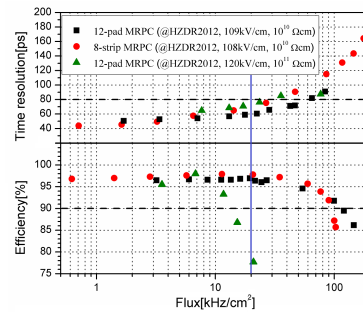
Figure 3: Performances VS average flux

As a summary, the requirements of the CBM-TOF wall have been fulfilled by resorting to real-size pad MRPC modules based on the newly developed Chinese doped glass. The pad counter prototype can run with a tolerable performance degradation up to 55 - 65 kHz/cm^2. An 8-strip RPC shows a rate capability up to 25 - 30 kHz/cm^2. The uncertainty in the quoted flux ranges is related to the uncertainty in the spatial beam profile due to the observed additional broadening by a factor of about 1.2 of the electron beam due to multiple scattering inside the RPC.

References

[1] I. Deppner *et al.*, Nucl. Instrum. Methods **A 661** (2012) 121

[2] J. Wang *et al.*, Nucl. Instrum. Methods **A 621** (2010) 151

[3] J. Wang *et al.*, JINST **7** (2012) P10004

The online data pre-processing for CBM-TOF

C. Xiang[1,2], N. Herrmann[2], P.-A. Loizeau[2], I. Deppner[2], S. Manz[3], J. Frühauf[4], and S. Linev[4]

[1]Key Laboratory of Quark and Lepton Physics (MOE) and Institute of Particle Physics, Central China Normal University, Wuhan, China; [2]Physikalisches Institut, Universität Heidelberg, Germany; [3]Kirchhoff-Institut für Physik, Heidelberg, Germany; [4]GSI, Darmstadt, Germany

The Compressed Baryonic Matter (CBM) experiment will operate a free streaming data acquisition system. In order to optimize the data bandwidth and to achieve high performance, a data pre-processing unit is designed for the readout chain of the CBM-TOF detector and implemented in the ROC firmware [1]. It consists of three modules, a data pre-processing module, a monitor module and a control module [2]. The data pre-processing module (DPM) which is the main part of the unit has two functions, hit building and cluster building, which are designed in two steps (see Fig. 1). As indicated in Fig.1 and as a first step
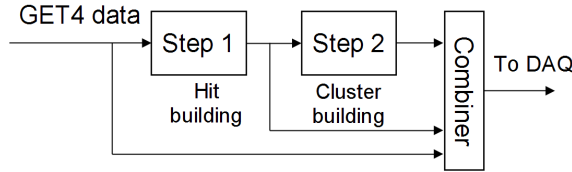
Figure 1: Structure of data pre-processing module

a hit is built from the rising edge and a matched falling edge of the GET4 data [3]. The hit contains the rising edge time stamp and Time-Over-Threshold (TOT) information which is the time difference between the rising and the falling edge. In the second step clusters are built from 8 channels of two GET4 chips which are connected to the two side of 4 neighbouring Resistive Plate Chamber (RPC) strips. A cluster is characterized by the common hit times within a certain time slice and corresponds to a single particle traversing the detector. All the data are combined together and sent to the DAQ for further processing.

	RAW data	DPM data	
Number of data	2.28E+08	1.39E+06	99.4%
Number of hits	967749	967604	0.015%
Number of events	237856	237848	0.003%

Table 1: Data with/without DPM

The data pre-processing module implemented in the ROC firmware was tested at COSY with a proton beam in November 2011 operating on online data of a MM-RPC detector[4]. A possible reduction of the data volume by means of online pre-processing in the DPM is demonstrated in Tab. 1. In the table, the 2nd column *Raw data* is the result of an offline analysis of GET4 data, and the 3rd column *DPM data* is the result of an online analysis including the 1st step of the data pre-processing module. The last

column shows the resulting difference between offline and online analysis normalized to the *Raw data* values. The final reduction of the output data volume depends on the hit rate, because most of the reduction is due to the rejection of the epoch data. In the case of hit rates in the order of 50 Hz per channel, as encountered during the test beam-time, a reduction of about 99.4% was achieved. As shown in table 1, during the test running for about 50 minutes, the DPM lost only 145 hits (0.015%), and only 8 events (0.003%).

The ROC firmware in which cluster building was implemented was tested in the lab in July 2012. Input signals were generated by splitting the signal of a signal generator and fed into a GET4 chip. In principle, the number of *Raw data* of the two channels of the GET4 chip should be equal. As shown in table 2, however, the observed numbers differ (2nd row of the table). After the 2nd step of data pre-processing, eliminating the mismatches, the number of data from both channels are the same. This demonstrates the feasibility to reject single hits in a time slice. Note that this causes no loss of information since single hits are meaningless from a strip detector point of view.

	Chn. 1	Chn. 6
Raw data	2507905	2507991
1st step DPM data	2507243	2507217
Hit lost	0.0264%	0.0309 %
2nd step DPM data	2506236	2506236
Hit lost	0.07%	0.07%

Table 2: Number of obtained hits from different data pre-processing level

These two tests show that the data pre-processing module was fully functional and demonstrate the potential of implementing an on-line inspection of the data. Further features, like threshold self-adjusting can also be done in the readout chain and will be explored in the future.

References

[1] S. Manz, *et al.*, JINST **5** (2010) C11017

[2] C. Xiang *et al.*, CBM Progress Report 2011, p. 60

[3] H. Flemming and H. Deppe, *The GSI event-driven TDC with 4 channels GET4*, IEEE Nucl. Sci. Symp. Conf. Rec. 2009, 295

[4] I. Deppner *et al.*, JINST **7** (2012) P10008

Superconducting dipole magnet for the Compressed Baryonic Matter (CBM) experiment at FAIR

P. Akishin[1], A. Bychkov[1], E. Floch[2], Yu. Gusakov[1], V. Ivanov[1], P. Kurilkin[1], V. Ladygin[1], H. Leibrock[2], A. Malakhov[1], G. Moritz[2], C. Muehle[2], W. F. J. Müller[2], W. Niebur[2], I. Pschorn[2], P. Senger[2], A. Shabunov[1], P. Szwangruber[2], Y. Xiang[2], and C. Will[2]

[1]JINR, Dubna, Russia; [2]GSI, Darmstadt, Germany

The CBM superconducting dipole magnet is a central part of the detector system. The target station and the Silicon Tracking System are placed in the magnet gap. The magnet has to provide a vertical magnetic field with a bending power of 1 Tm over a length of 1 m from the target. A perspective view of the magnet is shown in Fig. 1.

The magnet gap has a height of 140 cm and a width of 250 cm in order to accommodate the STS with a polar angle acceptance of $\pm 25°$ and a horizontal acceptance of $\pm 30°$. The magnet is of H-type with a warm iron yoke/pole and cylindrical superconducting coils in two separate cryostats like the SAMURAI magnet at RIKEN [1, 2]. The potted coil has 1749 turns. The wire, similar to the CMS wire, has Nb-Ti filaments embedded in a copper matrix and is soldered in a copper stabilizer with a total Cu/SC ratio of about 13 in the conductor. The operating current and the maximal magnetic field in the coils are 686 A and 3.25 T, respectively. The coil case made of stainless steel contains 20 liters of liquid helium for one coil. The vertical force in the coils is about 250 t. The cold mass is suspended from the room temperature vacuum vessel by six suspension links. Six cylindrical support struts compensate the vertical forces.

The energy stored in the magnet is about 5 MJ. The magnet will be self-protecting. However, in order to limit the temperature rise to 100 K in case of a quench, the energy will be dumped in an external resistor. The parameters of the magnet are listed in Table 1.

Table 1: Parameters of the magnet

Type	H-type, SC magnet
number of turns	1749 per coil
windings of coil	impregnated close coiling
maximum current	686 A
magnetomotive force	1.2 MA turns/coil
current density	48 A/mm^2
central field	1.08 T
field integral	1 Tm
maximum field at coil	3.25 T
inductance	396 – 150 H
stored energy	5.15 MJ
Coil	
inner diameter	1.37 m (at 4 K)
outer diameter	1.82 m (at 4 K)
cross section	149.2 x 168 mm^2 (at 4 K)
weight	1644 kg/coil
Pole	
shape	circular type
gap	1.4 m
diameter	2.0 m
height	0.5 m
Yoke	
width	4.4 m
depth	2.0 m
height	3.7 m
weight	250 t

Figure 1: View of the CBM superconducting magnet

References

[1] H. Sato *et al.*, *Design of a large-gap superconducting dipole magnet for the SAMURAI spectrometer*, RIKEN Accel. Prog. Rep. **43** (2010) 180

[2] H. Sato *et al.*, IEEE Trans. ASC **23** (2013) 4500308

Design calculations for the superconducting dipole magnet for the Compressed Baryonic Matter (CBM) experiment at FAIR

P. Akishin[1], A. Bychkov[1], E. Floch[2], Yu. Gusakov[1], V. Ivanov[1], P. Kurilkin[1], V. Ladygin[1],
H. Leibrock[2], A. Malakhov[1], G. Moritz[2], C. Muehle[2], W. F. J. Müller[2], W. Niebur[2], I. Pschorn[2],
P. Senger[2], A. Shabunov[1], P. Szwangruber[2], Y. Xiang[2], and C. Will[2]

[1]JINR, Dubna, Russia; [2]GSI, Darmstadt, Germany

Calculations have been performed to design the coil case, the coil vessel, the support links and the quench protection scheme for the CBM superconducting dipole magnet. The general parameters of the magnet are discussed in a separate contribution to this Progress Report. The code TOSCA was used for calculating electromagnetic forces exerted on the coil, while the structural analysis was made using the code ANSYS. The radial and vertical forces F_r and F_y were calculated at 1.08 T with TOSCA as a function of the azimuthal angle of the coil. The radial force points towards the outer direction, while the vertical force attracts the coil toward the iron yoke. The integrated forces along the coil circumference are radially 60 t and vertically 254 t. The ANSYS calculation was based on the results of TOSCA.

Coil case

The coil case is designed considering two main functions: one is to protect the windings against magnetic forces during operation, and the other is to use the case as a container for liquid helium (LHe) to cool the winding. The volume of the LHe in the case is about 20 liters for one coil, including the LHe stored in the current leads box. The case is welded of stainless steel 316LN [1]. The minimal thickness of the case is 20 mm. The steel magnetic permeability is about 1.01 – 1.02. The cross section of the coil has a height of 236 mm and a width of 22 mm. The coil occupies only a part of the internal space of the case. The rest of the space is filled with spacers made of NEMA G10 and an aluminum circular shim (AW6061 or AW3003). In addition, the shim provides good thermal conduction, which allows to distribute the heat load caused by friction if the coil moves or cracks under the Lorentz forces. The large cross section is necessary to have a very rigid structure. The case should transmit huge vertical forces from the coil to the supports. It is supported by six main cylindrical supports and six tie rods. To reduce the heat flux to the helium system, the outer surface of the casing will be wrapped with 10 layers of a multi-layer insulation.

Thermal shield

The thermal shield must have good thermal conductivity and a good ratio of rigidity to weight, and it should be easy to fabricate and assemble. The thermal shield consists of two main pieces: the top shield and the cover. The shield has a radial cut for an electrical break. All pieces are made of copper sheets each 2 mm thick. The forced-flow cryogen for cooling the thermal shield is cold helium gas to intercept thermal radiation from the cryostat. The cooling pipes are made of a 1 mm thick copper tube having a rectangular shape with an outer dimension of 20 mm × 8 mm. To reduce the heat flux to the helium system, the outer surface of the thermal shield will be wrapped with an insulation of 20 layers. The thermal shield is fixed to the main cylindrical supports.

Suspension

The cold mass is suspended from the room temperature (RT) vacuum vessel using 6 support struts and 6 tie rods (Fig. 1 left). These support struts are described as "warm-to-cold" because the warm end is attached to the RT vacuum vessel and the cold end is attached to the cold mass. The suspension during the working cycle has two types of loading. When the magnet is switched off, only the weight of the cold mass is applied to the suspension. In this case the vertical force is about 2000 kg. When the magnet is switched on, the vertical component of the Lorenz forces should be added to the weight of the cold mass. The maximum vertical force in this case is 254 t. The lateral forces should not exceed a few hundred kilograms because of the symmetry of the magnet. The support struts are typically compressed. Only the green parts require pre-compression while manufacturing the CBM dipole magnet. The tie rods will provide this pre-compression. The support struts have a nominal compression force of 42 t [2]. The tie rods are tensed with the force of 500 kg.

The support strut consists of four composite tubes nested coaxially in each other and connected in series by three stainless steel tubes with Z-shaped cross section. The com-
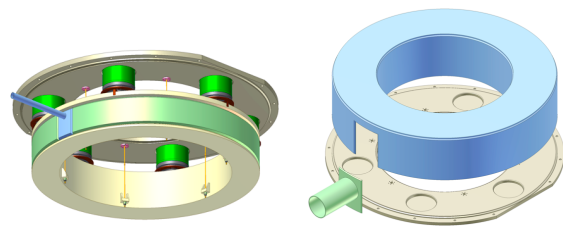
Figure 1: Suspension on the coil (left) and vacuum vessel (right)

posite tubes are polar wound tubes with glass fibers and epoxy resin. The axial winding angle is $\pm 15°$. Few layers have a winding angle of $90°$ to fix the main layers. The glass fiber composite has small thermal conductivity at low temperature. The Z-shape tubes are made of the stainless steel SAE 304. Five layers of MLI are inserted in each gap between the tubes. The middle tube is connected with the thermo shield at a temperature of 80 K.

The tie rods are used to sustain the cold mass and preload the support struts. The tie rods, which are attached on one side to the vacuum vessel and on the other side to the coil case, are subjected to a thermal gradient from 4.5 K till room temperature. The titanium alloy Ti 5Al 2.5Sn has been chosen as tie rod material for its low thermal conductivity and high mechanical strength [3]. The tie rods have spherical hinges on both sides. The hinge attached to the vacuum vessel is fixed with a key. The hinge on the other side has a thread for adjusting. On 1/3 of the length from the vacuum vessel it has a shoulder for a thermo bridge [4].

Vacuum vessel

The vacuum vessel seals the vacuum around the cold mass to allow the cooling system to reach the desired cryogenic temperature. The vacuum vessel consists of a support ring, a shell and a weldolet (see Fig. 1 right). The rest of the parts are made of the stainless steel SAE 304 [1]. The thickness of the shell is 15–20 mm. The support ring is 48 mm thick. All parts of the vacuum vessel will be assembled by welding.

The gap between the spacers is used for the liquid helium circulation. Over the spacers there is a tray made from thin G-10 Glass Epoxy laminate and covered by few layers of fiber glass fabric with epoxy resin with a total thickness of 2 mm. The coil is wound inside this tray. Each layer is insulated with three layers of 0.1 mm fiber glass fabric with epoxy resin. Since the coils and the conductor experience radial and axial forces of a high magnitude, the winding is required to be done at high tension of 20 kg, and the gaps between the turns need to be filled with epoxy resin to restrict the movement of the conductor. This impregnation should be done with a brush. The last layer should be wrapped with six layers of 0.1 mm fiber glass fabric with epoxy resin. Then aluminum banding is carried out around the coil at 200 kg tension for restricting the movement of the conductor and the coil while the magnet is energized. Aluminum banding gives more compressive stress to the coil at 4.5 K as compared to SS because of the higher thermal contraction coefficient. A special grade of aluminum (5052 - H34) strip having high hardness and a tensile strength of 267 MPa is used. The strip has a cross section of 2.5 mm $\times$ 5 mm.

Instantaneous quench

Figure 2 shows the instantaneous quench calculation results [5, 6]. This calculation was done with a constant in-

ductance of 21.9 H (Lw at 686 A). The average temperature is 81 K. The resistance of the quenched pole is $2.6\,\Omega$ and the maximum quench voltage is 737 V. The quench detection and protection scheme is shown in Fig. 3.
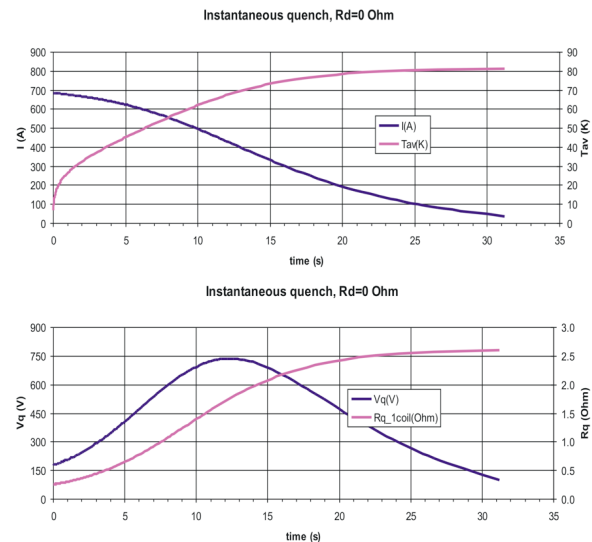
Figure 2: Instantaneous quench calculations for the CBM dipole magnet. Upper panel: magnet current and average coil temperature; lower panel: quench voltage and quench resistance.
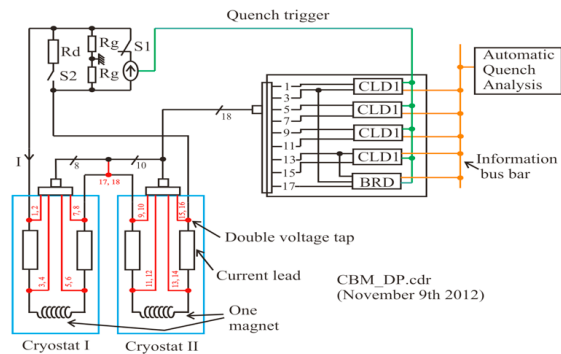
Figure 3: Quench detection and protection scheme (including voltage taps)

References

[1] R. Walsh *et al.*, AIP Conf. Proc. **1435** (2012) 63

[2] T. Kabo (RIKEN), private communication

[3] M. Reytier, F. Kircher and B. Levesy, submitted to Adv. Cryogenic Eng.

[4] B. Cure *et al.*, IEEE Trans. ASC **12** (2002) 872

[5] P. Swangruber *et al.*, Phys. Proc. **36** (2012) 872

[6] E. Floch, GSI F-MT internal note MT-INT-ErF-2009-010

Common CBM beam test of the RICH, TRD and TOF subsystems at the CERN PS T9 beam line in 2012

D. Emschermann[1], J. Adamczewski-Musch[2], A. Arend[3], C. Bergmann[1], C. Garcia[4], N. Heine[1], S. Linev[2], T. Morhardt[2], C. Pauly[5], M. Petriş[6], M. Petrovici[6], W. Verhoeven[1], and J. P. Wessels[1]

[1]Institut für Kernphysik, Münster, Germany; [2]GSI, Darmstadt, Germany; [3]Institut für Kernphysik, Frankfurt/M, Germany; [4]IRI, Frankfurt/M, Germany; [5]Bergische Universität Wuppertal, Germany; [6]NIPNE, Bucharest, Romania

A common beam test of the CBM Ring Imaging CHerenkov (RICH), Transition Radiation Detector (TRD) and Time Of Flight (TOF) subsystems was performed at the CERN Proton Synchrotron (PS) accelerator in October/November 2012. The measurements were carried out at the T9 beam line in a mixed beam of electrons and pions with momenta from 2 to 10 GeV/c. In addition to the above mentioned detectors, the setup consisted of two Cherenkov detectors, two fiber trackers, beam trigger scintillators and a lead-glass calorimeter. The first fiber tracker was placed at the upstream end of the setup, followed by a large-volume RICH prototype, 8 real-size TRD prototypes, 2 TOF detectors and finally the second fiber tracker at the downstream end (see Fig. 1).
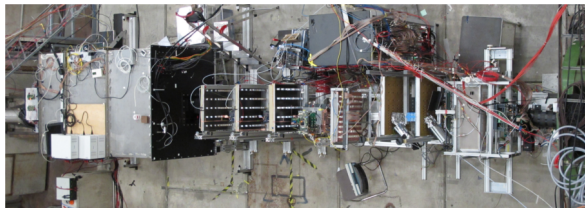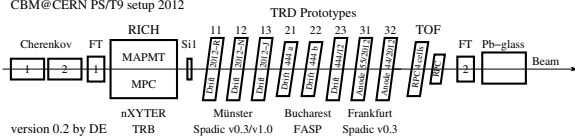
Figure 1: Setup of CBM in the PS/T9 beam line in 2012

The RICH prototype [1] was based on a mirror-focusing setup with CO_2 gas as radiator. The photon camera was composed of 4 micro channel plate (MCP) detectors plus 20 Hamamatsu multi-anode photo-multipliers (MAPMTs). Two concurrent approaches to readout the RICH camera were tested: the traditional triggerless n-XYTER front-end as well as a free streaming approach based on the HADES Trigger and Readout Board (TRB3).

The TRD laboratories in Münster [2], Bucharest [3, 4] and Frankfurt [6, 7] have built real-size (59×59 cm^2) detector modules based on MWPC technology with cathode pad readout. The large size of the TRDs has triggered innovative developments to stabilize the entrance window to the gas volume while minimizing the loss of transition radiation between the radiator and the detection volume. The readout of the Bucharest prototypes was based on the

Fast Analog Signal Processor (FASP) ASIC, either digitized in a VME-based MADC32 or using free streaming MAXIM [5] based converters. The signal processing on the TRD modules from Münster and Frankfurt was performed with the SPADIC v0.3 of 2011. A TRD prototype from Münster served as platform to compare the performance of the FASP, the SPADIC v0.3 and the recently developed SPADIC v1.0 [8, 9]. The latter reads out 32 channels in self-triggered mode and implements the CBMnet protocol on the ASIC. The TRD test program consisted of a systematic study of different radiator prototypes with a Xe(80%)+CO$_2$(20%) gas mixture in the detection volume, as well as beam momentum and high-voltage scans.

Bucharest completed the setup with a segmented TOF prototype, consisting of 4 partially overlapping RPC cells, combined with a single RPC cell reference TOF prototype from 2011. These two TOF modules were again tested using a $C_2F_4H_2$(90%)+SF_6(5%)+iso-C_4H_{10}(5%) gas mixture allowing for fast signal generation.

All prototypes under test were read out in a common hybrid data acquisition system based on MBS and DABC.

References

[1] S. Reinecke *et al.*, *Overview RICH prototype beamtest 2012 at CERN-PS*, this report

[2] C. Bergmann *et al.*, *Test of Münster CBM TRD prototypes at the CERN PS/T9 beam line*, this report

[3] M. Petriş *et al.*, *e/π identification and position resolution of high granularity TRD prototype based on MWPC*, this report

[4] M. Tarzila *et al.*, *Two dimension position sensitive real size CBM-TRD protype*, this report

[5] F. Constantin *et al.*, *FPGA-based freer running mode acquisition for high counting rate TRD*, this report

[6] E. Hellbär *et al.*, *Construction and simulations of full-size CBM-TRD prototypes without drift region*, this report

[7] P. Dillenseger *et al.*, *In-beam performance studies of the first full-size CBM-TRD prototypes developed in Frankfurt*, this report

[8] T. Armbruster *et al.*, *SPADIC 1.0 - a self-triggered amplifier/digitizer ASIC for CBM-TRD*, this report

[9] C. Garcia *et al.*, *Beamtest results of the CBM TRD feature extraction using SPADIC v1.0*, this report

Design of the beam dump for HADES at SIS-100

A. Senger

GSI, Darmstadt, Germany

HADES at SIS-100 will be placed in front of the CBM experiment as sketched in Fig. 1. The beam can be focused either on the target of HADES (left setup) or on the CBM target (right setup). The possibility to run the HADES experiment with the CBM experiment in place was studied using FLUKA [1, 2].
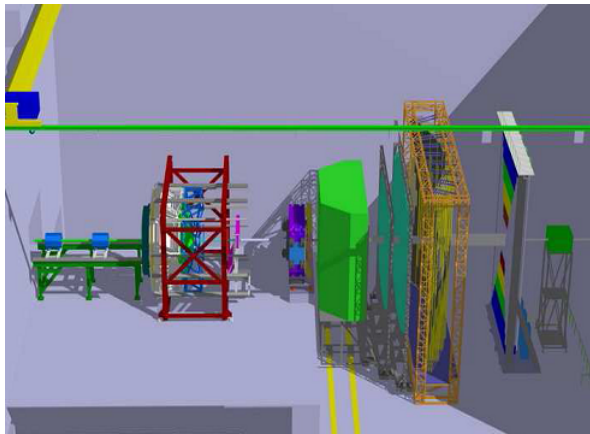
Figure 1: Experimental setup with HADES (left) and CBM (right)

If the beam is focused on the HADES target, the beam size in the CBM Silicon Tracking System (STS) will be larger than the CBM beam pipe. FLUKA calculations have been performed to study the non-ionizing energy loss (NIEL) in the CBM cave for different scenarios. Figure 2 (left) illustrates the NIEL in the CBM cave for Ni+Ni col-
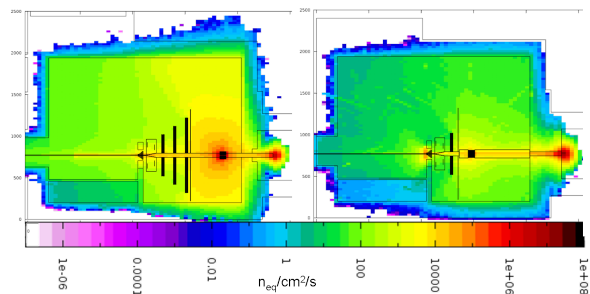
Figure 2: NIEL distributions in the CBM cave during a HADES run of Ni+Ni at 8 GeV/u with an intensity of 10^7 ions per second (left), and during a CBM run of Au+Au at 10 GeV/u with an intensity of 10^7 ions per second (right)

lisions at 8 GeV/u with an intensity of 10^7 ions per second on the HADES target. For comparison, in Fig. 2 (right) the NIEL distribution during a CBM run of Au+Au collisions at 10 GeV/u with an intensity of 10^7 ions per second is shown.

In order to protect the CBM experiment during runs with HADES, a beam dump will be placed in front of the CBM magnet. In a first step, the thickness of an iron beam dump was determined with FLUKA. It was found that a thickness of 1.5 m of iron is sufficient to fully stop the beam. However, the radiation level outside the iron is too high, as shown in Fig. 3 (left). In order to reduce this radiation, an additional concrete shielding was studied. It turns out that the radiation level can be drastically reduced by 50 cm of concrete around the iron core and 150 cm of concrete in front of the iron (see right panel of Fig. 3).
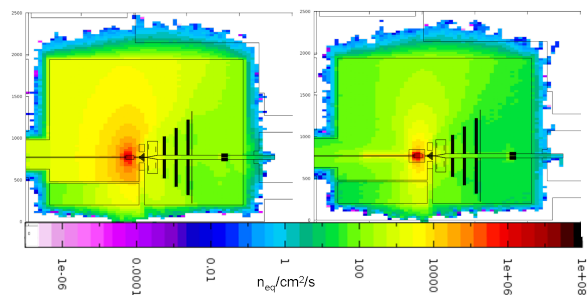
Figure 3: NIEL distributions in the CBM cave during a HADES run of Ni+Ni at 8 GeV/u with an intensity of 10^7 ions per second. Left: with 1.5 m iron as beam dump; right: with additional concrete around the iron (see text).

References

[1] G. Battistoni, S. Muraro, P. R. Sala, F. Cerutti, A. Ferrari, S. Roesler, A. Fasso' and J. Ranft: *The FLUKA code: Description and benchmarking*, in: Proceedings of the Hadronic Shower Simulation Workshop 2006, Fermilab 6-8 September 2006, M. Albrow, R. Raja (eds.), AIP Conference Proceeding **896** (2007) 31

[2] A. Fasso', A. Ferrari, J. Ranft and P. R. Sala: *FLUKA: a multi-particle transport code*, CERN-2005-10 (2005), INFN/TC_05/11, SLAC-R-773

A reaction detector for CBM

P. Koczoń

GSI, Darmstadt, Germany

A detector placed around the target outside of the CBM acceptance ($\theta > 25°$), registering reaction products of Au+Au @ $10A$ GeV and p+C @ 30 GeV interactions, was simulated. Equipped with a simple signal summing-up and threshold electronics, such a reaction detector (RD) can distinguish between central, minimum bias and empty reactions in case of Au+Au and can deliver a "time zero" signal for TOF measurements even for p+C reactions.

A detector in form of a ring consisting of eight trapezoidal tails installed side by side (as depicted in Fig. 1), covering polar angles from 30 to 60 degrees and the full azimuthal angle, was investigated in the framework of the FairRoot simulation system [1] using the Geant3 transport engine. A sensor material of 2 mm thickness and with the density of silicon was assumed for the flat dies installed at 60 mm distance from the target center (0.25 mm Au or 1 mm C). This thickness corresponds to either ceramic RPC or to MCP sensors - both possessing excellent timing properties and certain energy resolution. Standard URQMD events of Au+Au @ $10A$ GeV (both minimum bias and central) as well as p+C @ 30 GeV were used as input. The FairRoot class *FairIonGenerator* was used to simulate "empty events", i. e. the passage of heavy ions through the target material without any nuclear interaction, thus producing only delta electrons.
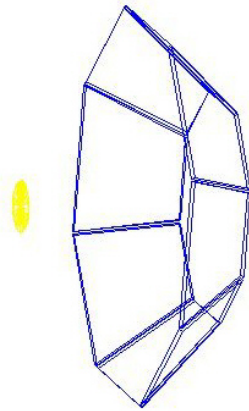
Figure 1: The reaction detector – a ring of eight trapezoidal segments around the target (yellow). The beam direction is horizontal.

The sum of energy loss signals of all products from a nuclear collision in the reaction detector differs significantly for minimum bias or central events and "empty events" as shown in Fig. 2. The lowest energy losses (below 10 MeV) and lowest multiplicities (8 ± 2.5) are registered mainly for "empty events". Minimum bias events are characterized by the sum of energy loss in the reaction detector in the range up to 50 MeV. The highest energy loss (and at the same time the highest particle multiplicity) is observed for central events. A simple threshold at 10 MeV of total energy loss per event would deliver a clear signature for nuclear reaction events, while losing about 10 % of peripheral interactions.
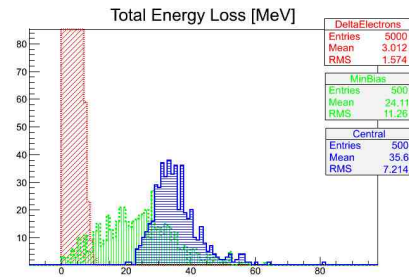
Figure 2: Total energy loss for central (blue, hatched horizontally), minimum bias (green, hatched vertically) and empty events (red, inclined hatching)

The total energy loss signal can not only be used for nuclear reaction tagging but also as a "time zero" for TOF measurements. Because of the axial symmetry of the RD around the target, the time spread of arriving particles is very narrow (RMS = 10 ps). For 30 GeV protons on a carbon target, a similar time resolution is achieved as shown in Fig. 3.
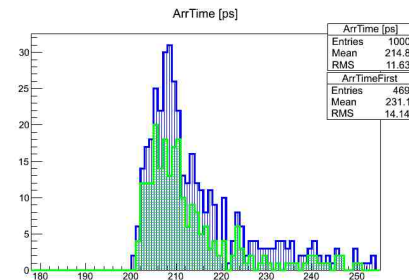
Figure 3: Time resolution for 30 GeV protons on a carbon target. An additional requirement of at least one double hit in the RD reduces the efficiency to 50 %.

References

[1] http://fairroot.gsi.de

Single Event Effects and beam diagnostic studies at the CBM proton test beam

S. Löchner[1], H. Graf[2], and B. Walasek-Höhne[2]

[1]Electronics Department (CSEE), GSI Darmstadt, Germany; [2]Beam Instrumentation Department (LOBI), GSI Darmstadt, Germany

Radiation damages to electronic components are an important issue for FAIR accelerator, FAIR experiments and the used equipment there. For the experiments, one of the preferred technology for Application Specific Integrated Circuit (ASIC) developments is the 180 nm UMC CMOS process. In this regard the ASIC design group of the GSI Electronics department (CSEE) has been launched a research project, including the development of the *GRISU* ASIC, with the main goal to characterise the Single Event Effects (SEE) on this process [1].

Within the CBM collaboration, a SEE test with 2 GeV protons was realised in August 2012 at the particle accelerator COSY in Jülich [2]. Two aspects were tested: mobile beam diagnostic devices and the SEE characterisation itself.

For the SEE cross section measurement it is essential to know the intensity and the position of the particle beam. The number of proton particles is measured with an ionising chamber [3], read out with a charge-to-frequency converter ASIC (QFW) [4]. An online measurement of the proton beam position is performed with a YAG:Ce scintillating screen and an attached CCD camera [5]. The entire setup is mounted on a moveable XY-table, and alignment is achieved with the feedback from the online measurement of the beam profile. Once the system is aligned, the scintillating screen is pneumatically moved out of the proton beam. In addition, the beam position has been approved by a self-developing dosimetry film [6]. A photography of the GSI test system at COSY is shown in Fig. 1 as well as a typical corresponding measured beam profile.
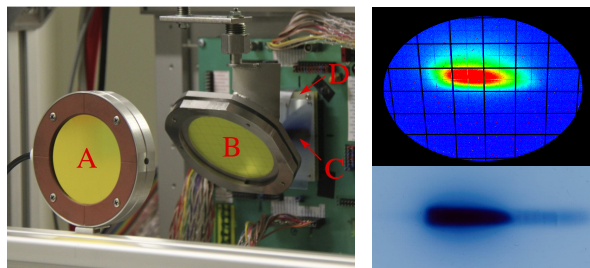
Figure 1: Left: SEE beam test system with ionising chamber (A), scintillating screen (B), dosimetry film (C) and device under test (D). Right: beam position and dosimetry film.

Single Event Effects (SEE) is the main generic term for immediate effects in semiconductor devices triggered by the impact of particles. Of great interest are the so-called Single Event Upset (SEU) and Single Event Transient (SET). These effects were studied in detail with heavy ions at the *GRISU* ASIC between 2008 and 2011 [1].

For proton radiation the SEE mechanism is different. Within the 2012 CBM proton test beam campaign at COSY, the SEE cross sections of all *GRISU* circuits were tested. At a proton energy of 2.0 GeV and a fluence of $4.9 \cdot 10^{12}$ p/cm^2, in total 456 SEE were measured. Figure 2 shows exemplary the SET cross section data as well as its corresponding Weibull fit of a minimum-sized inverter obtained from measurements with heavy ions. In the same diagram the saturated SET cross section region for proton radiation is drawn. This results for this inverter device in a ratio of maximum cross section between heavy ion and proton radiation of $\sigma_{\mathrm{sat,hi}} / \sigma_{\mathrm{sat,p}} \approx 4500$.
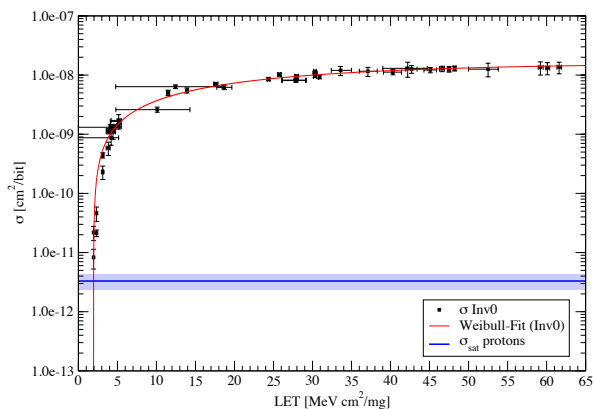
Figure 2: SET cross section for a minimum-sized inverter

References

[1] S. Löchner, CBM Progress Report 2009, p. 49

[2] http://www.fz-juelich.de

[3] GSI Detector Laboratory department (RBDL)

[4] H. Flemming and E. Badura, *A High Dynamic Charge to Frequency Converter ASI*, GSI Scientific Report 2004

[5] GSI Beam Instrumentation department (LOBI)

[6] GAFCHROMIC EBT self-developing dosimetry film, Sensitive dose ranges from about 1 cGy to 800 cGy.

Status of CBMnet integration and HUB design

F. Lemke, S. Schatral, S. Schenk, and U. Bruening

University of Heidelberg, Mannheim, Germany

For the CBM read-out chain from the FEE detector ASICs to the FLES cluster, a hierarchical network structure was developed and optimized for the CBM experiment [1]. In addition to providing a network communication built-in block, the idea was to create a set of modules with well-defined interfaces and functions, which can be used in different CBM network devices. Thus, they can benefit by reusing well-tested hardware. This approach saves design time and uses reliable components. The goal is to provide this set of generic modules not only to FPGAs, but also to FEE ASICs. The generic modules include the CBMnet implementation, some special PHY implementations, and deliver additional features generally required in CBM network devices. These additional features include an automatically generated register file (RF) supporting user-specific parts for analog designers, an I2C interface for debug and test purposes, special blocks for analog register chain access or sub RFs, and serializers/deserializers (SERDES) implementations for different technologies to provide the required communication bandwidth to all CBM network parts. Various FPGA implementations are using this concept, and it is used within a first FEE ASIC for its digital communication part, the SPADIC [2]. The test readout chain for SPADIC testing is shown in Fig. 1. After the first successful tests, configuring the SPADIC and reading out its configuration, it was verified that data, control, and synchronization messages work reliably. These results gave the confidence to integrate these modules also into other ASICs. Thus, they were integrated into the STS-XYTER, which has been submitted in fall 2012. All setups are prepared, and its testing is planned for spring 2013.
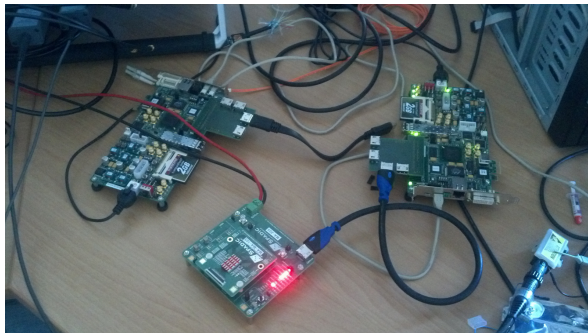
Figure 1: Beam time readout setup

Delivering the readout density required for CBM is a challenging task. Therefore a specific intermediate ASIC for early data aggregation and FEE control is planned. This device, the HUB ASIC [3, 4], is planned to provide at least 32 front-end links with 500 Mb/s each and up to 4 back-end links with at least 5 Gb/s. There are various difficult tasks to handle within this device including handling and deadlock avoidance for all traffic types. A block diagram of the inner HUB ASIC structure is presented in Fig. 2. It depicts the handling of the three virtual traffic classes and shows its general structure. First prototyping for design parts has been done using spartan 6 evaluation boards, and the new spartan-based ROC, currently developed in the collaboration, will provide a platform for further prototyping. The target technology for the HUB ASIC is 65 nm, and the first miniASIC submission will be prepared in 2013.
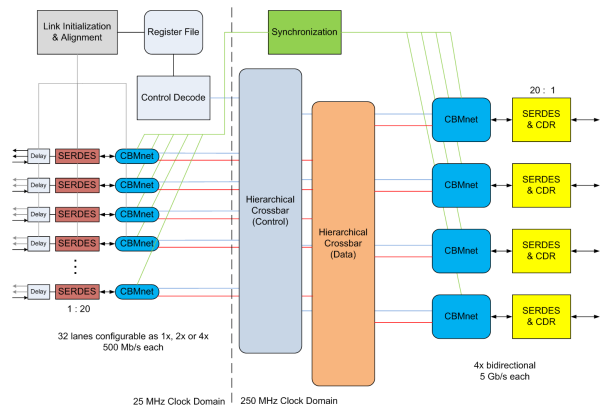
Figure 2: Block diagram of HUB ASIC data path

References

[1] F. Lemke, S. Schenk and U. Bruening, *The Hierarchical CBM Network Structure and the CBMnet V2.0 Protocol*, DPG Spring Meeting, March 19-23, 2012, Mainz, Germany

[2] T Armbruster *et al.*, *SPADIC 1.0 - a self-triggered amplifier/digitizer readout ASIC for the CBM-TRD*, this report

[3] F. Lemke and U. Bruening, *Design Concepts for a Hierarchical Synchronized Data Acquisition Network for CB*, IEEE RTC 2012, June 11-15, 2012, Berkeley, CA, USA.

[4] F. Lemke, *Unified Synchronized Data Acquisition Networks*, Ph.D. thesis, University of Mannheim, 2012

Radiation-tolerant 2.5 GHz Clock Multiplier Unit and 5 Gbps SERDES

T. K.Bhattacharyya, A. Halder, I. Som, A. Roy Chowdhury, U. Bhattacharya, S. Tapse, S. Dutta,
M. Mahalley, A. Chaudhary, N. Gaurav, D. Mandal, S. Haldar, and P. Banerjee

Indian Institute of Technology, Kharagpur, India

The HUB ASIC chip is to be employed for the purpose of data readout from the CBM experiments, and the Clock Multiplier Unit (CMU) is an integral part of the Serializer-Deserializer (SERDES) core of the chip. Keeping in mind the nature of application, radiation hardness and phase-noise are the desired performance measures.

The 2.5 GHz CMU has been designed and fabricated using 180 nm CMOS technology. The active silicon area of the CMU is approximately 1.4 mm × 1.5 mm. The chip has been tested as a soldered-down device on a printed circuit board (PCB) at room temperature using 1.8 Volt VDD.

The CMU is augmented with a memory block in the die in order to provide programmability to the design via an FPGA interface. This helps to test the individual blocks and to vary and calibrate certain design parameters like tail currents of Current Mode Logic (CML) blocks and the switchable capacitors of the LC-tank Voltage Controlled Oscillator (VCO). Figure 1 shows the frequency spectrum of the CMU output, when the VCO is locked at 2.5 GHz (f_{vco}) using a PLL reference frequency of 50 MHz (f_{ref}).
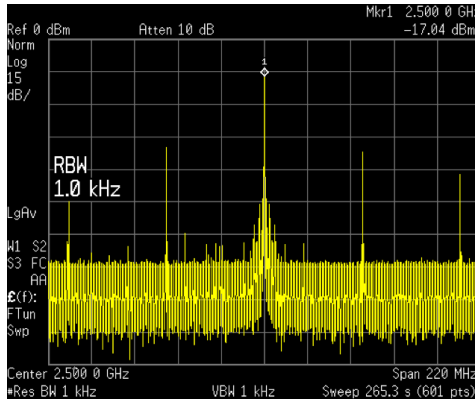
Figure 1: Spectrum of the CMU output signal (f_{vco} = 2.5 GHz, f_{ref} = 50 MHz)

The preliminary measurement shows the phase noise performance of the CMU output (locked at 2.5 GHz) to be -110 dBc/Hz at 1 MHz offset frequency. The degradation from the simulated value of -129 dBc/Hz (at 1 MHz offset frequency) may be attributed to inaccuracies in the phase noise models used in simulations. Further, -35 dBc spurs corresponding to the reference frequency and its harmonics were also observed. The settling time of a locked CMU for a frequency step of 20 MHz is 17 μs and it exhibits a static phase error of 0.1π radians. The tuning range of the VCO is measured to be 2.04–2.53 GHz. Further testing including

the jitter performance is in progress. However, one of the primary goals of this design is to achieve radiation hardness, which remains to be tested based on the availability of the beam line.

In collaboration with the Heidelberg team (led by Prof. U. Bruening), IIT-Kharagpur is in the process of designing the 4 x 5 Gbps serial-link architecture (Fig. 2). The total number of SERDES blocks per ASIC HUB is four. Each of the four SERDES supports 5 Gbps serial interface and 10 x 500 Mbps dual-data rate parallel interface. The salient features of the architecture are as follows:

- Received Signal Strength Indicator (RSSI) for monitoring the input signal amplitude;
- automatic switch-over to on-chip 2.5 GHz CMU output on the LOS events through a glitchless analog MUX;
- hand-shaking for sliding the Parallel Clock (P_CDR_CLK) by one Serial Clock (S_CDR_CLK) period for indefinite number of Parallel Clock cycles;
- Retiming circuit with digital control for sliding the re-sample time of the incoming 5 Gbps bit-stream:
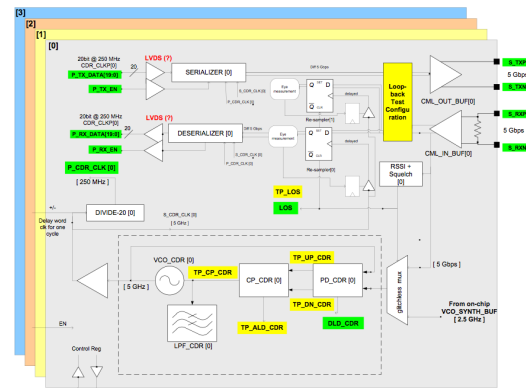
Figure 2: SERDES architecture for simultaneous operation across four 5 Gbps channels

Design and schematic level verification of various blocks are complete for the UMC 65 nm design. Migration to the TSMC 65 nm technology node, which is planned to be the fabrication platform for the first tape-out, is in progress. First prototype tape-out is planned on 24 September 2013.

References

[1] P. Moreira *et al.*, *A Radiation tolerant Gigabit Serializer for LHC data transmission*, Proc. 7th Workshop on Electronics for LHC Experiments, CERN-LHCC-2001-034 (2001) p. 145

Development and production of the ROC SysCore board V2.2

M. Dey[1], A. Roy[1], S. Chattopadhyay[1], N. Abel[2], S. Manz[2], and D. Gottschalk[3]

[1]Variable Energy Cyclotron Centre, Kolkata, India; [2]Goethe-Universität, Frankfurt, Germany; [3]Physikalisches Institut, Universität Heidelberg, Germany

The FPGA-based Readout Controller Board (ROC) is one of the important components in the DAQ chain of the CBM experiment. The requirement of implementing more logic blocks demands the migration from the ROC SysCore board V1 to higher versions. Moreover, the flat cable was not fully compatible to the data port of the n-XYTER front-end board. The cable assembly during experiments was time consuming and also needed extra precaution. These problems were taken care of with the next ROC SysCore V2.

In the first run, some design modifications were implemented to make the ROC compatible with newer versions of the n-XYTER board. Two such ROC boards were fabricated and tested. It was observed that one of the clock-capable LVDS pins from ROC to FEB was missing. The developed boards were used by swapping two pair of data ports. In the second run, after some design modifications, a single ROC board with XC4VFX60-10FFG672C was fabricated again. It was observed that only one data port of ROC could be used.

Based on the above feedback, a new layout design SysCore version 2.2 was implemented. During the fabrication of this version, checks of the integrity of each layer of the multilayer PCB with X rays and of the continuity of all nets by flying probes method were performed by the fabricators. The assembly of the components was checked visually, in some cases using magnifiers. The laboratory setup used to perform the test is shown in Fig. 1. The basic functionality of two ports, namely the Ethernet and optical (SFP) ports of the boards was checked downloading two sets of test bit files (ethernet.bit and optics.bit).

Figure 1: Laboratory setup with ROC boards

The functionality of the Ethernet and optical ports was determined by observing yellow blinking LED6. It started blinking after successful programming to FPGA. The observation of the procedures followed during programming of the ROC is listed in Table 1. It was observed that the current drawn by the boards after programming the FPGA for optics varied from 1.07 A to 1.27 A. In case of Ethernet bit file, it varied from 1.50 A to 1.81 A.

Table 1: Routine procedures followed to check the programmability of the ROC boards by downloading the bit files and measuring the current drawn by the boards

board ID	bit file	current [A]
13628-PAC003	Ethernet	1.55
13628-PAC003	Optical	1.11
13628-PAC004	Ethernet	1.60
13628-PAC004	Optical	1.13
13628-PAC005	Ethernet	1.51
13628-PAC005	Optical	1.08
13628-PAC006	Ethernet	1.53
13628-PAC006	Optical	1.09
13628-PAC007	Ethernet	1.56
13628-PAC007	Optical	1.09
13628-PAC008	Ethernet	1.50
13628-PAC008	Optical	1.06
13628-PAC009	Ethernet	1.80
13628-PAC009	Optical	1.18

In the development process outlined above, three types of Virtex-4 with the same footprint were used. Two modifications in the layout designs were required, which were ressourced from CBM groups. Table 2 gives the production status of the ROC boards. All boards were fabricated, assembled and tested in India. They were subsequently distributed among different CBM detector groups and are being used extensively in the CBM test runs.

Table 2: Production status of ROC boards

device	SysCore version	quantity
XC4VFX20-10FFG672C	V2	2
XC4VFX60-10FFG672C	V2.1	1
XC4VFX40-10FFG672C	V2.2	25

SysCore3 – A universal Read-Out Controller and Data Processing Board

J. Gebelein[1], D. Gottschalk[2], G. May[3], and U. Kebschull[1]

[1]Infrastructure and Computer Systems for Data Processing (IRI), Goethe University, Frankfurt/Main, Germany;
[2]Physikalisches Institut (PI), Heidelberg University, Heidelberg, Germany; [3]GSI, Darmstadt, Germany

The universal SysCore architecture was initially announced in 2007 to provide an optimum balance between fixed requirements and flexibility. The first instance of boards following this principle acted as development platform for FEE (Front End Electronic), especially the nXYTER with ADC (Analog Digital Converter) and ROC (Read Out Controller). The second, slightly modified instance of the board came into operation in several sub-detector systems of the CBM experiment, especially as ROC for the ToF (Time of Flight) system, where it is used for years now. To extend the usability spectrum whilst keeping the re-usability approach, a completely new and improved version 3 of the SysCore architecture board has been developed [1]. It allows the CBM collaboration not only to prototype FEE or to develop ROCs, but also to evaluate the DPB (Data Processing Board) capabilities for an optical readout in the CBM service building. In this specific context, feature extraction for the TRD (Transition Radiation Detector) is currently an active field of research.

Considering all requirements such as FMC HPC connectors for high-performance connectivity, USB for programming and data transfer, DDR3 for fast memory access, Jitter Cleaner for clock distribution across several boards, optical SFP connectors for CBMnet integration [2] and, not to forget, an inexpensive central processing FPGA which can be operated in radiation environments, the PCB got a size of 230x230 mm^2. It is made of 16 different layers with a track width/distance of 0,15-0,09 mm (micro fine lines). Length compensation for the most critical components such as DDR3, FMC and SFP has been performed. Functional blocks such as power supply, scrubbing controlling or high-performance data transfer have been locally combined to provide optimal results. The final board layout is shown in Fig. 1.

Programming of the major components on the board can be performed in different ways: The Spartan-6 FPGA itself can be programmed either via USB (Cypress FX2) or JTAG programmer or by the onboard Microsemi ProASIC3 scrubbing controller from a nearby flash memory. The PROASIC3 can be programmed via the Spartan-6 FPGA or a JTAG programmer. This combination allows remote configuration of both FPGAs on the board. Furthermore, the ProASIC3 acts as scrubbing controller for the ToF ROC when it is operated in radiation-susceptible environments [3, 4, 5]. This fault-tolerance approach has always been a major component of the SysCore architecture and can only be achieved when all components go together. Therefore, the major processing FPGA has been selected to support the background scrubbing feature, the flash memory holding its configuration is a Micron SLC NAND memory with durable charge pumps [6] and the power supply utilizes Linear Technology POL (Point of Load) converters.
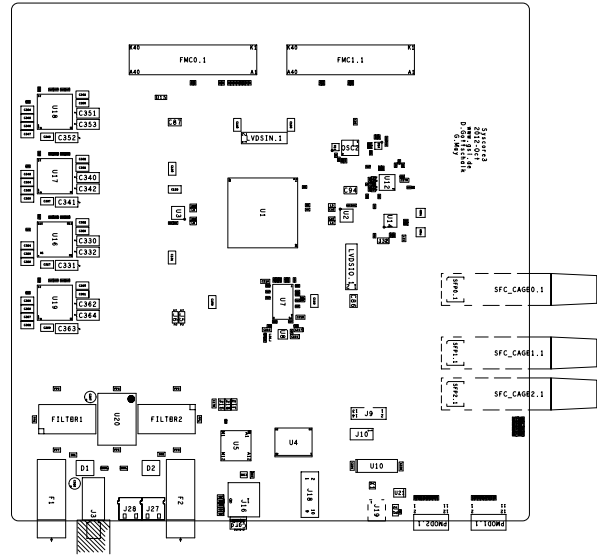
Figure 1: Top view of the SysCore3 PCB

References

[1] N. Abel *et al.*, *SysCore3 – a new board for the Universal ROC*, CBM Progress Report 2011, Darmstadt 2012, p. 60

[2] F. Lemke, *Unified Synchronized Data Acquisition Networks*, Dissertation, Universität Mannheim 2012

[3] N. Abel *et al.*, *Radiation tolerance of the Universal Read Out Controller*, CBM Progress Report 2010, Darmstadt 2011, p. 62

[4] J. Gebelein, H. Engel and U. Kebschull, *FPGA fault tolerance in radiation susceptible environments*, Proceedings of Radiation Effects on Components and Systems (RADECS) 2010, Austria, http://www.radecs2010.ait.ac.at/index.php?link=programme

[5] J. Gebelein and U. Kebschull, *Investigation of SRAM FPGA based Hamming FSM encoding in beam test*, Proceedings of Radiation Effects on Components and Systems (RADECS) 2012, France

[6] F. Irom and D. N. Nguyen, *Radiation Tests of Highly Scaled High Density Commercial Nonvolatile NAND Flash Memories*, JPL Publ. 2009-20 09/09 (2009)

ALICE C-RORC as CBM FLES Interface Board prototype

H. Engel and U. Kebschull

Goethe University, Frankfurt, Germany

The ALICE Common ReadOut Receiver Card (C-RORC) is a FPGA-based PCIe readout card with high-density parallel optical connectivity addressing the needs for the upcoming ALICE upgrade. This card is also considered as a prototype for the CBM First Level Event Selector Interface Board (FLIB), and CBM-related requirements have already been integrated during its development. First prototypes of this board have been produced and could be tested successfully.

The FLES Interface Board serves as an interface between the Data Processing Boards and the First Level Event Selector in the CBM readout chain. It is planned to be implemented as a FPGA-based PCI-Express plug-in card with optical interfaces at the FLES input nodes. Streaming data received on the optical interface from the front-end electronics via Read-Out Controllers and Data Processing Boards is received by the FLIB and provided to the host machine using Direct Memory Access (DMA). Prototype boards are required as a test platform for FLES hardware and software development as well as for testbeam and lab setup readout. A more detailed description of the FLES developments can be found in [1].

The C-RORC is a Xilinx Virtex-6 based FPGA board developed by ALICE to replace existing readout boards and enable upgrades of the current readout architecture. The board comes with an eight-lane PCI Express Gen2 interface to the host machine and 12 serial optical links of up to 6.6 Gbps using three QSFP modules. The highly parallel optical connectivity, the DDR3 RAM and its interface to the host machine makes this board a suitable prototype for first FLIB firmware developments. Requirements for the usage as FLIB prototype have already been considered during the development of the card. The layout of this board was completed in 2012, and first prototypes have been produced. A picture of the board is shown in Fig. 1.

Several hardware tests have been performed to confirm the correct operation of the board and have been compared to previous firmware tests with commercially available evaluation boards. The throughput of the PCIe interface has been directly compared with a reference implementation on the HitechGlobal board and could be confirmed to be identical. All DMA tests have been performed with a custom device driver and DMA engine. A generic device driver, DMA library and software architecture is currently being developed. More details on this can be found in [2]. The onboard flash memories are accessible with both the PCIe interface and the programming cable. The FPGA gets automatically configured from these memories on power-on, and the device is correctly detected on all tested host machines. The serial optical links have been tested with electrical and optical loopback adapters, optical QSFPs and active optical cables. A long-term test of a full setup with two boards interconnected with QSFP transceivers and parallel fibers did not show any bit errors. First DDR3 tests with SO-DIMM modules operating with 800 Mbps and 1066 Mbps could also be concluded successfully. The onboard microcontroller for configuration monitoring and control could also be verified. The board is accessible from the I2C chain of the host machine, the configuration status and the board voltages can be read out with I2C, and a reconfiguration of the FPGA from a selected flash partition can be triggered. There are no major PCB changes required for the next series of boards.
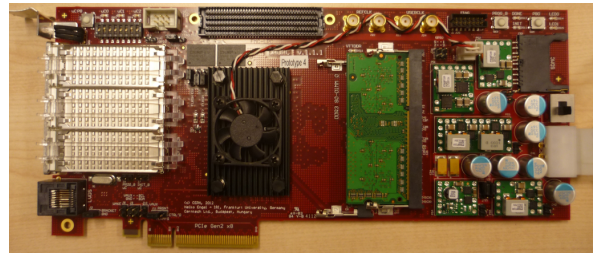
Figure 1: Photo of a C-RORC prototype with one DDR3 module

In summary, all hardware tests performed by now could be concluded successfully. All major interfaces have proved reliable behavior, and there are only a few untested aspects of the board remaining. A larger number of boards is going to be produced in 2013 and will be provided to several working groups to investigate the hardware more deeply and to continue the development of firmware and software.

References

[1] J. de Cuveland *et al.*, *Status of CBM FLES prototype developments*, this report

[2] D. Eschweiler and V. Lindenstruth, *Microdrivers in High-Throughput and Real-Time Environments*, FIAS Scientific Report 2012 (to appear)

Status of CBM First-Level Event Selector prototype developments

J. de Cuveland, D. Hutter, and V. Lindenstruth

FIAS Frankfurt Institute for Advanced Studies, Goethe-Universität Frankfurt am Main, Germany

The First-Level Event Selector (FLES) is the central event selection system in the CBM experiment. Its task is to select data for storage based on online analyses including a complete event reconstruction. To do so, the FLES time-slice building has to combine data from all input links to time intervals and distribute them via a high-performance network to the compute nodes. Data rates at this point are expected to exceed 1 TByte/s. It has proven practical to use an InfiniBand network for data transfer between the FLES nodes. Even so, further investigations are needed to design the final system and develop the required software algorithms.

To provide a small-scale, highly customizable platform for these studies, the *Micro-FLES* cluster was installed at GSI (see Fig. 1). Eight identical compute nodes provide a total of 192 logic cores and 512 GB memory. While consuming only 1 U of installation space, the nodes still provide PCIe 3.0 expansion slots for up to two FLES Interface Boards (FLIB) and three GPU cards. This allows additional tests of the full data transport chain and reconstruction algorithms in the future. In addition to the compute nodes, one head node provides infrastructure services such as storage and boot images. Although there is local storage in the compute nodes for test purposes, it is currently not used for operating the cluster.

Figure 1: The *Micro-FLES* cluster installed at GSI

For timeslice building the cluster is equipped with a state-of-the-art InfiniBand FDR network. Each node offers two 56 Gbit/s 4x FDR ports currently connected to one core switch. The availability of two ports per node easily allows the study of more complex network topologies.

Complementarily, the development of a timeslice-building test software based on InfiniBand Verbs has

started. Especially questions regarding data structures, buffer management, and network scheduling are addressed. Preliminary tests using the same data structures as intended for the final setup have shown promising results.

In the process of upgrading the CBMnet-based prototype read-out chain, a replacement for the currently used PC interface board (namely the ABB) is needed. For this purpose the FLIB prototype board derived from the ALICE C-RORC [1] has been chosen. Based on a Xilinx Virtex-6 FPGA, it features an eight-lane PCIe Gen 2 interface, up to 12 optical links and two DDR3 memory sockets.

In contrast to the final system, early prototype setups will not support the creation of microslice containers (MC) (as described in [2]). Hence, a firmware was developed that is capable of reading out raw CBMnet messages as delivered from the CBM front-end electronics.

The corresponding data path is shown in Figure 2. In the first step, incoming CBMnet messages are preprocessed in hardware to facilitate subsequent software processing. After preprocessing, a separate module packages the incoming data into simplified MCs, whose reduced data content requirements (in comparison to ordinary MCs) support not yet fully synchronized detector electronics. Finally, an address index table is created and MCs are written to the PC host memory via the PCIe interface. The chosen partitioning of the design and the creation of simplified MCs enables reuse of developed hardware and software components when migrating to a fully microslice-based read-out chain.
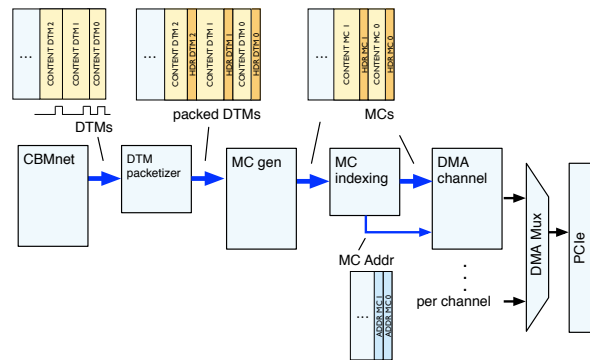
Figure 2: Schematic view of the FLIB read-out data path

References

[1] H. Engel and U. Kebschull, *ALICE C-RORC as CBM FLES interface board prototyp*, this report

[2] J. de Cuveland *et al*, CBM Progress Report 2011, Darmstadt 2012, p. 63

Intermediate mass fragments for the CBM simulation framework

C. Ristea, A. Jipa, O. Ristea, V. Baban, C. Beşliu, T. Eşanu, M. Călin, and V. Covlea

Atomic and Nuclear Physics Chair, Faculty of Physics, University of Bucharest, Romania

Intermediate-mass fragments (IMF) created at CBM energies determine the number of free spectator nucleons. Their generation is significant for semi-peripheral and peripheral events and marks the reaction plane determination. In CBM, the PSD detector will be used to reconstruct the event plane and to measure directed flow. This work reports on the implementation of IMF for simulations using the UrQMD event generator [1]. Previously, only the SHIELD code allowed the generation of IMF to be accounted for.

The current understanding of the IMF generation is depicted by the universality of spectator fragmentation at relativistic energies [2]. Experimental data from the ALADIN spectrometer at SIS-GSI showed that the Z_{bound} universality was obeyed by the fragment multiplicities and correlations. These observables are invariant with respect to the entrance channel if plotted as a function of Z_{bound}, where Z_{bound} is the sum of the atomic numbers Z_i of all projectile fragments with $Z_i \geq 2$.

In particular, no significant dependence on the bombarding energy nor the target mass was observed. The measured Z distributions of fragments with $Z_i \geq 2$ for Au+Au at different energies for distinct intervals of Z_{bound} were fitted with power-law functions $Z^{-\tau}$. The resulting τ values are the same regardless of projectile energy. The average number of IMF, the average maximum Z of fragments, the τ exponent of fragments Z distribution, and the average number of α particles were parametrized as polynomial functions of the variable Z_{bound}/Z_{proj}. The coefficients of these functions were obtained from fits to the experimental data.

The authors in [2] relied on the fact that the universal properties should persist up to much higher bombarding energies. We thus applied their parametrization to Au+Au collisions at $p_{lab} = 5\,\text{GeV}/c$ simulated with UrQMD and studied the response of the PSD located at 6 m from the interaction point. In order to express the functional above, we have followed closely the AliRoot implementation [3]. Once the IMF distribution is determined for a given impact parameter, the corresponding spectators - identified either by $p - p_\perp$ cuts or directly from UrQMD in the case of FORT14 output - are sub-sampled and removed from the input. Finally, the computed IMFs are added to the mainstream analysis.

Figure 1 demonstrates the effect of IMF generation by comparing the number of free spectator protons and neutrons without and with inclusion of this process. IMF generation severely influences the free spectator number for $b > 5\,\text{fm}$. Since fragments tend to pass through the beam hole of the PSD, the response of the latter is also strongly influenced as shown in Fig. 2.

Figure 2: Energy loss in the PSD @ 6 m. Left: no IMF taken into account; right: IMF included.

The implementation of IMF generation reported here allows the CBM simulation framework to more realistically model the UrQMD output in order to study the PSD capabilities to reconstruct the collisions centrality and the event plane.

References

[1] S. A. Bass *et al.*, Prog. Part. Nucl. Phys. **41** (1998) 255
    M. Bleicher *et al.*, J. Phys. **G 25** (1999) 1859

[2] A. Schüttauf *et al.* (ALADIN Coll.), Nucl. Phys. **A 607** (1996) 457

[3] `http://alisoft.cern.ch/viewvc/trunk/ZDC/?root=AliRoot`

Figure 1: Number of free spectator protons (left) and neutrons (right) in Au+Au collisions at $p_{lab} = 5\,\text{GeV}/c$. The open symbols shows the results without IMF, the full ones those with the inclusion of IMF generation.

Study of clustering algorithms for the MVD detector

G. Kozlov[1], V. Ivanov[1], A. Lebedev[1,2], and I. Vassiliev[2]

[1]LIT JINR, Dubna, Russia; [2]IKF, Goethe University, Frankfurt, Germany

Clustering algorithms are an important part of the event reconstruction in high energy physics. This holds in particular for the CBM experiment. These algorithms translate fired strips and pads into space coordinates (hits) which are later used in the track reconstruction algorithms. In this paper we discuss the clustering problem for the MVD (Micro Vertex Detector). The high interaction rate and the large amount of data lead to strong requirements to the clustering algorithms which have to perform fast and efficient and be able to deal with high track multiplicity.

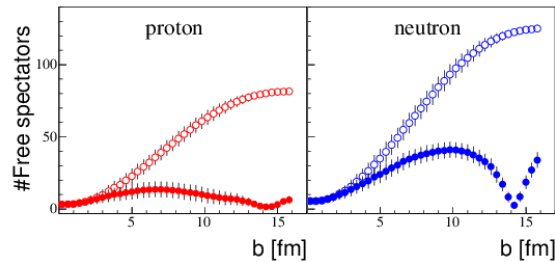Currently, two different clustering implementations for the MVD are under discussion. In the first case, each fired pixel provides information about the deposited charge. In the second case, a pixel can be either fired or not; then, the separation of overlapping clusters becomes a difficult task. The pixel size is 18.5 μm in both cases. The size of most clusters is larger than 10 pixels.

For clustering with charge information, we developed an algorithm which works by the following rule: every pixel with a local maximum of charge forms a separate cluster. All other active pixels are attached to the neighbor with the highest charge. This approach allows to clearly define clusters (each with its own local maximum of charge) and does not require complex calculations.

For clustering without charge information, we used an algorithm based on the single-linkage method. According to this algorithm, every group of neighboring fired pixels is combined into one cluster. In this approach, clustering is very fast, but the separation of overlapping clusters is not possible.

The developed algorithms were integrated into `cbmroot` and tested on various types of simulated events (p+C, C+C, Au+Au). The results presented in this report are based on the simulation of central Au+Au events at $25A$ GeV. The algorithm for clustering with charge information shows a hit finding efficiency of 97.81% and a hit position resolution of 0.9 μm. This high quality of clustering allows an efficient reconstruction of tracks in the MVD and their correct matching to the correspondent tracks in the STS (Fig. 1). The hit finding efficiency for the single-linkage method of clustering without charge information is 96.65% with a position resolution of 2.8 μm.
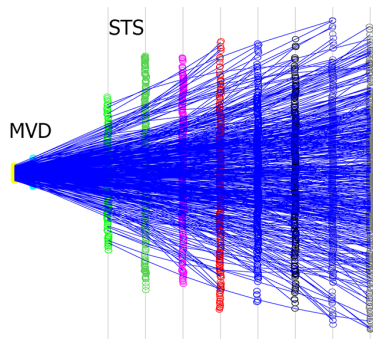
The problem of overlapping clusters in the single-linkage method was investigated. The use of cluster size and shape is not sufficient to disentangle neighboring clusters. The most appropriate method of cluster separation in this case is the application of a charge threshold for the activation of pixels. We have studied the effect of the threshold on the accuracy and efficiency of clustering and have determined the optimal value of the threshold to be 100. Using this threshold improves the efficiency from 96.65% to 97.25%, but leads to a drop in accuracy in comparison to clustering without threshold. In this case, the position resolution is 4.9 μm. This drop in accuracy is due to the loss of fired pixels in the clusters. Still, the error is much smaller than the pad size. The efficiency increases because of the separation of some neighboring clusters. Fig. 2 shows the distributions of position residuals for all cases of clustering.
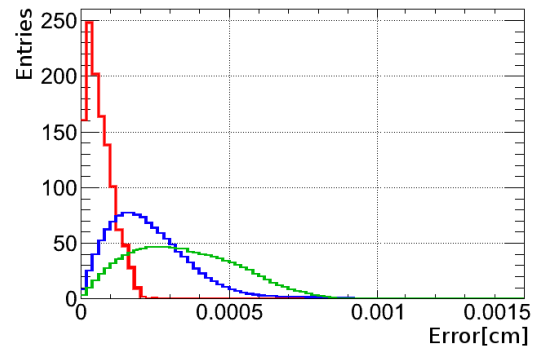
Figure 2: Distribution of position residuals. Red: with charge information; blue: single linkage method without threshold; green line: single linkage with threshold

In summary, we have developed clustering algorithms for the MVD detector in the environment of high track multiplicity. They have been tested on various types of simulated events (including central Au+Au events at $25A$ GeV) and have shown high efficiency and accuracy in all cases. The algorithms have been integrated into `cbmroot` and are ready to be used for clusterization.

Figure 1: Matching of tracks in the MVD and STS detectors

FLES: Standalone First Level Event Selection package for CBM

V. Akishina[1,2,3]*, I. Kisel*[1,2,4]*, I. Kulakov*[1,2,4]*, and M. Zyzak*[1,2,4]

[1]Goethe University, Frankfurt, Germany; [2]GSI, Darmstadt, Germany; [3]JINR, Dubna, Russia; [4]FIAS, Frankfurt, Germany

The main focus of the CBM experiment is the measurement of very rare probes, which requires interaction rates of up to 10 MHz. Together with the high multiplicity (up to 1000) of charged particles produced in heavy-ion collisions, this leads to huge data rates of up to 1 TB/s. Most trigger signatures are complex (short-lived particles, e. g. open charm decays) and require information from several detector sub-systems.

The First Level Event Selection (FLES) package of the CBM experiment is intended to reconstruct the full event topology including tracks of charged long-lived particles and short-lived particles. The FLES package consists of several modules (see Fig. 1): track finder, track fitter, particle finder and physics selection. As an input the FLES package receives the geometry of the tracking detectors and the measurements (hits) created by the charged particles crossing the detectors. The tracks of the charged particles are reconstructed by the Cellular Automaton track finder [1]. The Kalman filter based track fitter [2] is used for precise estimation of the track parameters. The KF Particle Finder [3] is used to find short-lived particles. In addition, a module for quality assurance is implemented which allows to monitor the quality of the reconstruction at all stages.

The package provides high reconstruction efficiency and high signal-to-background ratio (S/B) for the recon-

structed decays. For instance, for 240,000 minimum bias Au+Au UrQMD events at $25A$ GeV, the reconstruction efficiency (normalized to 4π) for the K_s^0 meson is 15.3 % with a S/B ratio of 3.5; the corresponding values for the Λ hyperon are 17.2 % efficiency and S/B = 5.1.

The first version of the FLES package is optimized with respect to speed and is intrinsically local and parallel. The implementation is based on the SIMD instructions and was parallelized between cores using the Intel Threading Building Blocks package [4], which provides scalable event-level parallelism with respect to the number of hardware threads and CPU cores. Four servers with Intel Xeon and AMD processors have been used for the scalability tests. The most powerful server has 4 processors with 10 physical cores each, providing 80 logical cores in total. Figure 2 shows a strong scalability for all many-core systems. The achieved reconstruction speed is 1700 events per second on the 80-core server.

Figure 2: Scalability of the FLES package on many-core servers

References

[1] I. Kisel, Nucl. Instrum. Methods **A 566** (2006) 85

[2] S. Gorbunov *et al.*, Comp. Phys. Comm. **178** (2008) 374

[3] M. Zyzak *et al.*, *The KF Particle Finder package for the reconstruction of short-lived particles in CBM*, this report

[4] ITBB Reference Manual,
`http://threadingbuildingblocks.org`
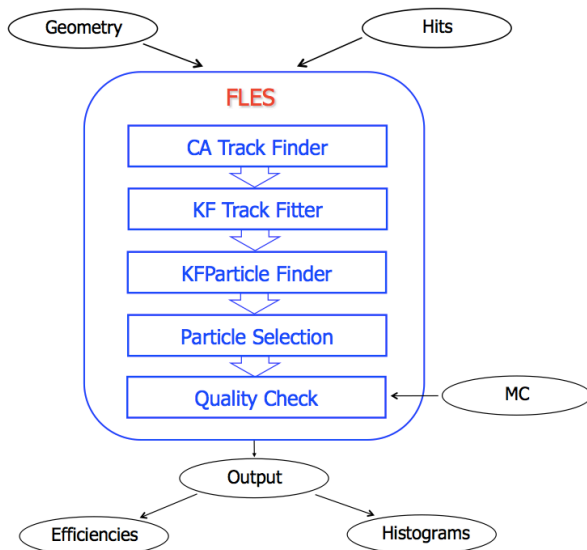
Figure 1: Block diagram of the FLES package

The Cellular Automaton track finder at high track multiplicities for CBM

V. Akishina[1,2,3]*, I. Kisel*[1,2,4]*, I. Kulakov*[1,2,4]*, and M. Zyzak*[1,2,4]

[1]Goethe-Universität, Frankfurt, Germany; [2]GSI, Darmstadt, Germany; [3]JINR, Dubna, Russia; [4]FIAS, Frankfurt, Germany

The CBM experiment at FAIR is being designed to study heavy-ion collisions at extremely high interaction rates (up to 10 MHz) and with high track multiplicities (up to 1000). At such interaction rates, events will be close or even overlapping in time. Measurements in this case will be 4-dimensional (x, y, z, t). Thus, reconstruction will act on time slices rather than on events. In addition to such high input rate and complicated event topology, full event reconstruction and selection is required at the First Level Event Selection (FLES) stage. Therefore, both the speed of the reconstruction algorithms and their efficiency are crucial.

The Cellular Automaton (CA) track finder [1] is fast and robust and will therefore be used for both online and offline track reconstruction in the CBM experiment. The algorithm creates short track segments in each three neighbouring stations, combines them into track candidates and selects the best tracks according to the maximum length and minimum χ^2 criteria. The algorithm was further optimized for the case of high track multiplicity with respect to time: additional sorting of found hits according to a two-dimensional (y, z) grid was introduced in order to speed up the search for the next hit.
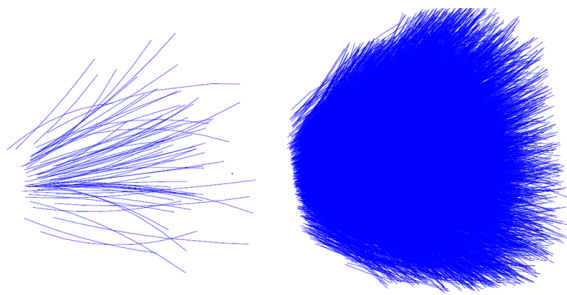
Figure 1: Reconstructed tracks in a minimum-bias event (left) and in a packed group of 100 minimum-bias events (right), with 109 and 10,340 tracks, respectively

The standalone FLES package [2] was used to investigate the stability of the CA track reconstruction with respect to the track multiplicity per event. For this study, 1000 minimum-bias Au+Au events at $25A$ GeV were generated with UrQMD and simulated in the CBM-STS. As a first step towards 4-D tracking, the hits from a number of minimum bias events (up to 100) were packed into one group without taking into account the timing information. The group was treated by the CA track finder as a single

event, and the regular reconstruction procedure was performed (Fig. 1).

The dependence of the track reconstruction efficiency on the track multiplicity was found to be stable (Fig. 2). In particular, the efficiency of the algorithm decreases only by 4 % for 100 minimum bias events in one group, compared to the case of a single minimum bias event. The efficiency for reference tracks ($p > 1$ GeV/c), which are of relevance for a large part of the CBM physics, remains high for the entire range of track multiplicities. The efficiencies for low-momentum tracks ("ExtraPrim", 100 MeV/$c < p < 1$ GeV/c) and secondary tracks are also stable. The level of ghost tracks stays below 10 %.
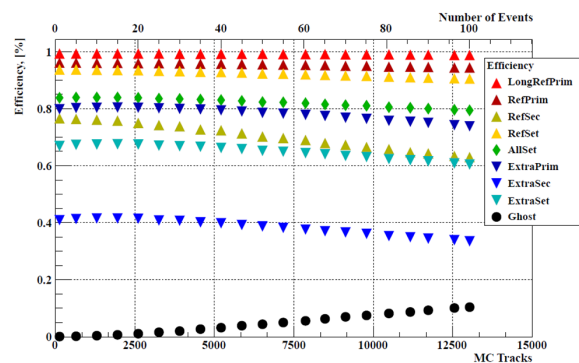
Figure 2: Track reconstruction efficiencies for different track classes and ghost rate as function of track multiplicity

The speed of the algorithm was also studied as a function of track multiplicity. The time the algorithms needs to process a group of events was found to behave like a second order polynomial with respect to the number events in the group. As a consequence, the CA track finder needs less than two seconds to reconstruct a group of 100 overlaid minimum-bias events, which contains about 10,000 reconstructed tracks.

To summarize, the CA track finder reconstruction algorithm shows high speed performance and stability with respect to track multiplicity, up to the extreme case of about 10,000 reconstructed tracks per event.

References

[1] I. Kisel, Nucl. Instrum. Methods **A 566** (2006) 85

[2] V. Akishina *et al.*, *FLES: Standalone First Level Event Selection package for the CBM experiment*, this report

The KF Particle Finder package for the reconstruction of short-lived particles in CBM

M. Zyzak[1,2,3], *I. Kisel*[1,2,3], *I. Kulakov*[1,2,3], *and I. Vassiliev*[1,3]

[1]Goethe University, Frankfurt am Main, Germany; [2]FIAS, Frankfurt am Main, Germany; [3]GSI, Darmstadt, Germany

A large part of the physics of CBM is hidden in the properties of short-lived particles which cannot be registered directly by the detector system, but only reconstructed from their decay products. Of particular interest are short-lived particles with a very small production probability. Thus, a statistically significant result can only be obtained with high collision rates of up to 10^7 Hz. This raises the problem of data processing and storage. Therefore only those events are selected for the further analysis that potentially contain interesting particles. The CBM experiment requires the full reconstruction of events, including reconstruction of short-lived particles, already at the selection stage.

A fast and efficient KF Particle Finder package for the reconstruction and selection of short-lived particles is being developed for the CBM experiment. A search for about 50 decay channels is currently implemented. First, all tracks are divided into the groups of secondary and primary tracks for further analysis. Primary tracks are those which are produced directly in the collision of beam and target ions. Tracks from decays of resonances (strange, multi-strange and charmed resonances, light vector mesons, charmonium) are also considered as primaries since they are produced directly at the point of the primary vertex. Secondary tracks are produced by the short-lived particles which do not decay in the primary vertex point and can thus be well separated. These particles include strange particles (K_s^0 and Λ), multi-strange hyperons (Ξ and Ω) and charmed particles (D^0, $D^\pm$, $D_s^\pm$ and Λ_c).
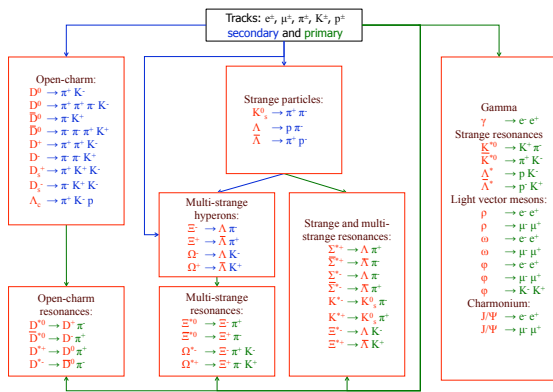
Figure 1: Block diagram of the KF Particle Finder algorithm

The tracks are then combined according to the block diagram in Fig. 1, and particle candidates are produced from these combinations. The particles are reconstructed with the KF Particle package [1], which is based on the Kalman filter (KF) method and reconstructs parameters of the particle such as decay vertex, momentum, energy, and mass together with their errors. All particles are reconstructed at once, which makes the algorithm local with respect to the data and therefore very fast.

The KF Particle Finder achieves a high efficiency for particle reconstruction. For example, the efficiencies of K_s^0, Λ, Ξ^- and Ω^- reconstruction are 15.3 %, 17.8 %, 5.0 % and 2.5 %, respectively. The corresponding signal-to-background ratios for 240,000 minimum bias Au+Au collisions at $25A$ GeV are 3.5, 5.1, 42.2 and 4.3.

In order to utilize all possible resources of modern CPUs and to achieve the highest possible speed, the KF Particle Finder is based on the SIMD instructions. In addition, the algorithm has been parallelized between cores of modern CPUs and demonstrates a strong linear scalability on many-core servers with respect to the number of cores (see Fig. 2).
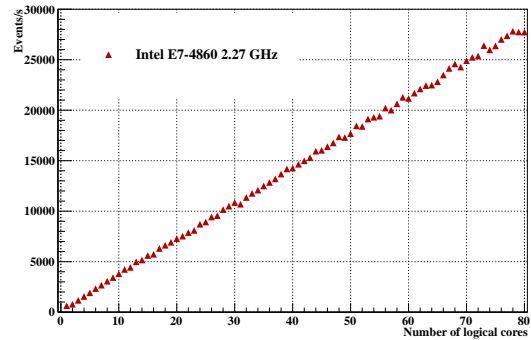
Figure 2: Scalability of the KF Particle Finder package for minimum bias Au+Au events at $25A$ GeV on the many-core server lxir075 equipped with four Intel E7-4860 (2.27 GHz) CPUs

In summary, the KF Particle Finder package reconstructs about 50 of the most important decay channels for the CBM experiment with high efficiency and high signal-to-background ratio, achieving a speed of 1.5 ms per Au+Au minimum bias collision at $25A$GeV on a single core.

References

[1] S. Gorbunov and I. Kisel, *Reconstruction of decayed particles based on the Kalman filter*, CBM-SOFT-note-2007-003

GPU-accelerated CA TRD track finder and J/ψ software trigger

E. Kaptur

University of Silesia, Katowice, Poland

The CBM experiment will study heavy-ion reactions with interaction rates of up to 10^7 collisions per second. The track multiplicity in the TRD is in the order of 600 tracks for a central Au+Au collision at $25A$ GeV beam energy. Such high interaction rates and track multiplicities require fast and efficient tracking algorithms.

A track finder based on the Cellular Automaton was developed in CUDA to work as an entry stage to an J/ψ event selection algorithm. The algorithm is based on earlier work by Arek Bubak and Maciej Krauze [1]. Both track finder and the event selection algorithms work fully in the CBMROOT framework. The algorithms are tuned to the `v11c` geometry of the TRD with 12 layers and are currently working on TRD hits produced by the `CbmTrdHitProducerSmearing` class.

The track finding algorithm consists of few distinct phases:

- copying ROOT hit data into C arrays,
- creation of space points (on GPU),
- creation of tracklets (on GPU),
- neighbour search (on GPU),
- creation of tracks (on CPU).

In order to increase the track finding efficiency, each event is processed twice. Hits attributed to a found track in the first pass are discarded for the second pass.

The performance of the algorithm was studied on a sample of 1,000 central Au+Au collisions generated by UrQMD und simulated in the detector setup. In each event, one electron-positron pair from the J/ψ decay generated by PLUTO was embedded. These signal tracks are primary tracks with high transverse momentum (>1 GeV/c). The track finding efficiency for such tracks is presented in Table 1.

Table 1: Track finding efficiency for tracks having 12 or >9 hits in the detector

	12-hits eff. [%]	>9-hits eff. [%]
Primary, high p_t	86.8	41.7
Other	65.2	28.1
Ghost rate	6.0	

The current version of the algorithm is unable to find tracks with less than 12 hits in the TRD detector. This results in a low average efficiency of finding tracks with more than 9 hits. The J/ψ detection efficiency suffers severely from this restriction because of the small amount of 12-hits signal tracks. Table 2 shows the percentage of events containing 12 hits, >9 hits and reconstructed signal tracks. An ideal reconstruction with the current algorithm would yield an efficiency equal to the percentage of events with 12-hits signal tracks.

Table 2: J/ψ finding efficiency. Shown is the percentage of events containing signal tracks with 12 hits, with more than 9 hits and with both signal tracks reconstructed by the algorithm.

12-hits [%]	>9-hits [%]	Reco. [%]
8.2	33.6	5.3

Figure 1 shows the execution time of different parts of the track finder. The handling of the ROOT objects (hits) takes most of the time. The need for this stage would be eliminated by a GPU hit finder. The second most time-consuming part is track creation, which is still executed on CPU in a non-optimised way. A breakdown of the execution time of the GPU routines is shown in Fig. 2.
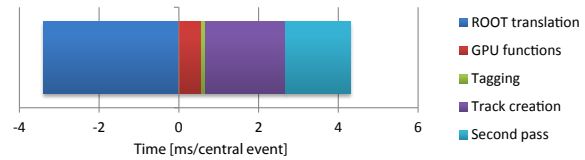
Figure 1: Execution time of the track finding algorithm

Figure 2: Execution time of the GPU routines

Next steps in developing the track finding and triggering algorithms will be the implementation of the search for short tracks, the implementation of a GPU hit finder, the implementation of GPU track fitting and event selection as well as further optimisation of the currently existing code.

References

[1] A. Bubak *et al.*, Acta Phys. Pol. **B 41** (2010) 3

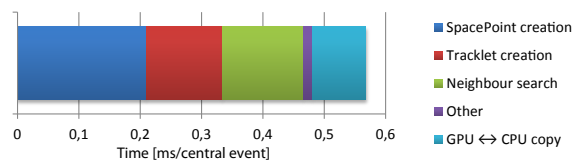# ω_n^k test vs. ANN in the J/ψ selection problem based on the TRD

O. Yu. Derenovskaya and V. V. Ivanov

LIT JINR, Dubna, Russia

In the CBM experiment, the reconstruction of the events of interest to physicists should be realized in real time. This imposes high requirements to the efficiency and speed of the processing algorithms. The measurement of the decay $J/\psi \to e^+ + e^-$ in a dominant background (mostly pions) is one of the key tasks of CBM. Currently, an artificial neural network (ANN) is used to identify the e^-/e^+ and suppress pions based on information from the TRD detector.

In [1], a comparative analysis of different methods, including those based on ANN [2], was performed. It was noted that, in order to correctly apply this method, adequate information about the energy loss distributions for both electrons and pions is required. The distribution of the ionization losses of pions in a substance has been well studied; it can be approximated with good accuracy by a log-normal law. The distribution of the energy loss of electrons in radiators are of a complex character, such that no correctness of results obtained with the help of the ANN can be guaranteed.

In addition, in order to carry out identification of particles with different momenta and/or different numbers of hits in the TRD (from 9 to 12), a corresponding adjustment of the ANN is required. This, together with the computational complexity of the ANN algorithm, leads to a huge amount of computing time for this approach.

Therefore we suggest an alternative method based on the ω_n^k goodness-of-fit criterion [1]:

$$\omega_n^k = -\frac{n^{\frac{k}{2}}}{k+1}\sum_{j=1}^{n}\left\{\left[\frac{j-1}{n}-\phi(\lambda_j)\right]^{k+1} - \right.$$

$$\left. - \left[\frac{j}{n}-\phi(\lambda_j)\right]^{k+1}\right\}, \qquad (1)$$

where k is the criterion degree and $\phi(\lambda)$ the Landau distribution function (which describes the energy loss of pions) with a new variable λ:

$$\lambda_i = \frac{\Delta E_i - \Delta E_{mp}^i}{\xi_i} - 0.225, \qquad i = 1,2,...,n,$$

where ΔE_i is the energy loss in the i-th TRD layer, ΔE_{mp}^i the value of most probable energy loss, $\xi_i = \frac{1}{4.02}$ FWHM of the distribution of the energy loss for pions, and n the number of TRD layers.

This approach has no specified disadvantage regarding its application and requires the knowledge of only two parameters (ΔE_{mp}^i and FWHM) describing the distribution of the pion ionization losses.

The formulas for the transformation parameters depending on the momentum are:

$$\Delta E_{mp}(p) = 0.00026p^3 - 0.008865p^2 + 0.1176p + 0.913,$$
$$\xi(p) = 0.0000894p^3 - 0.003022p^2 + 0.03999p + 0.5292.$$

In [1], the ω_n^k criterion was modified with respect to the most probable value of the TR counts in the TRD layers – about half of the total number of layers. Consequently, the ω_5^k or ω_6^k statistics should be applied for tracks with 9 to 12 hits in the TRD, respectively. However, our study has shown that it is possible to use the ω_6^k statistics with no efficiency loss for all cases. The criterion degree k was chosen to be 4. It should be noted that this modification significantly increased the power of the test [1].

Our study for the problem of the reconstruction of $J/\psi \to e^+ + e^-$, produced in Au+Au collisions at $10A$ GeV, has shown that the modified criterion ω_n^k is not inferior in power to ANN [3]. Figure 1 shows the distributions of the ω_6^4 value for this case.
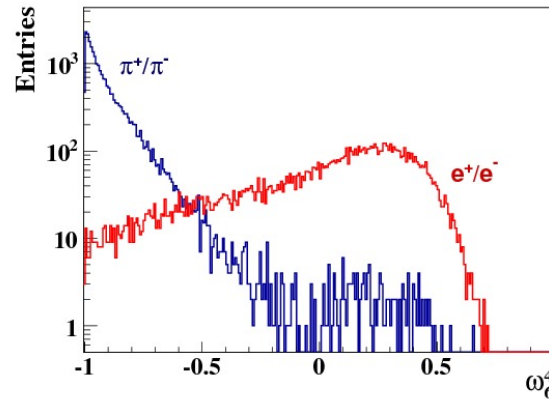
Figure 1: Distributions of the ω_6^4 value for e^-/e^+ (red) and π^-/π^+ (blue)

With this in mind and taking into consideration the very simple software implementation of the modified ω_n^k criterion, we conclude that it can be used, in particular, for real-time selection of J/ψ candidates.

References

[1] T. P. Akishina, Physics of Elementary Particles and Atomic Nuclei, Letters, 2012, Vol. 9, No. 3, 268

[2] T. P. Akishina *et al.*, Bulletin of PFUR, Series "Mathematics. Informatics. Physics", 2010, No. 1, 94

[3] O. Derenovskaya and I. Vassiliev, *J/ψ reconstruction in Au+Au collisions at 10A GeV*, this report

First Level Event Selection for MUCH using GPU

V. Singhal[1], *P. P. Bhaduri*[1], *A. Prakash*[2], *S. Chattopadhyay*[1], *and S. K. Aggarwal*[3]

[1]Variable Energy Cyclotron Centre, Kolkata, India; [2]Banaras Hindu University, Varanasi, India; [3]Indian Institute of Technology, Kanpur, India

At FAIR energies, the cross section for J/ψ production is extremely low, such that a measurement requires very high interaction rates of up to 10 MHz. The corresponding data volume has to be reduced online by selecting only events potentially containing a J/ψ. Here we report on the development of an event selection procedure on GPUs, which allow to execute thousands of threads in parallel. The algorithm was implemented on the NVIDIA Tesla C2075 card [1], using the Compute Unified Device Architecture [CUDA] [2].

To achieve a high execution speed of the event selection, the algorithm developed earlier [3] was modified and implemented in the C language using the CUDA API on TESLA C2075 Card. The algorithm is designed to select events likely to contain J/ψ. It is based on searching for the hit triplets which are formed using the spatial information associated with reconstructed hits. We tested and developed the algorithm on simulated J/ψ decays, generated by PLUTO, which were embedded into minimum-bias Au+Au collisions at $35A$ GeV from UrQMD.

The acceleration of the event selection was performed in several steps. First, the original procedure was implemented in CUDA (Opt-1). It was then optimized by using coalesced memory access according to the CUDA architecture (Opt-2). Further optimization was achieved by reducing the number of global reads (Opt-3). Fig. 1 shows a comparison of the execution time on CPU (entire code running on single core of CPU) and on GPU for the different optimization steps (Opt-1, Opt-2 and Opt-3), together with the data transfer time from CPU to GPU, as a function of the number of events processed in parallel. After the op-

timization of GPU code (Opt-3), the computation time is significantly reduced compared to execution on CPU, but the CPU to GPU data transfer time is substantial.

After analyzing this problem, we could, with little computation on the CPU, reduce the data volume which has to be transferred from CPU to GPU. Table 1 shows the results after this last optimization step. For 40,000 events, we achieved a speed-up by a factor of 35 on the GPU with respect to a single-core CPU. The data transfer time is reduced to a small fraction of the computation time.

Table 1: Final results for event selection algorithm

# Events	GPU Time (ms)	CPU-GPU Transfer Time(ms)	CPU Time (ms)	Speed Up
1000	30	1	120	4
2000	30	1	250	8
3000	30	10	370	12
4000	30	10	490	18
5000	40	10	610	15
10000	50	10	1230	25
20000	80	10	2470	31
40000	140	20	4920	35

In summary, we have demonstrated the implementation of an accelerated event selection for the MUCH detector based on GPU. Table 1 shows that we can process $3 \cdot 10^5$ to $4 \cdot 10^5$ events per second using one GPU Card. The present hardware supports up to four GPU cards on a single motherboard; thus, we can process more than 10^6 events per second, which is close to the targeted event rate.

The distribution of computation between GPU and CPU remains a subject of research. Our results suggest that the usage of GPUs can be beneficial for performing first level event selection in the CBM experiment. Our next step is to develop and implement 4-dimensional event reconstruction algorithms, with the time as 4th dimension, on GPU.
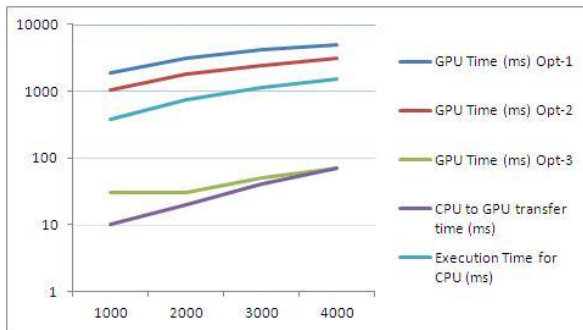

Figure 1: Time comparison between different optimization steps on GPU and on CPU as a function of the number of events processed in parallel

References

[1] www.nvidia.com/object/ workstation-solutions-tesla.html

[2] www.nvidia.com/cuda

[3] P. P. Bhaduri *et al.*, Proc. DAE Symp. on Nucl. Phys. **55** (2010) 640

Developments in the quality assurance tools for CBMROOT

A. Lebedev[1,3], S. Lebedev[2,3], and G. Ososkov[3]

[1]IKF, Goethe University, Frankfurt, Germany; [2]Justus Liebig University, Giessen, Germany; [3]LIT JINR, Dubna, Russia

The software framework of the CBM experiment - `cbmroot` - has been continuously growing over the years. The increasing complexity of the software calls for better maintenance and further developments. In this report we address the problem of software quality assurance and testing, which is of special importance for large, complex software systems. In general, the automatization of regularly performed tasks is an important component of a well-organized software development process. A reliable and automatized testing procedure can considerably improve the development process, since the developer has to be sure that changes made to the code do not lead to program crashes or incorrect results. Moreover, the automatization of this process can considerably reduce the development cycles.

Currently, the main developments are concentrated on the following issues: using regular expressions in the histogram manager; new structure and new interfaces of the report classes; using quality tools for large-scale simulations. In the following, we discuss these developments in detail.

In the analysis and testing software, users and developers of `cbmroot` often create a large number of histograms, graphs, profiles etc. In order to simplify the management of such large numbers of objects, a special class `CbmHistManager` has been developed. One of the important features of this class is the ability to retrieve an array of histograms by a regular expression. This is especially useful if histograms have to be created dynamically, e. g., based on the detector setup. The most obvious use case is to encode the histogram designation not in the C++ variable name but directly in the histogram name. For example, a histogram of tracking efficiency can be named to `hte_StsTrd_StsTrdTof_Primary_Eff_p`. A list of all efficiency histograms can be accessed with the regular expression `"hte_.+_Eff_.+"`. This rather simple and powerful tool allows to dramatically reduce the complexity and the amount of code and to speed up the development process since adding new histograms becomes much easier.

Working with the users feedback we have learned that the use of the report classes is quite complicated and, moreover, some functionality is not used at all. Thus we reworked and simplified the interfaces of the developed report classes. To simplify systematic studies of the CBM detector, a special study report was implemented, which allows to generate a summary report out of many different simulation results. This helps to improve and speed up such studies, easing the interpretation of simulation results.

With the increasing power of the computer farm, large-scale simulations become part of the developer's daily routine. The task of performance analysis of the full set of simulated events is one of the use cases for the developed tools. By employing ROOT's `hadd` and the new report classes, this task becomes trivial.

The improvements in the base classes described above have been implemented in the concrete quality assurance classes for simulation. For example, the tracking performance tool was significantly reorganized to be able to use the new features, mainly regular expressions in the histogram manager. This helps to dynamically create a list of required histograms based on the detector setup and simplify adding new histograms, for example, an additional track category (*all, primaries, muons, electrons* etc.) or dependence on a particular parameter (p, p_t, y etc.). Currently, the tracking performance tool allows to calculate tracking efficiency in the STS, TRD, MUCH, and TOF detectors as well as global tracking efficiency, ring reconstruction efficiency in the RICH detector, electron identification and pion suppression performance and other useful quality figures.
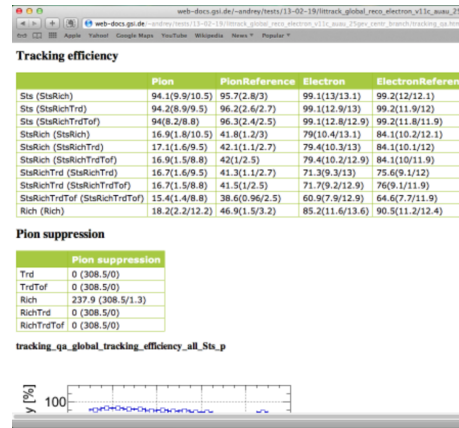
Figure 1: Example of the HTML report for the tracking performance

The combination of the described tools allows to automatize the quality monitoring of the event reconstruction. The simulation and reconstruction is run by the standard `cbmroot` dashboard which is based on `cdash`. The final HTML report is generated and copied to the web server. An example of such a report is shown in Fig. 1.

The developed QA routines allow to improve the `cbmroot` testing procedure without requiring any additional efforts from the developers since testing is done automatically. The developed prototype of the quality monitoring of the event reconstruction can be found in `http://web-docs.gsi.de/~andrey/wwwqa`.

Reaction plane reconstruction in the CBM experiment at SIS-300

S. Seddiki[1] and F. Rami[2]

[1]GSI, Darmstadt, Germany; [2]IPHC, Strasbourg, France

Determining the azimuthal orientation of the reaction plane in nucleus-nucleus collisions with good precision is crucial, in particular for anisotropic flow measurements. In the CBM experiment, the reaction plane can be measured from the sidewards deflection of spectator particles using a forward hadronic calorimeter, referred to as the Projectile Spectator Detector (PSD). The Silicon Tracking System (STS) of the experiment, designed to cover a different region of particle rapidity, can provide another independent and complementary measurement. This work consisted in investigating the capabilities of each of these detectors for reconstructing the reaction plane at SIS300 energies.

The simulations were carried out for Au(25A GeV)+Au collisions in the `cbmroot` environment, using the event generator UrQMD and the transport code GEANT, the latter being complemented with the hadronic interaction package GEISHA. A realistic model of the CBM detector was considered, including a 250 μm thick Au target, a STS consisting of 8 silicon stations located between 30 cm and 1 m from the target and embedded in a dipole magnet, and a PSD positioned at 15 m. The latter is transversally constituted of 12×9 modules of $10 \times 10\,cm^2$, each composed, along the beam axis, of 60 layers with combined lead absorber and scintillator material.

The azimuthal orientation of the reaction plane was determined with the help of the so-called event plane method [1, 2], which uses the anisotropic flow of emitted particles. This flow can be exploited directly by measuring the momentum of charged particles in the STS, while it is reflected in the azimuthal distribution of the energy deposited by projectile spectators in PSD modules. In the STS (PSD), the calculations make use of the elliptic (directed) flow since the detector covers the mid-rapidity (projectile rapidity) region where it is maximum. Therefore the reconstructed event plane is said to be of 2nd (1st) order. Note that in the STS, the reconstructed particle tracks have been used in the calculations.

The reaction plane resolutions shown in Fig. 1 are expressed in terms of the Gaussian width (σ) of the distribution of the event plane (Ψ_1) around the true reaction plane angle (Ψ_R). In Fig. 2, the resolutions are expressed in terms of the $\langle cos(2 \times (\Psi_n - \Psi_R)) \rangle$ factor needed to correct the observed elliptic flow for the reaction plane resolution.

We found that the elliptic flow analysis can be performed quite accurately in CBM, over a large impact parameter range, using either the 1st order event plane from the PSD or the 2nd order event plane from the STS. Both detectors provide a similar accuracy on the reconstruction of the reaction plane, in particular for semi-peripheral collisions (in the impact parameter range from 5 to 9 fm) where the best
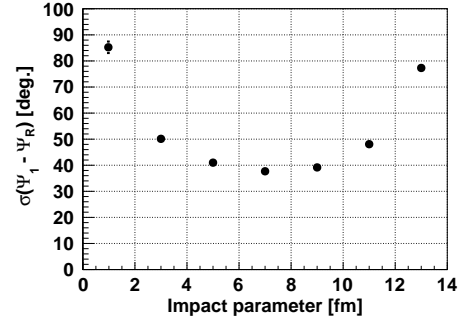
Figure 1: Reaction plane resolution achieved with the PSD detector in Au(25A GeV)+Au collisions as a function of the collision impact parameter. The resolutions are obtained using the 1st order event plane. The error bars represent the statistical uncertainties.

resolution was obtained: an azimuthal angular resolution of about 40°, or accordingly, a correction factor of about 0.4. These results show that STS and PSD can provide independent and fairly precise reaction plane estimates in CBM at SIS-300.
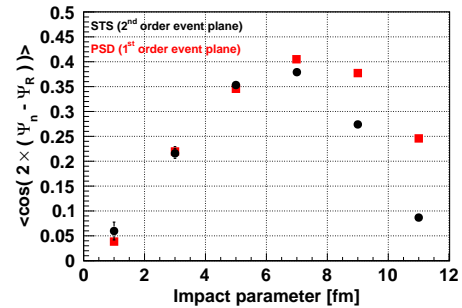
Figure 2: Reaction plane resolution in Au(25A GeV)+Au collisions as a function of the collision centrality. It is expressed in terms of the $\langle cos(2 \times (\Psi_n - \Psi_R)) \rangle$ factor (see text). The black circles correspond to the resolutions obtained using the 2nd order event event plane (n=2) reconstructed with the STS. The red squares are those obtained using the 1st order event plane (n=1) evaluated with the PSD calorimeter, as presented in Figure 1. The error bars represent the statistical uncertainties.

References

[1] A. M. Poskanzer and S. A. Voloshin., Phys. Rev. **C 58** (1998) 1671

[2] S. Seddiki, PhD thesis, Strasbourg and Frankfurt 2012

Reconstruction of multi-strange baryons in the CBM experiment

I. Vassiliev[1,2], *I. Kisel*[1,3], *I. Kulakov*[1,3], *A. Lebedev*[1,4], *and M. Zyzak*[1,3]

[1]IKF, Goethe-Universität, Frankfurt am Main, Germany; [2]GSI, Darmstadt, Germany; [3]FIAS, Goethe-Universität, Frankfurt am Main, Germany; [4]JINR, Dubna, Russia

One of the predicted signatures of the phase transition from nuclear matter to a deconfined quark-gluon plasma is the enhanced production of multi-strange particles. The yield of particles carrying strange quarks is also expected to be sensitive to the fireball evolution. The CBM detector will provide an unique opportunity to measure yields and directed and elliptic flow of multi-strange baryons in heavy-ion collisions at different beam energies and sizes of the colliding nuclei. To study the feasibility of such measurements in the CBM experiment, sets of 10^6 central Au+Au events from UrQMD at each of the beam energies 2, 4, 6, 8, 10, 15, 20, 25, 30 and 35 AGeV were simulated. The high events statistic allows to study even the $\Omega^\pm$ reconstruction directly, avoiding signal embedding into the UrQMD events.

Multi-strange baryons will be measured in CBM by their decay into charged hadrons which are detected in the Silicon Tracking System (STS) and in the Time-of-Flight detector (TOF). The Ω^- decays into $\Lambda + K^-$ with a branching ratio of 67.8 % and $c\tau = 2.46$ cm; the Ξ^- decays into $\Lambda + \pi^-$ with a branching ratio of 99.89 % and $c\tau = 4.92$ cm. The decays of the secondary Λ happen most often in the STS detector. The STS geometry with 8 double-sided strip detectors and realistic material budget, including analog cables, was used in the simulations. Identification of the charged final-state particles by time-of-flight was applied. The KFParticleFinder package was used to simultaneously reconstruct about 50 particles and resonances including $\Omega^\pm$, $\Xi^\pm$, Λ and $\bar\Lambda$.

$\Omega^\pm$ or $\Xi^\pm$ candidates are accepted if their decay vertex is reconstructed farther than 3 cm downstream of the target plane, and fulfills geometrical and topological quality constraints ($\chi^2_{geo} < 3\sigma$, $\chi^2_{topo} < 3\sigma$). A typical result is given in Fig. 1, showing the ΛK^- invariant-mass spectrum after all cuts at 35A GeV. The Ω^- reconstruction efficiency is about 1.8 % for central events. The reconstructed mass value (1.672 ± 0.003) GeV/c^2 is in a good agreement with the simulated book value. The invariant-mass resolution for Ω^- is 2.3 MeV/c^2.

Figure 2: Reconstructed ratios of anti-hyperon to hyperon yields as function of beam energy

The wide range beam energies allows to investigate the systematic behavior of different physics observables like directed and elliptic flow, excitation functions, anti-baryon to baryon ratios and many others. Figure 2 shows the reconstructed anti-hyperon to hyperon production ratios as function of beam energy. A hierarchy with the number of strange valence quarks is clearly visible. The black symbols correspond to the Ω^+/Ω^- ratio (S = 3), the red symbols to the Ξ^+/Ξ^- ratio (S = 2) and the blue ones to the $\bar\Lambda/\Lambda$ ratio (S = 1).

Figure 1: Reconstructed invariant-mass distribution of ΛK^- pairs in central Au+Au collisions at 35A GeV. The full line shows a fit of the Gaussian signal on top of a polynomial background.

Reconstruction of anti-hyperons in the CBM experiment

I. Vassiliev[1,2], I. Kisel[1,3], I. Kulakov[1,3], and M. Zyzak[1,3]

[1]IKF, Goethe-Universität, Frankfurt am Main, Germany; [2]GSI, Darmstadt, Germany; [3]FIAS, Goethe-Universität, Frankfurt am Main, Germany

One of the most challenging tasks of the CBM experiment is to measure yields, excitation functions and flow of anti-hyperons like Ω^+ and Ξ^+. These particles will be measured in the CBM detector by the decay into charged hadrons, which are detected in the Silicon Tracking System (STS) and in the Time-of-Flight detector (TOF). The key role of the TOF detector is anti-proton selection in a very dense environment of negatively charged pions and kaons. Figure 1 shows the m^2 calculated from the TOF measurement versus the particle momentum. Negatively charged tracks with $\mid m^2 - m_p^2 \mid < 2\sigma$ and $\mid m^2 - m_K^2 \mid > 3\sigma$ and $\mid m^2 - m_\pi^2 \mid > 3\sigma$ were used as anti-proton candidates to reconstruct $\bar{\Lambda}$. The `KFParticleFinder` was used to reconstruct $\bar{\Lambda}$ by combining secondary $\bar{p}$ and π^-.
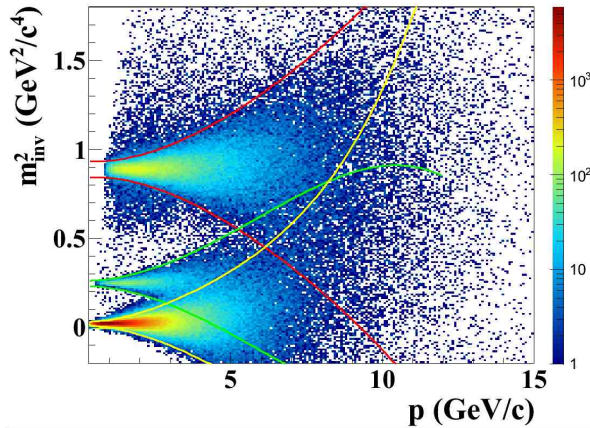
Figure 1: m^2 versus particle momentum for reconstructed tracks in the TOF detector

Figure 2 shows the invariant-mass distribution of $\bar{p}\,\pi^+$ pairs. A clear $\bar{\Lambda}$ peak is visible. The $\bar{\Lambda}$ reconstruction efficiency is 14 % for $35A$ GeV and achieves its maximum of about 22 % at $8A$ GeV. The selection of anti-proton track candidates (one or two per event) allows to significantly reduce the combinatorial background. The signal-to-background ratio is 3.4 for central Au+Au collisions at $35A$ GeV.

Combining $\bar{\Lambda}$ with a positively charged secondary kaon or pion, Ω^+ and Ξ^+ candidates are constructed. A candidate is accepted if its decay vertex is more than 3 cm downstream of the target and fulfills the geometrical and topological quality criteria $\chi^2_{geo} < 3\sigma$, $\chi^2_{topo} < 3\sigma$.

The reconstruction of multi-strange anti-hyperons was tested for central Au+Au collisions at the beam energies
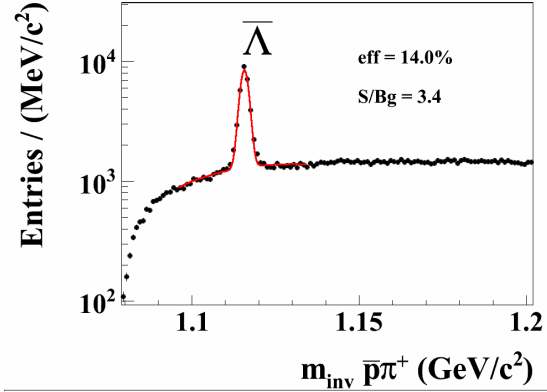
Figure 2: Reconstructed invariant-mass distribution of $\bar{p}\,\pi^+$ pairs in central Au+Au collisions at $35A$ GeV. The full line shows the Gaussian signal fit on top of a polynomial background.

$2A$, $4A$, $6A$, $8A$, $10A$, $15A$, $20A$, $25A$, $30A$ and $35A$ GeV. For each energy, 10^6 events were generated by UrQMD and simulated in the CBM setup. A typical invariant-mass spectrum is shown in Fig. 3. The Ξ^+ reconstruction efficiency is about 3.1 % at $35A$ GeV. The reconstructed mass value of (1.321 ± 0.003) GeV/c^2 is in a good agreement with the simulated book value. The invariant mass resolution is 2.3 MeV/c^2.
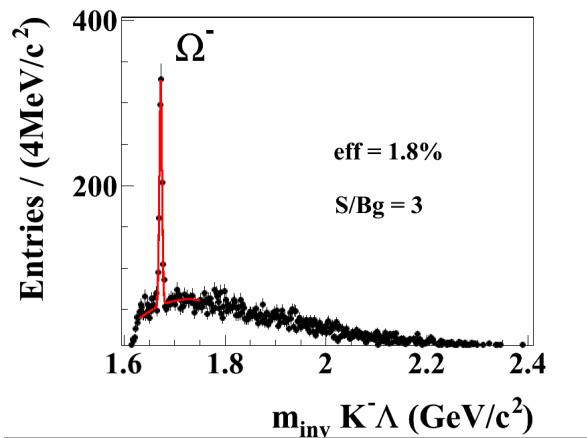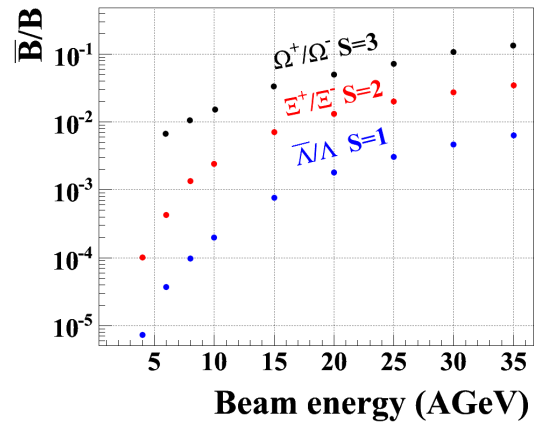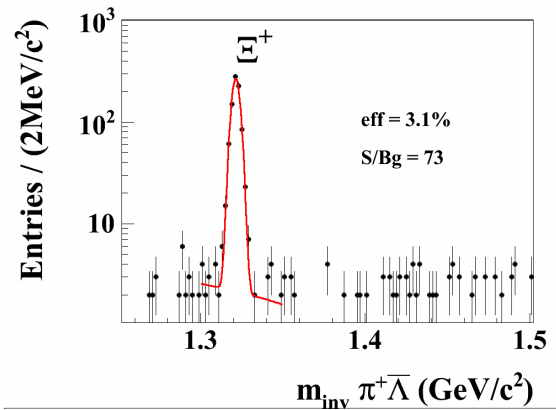

Figure 3: Reconstructed invariant-mass distribution of $\bar{\Lambda}\,\pi^+$ pairs in central Au+Au collisions at $35A$ GeV. The full line shows the Gaussian fit to the signal plus a polynomial background.

Σ* **decay reconstruction in the CBM experiment**

I. Vassiliev[1,2], I. Kisel[1,3], I. Kulakov[1,3], and M. Zyzak[1,3]

[1]IKF, Goethe-Universität, Frankfurt am Main, Germany; [2]GSI, Darmstadt, Germany; [3]FIAS, Goethe-Universität, Frankfurt am Main, Germany

The investigation of p+A collisions up to $30\,$GeV and A+A collisions from $4A$ to $11A$ GeV beam energies is considered an integral part of the CBM research program and will be performed in the first phase of FAIR with a start version of the CBM detector at the SIS-100 accelerator. This start version consists of two detector systems: the Silicon Tracking System (STS) placed in a magnetic field for the measurement of momenta and vertices, and a Time-Of-Flight (TOF) wall placed at 6–10 meter downstream of the target for hadron identification. $\Sigma^{*\pm}$ are members of the multi-strange hyperon family, consisting of uus (Σ^{*+}) and dds quarks (Σ^{*-}), respectively. In contrast to $\Omega^{\pm}$ or $\Xi^{\pm}$, $\Sigma^{*\pm}$ hyperons have a very short lifetime and thus decay predominantly inside the fireball, carrying out information about the fireball evolution.

To study the feasibility of the reconstruction of $\Sigma^{*\pm}$ decays in the CBM experiment, a set of $6 \cdot 10^6$ central C+C UrQMD events at $10A$ GeV was simulated. The high statistics allowed to use the $\Sigma^{*\pm}$ generated by UrQMD directly, without having to embed additional signals into the UrQMD background.

The detection is via the decay into $\Lambda + \pi^{\pm}$ with a branching ratio of $87\,\%$. The Λ daughters decay predominantly in the STS detector consisting of 8 layers of double-sided silicon strip sensors. The STS was simulated with realistic material budget, including passive materials like readout cables. The L1 package [1] was used for track reconstruction in the STS. Identification of charged secondaries by TOF was applied. In order to reconstruct Σ^*, all primary pions were combined with all reconstructed primary lambdas, using the KFParticleFinder. Pairs are accepted as Σ^* candidates if their common vertex fulfills geometrical and topological quality criteria: ($\chi^2_{geo} < 3\sigma$, $\chi^2_{topo} < 3\sigma$).
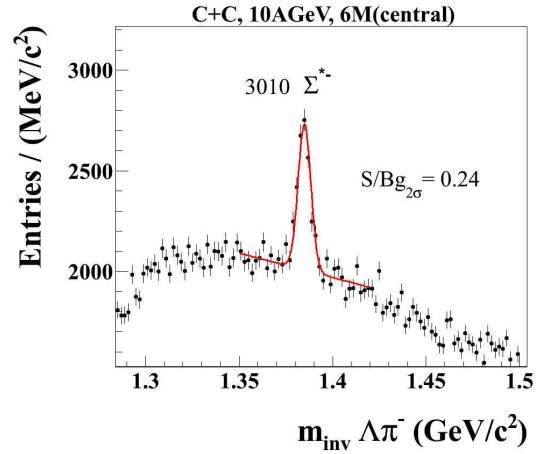
Figure 2: Reconstructed invariant-mass distribution of pairs of primary π^- and Λ in central C+C collisions at $10A$ GeV. The full line shows a Gaussian fit to the signal on top of a polynomial background.

Figures 1 and 2 show the resulting invariant-mass spectra of $\pi^+\Lambda$ and $\pi^-\Lambda$, respectively. In both cases, clear signal peaks are observable on top of the combinatorial background. The signal-to-background ratios are 0.16 and 0.24, respectively. We find the reconstructed mass value of (1.383 ± 0.003) GeV/c^2 in good agreement with the simulated value.

References

[1] I. Kisel, Nucl. Instrum. Methods **A 566** (2006) 85
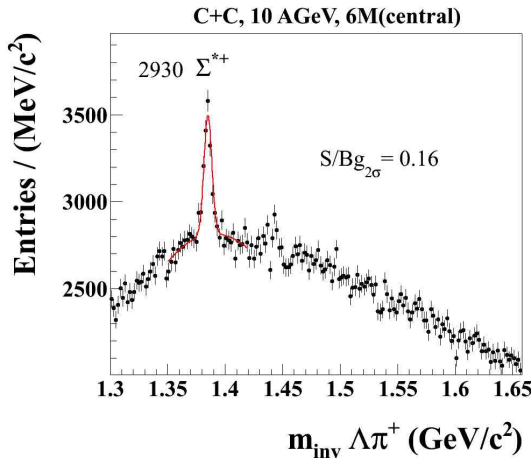

Figure 1: Reconstructed invariant-mass distribution of pairs of primary π^+ and Λ in central C+C collisions at $10A$ GeV. The full line shows a Gaussian fit to the signal on top of a polynomial background.

Reconstruction of $\omega \to \pi^+\pi^-\pi^0$ with light ECAL in p+C at SIS-100

S. M. Kiselev

ITEP, Moscow, Russia

The feasibility of the reconstruction of the decay $\omega \to \pi^+\pi^-\pi^0$ was studied on a sample of 10^6 p+C events (b = 0 fm) from UrQMD at the SIS-100 energy 30 GeV, using the `cbmroot` trunk version of September 2010. The set-up consists of MVD, STS and the light ECAL of the size $5.28 \times 4.32 \, \mathrm{m}^2$ at 6 m distance from the target. Reconstructed photons with $p > 0.5$ GeV/c and $\chi^2_{cluster} < 1000$ were used for the analysis.

The $\pi^+\pi^-\pi^0$ invariant-mass spectrum for primary Monte-Carlo tracks shows the ω peak on top of a large combinatorial background (Fig. 1). When analyzing the reconstructed signal, we consider each triplet with $0.770 \, \mathrm{GeV} < m < 0.796 \, \mathrm{GeV}$ a signal. The fraction of true ω in this selection is about 18 %.

Figure 2 shows the invariant-mass distribution for pairs of reconstructed photons with $p_t^{\gamma\gamma} > 0.2$ GeV. The π^0 peak has a width of $\sigma \sim 6$ MeV. Pairs with $0.125 \, \mathrm{GeV} < m_{\gamma\gamma} < 0.145 \, \mathrm{GeV}$ were selected as π^0 candidates.

No particle identification was applied for the selection of π^+ and π^- candidates, but a cut on the impact parameter in the target plane ($< 4\,\sigma$) was used to suppress secondary charged tracks. This selection of candidates for π^0, π^+ and π^- results in an average geometrical acceptance of 21 %, a reconstruction efficiency of 59 % and a cut efficiency of 41 %.

Figure 1: Invariant-mass spectra of primary $\pi^+\pi^-\pi^0$ triplets of for p+C at 30 GeV. The line is a fit by a Breit-Wigner function (BW) on top of a linear background.
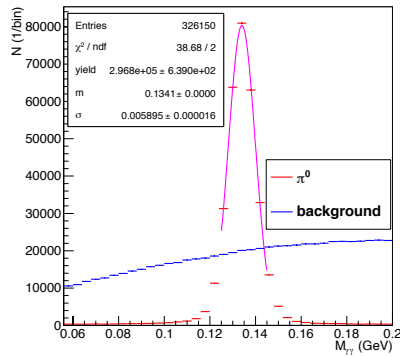
Figure 2: Invariant-mass spectra of $\gamma\gamma$ pairs with $p_t^{\gamma\gamma} > 0.2$ GeV for p+C at 30 GeV
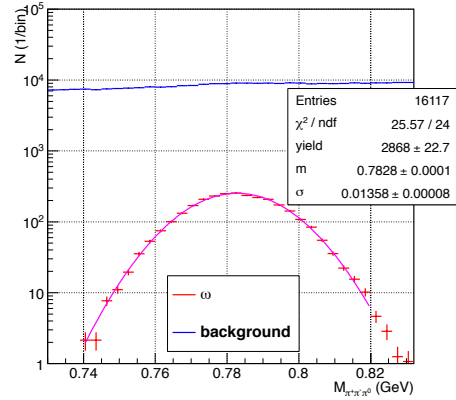
Figure 3: Invariant-mass spectra of signal and background $\pi^+\pi^-\pi^0$ triplets for p+C at 30 GeV

Fig. 3 shows the invariant mass distributions of signal and background $\pi^+\pi^-\pi^0$ triplets. We obtain a signal-to-background ratio (S/B) of about 1.7 %; the significance is 6.8. This is to be compared to the S/B in the $\pi^0\gamma$ channel, which was found to be 3.7 % [1]. The values for S/B and significances in different p_t bins are given in Table 1.

Table 1: S/B and significance for $\omega \to \pi^+\pi^-\pi^0$, calculated in the $\pm 2\sigma$ mass region, for different p_t bins

p_t [GeV]	0.0-0.4	0.4-0.8	0.8-1.2	1.2-1.6	1.6-2.0
S/B [%]	1.3	1.7	2.8	5.1	6.5
signif.	2.8	4.6	4.6	3.7	2.2

References

[1] S. M. Kiselev, CBM Progress Report 2011, p. 82

Reconstruction of $\eta'(958)$ with light ECAL in p+C at SIS-100

S. M. Kiselev

ITEP, Moscow, Russia

The feasibility of $\eta'(958)$ reconstruction using the light ECAL was studied on a sample of 10^6 p+C (b = 0 fm) events from UrQMD at the SIS-100 energy 30 GeV. The detector geometry and software version are described in [1]. We analyzed the three decay channels $\gamma\gamma$, $\pi^0\pi^0\eta$ and $\pi^+\pi^-\eta$.

1. $\eta' \rightarrow \gamma\gamma$ (BR = 2 %). The MC reference is a pair of primary γ with 0.957 GeV $< m_{\gamma\gamma} <$ 0.959 GeV. The acceptance and reconstruction efficiencies for the signal are 30 % and 96 %, respectively. The invariant-mass spectrum for reconstructed $\gamma\gamma$ pairs in the η' range is shown in Fig. 1. The S/B ratio is 0.3 %. With the simulated statistics, the significance is 0.5.
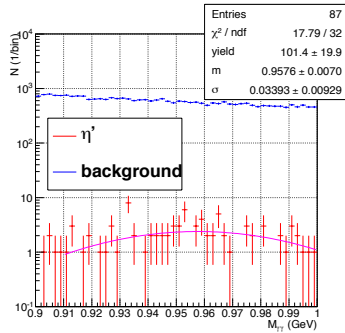
Figure 1: Invariant-mass spectra of reconstructed $\gamma\gamma$ pairs for p+C at 30 GeV

2. $\eta' \rightarrow \pi^0\pi^0\eta$ (BR = 21 %). We assume triplets of primary $\pi^0\pi^0\eta$ in the range 0.95 GeV $< M_{\pi^0\pi^0\eta} <$ 0.96 GeV to be the η' signal. Candidates for π^0 and η are reconstructed $\gamma\gamma$ pairs in the mass range 0.125 GeV $< m_{\gamma\gamma} <$ 0.145 GeV and 0.5 GeV $< m_{\gamma\gamma} <$ 0.6 GeV, respectively. We find an acceptance of 4 %, a reconstruction efficiency of 25 % and a cut efficiency of 26 %. Figure 2 shows the invariant-mass distributions for signal and background. The S/B ratio of 3.2 % is one order of magnitude higher than for the $\gamma\gamma$ channel; the significance is 0.5.

3. $\eta' \rightarrow \pi^+\pi^-\eta$ (BR = 45 %). We consider triplets of primary π^+, π^- and η in the mass range 0.960 GeV $< m_{\pi^+\pi^-\eta} <$ 0.964 GeV to be η' signals. No PID information was used for the selection of π^+ and π^- candidates, but secondary charged tracks were suppressed by a impact parameter cut $< 4\sigma$. As η candidates, we select photon pairs with $p_t^{\gamma\gamma} > 0.2$ GeV and 0.53 GeV $< m_{\gamma\gamma} <$ 0.56 GeV. The average values of acceptance, reconstruction and cut efficiencies are 8 %, 92 % and 37 %, respectively. The total detection efficiency of 3 % is one order of magnitude larger than for the $\eta' \rightarrow \pi^0\pi^0\eta$ channel.
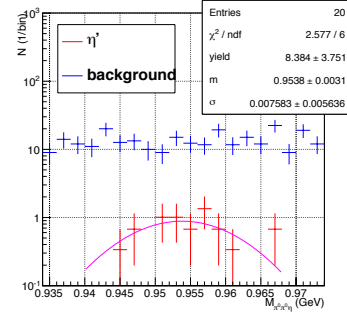
Figure 2: Invariant-mass spectra of reconstructed $\pi^0\pi^0\eta$ triplets with $p_t > 0.3$ GeV for p+C at 30 GeV

The invariant-mass distributions for the selected $\pi^+\pi^-\eta$ triplets is shown in Fig. 3. The S/B ratio $((S/B)_{2\sigma} = 1\%)$ is three times smaller than for the $\eta' \rightarrow \pi^0\pi^0\eta$ channel; the significance is 0.4. However, S/B increases considerably with the transverse momentum (see Table 1).
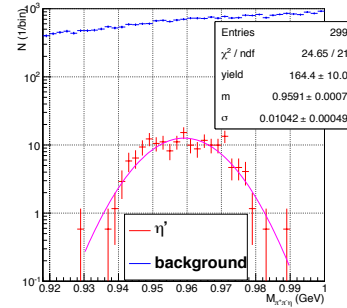
Figure 3: Invariant-mass spectra of reconstructed $\pi^+\pi^-\eta$ triplets for p+C at 30 GeV

Table 1: S/B and significance for the decay $\eta' \rightarrow \pi^+\pi^-\eta$ for different p_t bins

p_t [MeV/c]	0.4 - 0.8	0.8 - 1.2	1.2 - 2.0
S/B [%]	1.0	1.7	6.6
signif.	0.9	0.9	1.3

References

[1] S. M. Kiselev, *Reconstruction of $\omega \rightarrow \pi^+\pi^-\pi^0$ with light ECAL in p+C at SIS-100*, this report

Reconstruction of Σ hyperons with light ECAL in p+C at SIS-100

S. M. Kiselev

ITEP, Moscow, Russia

The feasibility of Σ hyperon reconstruction using the light ECAL was studied on a sample of 10^6 p+C (b = 0 fm) events from UrQMD at the SIS-100 energy 30 GeV. The detector geometry and software version are described in [1]. We analyzed the decays $\Sigma^0 \to \Lambda\gamma$ and $\Sigma^+ \to p\pi^0$.

For the channel $\Sigma^0 \to \Lambda\gamma$, the Λ hast to be reconstructed through its decay into $p\pi^-$. For the selection of Λ candidates, no PID is used, but we apply single-track cuts on the impact parameter in the target plane ($> 4\,\sigma$) as well as pair cuts on the vertex quality ($\chi^2_{\mathrm{vertex}} < 2$, distance of closest approach < 2 cm). In addition, topological cuts on the pair were applied (impact parameter of pair momentum < 0.15 cm; decay vertex z position $3 - 35$ cm). Pairs of oppositely charged tracks fulfilling these criteria and having an invariant mass of $m_\Lambda \pm 25$ MeV under the p / π mass hypothesis were taken as a Λ candidate and were combined with reconstructed photons with $p_t > 0.3$ GeV and $\chi^2_{\mathrm{cluster}} < 1000$ to form Σ^0 candidates.

background ratio ($S/B_{2\sigma}$) of about 9.2 %; the significance is 5.2. The geometrical acceptance is 6.5 %, the reconstruction efficiency 53 % and the cut efficiency 33 %. S/B and significance for different p_t bins are given in Table 1.

For the channel $\Sigma^+ \to p\pi^0$, we construct π^0 candidates from γ pairs with 0.124 GeV $< m_{\gamma\gamma} < 0.144$ GeV. No PID was used to select the proton candidates, but primary tracks were suppressed by a cut in the impact parameter in the target plane ($> 5\,\sigma$). The average values of acceptance, reconstruction efficiency and cut efficiency are 5.6 %, 45 % and 15 %, respectively. The resulting invariant-mass distribution is shown in Fig. 2. The signal-to-background ratio ($S/B_{2\sigma}$) is 7.9 %, the significance is 2.8. The values for S/B and significance in different p_t bins are given in Table 2.
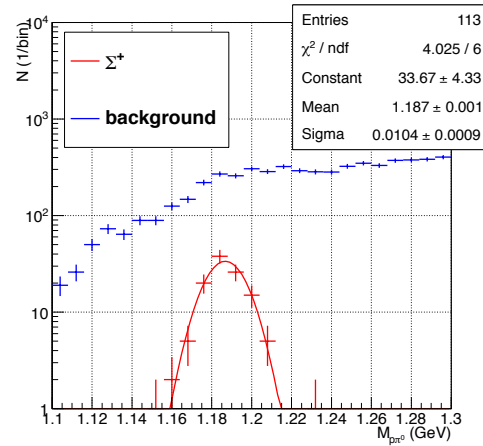
Figure 2: $p\pi^0$ invariant-mass spectra of signal and background pairs for p+C at 30 GeV

Figure 1: $\Lambda\gamma$ invariant-mass spectra of signal and background pairs for p+C at 30 GeV

Table 1: S/B and significance for $\Sigma^0 \to \Lambda\gamma$, calculated in the $\pm 2\,\sigma$ mass region for different p_t bins

p_t [GeV]	0.4 - 2.0	0.8 - 2.0	1.2 - 2.0
S/B [%]	9.4	11.2	13.9
signif.	4.6	2.8	1.4

Table 2: S/B and significance for $\Sigma^+ \to p\pi^0$, calculated in the $\pm 2\sigma$ mass region, for different p_t bins

p_t [GeV]	0.6 - 2.0	1.0 - 2.0
S/B [%]	10.3	18.5
signif.	2.9	2.4

Figure 1 shows the $\Lambda\gamma$ invariant-mass distributions for signal and background pairs. We obtain a signal-to-

References

[1] S. M. Kiselev, *Reconstruction of $\omega \to \pi^+\pi^-\pi^0$ with light ECAL in p+C at SIS-100*, this report

Status of low-mass di-electron simulations in the CBM experiment

E. Lebedeva and C. Höhne

Justus Liebig University, Gießen, Germany

The reconstruction of low-mass vector mesons is one of the main goals of the CBM experiment at FAIR. The CBM experiment will be able to reconstruct low-mass vector mesons in both the di-electron and the di-muon decay channel. The current status of low-mass di-electron simulations in central Au+Au collisions at $8A$ GeV (SIS-100) and $25A$ GeV (SIS-300) beam energy is presented in this report.

Results were obtained with the latest version of the `cbmroot` software (January 2013) which includes realistic detector descriptions. The background was generated using the transport code UrQMD including di-electron pairs from γ conversions, π^0- and η-Dalitz decays. Di-electron pairs from ρ, ω, ϕ, and ω-Dalitz decays were simulated by the PLUTO event generator and embedded into UrQMD events. The detector setup includes the STS, RICH, TRD and TOF detectors. For $8A$ GeV beam energy, the TRD detector was excluded from the simulations. A 25 μm thick gold target was used in order to avoid additional background from γ conversions in the target.

An electron candidate has to be reconstructed and identified in all detectors, namely RICH, TRD and TOF. Since the TRD is not used for 8 AGeV beam energy simulations, an additional momentum cut at 5.5 GeV/c was implemented in order to reject large-momentum pions.

The background rejection strategy includes several cuts. The first cut is based on the assumption that all pairs with $M_{ee} < 25\,\text{MeV}/c^2$ stem from γ conversion; such pairs are fully removed from further combinatorics. The aim of the next two cuts is to reject $e^{\pm}$ pairs where one partner is reconstructed only in the STS (segment track) or was fully reconstructed but not identified as electron. The last cut is a transverse momentum cut.

The dominant background source are random combinations of $e^{\pm}$ from π^0-Dalitz decays and γ conversions. For $8A$ GeV beam energy, the main contributions to back-
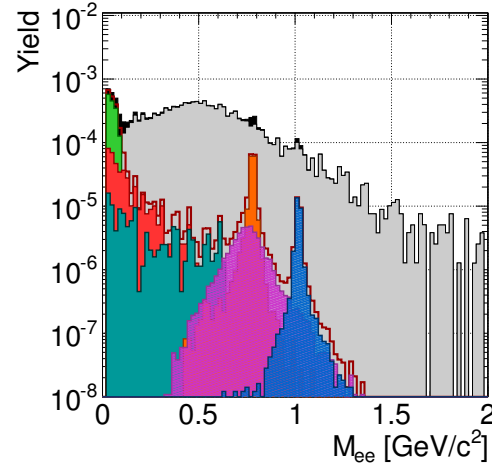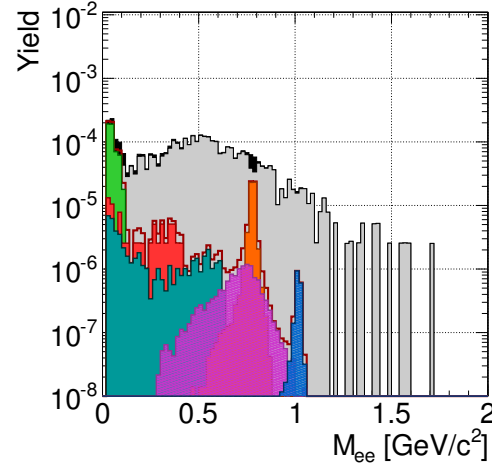
Figure 1: Invariant-mass spectra after applying all cuts for central Au+Au collisions at a beam energy of $8A$ GeV (upper panel, 100k events) and $25A$ GeV (lower panel)

ground pairs come from combinations of $e^{\pm}$ from π^0-Dalitz decays and other particles (35 %), $e^{\pm}$ from π^0-Dalitz and γ conversion (23 %) and $e^{\pm}$ from different π^0-Dalitz decays (18 %). The numbers for $25A$ GeV beam energy are 23 %, 31 % and 29 %, respectively.

The invariant-mass spectra after applying all cuts are presented in Fig. 1 for $8A$ GeV beam energy (upper plot) and for $25A$ GeV beam energy (lower plot). S/B ratio and reconstruction efficiency for ρ^0, ω and ϕ mesons and for different invariant-mass regions are summarized in Table 1.

Table 1: S/B ratio and reconstruction efficiency after applying all cuts

	8A GeV		25A GeV	
	S/B	Eff.[%]	S/B	Eff.[%]
ρ	-	3.12	-	4.39
ω	0.64	4.11	0.31	5.53
ϕ	0.04	4.89	0.11	7.08
M_{ee}:0.0-0.2	1.94	-	1.44	-
M_{ee}:0.2-0.6	0.031	-	0.019	-
M_{ee}:0.6-1.2	0.067	-	0.053	-

J/ψ reconstruction in Au + Au collisions at $10A$ GeV

O. Derenovskaya[1] and I. Vassiliev[2,3]

[1]LIT JINR, Dubna, Russia; [2]GSI, Darmstadt, Germany; [3]Goethe-Universität, Frankfurt, Germany

In this report, we discuss the feasibility of J/ψ reconstruction through its decay into e^+e^- in Au + Au collisions at the sub-threshold beam energy of $10A$ GeV, the lowest accessible beam energy from SIS-300.

In order to simulate this decay, the electron-positron pair, generated by PLUTO, was embedded into a central Au+Au UrQMD event. The STS geometry v12b with 8 layers of double-sided strip detectors, cables and support frames was used for this simulations. The electrons and positrons were identified by the RICH, TRD and TOF detectors corresponding to the full CBM setup.

The radius of the reconstructed rings in the RICH detector is shown in Fig. 1 as a function of the particle momentum. A maximal distance of 1 cm was allowed for ring-track matching. The cuts applied to the ring parameters to separate electrons from pions are shown as red lines in Fig. 1.
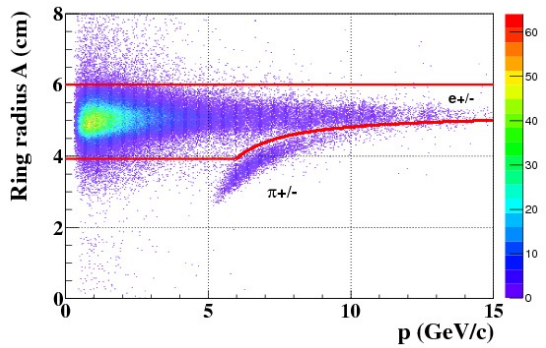
Figure 1: Radius of the reconstructed rings as a function of the particle momentum

Based on the individual and total energy loss, the modified ω_n^k criterion [1] was used for the selection of electrons and suppression of pions in the TRD. The information from TOF is also used to select low-energy electrons by a cut on the squared mass versus momentum as indicated by the red line in Fig. 2.

Oppositely charged tracks emerging from the target and identified as electrons or positrons by the RICH, TRD and TOF were combined to construct a J/ψ candidate. The KFParticle package [2] was used to reconstruct the signal event topology. In order to suppress the physical electron-positron background, a transverse momentum cut at 1 GeV/c was applied.

The resulting e^+e^- invariant-mass spectrum after electron identification and background rejection cuts is shown in Fig. 3 for 10^{12} central events. The combinatorial
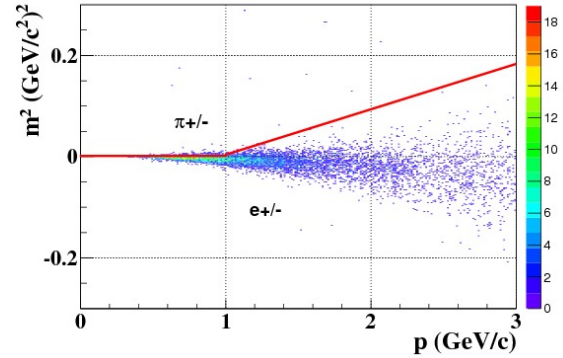
Figure 2: Squared mass calculated from the TOF measurement as a function of the particle momentum

background was obtained by the event mixing technique and scaled according to the assumed J/ψ multiplicity ($1.74 \cdot 10^{-7}$ from the HSD model) and the branching ratio (6 %). The signal is clearly visible above the background; the signal-to-background ratio is 0.12.

We obtain a J/ψ reconstruction efficiency of 12 %. Assuming the multiplicity as predicted by HSD and an interaction rate of 10 MHz, the CBM detector allows to collect about 43 J/ψ per hour.
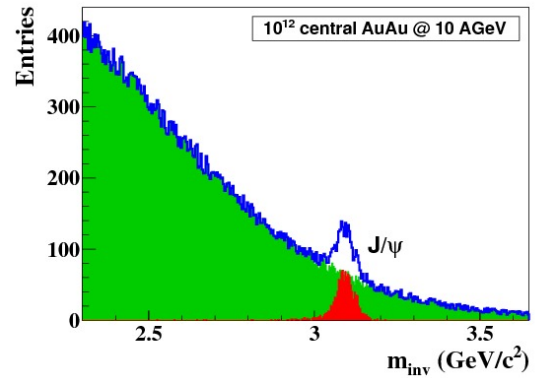
Figure 3: Reconstructed e^+e^- invariant-mass spectrum for central Au+Au collisions at $10A$ GeV

References

[1] O. Derenovskaya and V. Ivanov, ω_n^k *test vs. ANN in the J/ψ selection problem based on the TRD*, this report

[2] S. Gorbunov and I. Kisel, *Reconstruction of decayed particles with the Kalman Filter*, CBM-SOFT-note-2007-003

Study of the CBM detector capabilities for open charm elliptic flow measurements

S. Seddiki[1] and F. Rami[2]

[1]GSI, Darmstadt, Germany; [2]IPHC, Strasbourg, France

The measurement of the elliptic flow of open charm mesons in heavy ion collisions at FAIR energies is interesting for the investigation of a possible phase transition from hadronic matter to a deconfined quark gluon plasma. It is, however, very challenging at FAIR, close to the charm production threshold. It is not only limited by the maximum collision rate that can be achieved in the experiment (constrained mostly by the read-out time of the MVD) but also relies on the possibility to accurately measure the azimuthal orientation of the reaction plane. The purpose of this work was to assess the statistical accuracy with which the D-meson elliptic flow can be measured in CBM. This was done for semi-peripheral Au($25A$ GeV)+Au collisions using the `cbmroot` simulation framework.

In CBM, the reaction plane can be determined independently by two sub-detectors (covering different rapidity regions), namely the PSD calorimeter and the STS tracker. The performance of each of those sub-detectors was investigated using the UrQMD event generator, the transport code GEANT, detailed simulations (accounting for the track reconstruction in the STS, the energy resolution in the PSD, etc.) and the event plane method [1]. Both detectors were found to provide a similar accuracy, in particular for semi-peripheral collisions (in the impact parameter range from 5 to 9 fm) where the best resolution was obtained: an azimuthal angular resolution of about 40°[2].
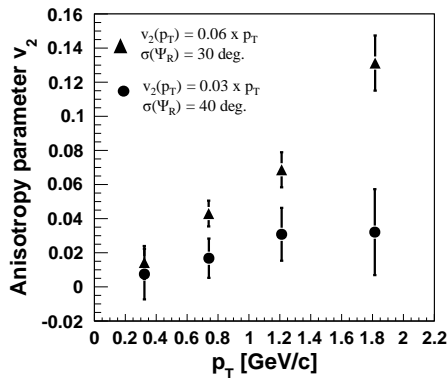
distributions of these mesons. This simple procedure was justified by the good performances of CBM for D-meson reconstruction in Au($25A$ GeV)+Au collisions (e.g., a good ratio S/B) [3]. D-meson azimuthal angles were smeared with the estimated reaction plane resolution, and the resulting distributions were analyzed to extract v_2 as a function of transverse momentum. The obtained v_2 values, after being corrected for the reaction plane resolution, are shown in Fig. 1. Two assumptions were made: i) the p_t-differential v_2 of mid-rapidity D-mesons predicted by HSD [4]: $v_2 \sim 0.03 \times p_t$ (up to $p_t = 2$ GeV/c), ii) a flow effect higher by a factor of two if partonic interactions take place at FAIR energies (supported by PHSD [5] for charged particles at mid-rapidity). Table 1 presents the statistical uncertainties on the integrated v_2 in case ii.

Table 1: Statistical uncertainties for the p_t-integrated v_2 of D-mesons, obtained in case ii (see text) and for the same event sample as in Fig. 1

particles	yield/year	v_2	$\delta v_2/v_2$
N_D	6.0×10^4	0.049 ± 0.005	10 %
D^+	1.3×10^4	0.054 ± 0.010	18 %
D^-	2.0×10^4	0.055 ± 0.009	16 %
D^0	7.0×10^3	0.062 ± 0.015	24 %
$\bar{D}^0$	2.0×10^4	0.055 ± 0.009	16 %

We conclude that even very small magnitudes of D-meson v_2 can be measured in one year of data taking with the CBM detector (see Figure1). If partonic interactions take place at FAIR, the experiment will be able to measure accurately its integrated magnitude (see Table 1). However, more detailed p_t-differential measurements would be feasible (with moderate statistical precision) only if all reconstructed D-mesons are included (see Figure 1). Performing such measurements for individual D-meson species would require higher statistics and hence higher collision rates, beyond the expected limit tolerable by the MAPS sensors.

Figure 1: Elliptic flow parameter v_2 of D-mesons as a function of transverse momentum in semi-peripheral Au($25A$ GeV)+Au collisions, shown for two assumptions on the flow magnitude (see text). The statistical uncertainties are obtained for 6×10^4 D-mesons, measurable in 8 weeks "beam on target" at a collision rate of 400 kHz[3] (limited by the MAPS read-out time of 10 μs expected at SIS-300).

To study the D-meson elliptic flow, a p_t-dependent anisotropy was added to the generated (uniform) azimuthal

References

[1] A. M. Poskanzer and S. A. Voloshin., Phys. Rev. **C 58** (1998) 1671

[2] S. Seddiki, *Reaction plane reconstruction in the CBM experiment at SIS-300*, this report

[3] S. Seddiki, PhD thesis, Strasbourg and Frankfurt 2012

[4] O. Linnyk, E. L. Bratkovskaya and W. Cassing, Int. J. Mod. Phys. **E 17** (2008) 1367

[5] V. P. Konchakovski *et al.*, Phys. Rev. **C 85** (2012) 044922

CBM publications 2012

- A. Abuhoza *et al.*:
  Study of the Influence of Construction Materials on the Ageing Properties of High Rate Gas Detectors
  Phys. Proc. **37** (2012) 442
  doi:10.1016/j.phpro.2012.02.391

- J. Adamczewski-Musch *et al.*:
  Data acquisition and online monitoring software for CBM test beams
  J. Phys.: Conf. Ser. **396** (2012) 012001
  doi:10.1088/1742-6596/396/1/012001

- M. Al-Turany *et al.*:
  The FairRoot framework
  J. Phys.: Conf. Ser. **396** (2012) 022001
  doi:10.1088/1742-6596/396/2/022001

- I. Deppner *et al.*:
  The CBM time-of-flight wall
  Nucl. Instrum. Methods **A 661** (2012) S121
  doi:10.1016/j.nima.2010.09.165

- I. Deppner and N. Hermann:
  A Multistrip-MRPC prototype for the CBM Time-of-Flight wall
  Pos(RPC2012)016
  http://pos.sissa.it/archive/conferences/159/016/RPC2012_016.pdf

- M. Deveaux *et al.*:
  A first generation prototype for the CBM micro vertex detector
  Nucl. Instrum. Methods **A**, in press
  doi:10.1016/j.nima.2012.10.013

- J. Eschke:
  Compressed baryonic matter experiment at FAIR
  EPJ Web Conf. **20** (2012) 05002
  doi:10.1051/epjconf/20122005002

- V. Friese:
  The CBM Experiment - A Status Report
  Phys. Atom. Nucl. **75** (2012) 585
  doi:10.1134/S1063778812050079

- V. Friese:
  Computational Challenges for the CBM Experiment
  Lect. Notes Comp. Sci. **7125** (2012) 17
  doi:10.1007/978-3-642-28212-6_2

- D. Gonzalez-Diaz
  Simulation of resistive plate chambers with multi-strip readout
  Nucl. Instrum. Methods **A 661** (2012) S172
  doi:10.1016/j.nima.2010.09.067

- D. Gonzalez-Diaz, H. Chen and Y. Wang:
  RPC simulations from a current stand-point
  Pos(RPC2012)035
  http://pos.sissa.it/archive/conferences/159/035/RPC2012_035.pdf

- A. Laso Garcia *et al.*:
  Ceramic Resistive Plate Chambers for High Rate Environments
  Pos(RPC2012)066
  http://pos.sissa.it/archive/conferences/159/066/RPC2012_066.pdf

- S. Lebedev *et al.*:
  Electron reconstruction and identification capabilities of the CBM Experiment at FAIR
  J. Phys.: Conf. Ser. **396** (2012) 022029
  [doi:10.1088/1742-6596/396/2/022029](doi:10.1088/1742-6596/396/2/022029)

- S. Lebedev *et al.*:
  Algorithms and Software for Event Reconstruction in the RICH, TRD and MUCH Detectors of the CBM Experiment
  Lect. Notes Comp. Sci. **7125** (2012) 246
  [doi:10.1007/978-3-642-28212-6_28](doi:10.1007/978-3-642-28212-6_28)

- P. A. Loizeau and N. Herrmann:
  A Free-Streaming Readout for the CBM Time of Flight wall
  Pos(RPC2012)082
  http://pos.sissa.it/archive/conferences/159/082/RPC2012_082.pdf

- M. Petris *et al.*:
  Toward a high granularity and high counting rate, differential readout timing MRPC
  Nucl. Instrum. Methods **A 661** (2012) S129
  doi:10.1016/j.nima.2010.09.162

- M. Petrovici *et al.*:
  High counting rate, differential, strip read-out, multi gap timing RPC
  Pos(RPC2012)067
  http://pos.sissa.it/archive/conferences/159/067/RPC2012_067.pdf

- J. Wang *et al.*:
  A prototype of strip readout MRPC for CBM-TOF
  Nucl. Instrum. Methods **A 661** (2012) S125
  doi:10.1016/j.nima.2010.09.068

- J. Wang *et al.*:
  Conceptual design of the CBM-TOF wall with real-size high-rate MRPC modules based on the newly developed Chinese doped glass
  Pos(RPC2012)015
  http://pos.sissa.it/archive/conferences/159/015/RPC2012_015.pdf

- Yi Wang *et al.*:
  Progress of R&D and production of timing RPCs in Tsinghua University
  Nucl. Instrum. Methods **A 661** (2012) S134
  doi:10.1016/j.nima.2010.08.076

- Yi Wang *et al.*:
  Aging test of high rate MRPC
  Pos(RPC2012)014
  http://pos.sissa.it/archive/conferences/159/014/RPC2012_014.pdf

- J. Yi *et al.*:
  Research and development of a CBM-RICH prototype
  EPJ Web Conf. **20** (2012) 05004
  doi:10.1051/epjconf/20122005004
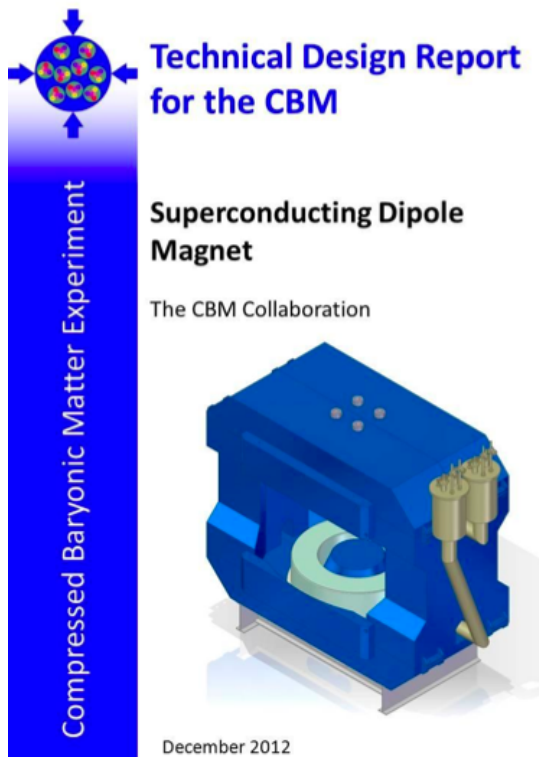
Submitted to FAIR-ECE December 2012

Submitted to FAIR-ECE December 2012

CBM presentations 2012

`http://cbm-wiki.gsi.de/cgi-bin/view/Public/PublicPresentations2012`

Doctoral, diploma, master and bachelor theses 2012

`http://cbm-wiki.gsi.de/cgi-bin/view/Public/Thesis2012`

CBM FEE/DAQ/FLES Workshop

25 – 27 January 2012, Mannheim, Germany

CBM will use free-streaming read-out electronics which leads to very high data bandwidth requirements between the front-end ASCIs and the first data processing stages located in the CBM annex building and the FAIR Tier 0 computing center where CBM 'First Level Event Selector' (FLES) will be located. The goal of the workshop was to discuss the main challenges of the front-end electronics and read-out chain, especially the front-end ASICs, the data transport chain from detector to CBM annex building and further on to FLES, and the hit-level data pre-processing. The agenda covered the status of all ongoing ASIC developments, the potential of FPGA based front-end concepts, as well as a session devoted to the CBM radiation environment. In addition to contributions from CBM collaborators, Ken Wyllie presented an overview of the LHCb front-end electronics.

https://indico.gsi.de/conferenceDisplay.py?confId=1412

19th CBM Collaboration Meeting and CBM Physics Workshop

26 – 30 March 2012, Darmstadt, Germany

https://indico.gsi.de/conferenceDisplay.py?confId=1368

First Workshop on Quality Assurance for the CBM Silicon Tracking System
14 – 15 June 2012, Tübingen, Germany

The development of quality assurance procedures and laboratory infrastructure is of central importance for the preparation of a yield-maximized production of the highly-integrated module and ladder components that will build up the Silicon Tracking System.

Members of the STS project from GSI, the Goethe University Frankfurt, JINR, the Kiev Institute for Nuclear Research and the University of Tübingen met on 14 and 15 June, 2012 for a first dedicated workshop on this topic. The meeting was hosted by the CBM group at the Eberhard Karls University in Tübingen, Germany. The subject is closely related to the Joint Research Activity ULISINT of the EU-FP7 project HadronPhysics3 through which travel support was realized.

The workshop started with reviews of the approaches made for the large-scale productions of components for the silicon tracking detector projects of the LHC experiments, where significant experience has been gained. The agenda continued with summaries of achievements and open issues made in the STS team with the quality characterization of CBM prototype silicon microstrip sensors, cables and front-end electronics available to date. For the tests of those basic components a rather clear view emerged of the test procedures and the required equipment. For the higher integrated objects, i.e. modules and ladders, no clear procedures could be named as they strongly depend on the exact details of the structures. Further work is needed to develop the technical approach towards their assembly. The quality assurance tasks will be performed in several test centers. The same test standards and infrastructures have to be established there. The development and deployment of a data base will be important to gather the information from all test centers. Follow-up workshops will be organized to further advance the project.

https://indico.gsi.de/conferenceDisplay.py?confId=1621

CBM Workshop on Online Data Processing
10 – 12 September 2012, Darmstadt, Germany

The triggerless data acquisition concept of CBM poses novel challenges to the various steps of online data processing, from the self-triggered front-end electronics to the real-time reconstruction and data selection. While the components of the data processing chain have been subject of research and development in the past years, a realization of the entire data flow has not yet been demonstrated. This workshop aimed at reviewing the present status of developments and to discuss, shape and coordinate the further efforts towards the full CBM online data processing chain. To this behalf, 26 participants convened at GSI in September 2012. Specific topics were: data sources (FEE), data transport and pre-processing (DPB), First-Level Event Selection farm (FLES), online reconstruction software, controls, and offline software framework and simulations of the online data flow. A tentative structure of an CBM Online Project was worked out, which is to be proposed to the Collaboration Board in spring 2013.

https://indico.gsi.de/conferenceDisplay.py?confId=1838

20th CBM Collaboration Meeting

24 – 28 September 2012, Kolkata, India

http://indico.vecc.gov.in/indico/internalPage.py?pageId=0&confId=16

Workshop on Module Assembly for the CBM Silicon Tracking System

3 – 7 December 2012, Darmstadt, Germany

The understanding of the challenges with the module assembly for the Silicon Tracking System, and the elaboration of a feasible assembly procedure were in the focus of a workshop held at GSI from 3 to 7 December 2012. The participants comprised the STS team based at GSI and experts from the State Enterprise Scientific Research Technological Institute of Instrument Engineering (SE SRTIIE), Kharkov, Ukraine. Support was realized through the EU-FP7 Hadron-Physics3 joint research activity "ULISINT", to which the event served as a work meeting.

The STS module is built using micro cable technology whose manufacturing procedures and challenges were discussed in particular with respect to maximizing yield and reliability. The discussions were augmented with hands-on work at dedicated bonding equipment in the GSI's detector laboratory clean room space.

As an outcome of the workshop a focussed R&D project was elaborated. Starting with the cable preparation for a STS module to be used in a beam test in 2013 and the evaluation of technological options of cable-to-sensor and cable-to-electronics tab-bonding, an optimum design and assembly procedure for the STS modules is targeted, leading to quantitative estimates on yield and production effort. An adequate structure is being worked out for a continued GSI - SE SRTIIE R&D cooperation, necessary work packages and development tasks.

https://indico.gsi.de/conferenceDisplay.py?confId=2021

2nd **CBM Software Workshop**

4 – 6 December 2012, Ebernburg, Germany

The second CBM Software Workshop united 21 participants in the beautiful scenery of Ebernburg Castle. Unlike its predecessor, the workshop concentrated on the discussion among developers and excluded training aspects, which were taken care of in a separate software school.

The focus of the workshop was put on software issues hardly addressed so far, but where activities need to be started urgently, such as alignment and calibration. The direction in which to continue the time-based simulations and reconstruction was a vivid subject of discussions as well as the structure of the repository and the relationship of online and offline software. The latter addressed both the L1 package developed for deployment on the FLES and the DABC/Go4 software currently used for in-beam detector tests. Apart from such strategical discussions, very practical aspects like a common geometry format and a framework for quality assurance were brought up.

Like in 2011 at the occasion of the first CBM Software Workshop, Ebernburg Castle provided a nice working atmosphere and proved to be a quite adequate site for this meeting. If possible, it will be made the regular place to host the workshop series.

https://indico.gsi.de/conferenceDisplay.py?confId=1810

The CBM Collaboration

- **Aligarh, India, Department of Physics, Aligarh Muslim University**

  N. Ahmad, M.D. Azmi, M. Irfan, M.M. Khan

- **Beijing, China, Department of Engineering Physics, Tsinghua University**

  Jianping Cheng, Zhi Deng, Jin Li, Yuanjing Li, Yulan Li, Yi Wang, Qian Yue, Xianglei Zhu

- **Bhubaneswar, India, Institute of Physics**

  D.P. Mahapatra, P.K. Sahu

- **Bucharest, Romania, Horia Hulubei National Institute of Physics and Nuclear Engineering (IFIN-HH)**

  C. Andrei, D. Bartoş, I. Berceanu, G. Caragheorgheopol, V. Cătănescu, F. Constantin, A. Herghelegiu, M. Petriş, A. Petrovici, M. Petrovici, A. Pop, C. Schiaua, M.-G. Târzilă

- **Bucharest, Romania, Atomic and Nuclear Physics Department, University of Bucharest**

  D. Argintaru, V. Baban, C. Beşliu, M. Cãlin, V. Covlea, T. Eşanu, A. Jipa, I. Lazanu, C. Ristea, O. Ristea, A. Scurtu

- **Budapest, Hungary, Eötvös Loránd University (ELTE)**

  B. Bozsogi, M. Csanád, Á. Fülöp, A. Kiss

- **Budapest, Hungary, KFKI Research Institute for Particle and Nuclear Physics (KFKI-RMKI)**

  T. Kiss, T. Tolyhi, Gy. Wolf

- **Chandigarh, India, Department of Physics, Panjab University**

  M.M. Aggarwal, A.K. Bhati, M. Kaur

- **Darmstadt, Germany, Facility for Antiproton and Ion Research in Europe GmbH (FAIR)**

  J. Eschke[1], W.F.J. Müller[1]

- **Darmstadt, Germany, GSI Helmholtzzentrum für Schwerionenforschung GmbH (GSI)**

  A. Abuhoza[7,2], J. Adamczewski-Musch, M. Al-Turany, A. Andronic, E. Badura, T. Balog[8], E. Berdermann, D. Bertini, S. Chatterji, M.I. Ciobanu[9], H. Deppe, H. Flemming, U. Frankenfeld, V. Friese, J. Frühauf, J. Hehner, J.M. Heuser, R. Holzmann, R. Karabowicz, M. Kiš, V. Kleipa, K. Koch, P. Koczoń, B.W. Kolb, D. Kresan, J. Kunkel, S. Linev, S. Löchner, W. Niebur, J. Pietraszko, J. Sanchez Rosado, C.J. Schmidt, S. Seddiki, A. Senger, P. Senger[2], C. Simons, D. Soyk, C. Sturm, F. Uhlig, P. Zumbruch

- **Darmstadt, Germany, Institut für Kernphysik, Technische Universität Darmstadt**

  T. Galatyuk

- **Dresden, Germany, Institut für Strahlenphysik, Helmholtz-Zentrum Dresden-Rossendorf (HZDR)**

  K. Heidel, J. Hutsch, B. Kämpfer, R. Kotte, A. Laso Garcia, L. Naumann, C. Wendisch, J. Wüstenfeld

- **Dubna, Russia, Laboratory of Information Technologies, Joint Institute for Nuclear Research (JINR-LIT)**

  P. Akishin, E. Akishina, T. Akishina, S. Baginyan, O. Derenovskaya, Valery Ivanov, Victor Ivanov, P. Kisel, G. Kozlov, E. Litvinenko, G. Ososkov, A. Raportirenko, P. Zrelov

- **Dubna, Russia, Veksler and Baldin Laboratory of High Energy Physics, Joint Institute for Nuclear Research (JINR-VBLHEP)**

  Yu. Anisimov, S. Avdeyev, A. Bychkov, V. Chepurnov, S. Chernenko, K. Davkov, V. Davkov, S. Dubnichka, A. Dubnichkova, O. Fateev, V. Golovatyuk, Yu. Gusakov, A. Ierusalimov, E.-M. Ilgenfritz, V. Karnaukhov, G. Kekelidze, V. Kirakosyan, V. Ladygin, A. Malakhov, J. Manjavidze, V. Mialkovski, Yu. Murin, S. Parzhitskiy, D. Peshekhonov, V. Peshekhonov, E. Plekhanov, S. Razin, A. Shabunov, I. Tsakov, T. Vasiliev, Yu. Zanevsky, A. Zinchenko, V. Zryuev

- **Frankfurt, Germany, Frankfurt Institute for Advanced Studies, Goethe Universität Frankfurt (FIAS)**

  M. Bach, J. de Cuveland, S. Gorbunov, D. Hutter, S. Kalcher, I. Kisel, M. Kretz, I. Kulakov[1], V. Lindenstruth[1], M. Zyzak[1]

- **Frankfurt, Germany, Institut für Kernphysik, Goethe Universität Frankfurt**

  V. Akishina[3,1], S. Amar-Youcef, H. Appelshäuser, A. Arend, C. Baumann, T. Bel, C. Blume, M. Deveaux, P. Dillenseger, D. Doering, I. Fröhlich, P. Ghosh[1], E. Hellbär, A. Kotynia[1], M. Koziel, E. Krebs, P. Larionov[1], A. Lebedev[3], Qiyan Li[4], H. Malygina[5,1], J. Michel, B. Milanović, C. Müntz, B. Neumann, P. Reichelt, M. Singla[1], I. Sorokin[5,1], J. Stroth[1], T. Tischler, C. Trageser, I. Vassiliev, B. Wiedemann

- **Frankfurt, Germany, Institute for Computer Science, Goethe Universität Frankfurt**

  S. Böttger, T. Breitner, H. Engel, C. García Chávez, J. Gebelein, T. Janson, U. Kebschull, C. Lara, J. Lehrbach, S. Manz, A. Oancea

- **Gatchina, Russia, Petersburg Nuclear Physics Institute, NRC Kurchatov Institute (PNPI)**

  V. Baublis, V. Dobyrn, V. Golovtsov, Vladimir Ivanov, A. Khanzadeev, L. Kochenda, B. Komkov, P. Kravtsov, E. Kryshen, L. Kudin, N. Miftakhov, V. Nikulin, V. Poliakov, E. Rostchin, Yu. Ryabov, V. Samsonov, O. Tarassenkova, S. Volkov, E. Vznuzdaev, M. Vznuzdaev, M. Zhalov

- **Gießen, Germany, II. Physikalisches Institut, Justus-Liebig-Universität Gießen**

  C.A. Dritsa, C. Höhne, S. Lebedev[3], E. Lebedeva, T. Mahmoud

- **Guwahati, India, Department of Physics, Gauhati University**

  B. Bhattacharjee, B. Debnath, K. Dey, R. Talukdar

- **Hefei, China, Department of Modern Physics, University of Science & Technology of China (USTC)**

  Hongfang Chen, Cheng Li, Haiping Peng, Ming Shao, Yongjie Sun, Zebo Tang, Yifei Zhang

- **Heidelberg, Germany, Physikalisches Institut, Universität Heidelberg**

  I. Deppner, D. Gottschalk, N. Herrmann, Tae Im Kang, P.-A. Loizeau, C. Simon, Ya Peng Zhang

- **Heidelberg, Germany, Zentrales Institut für Technische Informatik, Universität Heidelberg, Standort Mannheim**

  T. Armbruster, U. Brüning, P. Fischer, C. Kreidl, M. Krieger, F. Lemke, M. Nüssle, I. Peric, S. Schatral, D. Wohlfeld

- **Jaipur, India, Physics Department, University of Rajasthan**

  R. Raniwala, S. Raniwala

- **Jammu, India, Department of Physics, University of Jammu**

  A. Bhasin, A. Gupta, S. Mahajan, B.V.K.S. Potukuchi, S.S. Sambyal, M.K. Sharma

- **Katowice, Poland, Institute of Physics, University of Silesia**

  A. Bubak, A. Grzeszczuk, E. Kaptur, S. Kowalski, K. Schmidt, E. Stephan, W. Zipper

- **Kharagpur, India, Indian Institute of Technology**

  P. Banerjee, T.K. Bhattacharyya, A. Haldar, S. Haldar, A.K. Singh

- **Kolkata, India, Department of Physics, Bose Institute**

  S. Das, S.K. Ghosh, S. Raha, R. Ray

- **Kolkata, India, Department of Physics and Department of Electronic Science, University of Calcutta**

  S. Bandyopadhyay, A. Bhattacharyya, A. Chakrabarti, Sanatan Chattopadhyay, G. Gangopadhyay

- **Kolkata, India, Variable Energy Cyclotron Centre (VECC)**

  Z. Ahammed, P.P. Bhaduri, S. Biswas, Subhasis Chattopadhyay, M. Dey, A.K. Dubey, M.S. Ganti, S.A. Khan, T. Nayak, S. Pal, A. Roy, J. Saini, R.N. Singaraju, V. Singhal, P. Trivedy, Y.P. Viyogi

- **Kraków, Poland, AGH University of Science and Technology (AGH)**

  M. Baszczyk, A. Drozd, J. Gajda, P. Gryboś, K. Kasiński, R. Kłeczek, P. Kmon, W. Kucewicz, P. Maj, P. Otfinowski, J. Rauza, R. Szczygieł, M. Żoładź

- **Kraków, Poland, Marian Smoluchowski Institute of Physics, Jagiellonian University**

  M. Adamczyk, T. Barczyk, J. Brzychczyk, L. Dutka, Z. Majka, R. Najman, R. Płaneta, Z. Sosin, P. Staszel, A. Wieloch

- **Kyiv, Ukraine, High Energy Physics Department, Kiev Institute for Nuclear Research (KINR)**

  M. Borysova, A. Kovalchuk, V. Kyva, V. Militsija, I. Panasenko, V. Pugatch, D. Storozhyk

- **Kyiv, Ukraine, Department of Nuclear Physics, National Taras Shevchenko University of Kyiv**

  O. Bezshyyko, I. Kadenko, Y. Onishchuk, V. Plujko

- **Moscow, Russia, Institute for Nuclear Research (INR)**

  M. Golubeva, F. Guber, A. Ivashkin, O. Karavichev, T. Karavicheva, E. Karpechev, A. Kurepin, A. Maevskaya, V. Marin, O. Petukhov, I. Pshenichnov, A. Reshetin, A. Sadovsky, V. Tiflov, N. Topil'skaya, E. Usenko

- **Moscow, Russia, Institute for Theoretical and Experimental Physics (ITEP)**

  A. Akindinov, S. Belogurov, A. Chernogorov, D. Golubkov, F. Khasanov, S. Kiselev, I. Korolko, K. Mikhailov, E. Ovcharenko, P. Polozov, M. Prokudin, I. Rostovtseva, A. Semennikov, A. Stavinskiy, Yu. Zaitsev

- **Moscow, Russia, Kurchatov Institute**

  D. Blau, A. Kazantsev, V. Manko, I. Yushmanov

- **Moscow, Russia, National Research Nuclear University MEPhI**

  E. Atkin, Yu. Bocharov, O. Malyatina, A. Petrovskiy, V. Shumikhin, A. Simakov, M. Strikhanov, Yu. Volkov

- **Moscow, Russia, Skobeltsyn Institute of Nuclear Phyiscs, Lomonosov Moscow State University (SINP-MSU)**

  N. Baranova, D. Karmanov, M. Korolev, M. Merkin, V. Popov, A. Voronin

- **Münster, Germany, Institut für Kernphysik, Westfälische Wilhelms Universität Münster**

  R. Berendes, C. Bergmann, D. Emschermann, N. Heine, Ch. Klein-Bösing, W. Verhoeven, J.P. Wessels

- **Obninsk, Russia, National Research Nuclear University**

  N. D'Ascenzo, A. Galkin, V. Galkin, D. Ossetski, V. Saveliev

- **Prag, Czech Republic, Czech Technical University (CTU)**

  V. Petráček, V. Pospisil, L. Škoda

- **Protvino, Russia, Institute for High Energy Physics (IHEP)**

  S. Golovnya, I. Lobanov, E. Lobanova, V. Rykalin, S. Sadovsky, Yu. Tsyupa, A. Vorobiev

- **Pusan, Korea, Pusan National University (PNU)**

  Kunsu Oh, Jihye Song, Jun-Gyu Yi, In-Kwon Yoo

- **Řež, Czech Republic, Nuclear Physics Institute, Academy of Sciences of the Czech Republic**

  A. Kugler, O. Svoboda, P. Tlustý

- **Split, Croatia, University of Split**

  M. Anđelić, I. Carević, M. Dželalija

- **Srinagar, India, Department of Physics, University of Kashmir**

  F. Ahmad, S. Ahmad, S. Bashir, F. Mir, W. Raja

- **St. Petersburg, Russia, Ioffe Physico-Technical Institute, Russian Academy of Sciences**

  V. Eremin, E. Verbitskaya

- **St. Petersburg, Russia, V.G. Khlopin Radium Institute (KRI)**

  O. Batenkov, V. Jakovlev, V. Kalinin, A. Veshikov

- **St. Petersburg, Russia, St. Petersburg State Polytechnic University (SPbSPU)**

  A. Berdnikov, Y. Berdnikov

- **Strasbourg, France, Institut Pluridisciplinaire Hubert Curien (IPHC), IN2P3-CNRS and Université de Strasbourg**

  G. Claus, A. Dorokhov, W. Dulinski, M. Goffe, A. Himmi, K. Jaaskelainen, F. Rami, I. Valin, M. Winter

- **Tübingen, Germany, Physikalisches Institut, Eberhard Karls Universität Tübingen**

  B. Heß, E. Lavrik, A. Lymanets[5], H.R. Schmidt, J. Wiechula

- **Varanasi, India, Department of Physics, Banaras Hindu University**

  A. Prakash, B.K. Singh, C.P. Singh

- **Warsaw, Poland, Institute of Experimental Physics, University of Warsaw**

  M. Kirejczyk, T. Matulewicz, K. Piasecki, K. Poźniak[10], J. Rożynek, B. Sikora, K. Siwek-Wilczyńska, I. Skwira-Chalot, J. Tarasiuk, A. Turowiecki, K. Wiśniewski, W. Zabołotny[10]

- **Wuhan, China, Institute of Particle Physics, Hua-zhong Normal University (CCNU)**

  Xu Cai, Guangming Huang, Feng Liu, Dong Wang, Yaping Wang, Changzhou Xiang[6], Nu Xu, Zhongbao Yin, Daicui Zhou

- **Wuppertal, Germany, Fachbereich Physik, Bergische Universität Wuppertal**

  K.-H. Becker, K.-H. Kampert, J.M. Kopfer, C. Pauly, J. Pouryamout, S. Querchfeld, J. Rautenberg, S. Reinecke

- **Zagreb, Croatia, Ruđer Bošković Institute**

  Z. Basrak, R. Čaplar, I. Gašparić

Additional affiliations:

[1] GSI Helmholtzzentrum für Schwerionenforschung GmbH (GSI), Darmstadt, Germany

[2] Institut für Kernphysik, Goethe Universität Frankfurt, Frankfurt, Germany

[3] Laboratory of Information Technologies, Joint Institute for Nuclear Research (JINR-LIT), Dubna, Russia

[4] Institute of Particle Physics, Hua-zhong Normal University (CCNU), Wuhan, China

[5] High Energy Physics Department, Kiev Institute for Nuclear Research (KINR), Kyiv, Ukraine

[6] Physikalisches Institut, Universität Heidelberg, Heidelberg, Germany

[7] also: King Abdulaziz City for Science and Technology (KACST), Riyadh, Saudi Arabia

[8] also: Comenius University in Bratislava, Bratislava, Slovakia

[9] also: Institute of Space Science, Bucharest, Romania

[10] also: Institute of Electronic Systems, Warsaw University of Technology, Warsaw, Poland

Contacts

Chairman of the Collaboration Board
Yogendra P. Viyogi
viyogi@veccal.ernet.in

Spokesman
Peter Senger
p.senger@gsi.de

Deputy Spokesman   **Deputy Spokesman**
Yuri Zaitsev   Subhasis Chattopadhyay
zaitsev@itep.ru   sub@veccal.ernet.in

Technical Coordinator
Walter Müller
w.f.j.mueller@gsi.de

Physics Coordinator
Volker Friese
v.friese@gsi.de

Ressource Coordinator
Jürgen Eschke
j.eschke@gsi.de

Management Board
S. Chattopadhyay, N. Herrmann, M Petrovici, F. Rami, J. Stroth, Y. Zaitsev

http://www.fair-center.eu/for-users/experiments/cbm.html